

**FLUID-STRUCTURE INTERACTION (FSI) OF FLOW PAST
ELASTICALLY SUPPORTED RIGID STRUCTURES**

A Thesis
Presented to
The Academic Faculty

by

Mustafa Can Kara

In Partial Fulfillment
of the Requirements for the Degree
Doctor of Philosophy in the
School of Civil and Environmental Engineering

Georgia Institute of Technology
May 2013

COPYRIGHT 2013 BY MUSTAFA CAN KARA

**FLUID-STRUCTURE INTERACTION (FSI) OF FLOW PAST
ELASTICALLY SUPPORTED RIGID STRUCTURES**

Approved by:

Dr. KENNETH M. WILL, Advisor
School of Civil and Environmental
Engineering
Georgia Institute of Technology

Dr. THORSTEN STOESSER, Advisor
Hydro-Environmental Research Center
Cardiff School of Engineering
Cardiff University

Dr. DONALD W. WHITE
School of Civil and Environmental
Engineering
Georgia Institute of Technology

Dr. DONALD R. WEBSTER
School of Civil and Environmental
Engineering
Georgia Institute of Technology

Dr. CYRUS K. AIDUN
School of Mechanical engineering
Georgia Institute of Technology

Date Approved: March 11, 2013

Dedicated to my wife Sibel Kara

ACKNOWLEDGEMENTS

I am indebted to a number of people, some of whom are detailed below.

First of all, I would like to express my sincere and deepest gratitude to my supervisors Dr. Kenneth M Will and Dr. Thorsten Stoesser for their generous support, great patience and enormous encouragement throughout my research. Dr. Will motivated me with his great advising experience and positive suggestions from the start of my PhD until I finish writing my dissertation. Also, I am greatly indebted to Thorsten who provided me an excellent opportunity to work on computational fluid dynamics and to develop new techniques under his guidance with his immense knowledge and experience in hydraulic engineering. This thesis without his guidance would not exist in its present form.

I am very grateful to the members of my advisory committee, Dr. Donald R Webster, Dr. Donald W White and Dr. Cyrus K Aidun for reading this study and providing many constructive, valuable comments and discussions. Their suggestions and recommendations on different aspects of my research helped me improve my dissertation.

I would like to thank Dr. Phanish Suryanarayana for providing me his cluster to run my last three-dimensional simulations in my research, which saved time during the course of this work.

I am very grateful to my friends in Atlanta who made my life and study enjoyable. Many thanks are due to Ercan Cacan, Hatun Cacan and “tombis” Hazal for their endless support, understanding and encouragement. Special thanks to “Busracan” (Onur Celik)

and “Abla” (Dr. Gence Genc) for providing a pleasant and friendly atmosphere during their stay in Atlanta.

I would like to acknowledge the help of my lab mates, Sandeep Kumar Bomminayuni, Dr Dongjin Kim, Dr Sujin Kim and Mehtap Cevheri for their help and cooperation during my study. Many thanks to my colleagues and friends from Structures group including Dr. Ben Deaton, Dr. Efe Guney, Dr. Yavuz Menten, Dr. Cagri Ozgur and Dr. Ilker Kalkan for their moral support during the five years I worked there.

My appreciation goes to all my friends in Atlanta including Hilal Menten, Derya Aksaray, Yasin Yazicioglu, Nazli Donmezer, Necmettin Cevheri, Ilker Telci, Ayten Telci and “hey man” Deniz Telci. I am also grateful to my fellow Resident Advisor (RA) friends and my supervisor Shannon Hobbs at 10th and Home.

I wish to thank my parents in Turkey Aysel, Ali Osman Kara, Aynur Kerpici and my brother Aycan Kara, my sister Mine Kerpici (“karakiz”), my sister-in-law Gul Kara and my niece “japon” Dilara for their understanding and encouragement during my studies. I owe them everything and their love provided my inspiration during my study.

Last, but not the least, I am forever indebted to my wife Sibel Kara for her unrequited love, endless patience and continuous encouragement when it was most required not only during the course of this work but also at times I really needed help. Her unconditional support and love was what turned this adventure into a success eventually. This study would not have been completed without her unyielding love and devotion.

TABLE OF CONTENTS

	Page
ACKNOWLEDGEMENTS	iv
LIST OF TABLES	x
LIST OF FIGURES	xi
LIST OF SYMBOLS	xxii
LIST OF ABBREVIATIONS	xxvi
SUMMARY	xxviii
 <u>CHAPTER</u>	
1 INTRODUCTION	1
1.1 Statement of the Problem	1
1.2 Research Objectives and Scope	6
1.3 Organization of Dissertation	8
2 INTRODUCTION TO VORTEX-INDUCED VIBRATIONS (VIVs)	10
2.1 Review of Previous Work	11
2.1.1 Fluid-Structure Interaction	11
2.1.2 Numerical Modeling of VIVs	14
2.2 Research Gaps and Objectives of this Study	23
3 NUMERICAL METHODOLOGY	26
3.1 Basic Navier-Stokes (NS) Solver	26
3.1.1 Formulation in Cartesian Coordinates	26
3.1.1.1 Governing Equations	26
3.1.1.2 Spatial Discretization and Local Mesh Refinement (LMR)	29

3.1.1.2	Time Advancement Scheme	31
3.1.2	Poisson Equation and the Solution Procedure	32
3.1.3	Implementation of Boundary Conditions	34
3.1.3.1	Dirichlet and Neumann Boundary Conditions	34
3.1.3.2	Convective Boundary Condition	36
3.1.3.2	Periodic Boundary Condition	36
3.2	Structural Solver	37
3.2.1	Problem Formulation	37
3.2.2	Ordinary Differential Equation (ODE)	38
3.3	Strong Coupling Scheme using Hamming's 4 th Order Predictor-Corrector Method	40
3.4	Parallelization	45
4	IMMERSED BOUNDARY METHOD (IBM) AND ITS VALIDATION	47
4.1	Direct Forcing Method	49
4.1.1	Geometric Definitions	49
4.1.2	Force Formulation	51
4.2	Choice of the Regularized Delta Functions	53
4.2.1	Regular Discrete Delta Function (RDDF)	54
4.2.2	Smoothed Discrete Delta Function (SDDF)	55
4.3	Validation of the IB method	57
4.4	Summary	67
5	TWO-DIMENSIONAL (2D) VALIDATION CASES ON FREE AND FORCED VIBRATION OF CYLINDERS	68
5.1	Flow Around a Stationary Cylinder	71
5.2	Forced Vibration of a Cylinder	74
5.2.1	Flow Over an In-line Oscillating Cylinder	75

5.2.3	Flow over a Transversely Oscillating Cylinder	80
5.3	Vortex-Induced Vibration (VIV) of Cylinder	87
5.4	Flow Past Two Cylinders in Tandem Arrangement	106
5.4.1	Unsteady Flow Past Two Stationary Cylinders in Tandem Arrangement	106
5.4.1.1	Re=100 Flow Past Two Stationary Cylinders in Tandem Arrangement $L_x = 6.0D$	110
5.4.1.2	Re=100 Flow Past Two Stationary Cylinders in Tandem Arrangement $L_x = 2.5D$	114
5.4.2	Vortex-Induced Vibration (VIV) of Two Cylinders in Tandem Arrangement	119
5.5	Summary	144
6	THREE-DIMENSIONAL (3D) VALIDATION CASES ON STATIONARY AND FORCED VIBRATION OF A CYLINDER	146
6.1	Large-Eddy Simulation (LES) of the Flow over a Circular Cylinder at Reynolds Number 3900	146
6.2	Large-Eddy Simulation (LES) of the Flow over an Oscillating Circular Cylinder at Reynolds Number 3900	171
6.3	Summary	183
7	CONCLUSIONS AND RECOMMENDATIONS FOR FUTURE RESEARCH	184
7.1	Summary	184
7.2	Conclusions	184
7.2.1	An improved Immersed Boundary Method (IBM)	185
7.2.2	A Simple and Better Boundary Definition	185
7.2.3	Validation of the Method for Moving Boundary Problems	186
7.2.4	Flow Interference between Multiple Stationary and Oscillating Cylinders	186
7.2.5	LES of Turbulent Flow Past a Stationary and Oscillating Cylinder	187

7.3 Unique Contributions	187
7.4 Recommendations for Further Research	188
APPENDIX A: Computation of the Hydrodynamic Forces	190
REFERENCES	191
VITA	205

LIST OF TABLES

	Page
Table 4-1 Time-averaged drag and amplitude of lift coefficients, and the Strouhal number for flow around a stationary square cylinder at $Re = 100$	65
Table 5-1 Time-averaged drag and amplitude of lift coefficients, and the Strouhal number for flow around a stationary cylinder at $Re = 100$.	73
Table 5-2 Dimensionless coefficients for flow around an oscillating cylinder at $Re = 185$ which has near the natural shedding frequency. Resolution near the structure is $\Delta x = \Delta y = 0.0156D$ and the time step Δt is 3×10^{-3}	81
Table 5-3 Summary of the aerodynamic data for flows past a single cylinder (Case 1), two cylinders in tandem arrangement at $L_x = 2.5D$ (Case 2) and $L_x = 6.0D$ (Case 3) at $Re = 100$.	119
Table 6-1 Comparison of flow parameters of the experimental and LES studies for flow around circular cylinder at $Re = 3900$	155

LIST OF FIGURES

	Page
Figure 1-1 Tacoma Narrows Bridge collapse in 1940: (a) onset of twisting by VIV (b) total collapse. Source: http://www.math.utah.edu/~gustafso/tnarrows/tnarrows_intro.html	3
Figure 1-2 (a) Individual Wind Turbine (b) Wind Farm. Source: http://www.energyacuity.com/blog/bid/198593/Vague-Maritime-Laws-Preventing-U-S-Offshore-Wind-Development	4
Figure 1-3 A Tension Leg Platform (TLP).Source: http://www.nd.edu/~nathaz/research/Luigi.html	6
Figure 2-1 Grid around a cylinder (a) Traditional body fitted grid (b) Cartesian grid with an immersed boundary.	15
Figure 2-2 Typical 2D Stencil showing an interpolation strategy using three fluid cells in in-line and cross-flow directions for the cell cut by the cylinder boundary in (x,y) plane.	18
Figure 2-3 Time histories of pressure drag coefficient for horizontally oscillating cylinder; comparison between the original sharp-interface IBM and the regionally conservative cut-cell method by Seo and Mittal (2011)	22
Figure 3-1 Schematic representation of a grid cell (i,j,k) in Cartesian coordinates and its staggered variable arrangement with u, v and w being the velocity components in global X, Y and Z direction, respectively at the cell face centers and p being the pressure at the cell center.	28
Figure 3-2 A partial grid example with 2 levels of refinement, r. Pressure cells are shown at the center of each grid cell.	30
Figure 3-3 The implementation of proper Dirichlet and Neumann boundary condition on XY plane of the computational domain	35
Figure 3-4 The implementation of proper periodic boundary condition on XY plane of the computational domain for pressure cells. Arrows show the directions of data duplication.	37
Figure 3-5 Schematic representation of the translation of a cylinder (yc(t)) with an incoming flow, U_∞ , mass M, spring constant K, damping C and diameter D.	38
Figure 3-6 A schematic representation of the strong coupling scheme	42

Figure 3-7 Exchange of pressure and velocity values for one ghost cell slice. White bricks denote ghost cell values and black bridges refer to subdomain values (Croce et al., 2004)	46
Figure 4-1 The definition of marker elements along the circumference of a circular structure for interface forcing scheme (Left graph) and in the entire solid domain for solid domain forcing scheme (Right graph). Small solid circles indicate the (equidistant) locations of marker points.	50
Figure 4-2 Comparison of a regular discrete delta function ϕ_3 and its corresponding smooth function ϕ_3^* (This figure is taken from Yang et al. (2009))	56
Figure 4-3 Definition of the geometry and integration domain by Breuer et al. (2000)	58
Figure 4-4 Geometry of the computational domain around a rectangular structure. Local Mesh Refinement (LMR) is used to increase the resolution around the immersed structure (every 5th grid point is shown).	59
Figure 4-5 The definition of marker elements along the circumference of a square structure for interface forcing scheme (Left graph) and in the entire solid domain for solid domain forcing scheme (Right graph). Small solid squares indicate the (equidistant) locations of marker points.	60
Figure 4-6 Streamlines around the square cylinder at Reynolds number 30. Top figure corresponds to results through interface forcing while the bottom one is the result of the simulation through solid domain forcing. Recirculation is depicted in the top figure in black.	61
Figure 4-7 Iso-contours of the pressure field of the channel flow around a fixed cylinder at $Re = 30$ (top row) and $Re = 100$ (bottom row). Interface forcing around the circumference (left column) and solid domain forcing including interior (right column) of the structure.	63
Figure 4-8 Time series of drag and lift coefficients at $Re = 100$ using two different forcing configurations.	64
Figure 4-9 Flow visualization of U velocity, V velocity and Z vorticity contour plots for $Re = 30$ (top) and $Re = 100$ (bottom) via solid domain forcing.	66
Figure 5-1 A sketch of the grid employed in the vicinity of the cylinder for current simulations. The domain size is $52D \times 36D$. A uniform velocity boundary is specified at the inlet; a convective boundary condition is used at the outlet; symmetric boundary (every 6th grid point is shown)	70

Figure 5-2 Contour plots and flow visualization around cylinder at $Re = 100$. Top: U-velocity contour. Middle: V-velocity contour. Bottom: Z-Vorticity Contour	72
Figure 5-3 Distribution of Strouhal Number (St) versus Reynolds number (Re) (logarithmic scale is used on the horizontal axis)	74
Figure 5-4 In-line oscillating cylinder in a quiescent fluid at $Re = 100$, $KC = 5$. Pressure and vorticity contours at four different phase-angles. $-1.1 < P < 0.6$ with intervals of 0.09 and $26.0 < \omega z < 26.0$ (a) 0° (b) 96° (c) 192° (d) 288°	77
Figure 5-5 In-line oscillating cylinder in a quiescent fluid at $Re = 100$ and $KC = 5$. Velocity Profiles at three different phase angles (a) 180° (b) 210° (c) 330° . Lines are the present computation, symbols are the experimental data of Dutsch et al. (1998) at $x = -0.6D$, $x = 0.0D$, $x = 0.6D$ and $x = 1.2D$.	79
Figure 5-6 Evolution in time of the drag force on a cylinder oscillating in a quiescent flow at $Re = 100$ and $KC = 5$. (o) boundary conforming simulation (Dutsch et al., 1998); (---) present computation	79
Figure 5-7 Time-periodic variation of the drag coefficient in the case of a translationally oscillating cylinder in uniform cross-flow at $Re = 185$ and $CFL = 0.2$. Top left: present method using interface forcing with 3-point smooth Dirac Delta function with $0.05D \times 0.05D$ uniform grid throughout the domain. Top right and Bottom left: present method using solid domain forcing with 3-point regular and smooth dirac delta function, respectively with $0.0156D \times 0.0156D$ grid resolution near cylinder. Bottom right: method of Kajishima and Takiguchi (2002) implemented into Uhlmann (2005)'s solver which utilizes interface forcing method.	83
Figure 5-8 Time periodic variation of the lift coefficients for flow past an oscillating cylinder at $Re = 185$ and $CFL = 0.2$. Top left: present method using interface forcing with 3-point smooth dirac delta function with $0.05D \times 0.05D$ uniform grid throughout the domain. Top right and Bottom left: present method using solid domain forcing with 3-point regular and smooth dirac delta function, respectively with $0.0156D \times 0.0156D$ grid resolution near cylinder. Bottom right: results of Yang et al (2009) using a 2-point hat function for the oscillating cylinder.	84

Figure 5-9 Pressure contours around cylinder at an arbitrary instant of time during the transverse oscillation of the cylinder at $Re = 185$. The location of the cylinder is shown at the bottom left of each figure. Left: Present method via Interface forcing. Right: Present method via Solid domain forcing. Both figures are produced utilizing smooth 3-point delta function.	85
Figure 5-10 Contour plots around cylinder at an arbitrary instant of time during the transverse oscillation of the cylinder at $Re = 185$. The location of the cylinder is at $X = 22 D$ and at $Y = 18.2D$. Top: U-velocity contour. Middle: V-velocity contour. Bottom: Z-Vorticity Contour	86
Figure 5-11 Experiment conducted by Anagnostopoulos and Bearman (1992) ($k = 69.48 \text{ kN/m}$, $c=0.0039 \text{ Ns/m}$, $D=1.6 \text{ mm}$, $fN = 7.016 \text{ Hz}$, $m=35.75 \text{ g}$, $\xi=0.0012$)	88
Figure 5-12 Time histories of the displacements for the freely vibrating cylinder in the cross-stream direction at $Re = 90\sim 140$ at start-up phase. (a) $Re = 90$, (b) $Re = 95$, (c) $Re = 100$, (d) $Re = 105$, (e) $Re = 110$, (f) $Re = 115$, (g) $Re = 120$, (h) $Re = 125$, (i) $Re = 130$, (j) $Re = 135$, (k) $Re = 140$	91
Figure 5-13 Time histories of the displacements for the freely vibrating cylinder in the cross-stream direction at $Re = 90\sim 140$ at steady phase. (a) $Re = 90$, (b) $Re = 95$, (c) $Re = 100$, (d) $Re = 105$, (e) $Re = 110$, (f) $Re = 115$, (g) $Re = 120$, (h) $Re = 125$, (i) $Re = 130$, (j) $Re = 135$, (k) $Re = 140$	94
Figure 5-14 Instantaneous pressure contours of a freely vibrating cylinder in the cross-stream direction (a) $Re = 95$, (b) $Re = 100$, (c) $Re = 105$, (d) $Re = 110$, (e) $Re = 120$, (f) $Re = 130$	95
Figure 5-15 Instantaneous swirl strength contours of a freely vibrating cylinder in the cross-stream direction (a) $Re = 95$, (b) $Re = 100$, (c) $Re = 105$, (d) $Re = 110$, (e) $Re = 120$, (f) $Re = 130$	97
Figure 5-16 Instantaneous contours of U velocity, V velocity and spanwise vorticity for a freely vibrating cylinder in the cross-stream direction (a) $Re = 95$, (b) $Re = 100$, (c) $Re = 105$, (d) $Re = 110$, (e) $Re = 120$, (f) $Re = 130$	101
Figure 5-17 Time periodic variation of the drag and lift coefficients for flow past a freely vibrating cylinder in the cross-stream direction at steady phase in the lock-in regime (a) C_{drag} at $Re = 100$, (b) C_{lift} at $Re = 100$, (c) C_{drag} at $Re = 105$, (d) C_{lift} at $Re = 105$, (e) C_{drag} at $Re = 110$, (f) C_{lift} at $Re = 110$	102

Figure 5-18 Time periodic variation of the drag and lift coefficients for flow past a freely vibrating cylinder in the cross-stream direction at start-up and steady phases beyond lock-in regime (a) start-up at $Re = 95$, (b) steady at $Re = 95$, (c) start-up at $Re = 120$, (d) steady at $Re = 120$, (e) start-up at $Re = 130$, (f) steady at $Re = 130$	103
Figure 5-19 Comparison of maximum oscillation amplitude A_{max} (top) and frequency of the oscillation (bottom); o, present results; ----, experiment in Anagnostopoulos and Bearman (1992); \diamond , computation in Nomura (1983); ∇ , computation in Yang et al. (2008); +, computation in Wei et al. (1995); \square , computation in Schulz and Kallinderis (1998); Δ , computations in Li et al. (2002)	105
Figure 5-20 Classification of flow patterns for two tandem circular cylinders in cross-flow, from Igarashi (1981) (Figure taken from Sumner (2010))	107
Figure 5-21 A close snapshot of the grid employed in the vicinity of 2 cylinders for laminar flow past 2 structures in tandem arrangement, spaced relatively at 6.0D (Top) and 2.5D (Bottom). The domain size is 50D X 36D. A uniform velocity boundary is specified at the inlet; a convective boundary condition is used at the outlet; symmetric boundary (every 3th point is shown)	109
Figure 5-22 Instantaneous contours of U velocity (top), V velocity (middle) and spanwise vorticity (bottom) for flow over two tandem cylinders at $L_x = 6.0D$ at $Re = 100$	111
Figure 5-23 Instantaneous pressure (Top) and Swirl Strength (Bottom) contours of flow over two tandem cylinders at $L_x = 6.0D$ at $Re = 100$	112
Figure 5-24 Streamlines for flow over two tandem cylinders at $L_x = 6.0D$ at $Re = 100$	112
Figure 5-25 Time histories of lift and drag force coefficients for flow over two tandem cylinders at $L_x = 6.0D$ at $Re = 100$. Top: Forces acting on upstream cylinder; Bottom: Forces acting on downstream cylinder	113
Figure 5-26 Instantaneous contours of U velocity (top), V velocity (middle) and spanwise vorticity (bottom) for flow over two tandem cylinders at $L_x = 2.5D$ at $Re = 100$	116
Figure 5-27 Instantaneous pressure (Top) and Swirl Strength (Bottom) contours of flow over two tandem cylinders at $L_x = 2.5D$ at $Re = 100$	117
Figure 5-28 Streamlines for flow over two tandem cylinders at $L_x = 2.5D$ at $Re = 100$	117

- Figure 5-29 Time histories of lift and drag force coefficients for flow over two tandem cylinders at $L_x = 2.5D$ at $Re = 100$. Top: Forces acting on upstream cylinder; Bottom: Forces acting on downstream cylinder 118
- Figure 5-30 Schematic drawing of arrangement studied which is tandem arrangement of two identical, elastically mounted cylinders ($k = 69.48$ kN/m, $c=0.0039$ Ns/m, $D=1.6$ mm, $f_N = 7.016$ Hz, $m=35.75$ g., $\xi=0.0012$). 122
- Figure 5-31 6 different VIV Cases studied in the current research for two cylinders in tandem arrangement at $Re = 100$ ($k = 69.48$ kN/m, $c=0.0039$ Ns/m, $D=1.6$ mm, $f_N = 7.016$ Hz, $m=35.75$ g., $\xi=0.0012$). 123
- Figure 5-32 $Re = 100$ flow past two cylinders in tandem arrangement at $L_x = 6.0D$ in Case1A in which the upstream cylinder is fixed and the downstream cylinder is free to oscillate. Time-histories of the response (Top) of cylinder 1 and drag and lift coefficients (Bottom) of both of the cylinders. The quantities with suffix 1 are associated with upstream cylinder, while those with suffix 2 are for downstream cylinder. 126
- Figure 5-33 $Re = 100$ flow past two cylinders in tandem arrangement at $L_x = 2.5D$ in Case1B in which the upstream cylinder is fixed and the downstream cylinder is free to oscillate. Time-histories of the response (Top) of cylinder 1 and drag and lift coefficients (Bottom) of both of the cylinders. The quantities with suffix 1 are associated with upstream cylinder, while those with suffix 2 are for downstream cylinder. 128
- Figure 5-34 $Re = 100$ flow past two cylinders in tandem arrangement at $L_x = 6.0D$ in Case2A in which both cylinders are free to oscillate. Time-histories of the response (Top) of cylinder 1 and 2, and drag and lift coefficients (Bottom) of both of the cylinders. The quantities with suffix 1 are associated with upstream cylinder, while those with suffix 2 are for downstream cylinder. 129
- Figure 5-35 $Re = 100$ flow past two cylinders in tandem arrangement at $L_x = 2.5D$ in Case2B in which both cylinders are free to oscillate. Time-histories of the response (Top) of cylinder 1 and 2, and drag and lift coefficients (Bottom) of both of the cylinders. The quantities with suffix 1 are associated with upstream cylinder, while those with suffix 2 are for downstream cylinder. 130

- Figure 5-36 $Re = 100$ flow past two cylinders in tandem arrangement at $Lx = 6.0D$ in Case3A in which they are rigidly connected to each other and are free to oscillate in the cross-stream direction. Time-histories of the response (Top) of cylinders, and independent (Middle) and total (Bottom) drag and lift coefficients of the cylinders. The quantities with suffix 1 are associated with upstream cylinder, while those with suffix 2 are for downstream cylinder. 131
- Figure 5-37 $Re = 100$ flow past two cylinders in tandem arrangement at $Lx = 2.5D$ in Case3B in which they are rigidly connected to each other and are free to oscillate in the cross-stream direction. Time-histories of the response (Top) of cylinders, and independent (Middle) and total (Bottom) drag and lift coefficients. The quantities with suffix 1 are associated with upstream cylinder, while those with suffix 2 are for downstream cylinder. 133
- Figure 5-38 Flow past rigidly coupled cylinders in tandem arrangement ($Lx = 2.5D$) at $Re = 100$: Time periodic variation of drag and lift force coefficients (Top Left and Top Right) with respect to cylinders' displacement; power spectra of the time histories of drag coefficient (Middle) and lift coefficient (Bottom), respectively. 136
- Figure 5-39 Flow past rigidly coupled cylinders in tandem arrangement ($Lx = 6.0D$) at $Re = 100$: Time periodic variation of drag and lift force coefficients (Top Left and Top Right) with respect to cylinders' displacement; power spectra of the time histories of drag coefficient (Middle) and lift coefficient (Bottom), respectively. 137
- Figure 5-40 Pressure Contours (Left Column) and streamlines with vorticity contours (Right Column) for rigidly coupled cylinders in tandem arrangement at $Lx = 6.0D$, transversely oscillating at $Re = 100$ with $m^* = 150$, $\xi = 0.0012$ and $U_{red} = 5.58$. The horizontal red dash-dotted lines for pressure and vorticity plots in Phase angles (θ) 0° to 315° indicate the initial rest positions of the cylinders. The discussions in the text reveal an important vorticity interaction. The phase instants ($\theta = 0^\circ$.. 360°) are specified as black color filled red circles on the time-history of displacement at the bottom of the figure along with time histories of total drag and lift coefficients during one cycle of oscillation. C_{drag} (black solid line) and C_{lift} (blue solid line) refer to total drag and lift coefficients acting on the structures; $Y_c(t)/D$ is the position of the coupled cylinders in cross-stream direction. 140

- Figure 5-41 Pressure Contours (Left Column) and streamlines with vorticity contours (Right Column) for rigidly coupled cylinders in tandem arrangement at $L_x = 2.5D$, transversely oscillating at $Re = 100$ with $m^* = 150$, $\xi = 0.0012$ and $U_{red} = 5.58$. The horizontal red dash-dotted lines for pressure and vorticity plots in Phase angles (θ) 0° to 315° indicate the initial rest positions of the cylinders. The discussions in the text reveal an important vorticity interaction. The phase instants ($\theta = 0^\circ \dots 360^\circ$) are specified as black color filled red circles on the time-history of displacement at the bottom of the figure along with time histories of total drag and lift coefficients during one cycle of oscillation. C_{drag} (black solid line) and C_{lift} (blue solid line) refer to total drag and lift coefficients acting on the structures; $Y_c(t)/D$ is the position of the coupled cylinders in cross-stream direction. 143
- Figure 6-1 Computational setup and boundary conditions for the flow over a circular cylinder at $Re = 3900$. 149
- Figure 6-2 Top: Cross-sectional (X-Y plane) grid employed with Local Mesh Refinement (LMR) (every fifth computational cell of a locally-refined Cartesian grid is shown) for the flow over a circular cylinder at $Re = 3900$; Bottom: zoom into the cylinder region. 150
- Figure 6-3 Streamlines showing recirculation region behind the cylinder at $Re = 3900$; the top and bottom figures correspond to LES results of Breuer (1998) and present numerical method, respectively 152
- Figure 6-4 Time history of the lift coefficient CL and drag coefficient CD for the flow past a circular cylinder at $Re = 3900$. Top: Results of Breuer (1998). Bottom: Results from present computation. 154
- Figure 6-5 Instantaneous velocities in the ($x-z, y=0$) plane in the wake of a circular cylinder at $ReD = 3900$. Top: (Color) Instantaneous streamwise velocity with contours from -0.2 to 1.0. Middle: (Color) Instantaneous cross-flow velocity with contours from -1.0 to 1.0. Bottom: (Color) Instantaneous spanwise velocity with contours from -0.5 to 1.0. 156
- Figure 6-6 Iso-surfaces in the wake of a circular cylinder at $ReD = 3900$. Top: Iso-surface of normalized $\lambda_2 = 0.004$ obtained by Lysenko et al. (2012) via models (a) TKE b) SMAG. Bottom: Iso-surface of Q-criterion through present method with WALE model. 158
- Figure 6-7 Iso-surface of the fluctuating pressure at $p' = -0.1$ (WALE) for the flow over a circular cylinder at $Re = 3900$. 159
- Figure 6-8 Separating shear layers and development of Karman vortex street in the flow over a circular cylinder at $Re = 3900$. Shown are contours of instantaneous vorticity from $\omega D/U_\infty = 5.0$ to $\omega D/U_\infty = -5.0$. 160

Figure 6-9 The pressure coefficient C_p along the surface of a circular cylinder at $Re = 3900$ ($\theta=0^\circ$ in the stagnation point, \square experimental data of Norberg (1994) at $Re = 4020$, published in Meyer et al. (2010), - - numerical results of Kravchenko and Moin (2000), ... numerical results of Lysenko et al. (2012), ----Present results).	160
Figure 6-10 Mean streamwise velocity on the centerline of the cylinder for the flow over a circular cylinder at $Re = 3900$ (Δ : experimental data of Lourenco and Shih (extracted from Meyer et al. (2010)), o: experimental data of Parnaudeau et al. (2008) , - - -: numerical results of Kravchenko and Moin (2000),: numerical results of Lysenko et al. (2012), ----- Present results.	162
Figure 6-11 Mean streamwise velocity at different locations in the wake of a circular cylinder at $Re = 3900$ (Δ : experimental data of Lourenco and Shih (extracted from Meyer et al. (2010)), - - -: numerical results of Kravchenko and Moin (2000),: numerical results of Lysenko et al. (2012), ----- Present results.	163
Figure 6-12 Mean transverse velocity at different locations in the wake of a circular cylinder at $Re = 3900$ (Δ : experimental data of Lourenco and Shih (extracted from Meyer et al. (2010)), - - -: numerical results of Kravchenko and Moin (2000),: numerical results of Lysenko et al. (2012), ----- Present results.	164
Figure 6-13 Mean streamwise velocity fluctuations at different locations in the wake of a circular cylinder at $Re = 3900$ (Δ : experimental data of Lourenco and Shih (extracted from Meyer et al. (2010)),: numerical results of Lysenko et al. (2012), ----- Present results.	165
Figure 6-14 Mean transverse velocity fluctuations at different locations in the wake of a circular cylinder at $Re = 3900$ (Δ : experimental data of Lourenco and Shih (extracted from Meyer et al. (2010)),: numerical results of Lysenko et al. (2012), ----- Present results.	166
Figure 6-15 Mean streamwise velocity at different locations in the wake of a circular cylinder at $Re = 3900$ (o: experimental data of Ong and Wallace (1996) (extracted from Meyer et al. (2010)), - - -: numerical results of Kravchenko and Moin (2000),: numerical results of Lysenko et al. (2012), ----- Present results.	167
Figure 6-16 Mean transverse velocity at different locations in the wake of a circular cylinder at $Re = 3900$ (o: experimental data of Ong and Wallace (1996) (extracted from Meyer et al. (2010)),: numerical results of Lysenko et al. (2012), ----- Present results.	168

Figure 6-17 Mean streamwise velocity fluctuations at different locations in the wake of a circular cylinder at $Re = 3900$ (o: experimental data of Ong and Wallace (1996) (extracted from Meyer et al. (2010)),: numerical results of Lysenko et al. (2012), ----- Present results.	169
Figure 6-18 Mean transverse velocity fluctuations at different locations in the wake of a circular cylinder at $Re = 3900$ (o: experimental data of Ong and Wallace (1996) (extracted from Meyer et al. (2010)),: numerical results of Lysenko et al. (2012), ----- Present results.	170
Figure 6-19 Time histories of prescribed displacement, velocity, and acceleration in flow past an oscillation cylinder at $Re = 3900$ over two periods of oscillation with frequency, $foD/U_\infty = 0.178$ and maximum amplitude of vibration, $A/D = 0.2$.	173
Figure 6-20 Time histories of drag and lift coefficients in flow past an oscillating cylinder at $Re = 3900$ with oscillation frequency, $foD/U_\infty = 0.178$ and maximum amplitude of vibration, $A/D = 0.2$.	174
Figure 6-21 Vorticity contours for flow over a transversely oscillating cylinder at $Re = 3900$ with oscillation frequency, $foD/U_\infty = 0.178$ and maximum amplitude of vibration, $A/D = 0.2$. The horizontal red dash-dotted lines for the vorticity plots in Phase angles (θ) 270° (Top), 0° (Middle) and 90° (Bottom) indicate the initial rest position of the cylinder.	175
Figure 6-22 Mean streamwise velocity on the centerline of the cylinder for the flow over a stationary and oscillating circular cylinder at $Re = 3900$ (Δ : experimental data of Lourenco and Shih (extracted from Meyer et al. (2010), -----; Present results from flow over a stationary cylinder, -----; Present results from flow over an oscillating cylinder)	176
Figure 6-23 Mean streamwise velocity at different locations in the very near wake of a circular cylinder at $Re = 3900$ (-----; Present results from flow over a stationary cylinder, -----; Present results from flow over an oscillating cylinder).	177
Figure 6-24 Mean streamwise velocity at different locations in the far wake of a circular cylinder at $Re = 3900$ (-----; Present results from flow over a stationary cylinder, -----; Present results from flow over an oscillating cylinder).	178
Figure 6-25 Mean transverse velocity at different locations in the near wake of a circular cylinder at $Re = 3900$ (-----; Present results from flow over a stationary cylinder, -----; Present results from flow over an oscillating cylinder).	179

- Figure 6-26 Mean transverse velocity at different locations in the far wake of a circular cylinder at $Re = 3900$ (-----; Present results from flow over a stationary cylinder, -----; Present results from flow over an oscillating cylinder). 180
- Figure 6-27 Mean streamwise velocity fluctuations at different locations in the wake of a circular cylinder at $Re = 3900$ (-----; Present results from flow over a stationary cylinder, -----; Present results from flow over an oscillating cylinder). 181
- Figure 6-28 Mean transverse velocity fluctuations at different locations in the wake of a circular cylinder at $Re = 3900$ (-----; Present results from flow over a stationary cylinder, -----; Present results from flow over an oscillating cylinder). 182

LIST OF SYMBOLS

A	Oscillation amplitude of the structure
a_y	Acceleration of the structure in transverse direction
B	Blockage ratio
c	Damping coefficient
C	Damping matrix; Spatial operator for convection
C_p	Pressure coefficient
C_D	Drag coefficient
\bar{C}_D	Mean drag coefficient
$(C_D)_{\text{rms}}$	Root Mean Square of drag coefficient
C_L	Lift coefficient
\bar{C}_L	Mean lift coefficient
C_L'	Lift coefficient fluctuation
$(C_L)_{\text{rms}}$	Root Mean Square of lift coefficient
D	Diameter of cylinder; Spatial operator for diffusion
e_{trun}	Local truncation error
f	Scalar function; Frequency
f_i	Momentum forcing vector; Hydrodynamic force vector
f_o	Frequency of the oscillating cylinder
f_e	Shedding frequency of the stationary cylinder
f_n	Natural vibrating frequency of a structure
F_x	Generalized hydrodynamic force on a structure in streamwise direction
F_y	Generalized hydrodynamic force on a structure in transverse direction

H	Plane channel height
h	Mesh size
k	Sub-iteration index; Spring constant
K	Stiffness Matrix
KC	Keulegan-Carpenter number
L	Reference length scale; Span length of the cylinder; Domain length
L_r	Recirculation length
L_x	Distance of arrangement of tandem cylinders
l	Inflow length
m	Structural system mass
m^*	Mass ratio
m_f	Mass of the fluid replaced by the structure
M	Mass Matrix
n	Time step index in time-advancement scheme; Normal direction of the boundary; Number of degree of freedoms of the structure
N_L	Number of force points
p	Corrected pressure
p'	Fluctuating pressure
p^*	Pressure
p_∞	Time-averaged pressure at the inlet plane
Q	Q-criterion
\dot{q}	Generalized accelerations in equation of motion
r	Refinement factor
$r_{1,2}$	Inner and outer radii of a circular ring
r_c	Actual ring radius

Re	Reynolds number
St	Strouhal number
t	Time
t^*	Non-dimensional time
u_i	General notation for velocity components
u, v, w	Streamwise, cross-stream and spanwise velocity components, respectively.
\hat{u}_i	General notation for intermediate velocity components
u_c	Linear velocity of a rigid circle
U	Referenced velocity
u_b, v_b	Prescribed normal velocity component in streamwise and transverse directions
U_∞	Free-stream velocity
U^d	Desired velocity
U_{red}	Reduced velocity
U_{max}	Maximum velocity
V_c	Total volume enclosed by the immersed boundary
x_i	General notation for spatial coordinates
x	Spatial position of the cylinder in streamwise direction
x_c	Center locations of a rigid circle
X, Y, Z	Spatial global coordinates in streamwise, cross-stream and spanwise directions, respectively.
X_l	Location of the forcing points
y	Spatial position of the cylinder in cross-stream direction
w_c	Angular velocity of a circle
α_k	Factor in RK time-advancement scheme
β_k	Factor in RK time-advancement scheme for diffusion

δ	Discrete form of the partial operator
$\delta_{.ij}$	Kronecker's delta
$\Delta x, \Delta y, \Delta z$	Grid spacing in streamwise, cross-stream and spanwise directions, respectively.
Δt	Time step
ΔV_1	Volume of force point
μ	Dynamic viscosity of a fluid
ν	Kinematic viscosity of a fluid
ρ	Density of a fluid
ω	Angular frequency oscillation; Vorticity
ϑ_c	Angular position of the center of a rigid circle
τ_{ij}	Subgrid scale stress tensor at the grid-filter level
ζ	Damping ratio
ϑ	Phase angle
ϕ	Scalar to project the predicted velocity field into a divergence-free space
ϕ_3	3-point RDDF
ϕ_3^*	3-point SDDF
$\langle \rangle$	averaging operator
$()$	First Derivative
$(\ddot{ })$	Second Derivative
$\ S\ $	Rate of Strain tensor
$\ \Omega\ $	Vorticity tensor

LIST OF ABBREVIATIONS

2D	Two-dimensional
3D	Three-dimensional
AB	Adams-Bashforth
ALE	Arbitrary Lagrangian-Eulerian
AMD	Advanced Micro Devices
CDS	Central Differencing Scheme
CFL	Courant-Friedrichs-Levy
CFD	Computational Fluid Dynamics
CN	Crank-Nicholson
CPU	Central Processing Unit
DNS	Direct Numerical Simulation
EOM	Equation of Motion
FD	Finite Differences
FSI	Fluid-Structure Interaction
FVM	Finite Volume Method
IBM	Immersed Boundary Method
KH	Kelvin-Helmholtz
LBA	Lattice-Boltzmann Automata
LDA	Laser Doppler Velocimetry
LES	Large-Eddy Simulation
LFP	Lagrangian Force Point
LMR	Local Mesh Refinement

mgd2	two-dimensional multigrid solver
mgd3	three-dimensional multigrid solver
MPI	Message Passing Interface
NS	Navier-Stokes
ODE	Ordinary Differential Equation
PIV	Particle Image Velocimetry
RDDF	Regularized Discrete Delta Function
RHS	Right-Hand Side
RK	Runge-Kutta
RK2	2 steps Runge-Kutta
RK3	3 steps Runge-Kutta
SIMPLE	Semi-Implicit Method for Pressure-Linked Equations
SDDF	Smooth Discrete Delta Function
SGS	Subgrid Scale
TKE	Turbulence Kinetic Energy
TLP	Tension-Leg Platform
VIV	Vortex-Induced Vibration
WALE	Wall-Adopting Local Eddy-Viscosity

SUMMARY

Fluid-structure interaction (FSI) is an important physical phenomenon in many applications and across various disciplines including aerospace, civil and bioengineering. In civil engineering, ocean structures such as drilling risers, mooring lines, undersea piping and tension-leg platforms can be subject to strong ocean currents, and such structures may suffer from Vortex-Induced Vibrations (VIV's) leading to large amplitude vibrations. Over the past years, many experimental and numerical studies have been conducted to comprehend the underlying physical mechanisms. However, to date there is still limited understanding of the effect of oscillatory interactions between fluid flow and structural behavior though such interactions can cause large deformations.

This research proposes a mathematical framework to accurately predict FSI for elastically supported rigid structures. The numerical method developed solves the Navier-Stokes (NS) equations for the fluid and the Equation of Motion (EOM) for the structure and employs Finite Differences (FD) on Cartesian grids together with an improved, efficient and oscillation-free Immersed Boundary Method (IBM), the accuracy of which is verified for several test cases of increasing complexity. In particular, forced and a free vibration of a rigid cylinder including VIV of an elastically supported cylinder are presented and compared with reference simulations and experiments. Then, the interference between two cylinders in tandem arrangement at two different spacing is investigated. In terms of VIV, three different scenarios were studied for each cylinder arrangement to compare resonance regime to a single cylinder. Finally, the IBM is implemented into a three-dimensional Large-Eddy Simulation (LES) method and two high Reynolds number (Re) flows are studied for a stationary and transversely oscillating cylinder. The robustness, accuracy and applicability of the method for high-Re number flow is demonstrated by comparing the turbulence statistics of the two cases and discussing differences in the mean and instantaneous flows.

CHAPTER 1

INTRODUCTION

1.1 Statement of the Problem

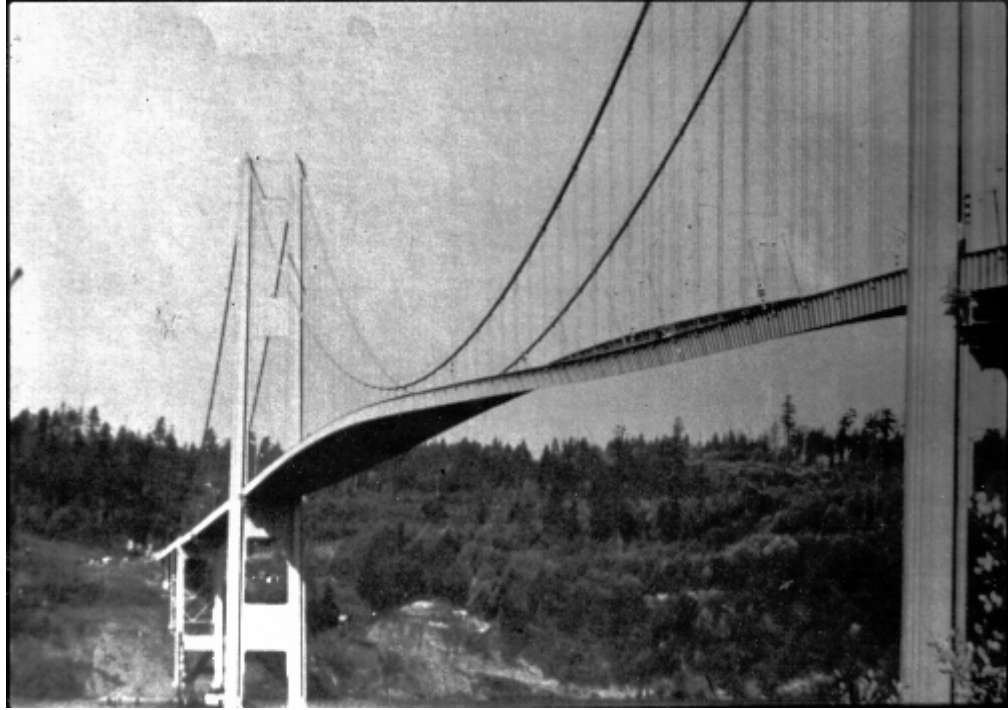
In many engineering applications, fluid-structure interaction (FSI) phenomena play a key role in the dynamic behavior of a structure (eg. Aircraft, wind turbines, suspension bridges...etc). Many natural and man-made transportation systems and/or machinery involve FSI. In civil engineering, examples include large scale applications which are design of wind turbines, pipelines, suspension bridges and offshore platforms. Design of aircraft wings, bridges, offshore wind farms, prosthetic heart valves, turbo-machinery, jet engines, floating of boats on the ocean and river and sloshing in the flexible containers are some other engineering applications. Therefore, the area of FSI is a part of a number of disciplines associated with fluid mechanics, acoustics, structural mechanics, Computational Fluid Dynamics (CFD), statistics and vibrations.

The flow over structures creates vortices that may induce vibrations in the structure. Vortex-Induced Vibrations (VIV's), where vortex shedding of the flow interacts with the structural properties, may result in large amplitude vibrations in both in-line and cross-flow directions. Indeed, VIV's are encountered today in many different fields of engineering as they occur in a large number of structures, principally in air or water flows. For instance, chimney stacks, buildings, airplane wings, and offshore structures all experience VIV. In civil engineering, ocean structures such as drilling risers, mooring lines, cables, undersea piping and tension-leg platforms can be subject to strong ocean currents, and such structures may suffer from VIV.

VIV triggers the cross-stream excitation of structures due to vortex shedding and this can result in a condition of resonance, where the vortex shedding frequency locks-in with the natural frequency, resulting in large amplitudes of cross-stream excitation of the structure. Over the past years, many experimental and numerical studies have been conducted in order to understand the underlying physical mechanism. However, there is only limited research considering the effect of oscillatory interactions which can result in large deformation of structures.

One of the design considerations of modern suspension bridges is to assess the influence of the wind forces on the structural response. The need for such analysis arose from the evolution of designs to progressively longer and more slender structures. The collapse of Tacoma Narrows Bridge in 1940's (see Figure 1-1a and b) showed engineers that resonance can cause disastrous influences on existing structures and cannot be underestimated in design calculations. It was also realized after this catastrophe that flexible bridges are susceptible to the dynamic effects of wind action. Only then was it revealed that these violent aerodynamic oscillations could not have been predicted by pseudo-static analysis. Therefore, research has mainly been directed towards the understanding of the phenomenon, its modeling and its reduction.

Applications in structural engineering are numerous and mainly concentrate on tall buildings like towers, masts, and skyscrapers and on bridges of flexible nature. The study of the collapse of the Tacoma Narrows Bridge, among them the works of Von Kármán (1938), Amann et al. (1941) and Farquharson and Vincent (1950) who first applied the airfoil theory to bridge decks in structural engineering.



(a)



(b)

Figure 1-1 Tacoma Narrows Bridge collapse in 1940: (a) onset of twisting by VIV (b) total collapse. Source: http://www.math.utah.edu/~gustafso/tnarrows/tnarrows_intro.html

Another application in structural engineering that deals with FSI is offshore wind turbines. Wind turbines that harvest wind energy and convert it to electrical power play an increasingly important role and are receiving much attention from governments and industry around the world while meeting rapidly increasing demand for energy and ensuring security of supply (Bazilevs et al. (2011)). The dynamic analysis of offshore wind turbines which are large-floating and/or slender-fixed structures is today one of the main areas of interest in ocean and offshore engineering. Figure 1-2a and b show an individual turbine and an array of wind turbines in an offshore wind farm, respectively.



a)



b)

Figure 1-2 (a) Individual Wind Turbine (b) Wind Farm. Source: <http://www.energyacuity.com/blog/bid/198593/Vague-Maritime-Laws-Preventing-U-S-Offshore-Wind-Development>

The offshore oil & gas industry is particularly faced with the problem of dealing with VIV. Since many of the onshore and shallow-water regions are reaching a peak in terms of reserves and production growth, exploration and production are moving to

deeper waters. In the offshore industry the long, slender, flexible pipes (risers) used to convey fluids from the sea bed to the surface experience wave-induced, vessel-induced movement as well as VIV. Due to the exploration and production in deeper waters, these risers become more flexible and vibrate producing fatigue damage and may ultimately fail. In addition, as water depths increase, wave and vessel motion-related damage remain at roughly the same level or even diminish, but as currents can act over the full length of the riser, VIV may be the the largest contributor to the overall riser fatigue damage (Bourdier (2008)).

The state of the art concerning the topic of VIV of rigid circular structures is now well advanced. FSI principles and their influence on the vortex wake have been largely investigated. However most of the studies consider the structures stationary (Mittal et al. (1997); Mohd-Yusof (1997); Papaioannou et al. (2006, 2008); Sumner (2010)) and little is known about the influence of the dynamics of the structure on the VIV. As the oil industry moves into deeper water in the search for additional supplies of oil and gas, new concepts are being used investigated for offshore platforms. The height of conventional fixed leg platforms is approaching the economic limit due to the very large amount of steel required and limitations imposed by fabrication and installation methods (Bourdier (2008)). On the other hand, the Tension Leg Platforms (TLPs) are floating structures whose mooring system is constituted by vertical tethers. This characteristic makes the structure very rigid in the vertical direction and very flexible in the horizontal plane. The vertical rigidity helps to tie in wells for production, while, the horizontal compliance makes the platform insensitive to the primary effect of currents and waves. In Figure 1.3 a floating tension leg offshore platform with 4 rigid cylinders (yellow) is depicted.



Figure 1-3 A Tension Leg Platform (TLP).Source:
<http://www.nd.edu/~nathaz/research/Luigi.html>

1.2 Research Objective and Scope

The main objective of the present research is to better understand the interaction between fluid flow and non-static bodies in the context of civil engineering structures. This research herein will develop a rigorous mathematical framework to accurately predict VIV. While the FSI mechanism is a general process, this dissertation will focus on oscillatory interactions between moving structures and fluid flow since such interactions can cause large deformations and eventually failure.

To achieve these objectives of this dissertation, the following research tasks are conducted:

- Develop a robust, fully-coupled numerical method that solves the Navier-Stokes equations for the fluid and the equation of motion for the structure that allows calculation of hydrodynamics and the resulting excitation of elastically-mounted single, multiple and coupled circular structures.
- Perform a variety of two and three-dimensional FSI simulations to demonstrate the accuracy and the range of applicability of the method, such as forced vibration including in-line, transverse oscillation and VIV of a rigid, circular cylinder.
- Investigate the interference between two circular cylinders in tandem arrangement and at two different spacing by studying three different scenarios for each cylinder arrangement, and investigate how the resonance regime is affected in each scenario.
- Implement a three-dimensional methodology for the Large-eddy simulation (LES) method of turbulent flows interacting with a stationary and dynamically moving structure, hence demonstrate the robustness, accuracy and applicability of the method for high Reynolds number (Re) flows by comparing the turbulence statistics of these two cases and discussing differences in the mean and instantaneous flows.

1.3 Organization of Dissertation

The organization of this dissertation which includes 7 chapters is briefly described below:

Chapter 2 gives much of the background information on vortex shedding and a literature review of existing methodologies that are used to assess vortex-induced vibrations.

In Chapter 3, the basic fluid solver is described in detail. The governing equations, spatial discretization and time advancement schemes are documented. This chapter also presents the structural formulation, the strong coupling scheme for fluid-structure interaction problems, and the parallelization of the code.

In Chapter 4, fundamental tools for the immersed-boundary formulation are introduced. For the proposed formulation, the establishment of particular choice of regularized delta functions is discussed. Then, the two dimensional flow around a rectangle and a cylinder is computed to demonstrate the formal accuracy of the method.

A series of two-dimensional cases of increasing complexity are presented in Chapter 5. First, laminar flow problems involving prescribed motions of two-dimensional bodies including the flow induced by the harmonic in-line and transverse oscillations of a circular cylinder in a quiescent flow and free-stream respectively are simulated. Next, vortex-induced vibrations of circular cylinders are used to evaluate the accuracy and efficiency of the proposed fluid-structure interaction scheme. Then, the interference between two circular cylinders in tandem arrangement and at two different spacings is investigated. In terms of VIV, three different scenarios are studied for each cylinder arrangement: 1) the upstream cylinder is fixed and the downstream cylinder is free to

oscillate 2) both cylinders are free to oscillate 3) cylinders are rigidly connected to each other and are free to oscillate in the cross-stream direction.

In Chapter 6, two three-dimensional high Reynolds number simulations are presented. The first case is the classical stationary $Re = 3900$ cylinder flow for which extensive laboratory and previous Large-eddy simulation (LES) data are available to validate the LES method. The second case is a one-way coupled fluid structure interaction flow, here with prescribed motion of the cylinder at small oscillation amplitude ($A = 0.2D$) and at frequencies which are close to the frequency of the vortex shedding frequency of the stationary flow.

Chapter 7 summarizes the conclusions of this work, highlights the main results and findings obtained from this study and finally gives recommendations for future work.

CHAPTER 2

INTRODUCTION TO VORTEX-INDUCED VIBRATIONS (VIV'S)

Vortex Induced Vibrations (VIV's) for flow past structures which are immersed into the flow has been studied extensively and observed for centuries. Leonardo Da Vinci observed this phenomenon and named it as “Aeolian Tones”, circa 1500 A.D., a phenomenon that has been studied ever since. Strouhal (1878) conducted one of the first aero acoustical work in history. The study was on the Aeolian tones generated by a wire in an air flow. He came up with a functional relationship of the frequency f_n of the sound produced by that wire and the wind speed U divided by the wire diameter D , that is, $f_n = 0.185 U / D$. In addition, he noticed that the sound volume was greatly influenced by the concurrence of the natural tones of the wire and the Aeolian tones. One year later Lord Rayleigh (Rayleigh (1879)) showed that the vibrations occurred mostly in the cross-flow direction. However, the flow visualizations of Benard (1908) together with the stability analysis of Von Karman and Rubach (1912) showed that these vibrations were attributed to the shedding of vortices by the structure, hence the name Vortex-Induced Vibrations.

Vortex-induced vibrations are seen in various fields of engineering where a separated flow is generated by the immersed structure over a large proportion of its surface in a fluid flow. Under appropriate conditions, flow separation causes an unsteady flow, which generates the alternating shedding of vortices from one side of the structure to the other (Gerrard (1966)). The periodic pattern of vortices is called Von Karman Vortex Street. The shedding of vortices induces an oscillating pressure field around the

structure, resulting in vibration of the structure. Different forms of structures such as plates, sharp-edged or square cross-section bodies can be found in the study of VIV, however, circular cross-section bodies are attracting particular attention from the researchers as the cylinder is an important shape in many structural applications. The studies by Bearman (1984) and Parkinson (1989) and the book by Blevins (1990) discuss various immersed structures. As discussed in the previous section, Von Karman studied the Tacoma Narrows bridge collapse in 1940 and asserted that the cause of the destruction was as a consequence of VIV.

2.1 Review of Previous Work

2.1.1 Fluid-Structure Interaction

The formation of the vortex street is explained by Abernathy and Kronauer (1962) as the growth of two parallel shear layers. In a fluid flow, the presence of a structure such as a circular cylinder induces the separation of the flow and that causes the appearance of shear layers and triggers the alternative shedding of vortices behind the structure. The vortex-shedding frequency is usually characterized by the dimensionless Strouhal number, St ;

$$St = \frac{f_e D}{U_\infty} \quad (2-1)$$

f_e being the vortex shedding frequency at which pairs of vortices are shed from the structure, U_∞ being the free stream velocity and D the width of the structure. The Strouhal number depends on the Reynolds number as discussed in Blevins (1990), but it is almost constant and equal to 0.2 which is close to the value deduced by Strouhal in the

subcritical range of flow around circular cylinder ($300 \leq Re \leq 150000$) where most of engineering problems occur (Bourdier (2008)).

If one of the natural frequencies of the structure subjected to a flow is close to the vortex-shedding frequency and the system has low damping which does not sufficiently affect the amplitude of oscillations in an oscillatory system, self-excited vibrations can occur. The self-excited vibrations may induce destructive forces in designing structures or equipment. For instance, Sainsbury and King (1971); Wootton et al. (1972) discussed problems due to vortex-induced vibrations during construction of a large offshore oil platform at Immingham, England, in the tidal flow of the Humber estuary. They found out that these oscillations occurred when the frequency of the cylindrical structure was twice the vortex shedding frequency.

Bourdier (2008) defines Vortex-excited vibration as a “fluid-structure interaction phenomenon in which temporal synchronization of the evolutions of the flow field and the structure oscillation is dominant”. This phenomenon is crucial not only in the sense of the intensity of forces but also the simultaneity of evolution of fluid and structure (Facchinetti, 2003). As fluid passes over a structure, large vibration of the structure can be observed when the fluid dynamic forces on the body increase through a nonlinear interactive process. The structure can vibrate if it is movable as the shedding of vortices creates an oscillating pressure field around the body. The magnified vibration can control the flow pattern and can be further increased. Berger and Wille (1972) and Parkinson (1973) discussed these self-oscillatory, nonlinear body-wake systems.

When the vortex shedding frequency f_e and the natural frequency of the structure f_n are of the same order, the fluid-structure interaction becomes stronger. In this case, a

non-dimensional parameter called the reduced velocity, U_{red} is often used as a guide to determine if vortex-induced vibration is possible. The reduced velocity is defined by:

$$U_{red} = \frac{U_{\infty}}{f_n D} = O\left(\frac{U_{\infty}}{f_e D}\right) = O\left(\frac{1}{St}\right) \quad (2-2)$$

where U_{∞} is the velocity at far boundary, f_n and D is the natural oscillation frequency and the diameter of the structure, respectively. It reflects the synchronization of flow and the structure. Bourdier (2008) found that reduced velocity takes values close to 5 when synchronization occurred.

The simultaneous behavior of vibrations between vortex and vibration frequencies is a characteristic of fluid-structure interaction and is often referred to as “lock-in”. In this situation, the structure can be subject to large amplitude oscillations. Fluid-structure interaction can induce high amplitude oscillations of the structure over a whole range of flow velocities by driving the frequency of shedding of vortices to synchronize with the structure’s oscillation. This means that when the amplitude of structural oscillation passes a critical threshold, the structural vibration frequency becomes identical to the vortex-shedding frequency f_e , which differs from that estimated by the Strouhal relationship. In other words, synchronization occurs as the natural Strouhal frequency which is a characteristic of vortex shedding from a stationary cylinder is suppressed by the structural frequency.

In addition, the lock-in effect produces strong correlation of vortex-shedding with the structural motion. The structure can oscillate in both in-line and cross-flow directions as it is set free to move. However, the frequency of in-line oscillations is usually twice as high as that of cross-flow oscillations and the magnitude of in-line displacements are much smaller than those of the transverse direction. Therefore, most engineering

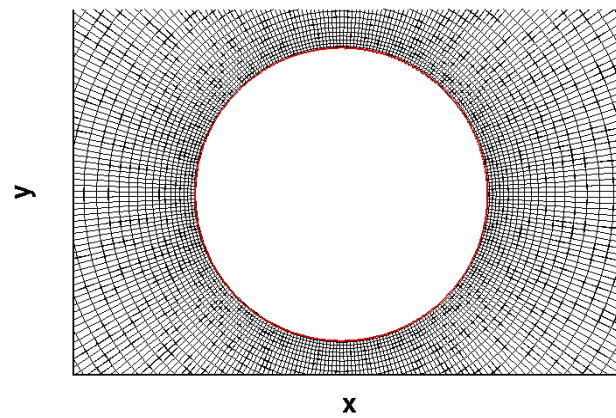
applications are concerned with cross-flow oscillations. This is the reason why the majority of the research conducted on VIV of a rigid circular cylinder considers the structure restrained to move only in the cross-flow direction although some researchers such as Jauvtis and Williamson (2003, 2004); Jeon and Gharib (2001); Sarpkaya (1995) studied cylinders with two degrees of freedom. Jauvtis and Williamson (2004) have shown that restriction on two dimensional movement of the cylinder does not significantly affect the VIV of the structure as long as the mass ratio, $m^* = m/\rho D^2$ (ρ being the fluid density and m the system mass) is greater than 6.

When the cross-stream directional oscillation of the structure is large enough, fluid-structure interaction can lead to an increase in the strength of the vortices or the mean drag on the structure. However, the phase, sequence and the pattern of the vortices in the wake region are altered by the motion of the cylinder (Blevins, 1990). This effect is also seen when a cylinder is forced to oscillate in a sinusoidal manner under a uniform current. Here, lock-in takes place either when the oscillation frequency on cross-stream direction becomes equal to the Strouhal frequency or when the driving frequency in the streamwise direction approaches twice the Strouhal frequency (Anagnostopoulos and Bearman, 1992). Therefore, nonlinear behavior of the body-wake is noticed as the cylinder vibrates transversely to the fluid flow.

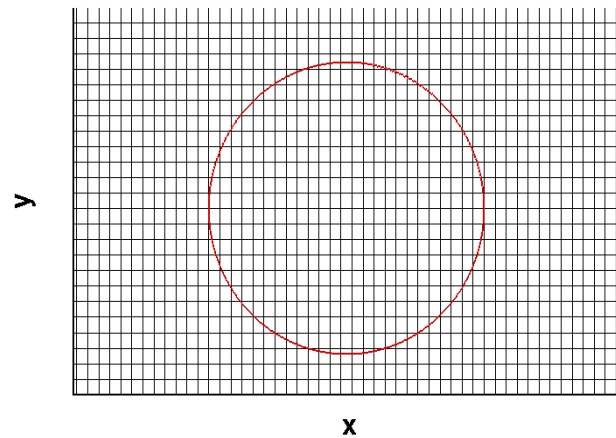
2.1.2 Numerical Modeling of VIVs

Computational Fluid Dynamics (CFD) typically involves flow through complex domains. Solving fluid dynamics equations in such geometries can be extremely challenging, and methods based on body-fitted grids which conform to the geometry can be difficult to implement. Especially for moving bodies, at every time step a new mesh

has to be generated. This requires a lot of computing time. Therefore, body conformal grids are being used less when studying fluid-structure interaction problems. Today, research has shifted towards fixed Cartesian grid arrangements with immersed boundaries for which special numerical treatment is employed. Figure 2-1 illustrates two different configurations of a numerical grid around a cylinder.



(a)



(b)

Figure 2-1 Grid around a cylinder (a) Traditional body fitted grid (b) Cartesian grid with an immersed boundary.

An increasingly popular approach is to solve the fluid on an Eulerian (i.e. Cartesian) grid while the moving structure is tracked in a Lagrangian fashion. Thus, the grid is not aligned with the immersed boundary. This approach has been employed in a variety of inviscid (Bayyuk et al., 1993; Dezeeuw and Powell, 1991; Quirk, 1994) and viscous (Udaykumar et al., 2001; Udaykumar et al., 1996; Ye et al., 1999) flow computations. The main advantage of a Cartesian grid is that there is no need for grid regeneration or grid deformation as the boundary moves. Elimination of the grid generation saves time in numerical studies. Therefore, an immersed boundary method uses less memory and CPU compared to a body fitted grid and its corresponding transformations. The boundary conditions on the structure are imposed using a variety of different immersed boundary strategies with different accuracy and efficiency. However, ensuring the accuracy and the conservation of mass of such numerical schemes are not straightforward.

An immersed boundary with an arbitrary shape can be modeled on a fixed Cartesian grid by imposing an external force field using immersed boundary methods. The method was first introduced by Peskin (1972) and has been applied in various problems, most of which contain biological flows including computations of flow patterns around heart valves (McQueen and Peskin, 1997; Peskin, 1977, 1982). Peskin's method is a mixed Euler-Lagrangian finite difference method for computing the flow interaction with a flexible immersed boundary. In this method, the fluid flow governed by the incompressible Navier-Stokes equations is solved on a Cartesian grid. The structure is represented by a set of massless elastic fibers and a collection of massless forcing points which are movable with the local fluid velocity which track the location of those fibers.

Goldstein et al. (1993), Saiki and Biringen (1996) modeled the flow around rigid bodies using a feedback forcing approach. In this approach, the force exerted by the body on the fluid is specified as a function of the velocity of fluid around it. This force adapts itself such that the no-slip boundary condition is retained on the body. The main drawback of this approach is the presence of two flow-dependent constants which need to be modified according to the frequencies of the flow. For an unsteady flow simulation, these constants take large values which lead to smaller time steps and hence increase the computational cost. Khadra et al. (2000) introduced a penalty method in which an additional term of volume drag is added to the governing equations. The so-called ‘‘Darcy Drag’’ term accounts for the action of the porous medium on the flow. The disadvantage of this method is that the proposed methodology may induce spurious oscillations. The ‘direct forcing method’ introduced by Mohd-Yusof (1997) utilizes a forcing term in the discretized momentum equation. It is equivalent to enforcing the boundary condition in the flow field by using a direct forcing term in the momentum equation as follows;

$$\frac{u^{n+1} - u^n}{dt} = (RHS)^{n+1/2} + f^{n+1/2} \quad (2-3)$$

where RHS contains convective, viscous and pressure gradient terms, u is the velocity, and f is the forcing term. This term is then calculated at the intermediate time step $n+1/2$ (where n , $n+1$ being current and the next time step, respectively), by imposing the boundary conditions where the structure and the fluid have the same velocity in magnitude. An interpolation is needed when the boundary is not aligned with the grid in a Cartesian grid. The interpolation proposed by Peller et al. (2006) is a least squares interpolation with third order accuracy. They use a polynomial so that the sum of the squares of the distance from the curve to the values at the fluid points is minimal. The

methodology utilizes a pseudo-forcing function calculated at discrete points with a stable second order least squares interpolation scheme for fixed and moving boundaries. It is directly applied to the right hand side of the momentum equation in order to satisfy the boundary conditions at the location of the structure. Bomminayuni (2010) utilized this immersed boundary technique for three dimensional turbulent flows over embedded boundaries. Figure 2-2 shows an example sketch of 2D implementation of an interpolation strategy which utilizes three fluid cells in two directions for a cut cell which has a cell center outside of the cylinder boundary.

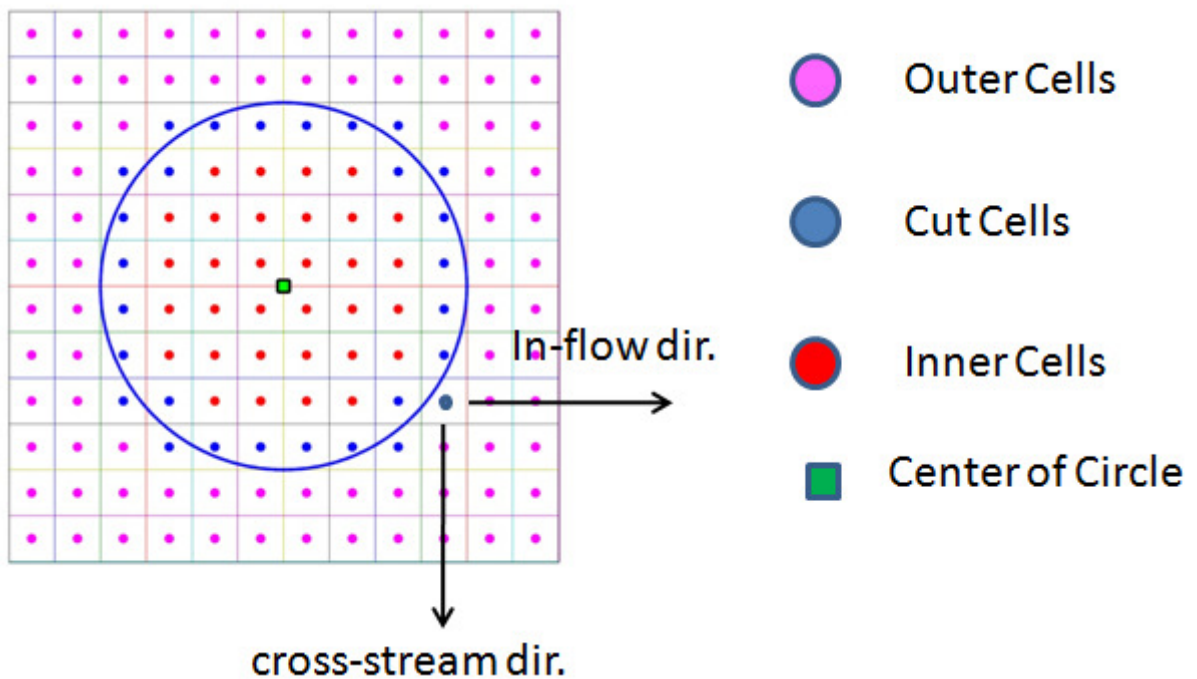


Figure 2-2 Typical 2D Stencil showing an interpolation strategy using three fluid cells in in-line and cross-flow directions for the cell cut by the cylinder boundary in (x,y) plane.

Fadlun et al. (2000) provided second order accuracy and also a better representation of the boundary for the distribution of forcing to neighboring grid points. Fadlun et al. (2000) also compared the efficiency and accuracy of the proposed approach to the feedback forcing approach of Goldstein et al. (1993), and suggested that for flow past complex geometries, his methodology provided better efficiency and accuracy. However, a limitation of this approach is that it requires huge clustering of grid points close to the body for a stable linear interpolation that yields accurate values. Hence, many researchers have worked on improving the interpolation procedure while simultaneously employing the direct forcing method.

Tseng and Ferziger (2003) employed a ghost-cell method where forcing was applied to grid cells inside the body such that the boundary condition is implicitly satisfied at the surface of the structure. A 2D linear interpolation scheme using two nearest fluid points was implemented and therefore, a more accurate representation of the boundary was achieved than by Fadlun et al. (2000), where interpolation was performed in x or y directions using only one neighboring fluid point. A major drawback of this interpolation scheme was the occurrence of large negative weighting coefficients, in cases where the inside (ghost-cell) points are very close to the boundary, leading to numerical instability. Overall, this ghost-cell method proposed by Tseng and Ferziger (2003) was efficient and fairly accurate in simulating flow past immersed bodies. Uhlmann (2005a) presented an improved Immersed Boundary Method (IBM) with a direct formulation of fluid-solid interaction force. The regularized delta function of Peskin (2002) is utilized for connecting arbitrary Lagrangian and discrete Eulerian positions. Su et al. (2007) proposes a new implicit force formulation on the Lagrangian

marker to satisfy the no-slip boundary condition at the immersed boundary. According to their methodology, the boundary forces are first computed on the Lagrangian markers and then distributed to the Eulerian grid via a discrete delta function. Their numerical results show that the proposed formulation does not change the stability limit.

In the literature, it is clearly seen that most of the researchers use finite difference techniques with reconstruction methodologies for simulations over flow in complex geometries (Kim et al. (2001); Yang et al. (2008); Yang and Balaras (2006)). These reconstruction procedures around the immersed structures can produce accurate results for stationary structures while the method produces unphysical pressure oscillations due to the violation of global mass conservation once the structure starts moving (Seo and Mittal (2011); Uhlmann (2005a)).

The unphysical oscillations in the forcing coefficients observed for the boundary motion were first pointed out by Uhlmann (2005a). In his study, a fictitious domain method was developed to smoothly transfer the forcing term and other quantities between Lagrangian and Eulerian positions. The proposed method produces less instability than the existing discrete forcing methods in calculation of the forces around the immersed boundaries and the oscillations due to a fixed grid are overcome. Later, Uhlmann (2005b) further reduced the velocity error which results in instability by introducing points over the entire structure in addition to points defined on the surface of the boundaries.

Seo and Mittal (2011) have recently analyzed these unphysical peaks in the forces, and they described those as the pressure oscillations resulting from the violation of the local mass conservation near the immersed boundary. They state that the primary source for this error is that for moving boundary problems, some grid cells (or grid

points) in the computational domain change from fluid to immersed boundary cells in time leading to spurious mass sources/sinks. According to IBM based on sharp interface treatment introduced by Mittal et al. (2008) the governing equations (mass and momentum conservation) are solved only on the cells in the fluid domain and for moving immersed boundaries, this results in the generation of fresh cells (cells that go from being inside the solid domain to being in the fluid domain) and dead cells (cells that go from being inside the fluid domain to being inside the solid domain). Luo et al. (2009) pointed out that the abrupt change of the stencils (a geometric arrangement of a nodal group that relate to the point of interest by using a numerical approximation routines as seen in Figure 2-2) for the flow reconstruction and a finite-differencing of the governing equations associated with these cells causes unphysical oscillations in the pressure field. Similar behavior is seen in IBM's using a direct forcing method (Lee et al. (2011); Liao et al. (2010); Uhlmann (2005a, b); Yang et al. (2009)) as numerical stencils for applying forcing terms are changing as the structure moves. Lee et al. (2011) defines two sources of the pressure oscillations in a discrete forcing IBM which are the temporal discontinuity in the velocity at the dead cell and the spatial discontinuity in the pressure across immersed boundary caused by the fresh cells. In order to reduce the spurious pressure oscillations, Seo and Mittal (2011) propose a strategy which incorporates mass conservation through a well-known cut-cell approach (Udaykumar et al. (2001); Ye et al. (1999)) into their ghost cell method (Mittal et al. (2008)). In this method, the boundary cells that are cut by the immersed boundary are restructured into non-rectangular control volumes. Moreover, a finite volume method is used to ensure the strict conservation of volume of the defined geometry using equations proposed by Kamakoti and Shyy (2004)

in addition to conservation of mass. With the help of this proposed strategy, no significant spurious pressure oscillations for moving boundary problems are encountered.

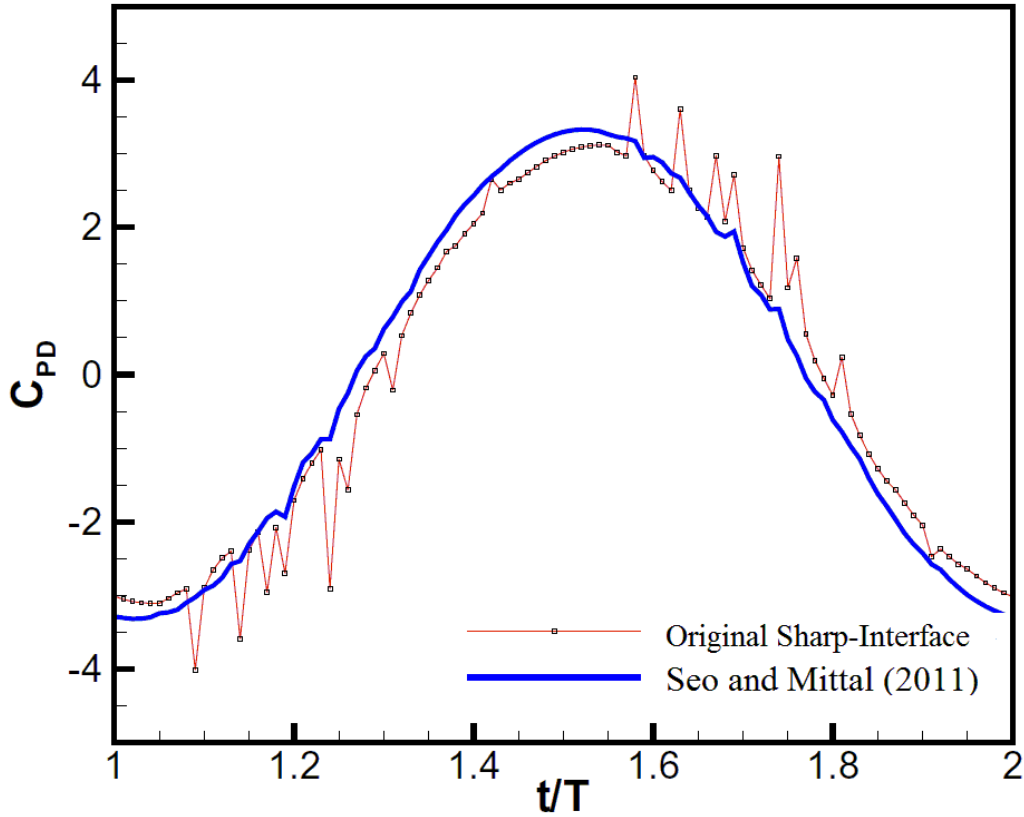


Figure 2-3 Time histories of pressure drag coefficient for horizontally oscillating cylinder; comparison between the original sharp-interface IBM and the regionally conservative cut-cell method by Seo and Mittal (2011)

In order to demonstrate the efficiency of their method, Seo and Mittal (2011) considered a cylinder with a diameter D oscillating sinusoidal in streamwise direction. Figure 2-3 shows the time series of the pressure drag coefficient for the original proposed ghost cell method and the method with the improved mass conservative cut cell approach. As seen from this figure, the pressure oscillations are significantly reduced although there

are still some local extremes (discontinuities on the results of their proposed method) in the plot. Their results confirm that the major cause of the spurious pressure oscillations is due to the fluid mass/volume loss. However, the implementation of this method is complex and increases the computational time.

2.2 Research Gaps and Objectives of this Study

A review of the existing literature, summarized in the previous section, identified several research gaps in current numerical simulation of vortex induced vibrations. Among those, the following appear to be particularly significant:

- Recent studies on moving immersed boundaries require knowledge of implementation of the boundary conditions in irregular cells which needs a large number of “special treatments”, resulting in complex coding logistics (Mittal et al. (2008); Peller et al. (2006); Seo and Mittal (2011)). Especially when using cut-cells, these cells should not become too small; otherwise this could not only result in stability problems, but also lead to slow convergence of the Poisson solver (discussed in later chapters). Finally, an iterative solution procedure may be required due to some irregular stencil near the embedded boundary (Choi et al. (2007)), which results in substantial increase in computational time.
- Existing studies mainly have considered static single structures (Fadlun et al. (2000); Kim et al. (2001); Mohd-Yusof (1997); Peller et al. (2006); Peskin (2002); Sarpkaya (1995); Udaykumar et al. (2001); Yang and Balaras (2006)). In such cases, the correlation between structure and the flow is manageable computationally because the structures are fixed in

location and relatively small in number. However, studying multiple structures such as structures in tandem arrangement along with analysis of the coherent structures and the interaction between them is rarely determined although it is formidable and interesting to understand in the context of flow dynamics. Investigation of coupled and uncoupled systems of structures and their response to the hydrodynamic forces is still missing in the research.

- Only a limited number of research studies have considered moving structures as fluid-structure interaction problem. While some of these studies have accounted for the motion of structures (Mittal et al. (2008); Seo and Mittal (2011); Uhlmann (2005a); Yang et al. (2009)), the configurations were limited to mainly two dimensional validations low Re flows. However, current research needs to extend the investigation of FSI phenomena from two-dimensional with low Re to three-dimensional with high Re.

As stated previously, the main research tasks of this dissertation are:

- 1) To employ a robust, efficient, oscillation free and fully-coupled numerical method which can handle problems that are unique to boundary formulations and are consequences of the boundary motion on a fixed grid without introducing any additional complexity in the solver.
- 2) To perform a variety of simulations with increasing complexity to demonstrate the accuracy and the range of applicability of the method, such as forced vibration including in-line, transverse oscillation and VIV of a rigid, circular cylinder.

- 3) To apply the numerical method into multiple structures in order to investigate the interactive flow structures between cylinders in tandem arrangement and at two different spacing by studying three different scenarios for each cylinder arrangement, and check how the resonance regime is affected in each scenario.
- 4) To extend the proposed method and implement it into a three-dimensional methodology for the Large-eddy simulation (LES) method of turbulent flows interacting with a stationary and dynamically moving structure, hence demonstrate the robustness, accuracy and applicability of the method for high-Re number flows by comparing the turbulence statistics of the two cases and discussing differences in the mean and instantaneous flows with respect to the experiments.

CHAPTER 3

NUMERICAL METHODOLOGY

The purpose of this study is to develop a computational tool for simulations of laminar and LES of turbulent flows interacting with moving boundaries. Rigid structures undergoing motion that is either prescribed or governed by additional Ordinary Differential Equations (ODEs) that have to be solved as a coupled system together with the Navier-Stokes equations are considered. In this chapter, the coupled solver will be introduced in two parts; the basic fluid solver in Cartesian coordinates and the structural solver which is capable of solution of the Equation of Motion (EOM). Both solvers are discussed in detail. In addition, the fluid-structure coupling scheme is provided at the end of this chapter. The treatment of the immersed boundary method and its validation will be discussed in detail in chapter 4.

3.1 Basic Navier-Stokes (NS) Solver

3.1.1 Formulation in Cartesian Coordinates

3.1.1.1 Governing Equations

In Cartesian coordinates, the governing equations for an unsteady, incompressible, viscous flow of a Newtonian fluid with constant density can be written as follows:

$$\frac{\partial u_i}{\partial x_i} = 0 \quad (3-1)$$

$$\frac{\partial u_i}{\partial t} + \frac{\partial(u_i u_j)}{\partial x_j} = -\frac{\partial p}{\partial x_i} + \frac{1}{Re} \frac{\partial^2 u_i}{\partial x_j \partial x_j} + f_i \quad (3-2)$$

where u_i and u_j ($i, j = 1, 2, 3$) are the velocity vector components in the corresponding directions (i.e. $u_1 = U$, $u_2 = V$ and $u_3 = W$ denoting the velocity components in x, y and z directions, respectively. See Figure 3-1 for the staggered variable arrangement), normalized by a reference velocity U_∞ , t is the time which is normalized by L/U_∞ with L being the reference length scale, p is the pressure normalized by ρU^2 with ρ being the density of the fluid, and Re is the Reynolds number defined as $Re = \rho U_\infty L / \mu$ with μ being the dynamic viscosity of the fluid. Similarly, x_i and x_j represent the spatial location vectors in global X, Y and Z axis directions, respectively. In equation 3-2, f_i represents an external body force field which is, in this case, designed to enforce the proper boundary conditions on an arbitrary immersed body (this will be discussed in detail in the next chapter).

For laminar flow cases, the fluid flow governing equations, Eqs (3-1) and (3-2) are directly integrated in time and space without introducing any model. On the other hand, the Large Eddy Simulation (LES) approach of 3D turbulent flow cases introduces a spatial filtering operation in order to separate the large, energy carrying eddies that are directly resolved and modeled. The present finite difference solver uses a top-hat filter by discrete operators. In the LES approach, scales smaller than the grid size are not resolved but accounted for through the subgrid scale (SGS) tensor given by

$$\tau_{ij} = \overline{u_i u_j} - \overline{u_i} \overline{u_j} \quad (3-3)$$

The resulting governing equations governing the evaluation of the large scales become:

$$\frac{\partial \bar{u}_i}{\partial t} + \frac{\partial (\bar{u}_i \bar{u}_j)}{\partial x_j} = -\frac{\partial \bar{p}}{\partial x_i} + \frac{1}{\text{Re}} \frac{\partial^2 \bar{u}_i}{\partial x_j \partial x_j} - \frac{\partial \tau_{ij}}{\partial x_j} \quad (3-4)$$

$$\frac{\partial \bar{u}_i}{\partial x_i} = 0 \quad (3-5)$$

where the overbar denotes an appropriately chosen low-pass filter and incompressibility is assumed.

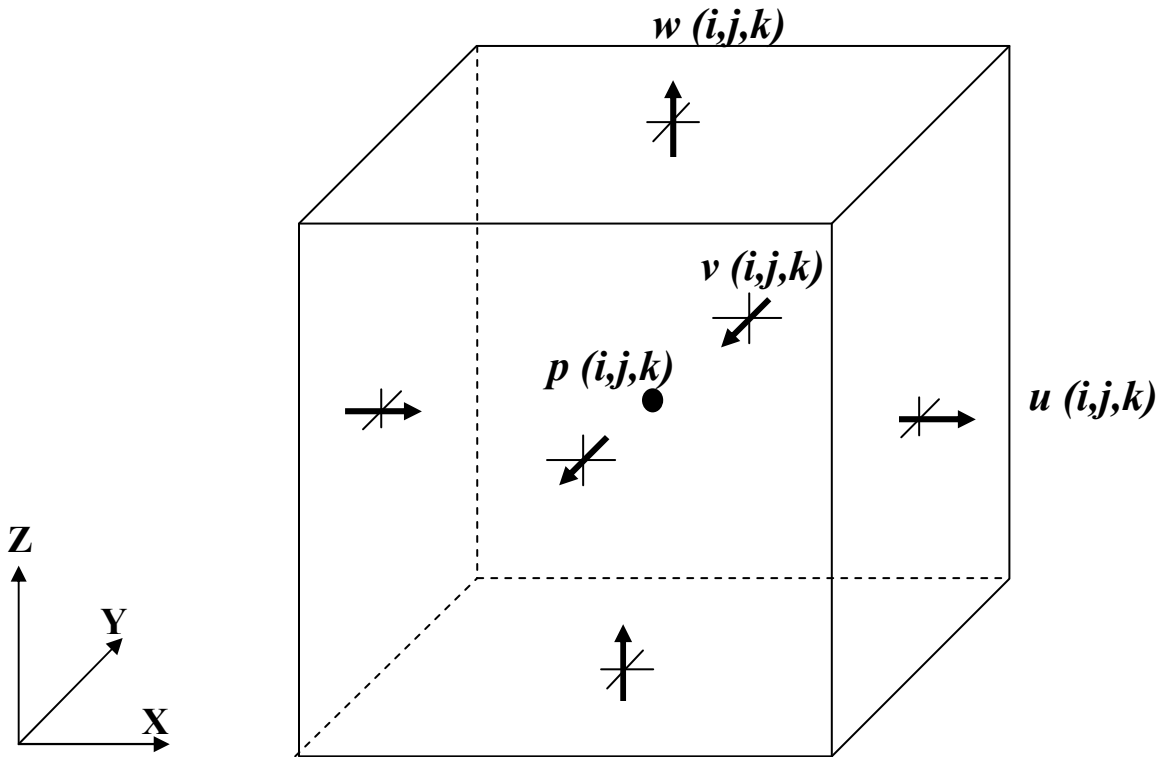


Figure 3-1 Schematic representation of a grid cell (i,j,k) in Cartesian coordinates and its staggered variable arrangement with u, v and w being the velocity components in global X, Y and Z direction, respectively at the cell face centers and p being the pressure at the cell center.

All calculations are conducted using Large-Eddy Simulation (LES). The WALE model (Nicoud and Ducros (1999)) is employed to compute SGS stresses and to close the filtered Navier-Stokes equations. Its advantage lies in the fact that it does not require near wall damping and hence makes it an ideal candidate for immersed boundary LES, in which the solid boundary is not sharply defined.

3.1.1.2 Spatial Discretization and Local Mesh Refinement (LMR)

The solver is implemented using a finite difference method on a Cartesian grid with staggered arrangement where the scalar variables such as pressure and density are stored in the cell centers of the control volumes, whereas the velocity or momentum variables are located at the cell faces (See Figure 3-1). A second-order central differencing scheme (CDS) on a staggered grid is used in the present study in order to approximate the convection $(\frac{\partial(u_i u_j)}{\partial x_j})$ and diffusion terms $(\frac{1}{\text{Re}} \frac{\partial^2 u_i}{\partial x_j \partial x_j})$ in the momentum equations as shown in Eqs (3-1) and (3-2). The second-order accuracy is ensured such that the error is proportional to the square of the spacing between grid lines. A typical grid cell and the staggered variable arrangement is shown in Figure 3-1, with the pressure and scalar variables located at the center of the grid cell and velocity components at the cell face centers.

In order to perform engineering applications that involve complex geometries, it becomes necessary to develop techniques for implementing refined grid methods on the computational domains to ensure better representation of boundaries of those geometries. One approach called Local Mesh Refinement (LMR) focuses on the decrement of computational effort by placing more grid points around critical regions to get higher

resolution and fewer grids to regions where coarse grid is adequate. In this research, a second-order accurate LMR methodology is implemented. In the developed software, refinement is performed as a block-based structure. In other words, blocks that are near critical regions are finer than other blocks. The refinement factor r , which is equal to the ratio of fine to coarse grid spacing, is set to two as seen in Figure 3-2.

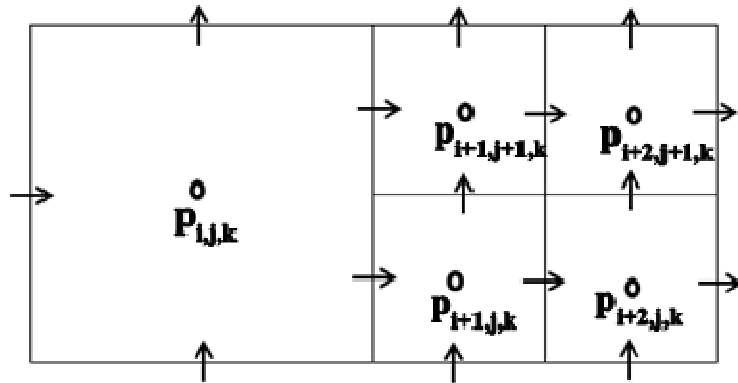


Figure 3-2 A partial grid example with 2 levels of refinement, r . Pressure cells are shown at the center of each grid cell.

For local mesh refinement, the most important point is to satisfy the conservation laws between blocks which have different resolutions. In order to prevent the discontinuities between the coarse-fine interfaces, there are several options which can be applied. As a first option, conservation can be maintained by the use of local corrections to these fine-coarse interfaces after the computations are performed. Secondly, a special numerical operator which is approximate projection operator can be applied to enable a composite solution across the boundary to solve the divergence free velocity field (Berger and Colella, 1989; Martin and Colella, 2000; Minion, 1996; Popinet, 2003; Zuzio and Estivalezes, 2011). Thirdly, higher order spatial and temporal interpolations can be

applied. In the present study, space is refined according to all of the options explained above but there is no refinement in time.

3.1.1.3 Time Advancement Scheme

In the present work, there are several choices of time advancement schemes. The convective terms are advanced in time using either the second-order Adams-Bashforth (AB2) or the low-storage third-order explicit three steps Runge-Kutta (RK3) scheme in which the governing equations are discretized in time providing second-order accuracy in time where all terms in the right hand side of momentum equations are advanced explicitly, while the diffusive terms are discretized in time via the second-order Crank-Nicolson (CN) scheme. In particular, the momentum equation is solved to find the intermediate velocity and first guess of the velocity field such as:

$$\frac{\hat{u}_i^k - u_i^{k-1}}{\Delta t} = \alpha_k C(u_i^{k-1}) + \beta_k C(u_i^{k-2}) + \frac{1}{2} \alpha_k D(u_i^{k-1} + \hat{u}_i^k) - \alpha_k \frac{\partial p^{k-1}}{\partial x_i} \quad (3-6)$$

$$u_i^k = \hat{u}_i^k - \alpha_k \Delta t \frac{\partial p^{k-1}}{\partial x_i} \quad (3-7)$$

where k is the substep index, which ranges from 1 to 3 for Runge-Kutta scheme (RK, RK2, RK3) and equals to 1 for Adams-Bashforth scheme, \hat{u}_i^k is the intermediate velocity, p^{k-1} is the pressure field. C and D are the spatial operators for convective, diffusive and SGS terms, respectively. Δt is the time step. The RK3 coefficients are

$$\alpha_1 = \beta_1 = 1/3 \quad \alpha_2 = \beta_2 = 1/2 \quad \alpha_3 = \beta_3 = 1 \quad (3-8)$$

and the AB2 coefficients are

$$\alpha_1 = 3/2 \quad \beta_1 = -1/2 \quad (3-9)$$

The following stability criterion, in other words the generalized Courant-

Friedrichs-Levy (CFL) number which is a necessary condition for convergence while solving partial differential equations and ,thus includes the time step constraint from the viscous terms which can be adopted as described in Akselvoll and Moin (1995):

$$CFL = \Delta t \left[\frac{|u|}{\Delta x} + \frac{|v|}{\Delta y} + \frac{|w|}{\Delta z} + 2\nu \left(\frac{1}{\Delta x^2} + \frac{1}{\Delta y^2} + \frac{1}{\Delta z^2} \right) \right] \quad (3-10)$$

Although the theoretical limit for the three step Runge-Kutta scheme is $\sqrt{3}$, the actual CFL number in the simulations is lower since the cross-terms are not included in the calculation of this criterion. A value of 0.3 for CFL is used in most of the simulations in this work. On the other hand, for the second order Adams-Bashfort scheme, the theoretical stability limit is $CFL < 1$. However, the actual CFL number in the simulations has to be lower, $CFL = 0.2$ in order to prevent the code from crashing since higher CFL values cause instability in the simulations. In the present work, the three steps Runge Kutta scheme is used together with Crank-Nicolson scheme in two-dimensional studies including flow over stationary structures and prescribed motion, Vortex-Induced Vibration of single and multiple structures. On the other hand, three dimensional stationary and prescribed motion cases utilize the Adams-Bashforth scheme for convective terms and the Crank-Nicolson scheme for diffusive terms.

3.1.2 Poisson Equation and the Solution Procedure

A parallel multigrid solver *mgd2* and *mgd3* originally written by Bunner (1998) is implemented in the present code which solves the non-separable Poisson equation:

$$\frac{\partial^2 \phi}{\partial x_i \partial x_i} = \frac{1}{\Delta t} \frac{\partial u_i}{\partial x_i} \quad (3-11)$$

It uses a domain decomposition technique and employs staggered grids with cell-centered operations. It uses full weighting for the restriction and bilinear interpolation for the correction. The discrete form of the above equation in 3D Cartesian coordinates for uniform grid spacing can be written as:

$$\left(\frac{\delta^2}{\delta^2 x} + \frac{\delta^2}{\delta^2 y} + \frac{\delta^2}{\delta^2 z}\right)\phi_{i,j,k} = \frac{1}{\Delta t} \left(\frac{u_{i,j,k} - u_{i-1,j,k}}{\Delta x} + \frac{v_{i,j,k} - v_{i,j-1,k}}{\Delta y} + \frac{w_{i,j,k} - w_{i,j,k-1}}{\Delta z}\right) \quad (3-12)$$

The solver developed for the calculation of the flow field utilizes the SIMPLE algorithm which stands for Semi-Implicit Method for Pressure-Linked Equations. The procedure adopted has been described in Patankar et al. (1975); Patankar and Spalding (1972) and used to integrate the governing equations in time. In particular, the important operations of the solution procedure in the order of their execution can be described in the following sequence of steps (*a* to *e*):

Step a: Store the velocity and pressure fields obtained at the end of previous time step.

Step b: The momentum equation is solved to find the intermediate velocity and first guess of the velocity field as in Eqs (3-6) and (3-7).

Step c: The pressure correction equation is solved to find the pressure scalar, ϕ .

Step d: The pressure and velocity field is corrected employing the following equations.

$$p^k = p^* + \phi^k \quad , \quad u_i^k = \hat{u}_i^k - \alpha_k \Delta t \frac{\partial p^k}{\partial x_i} \quad (3-13)$$

Step e: Treat the corrected pressure p^* as a new guessed pressure, return to *step c* and repeat the whole procedure until convergence for the momentum and pressure-correction equations is reached

As explained before, the solver employs a finite difference discretization on a Cartesian staggered grid and makes use of local mesh refinement (LMR) algorithm together with a multi-grid method to efficiently solve the Poisson equation. As discussed in the previous section LMR ensures adequate resolution in the region of interest at manageable computational costs by placing more grid points around critical regions to get higher resolution.

3.1.3 Implementation of Boundary Conditions

In the current study, ghost cells are used to impose the proper external boundary conditions (i.e. inlet, outlet, south, north, top and bottom boundaries). Its advantage lies in the fact that grid spacing near the boundary is continuous and the software can have generalized form for all grid points at which the equations are solved. Moreover, it makes the domain decomposition technique easier for parallelization.

3.1.3.1 Dirichlet and Neumann Boundary Conditions

A schematic representation of the Dirichlet and Neumann boundary conditions and their layout is shown in Figure 3-3, in which the lower-left corner of a X-Y plane of the computational domain and the collocation of the variables such as streamwise, transverse directional velocities, u , v along with pressure and viscosity, p , ν are given. For the given velocity component which is normal to the wall, e.g., u to the lower boundary and v to the left boundary in Figure 3-3, the Dirichlet condition can be written as

$$u_{1,j,k} = u_b \quad \text{and} \quad v_{i,1,k} = v_b \quad (3-14)$$

where u_b and v_b are the prescribed normal velocity components on the lower wall and left wall, respectively.

The no-slip conditions for the wall-tangential components are directly enforced through the use of ghost cells:

$$u_{i,1,k} = -u_{i,2,k} \quad \text{and} \quad v_{1,j,k} = -v_{2,j,k} \quad (3-15)$$

On the other hand, a homogeneous Neumann boundary condition for an arbitrary variable, ϕ can be implemented as

$$\frac{\partial \phi}{\partial n} = 0 \quad , \quad \phi_{1,j,j} = \phi_{2,j,j} \quad (3-16)$$

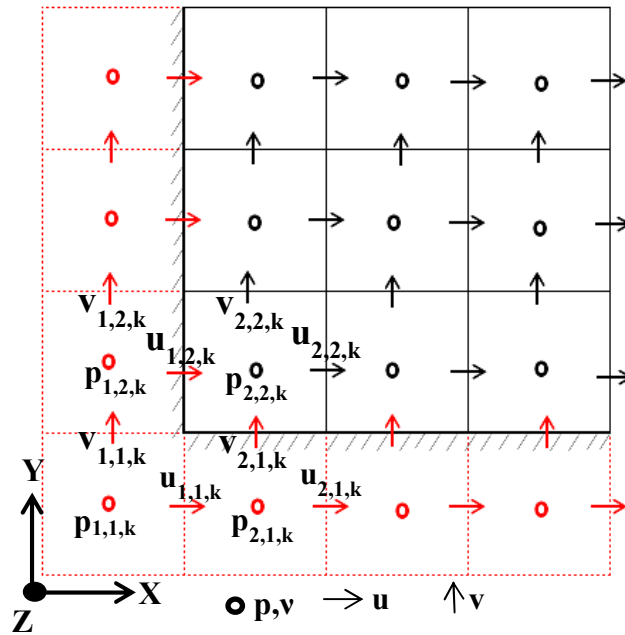


Figure 3-3 The implementation of proper Dirichlet and Neumann boundary condition on XY plane of the computational domain

3.1.3.2 Convective Boundary Condition

This study utilizes Orlanski (1976)'s proposed convective boundary condition for outflow boundaries. He found very successful in convecting coherent structures such as vortices out of the domain without distorting the flow in the computational domain. In other words, mass is conserved through the whole computational domain. In that case, the following equation can lead to a conservative boundary velocity as follows:

$$\frac{\partial u_i}{\partial t} + U_\infty \frac{\partial u_i}{\partial x_i} = 0 \quad (3-17)$$

in which u_i is any velocity component, and U_∞ is the convective velocity which is set to the mean streamwise velocity at the exit plane (this study sets $U_\infty = 1.0$ in free-stream flow simulations). The proposed equation is discretized using an explicit Euler scheme in time, one-sided difference for the streamwise velocity component and central difference for the other two velocity components in space. In addition, the streamwise velocity component is adjusted every time step to globally conserve mass.

3.1.3.3 Periodic Boundary Condition

As shown in Figure 3-4, the periodic boundary condition through ghost cells is implemented simply by copying values such as velocities (u, v, w) and pressure (p) on the left side directly to the ghost cells on the right side of the local domain and vice versa in such a way that:

$$\begin{aligned} u_{n_i, j, k} &= u_{2, j, k} \quad , \quad v_{n_i, j, k} = v_{2, j, k} \quad , \quad w_{n_i, j, k} = w_{2, j, k} \quad , \quad P_{n_i, j, k} = P_{2, j, k} \\ u_{1, j, k} &= u_{n_i-1, j, k} \quad , \quad v_{1, j, k} = v_{n_i-1, j, k} \quad , \quad w_{1, j, k} = w_{n_i-1, j, k} \quad , \quad P_{1, j, k} = P_{n_i-1, j, k} \end{aligned} \quad (3-18)$$

where n_i stands for the number of cells in X, Y and Z directions of the computational domain.

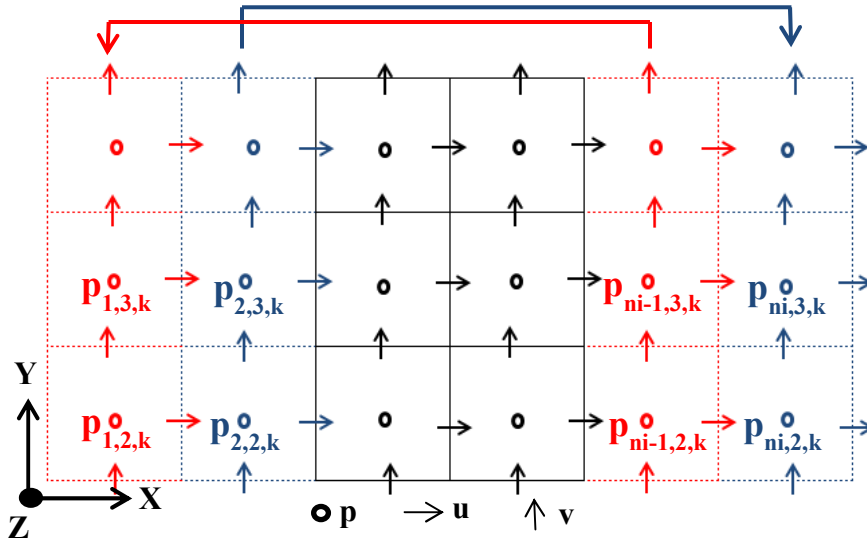


Figure 3-4 The implementation of proper periodic boundary condition on XY plane of the computational domain for pressure cells. Arrows show the directions of data duplication.

3.2 Structural Solver

3.2.1 Problem Definition

The Equation of Motion (EOM) that generally governs the motion of the structure for modeling elastically mounted rigid body oscillating in the transverse stream direction can be written as;

$$M \cdot \ddot{y}(t) + C \cdot \dot{y}(t) + K \cdot y(t) = F_y(t) \quad (3-18)$$

where $\dot{y}(t)$ and $\ddot{y}(t)$ denote the first and second derivative of the cross-stream displacement of the structure with respect to time t , respectively. In addition, M is the mass matrix, C is the damping matrix and K is the stiffness matrix (see Figure 3-5) and $F_y(t)$ is the vector of generalized hydrodynamic forces as a function of time per unit spanwise length.

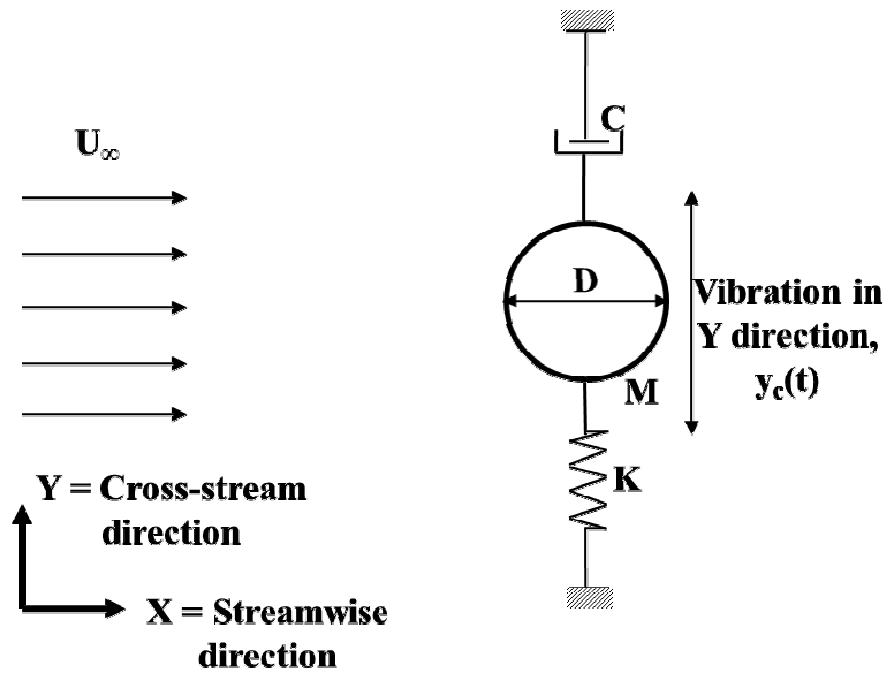


Figure 3-5 Schematic representation of the translation of a cylinder ($y_c(t)$) with an incoming flow, U_∞ , mass M , spring constant K , damping C and diameter D .

While Eqs (3-1) and (3-2) govern the dynamics of the fluid, Eq (3-18) governs the dynamics of the structure. These equations must be solved in a coupled fashion. The overall algorithm to predict the the coupling mechanism will be given later.

3.2.2 Ordinary Differential Equation (ODE)

In situations where the location of the structure is determined by the fluid forces, additional ODEs governing the motion of the structure have to be considered. Also the coupling between the Navier-Stokes equations and ODEs become an important aspect.

The equation of motion is a system of $2n$ first-order, nonlinear, ordinary differential equation where n stands for the number of degree of freedoms of the

structure. Then, Eq (3-18) can be rewritten in a non-dimensional form to match the same reference scales as in N-S equations (the cylinder diameter, D , and the freestream velocity, U_∞) as follows:

$$\frac{dv(t)}{dt} + (2\xi\omega) \cdot v(t) + \omega^2 \cdot y(t) = a_y(t) \quad (3-19)$$

where $v(t) = \frac{dy(t)}{dt}$ is the velocity of the structure in cross-stream direction with the displacement $y(t)$ in the corresponding direction, and $a_y(t) = \frac{2 \cdot C_L}{m^* \cdot \pi}$ is the acceleration of the rigid body in y-direction with C_L being the lift coefficient.

For a cylinder freely oscillating in the cross-stream direction, which is modeled as a mass-damper-spring system, the non-dimensional equation of motion (Eq (3-19)) in y-direction can be rewritten as;

$$\ddot{y}^*(t^*) + 2\xi\left(\frac{2\pi}{U_{red}}\right)\dot{y}^*(t^*) + \left(\frac{2\pi}{U_{red}}\right)^2 y^*(t^*) = \frac{2C_L}{m^* \pi} \quad (3-20)$$

where $m^* = \frac{m}{m_f} = \frac{m}{\pi\rho D^2 \frac{L^2}{4}}$ is the mass ratio

$U_{red} = \frac{U_\infty}{f_N D}$ is the reduced velocity

$f_N = \frac{1}{2\pi} \sqrt{\frac{k}{m}}$ is the natural vibration frequency of the cylinder.

with m_f the mass of fluid replaced by the bluff body, ρ the fluid density,

$y^*(t^*) = \frac{y(t)}{D}$ the non-dimensional vertical displacement,

$\xi = \frac{c}{2\sqrt{km}}$ the damping and

$$C_L(t^*) = \frac{F_y(t^*)}{\frac{1}{2} \rho U_\infty^2 DL} \quad \text{is the lift coefficient}$$

In the equations above, t^* is the nondimensional time, m is the system mass, c is the damping coefficient, k is the spring constant, $y(t)$ is the cross-stream displacement of the system center, L is the span length of the cylinder and $F_y(t^*)$ is the instantaneous lift coefficient. It is noticed that the same references such as approach flow velocity, U_∞ and cylinder diameter, D , are also used to derive the non-dimensional form of the equation of motion.

3.3 Strong Coupling Scheme using Hamming's 4th Order Predictor-Corrector

Method

In the present research, the fluid and the structure will be treated as elements of a single dynamical system, and all governing equations will be integrated with respect to time in an iterative manner. In such, a fundamental complication with the application of a time-domain approach to fluid-structure interaction problems is introduced and it can be explained as the necessity of the knowledge of the motion of the structure over the prediction of hydrodynamic loads and vice versa. In order to overcome this complication, an iterative predictor-corrector scheme that considers the interaction between the hydrodynamic loads and the motion of the structure has been developed. The algorithm is based on Hamming's 4th order predictor-corrector method (Carnahan et al., 1969). In the following paragraphs the structural solver and the coupling scheme will be discussed in detail.

According to the equilibrium conditions, the right hand side of the Eq (3-19) vanishes, i.e. $\frac{dv(t)}{dt} = 0$ and $\frac{dy(t)}{dt} = 0$ once equilibrium occurs.

Then, the right hand side and the left hand side of the system become:

$$\underline{F(t)} = \left\{ \begin{array}{c} v(t) \\ a_y(t) - (2\xi\omega) \cdot v(t) - \omega^2 \cdot y(t) \end{array} \right\} \quad \text{and}$$

$$\dot{q}(t) = \left\{ \begin{array}{c} \frac{dy(t)}{dt} \\ \frac{dv(t)}{dt} \end{array} \right\} \quad \text{where} \quad q(t) = \left\{ \begin{array}{c} y(t) \\ v(t) \end{array} \right\} \quad (3-21)$$

Now, the non-dimensional form of the equation of the motion can be written as follows;

$$\dot{q}(t) = \underline{F(t)} \quad (3-22)$$

in which generalized displacements and the corresponding generalized velocities are represented in the first row of vectors F and q whereas the second row of vectors describe the generalized velocities and the accelerations which are simply the generalized forces divided by the corresponding inertias, respectively. In order to integrate Eq. (3-22) in the time domain, Hamming's 4th order predictor-corrector method is implemented (Preidikman and Mook, 2000).

A schematic of the strong-coupling algorithm is shown in Figure 3-6 and details of it are presented below:

1. Given a time step, Δt , let $t_j = j \cdot \Delta t$ denote the time at j th time step and

$$q^j = q(t_j) = \left\{ \begin{array}{c} y(t_j) \\ v(t_j) \end{array} \right\}, \quad \dot{q}^j = \dot{q}(t_j) = \left\{ \begin{array}{c} \dot{y}(t_j) \\ \dot{v}(t_j) \end{array} \right\} \quad (3-23)$$

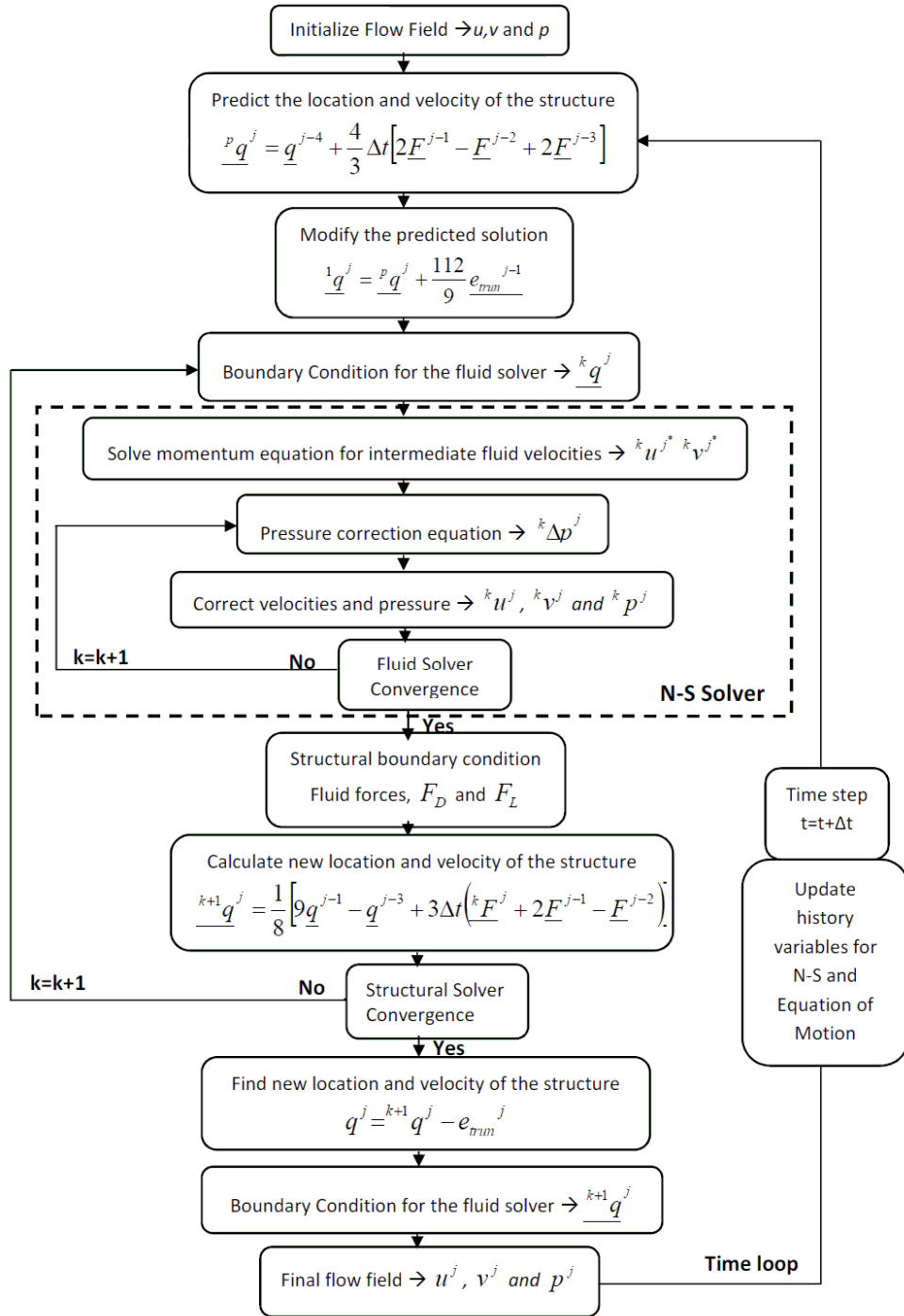


Figure 3-6 A schematic representation of the strong coupling scheme

where $\dot{\underline{q}}^j$ is the vector containing generalized velocities and the accelerations at j th time step of the computation.

$$\underline{F}^j = \underline{F}(\underline{q}(t_j)) = \begin{Bmatrix} v(t_j) \\ a_y(t_j) - 2\xi\omega \cdot v(t_j) - \omega^2 \cdot u(t_j) \end{Bmatrix} = \begin{Bmatrix} v(t_j) \\ \tilde{a}_y(t_j) \end{Bmatrix}, \text{ where } \tilde{a}_y(t_j) \text{ is the}$$

generalized force divided by the corresponding inertias in y direction.

2. Now, predict displacement and velocity of the structure, ${}^p\underline{q}^j$, and modify it (initial guess), ${}^1\underline{q}^j$, using a measure of the truncation error (i.e. the deviation from the exact solution from the approximate solution) from the previous time step.

$${}^p\underline{q}^j = \underline{q}^{j-4} + \frac{4}{3}\Delta t [2\underline{F}^{j-1} - \underline{F}^{j-2} + 2\underline{F}^{j-3}] \quad \text{or} \quad (3-24)$$

$$\begin{Bmatrix} {}^p y(t_j) \\ {}^p v(t_j) \end{Bmatrix} = \begin{Bmatrix} y(t_{j-4}) \\ v(t_{j-4}) \end{Bmatrix} + \frac{4}{3}\Delta t \left[2 \begin{Bmatrix} v(t_{j-1}) \\ \tilde{a}_y(t_{j-1}) \end{Bmatrix} - \begin{Bmatrix} v(t_{j-2}) \\ \tilde{a}_y(t_{j-2}) \end{Bmatrix} + 2 \begin{Bmatrix} v(t_{j-3}) \\ \tilde{a}_y(t_{j-3}) \end{Bmatrix} \right]$$

and

$${}^1\underline{q}^j = {}^p\underline{q}^j + \frac{112}{9} e_{trun}^{j-1} \quad \text{or} \quad \begin{Bmatrix} {}^1 y(t_j) \\ {}^1 v(t_j) \end{Bmatrix} = \begin{Bmatrix} {}^p y(t_j) \\ {}^p v(t_j) \end{Bmatrix} + \frac{112}{9} \begin{Bmatrix} e_{trun_1}^{j-1} \\ e_{trun_2}^{j-1} \end{Bmatrix} \quad (3-25)$$

3. Find the predicted fluid velocity and pressure fields using Navier-Stokes equation with the boundary conditions provided by step (2). Then compute the resulting loads on the structure

$${}^k a(t_j) \rightarrow {}^k \tilde{a}(t_j) \quad , \text{ where } k \text{ is the sub-iteration index}$$

4. Calculate the new location and velocity of the rigid body by

$$\underline{q}^{k+1} = \frac{1}{8} \left[9\underline{q}^{j-1} - \underline{q}^{j-3} + 3\Delta t \left({}^k \underline{F}^j + 2\underline{F}^{j-1} - \underline{F}^{j-2} \right) \right] \quad \text{or} \quad (3-26)$$

$$\begin{Bmatrix} {}^{k+1} y(t_j) \\ {}^{k+1} v(t_j) \end{Bmatrix} = \frac{1}{8} \left[9 \begin{Bmatrix} y(t_{j-1}) \\ v(t_{j-1}) \end{Bmatrix} - \begin{Bmatrix} y(t_{j-3}) \\ v(t_{j-3}) \end{Bmatrix} + 3\Delta t \left(\begin{Bmatrix} {}^k v(t_j) \\ {}^k \tilde{a}(t_j) \end{Bmatrix} + 2 \begin{Bmatrix} {}^k v(t_{j-1}) \\ {}^k \tilde{a}(t_{j-1}) \end{Bmatrix} - \begin{Bmatrix} v(t_{j-2}) \\ \tilde{a}(t_{j-2}) \end{Bmatrix} \right) \right]$$

5. Do a convergence check between sub-iterations before moving forward to next time step. If $\Delta \underline{q}^j$ is greater than a prescribed tolerance, ε , go back to step (3) otherwise if convergence is achieved, move to step (6) where velocity and displacement values are updated.

$$\Delta \underline{q}^j = \left\| {}^{k+1} \underline{q}^j - {}^k \underline{q}^j \right\| \leq \varepsilon \quad \text{or} \quad \begin{Bmatrix} \Delta y(t_j) \\ \Delta v(t_j) \end{Bmatrix} = \left\| \begin{Bmatrix} {}^{k+1} y(t_j) \\ {}^{k+1} v(t_j) \end{Bmatrix} - \begin{Bmatrix} {}^k y(t_j) \\ {}^k v(t_j) \end{Bmatrix} \right\| \leq \varepsilon = 10^{-8} \quad (3-27)$$

where a tolerance is defined as $\varepsilon = 10^{-8}$ here and in Yang et al. (2008) for all the computations in the analysis of one-directional strong coupling of fluid-structure interactions. In all computations presented in this research, the number of iterations at each time step ranged from 2 to 4 depending on the problem.

6. Finalize the algorithm by finding the displacement and velocity of the structure with the final velocity and pressure fields from the N-S equations. Compute the local truncation error (Hamming (1959)) to be used for the next time step as well.

$$\underline{e}_{trun}^j = \frac{9}{121} \left({}^{k+1} \underline{q}^j - {}^p \underline{q}^j \right) \quad \text{and} \quad \underline{q}^j = {}^{k+1} \underline{q}^j - \underline{e}_{trun}^j \quad (3-28)$$

$$\text{or} \quad \begin{Bmatrix} e_{trun_1}^j \\ e_{trun_2}^j \end{Bmatrix} = \frac{9}{121} \left(\begin{Bmatrix} {}^{k+1} y(t_j) \\ {}^{k+1} v(t_j) \end{Bmatrix} - \begin{Bmatrix} {}^p y(t_j) \\ {}^p v(t_j) \end{Bmatrix} \right) \quad \text{and} \quad \begin{Bmatrix} y(t_j) \\ v(t_j) \end{Bmatrix} = \begin{Bmatrix} {}^{k+1} y(t_j) \\ {}^{k+1} v(t_j) \end{Bmatrix} - \begin{Bmatrix} e_{trun_1}(t_j) \\ e_{trun_2}(t_j) \end{Bmatrix}$$

Note that in order to start up the strong-coupling algorithm; a four-step Runge-Kutta Algorithm is implemented to initiate the first four values of displacement and velocity of the immersed boundary. The same algorithm is also used in the studies of Yang et al. (2008)

3.4 Parallelization

The investigation of Vortex-Induced Vibration and forced vibration of an oscillating structure needs very small scales in order to understand the physical phenomena in the area of Fluid-Structure Interactions. In fact, Large Eddy Simulation (LES) on such scales requires a three-dimensional computational domain with extremely high resolution. Therefore, a big amount of computer memory and computing time is necessary to run these simulations. Hence, usage of massively parallel high-performance computers is a must for FSI problems in two and three space dimensions especially for high Reynolds numbers ($Re > 800$).

Parallelization of the present software is based on a classical domain decomposition method using the Message Passing Interface (MPI) (Gropp et al., 1999). The exchange of relevant information during the computation between different processors is obtained through one ghost cell slice as shown in Figure 3-7. As each domain has uniform grids only, the decomposition of the computational domain and the resulting communication is straightforward and can be found in (Croce et al. (2004); Griebel et al. (1997)). However, the communication volume is dependent purely on the employed finite difference method. The width of the finite difference stencils we employ in the software is one grid cell. This requires attaching one slice of boundary ghost cells to each neighboring subdomain. These values are not directly available to the processors

performing the computations. They are sent to the neighboring processors in a communication phase inside the time-stepping loop. Hence, the values for all ghost cells are being communicated in the FSI solver.

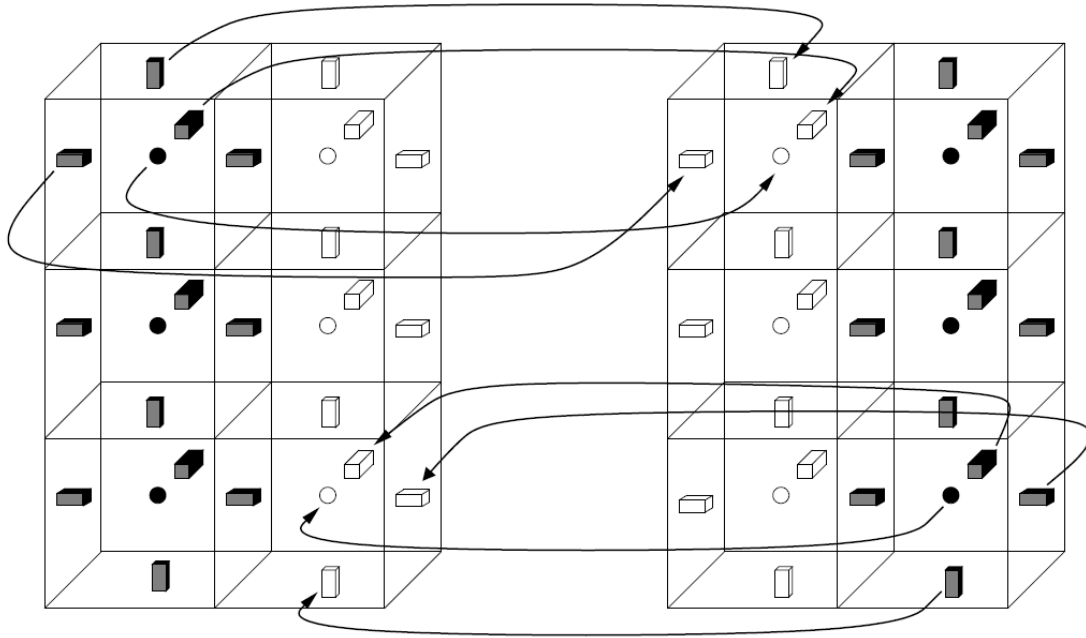


Figure 3-7 Exchange of pressure and velocity values for one ghost cell slice. White bricks denote ghost cell values and black bricks refer to subdomain values (Croce et al., 2004)

CHAPTER 4

IMMERSED BOUNDARY METHOD (IBM) AND ITS VALIDATION

In Chapter 2 of this research, several schemes for simulation of fluid-structure interaction problems by means of imposing the boundary conditions were compared and discussed. It is reported that the immersed boundary method as presented in Lai and Peskin (2000) is capable of producing satisfactory results in various test cases of moving boundary problems. However, the presence of some of the parameters which control the stiffness and damping characteristic of virtual forces that govern the motion of each element at the fluid-solid interface introduces a complexity in imposing boundary motion. In addition, this characteristic leads to quite severe restrictions of the time step during the simulation.

Uhlmann (2004) discusses alternative methods where additional forces which impose rigid body motion upon the fluid are determined directly. Those methods offer a clear advantage in terms of efficiency. However, their disadvantage lies in the fact that they present a different type of serious drawbacks in moving boundary computations in terms of mass conservation. For instance, the implicit method introduced by Fadlun et al. (2000) as well as the explicit method developed by Kim et al. (2001) both result in unacceptably strong oscillations in the force term as soon as the solid structure moves and is in motion with respect to the fixed (Eulerian) grid. This situation occurs due to insufficient smoothing techniques used during the interpolation procedure. On the other

hand, the “rigidity” method introduced by Kajishima and Takiguchi (2002) remedies this problem only partially via using the solid fraction of a grid cell as a weight factor for the forcing term.

In the present research, an efficient solid-domain direct forcing immersed boundary method is utilized. Here, the approach originally developed by Uhlmann (2005a) for fixed and moving boundaries is refined and employed. Uhlmann’s methodology utilizes a direct forcing method; however instead of formulating the force at (Eulerian) grid nodes of the fluid, it is calculated at (Lagrangian) locations on and in the immersed boundary for which the motion of the body is known. The forces are then transferred from Eulerian to Lagrangian and vice versa using a regularized Dirac delta function proposed by Peskin (2002), which provides a smooth transition between fluid and solid body movement. A couple of refinements to Uhlmann’s original method are adopted in this study: a) the Dirac delta function due to Yang et al. (2009) is employed and b) instead of restricting the Lagrangian forcing locations to the surface of the immersed structure, Lagrangian force points are also placed inside the structure, which is why Uhlmann (2005b) refers the improved method as “*solid-domain forcing*” in his study. Obviously, for stationary structures, this method may not be as accurate as sharp interface methods; however the method results in less non-physical pressure oscillations in the case of moving boundaries. The application of this scheme to several 2D and 3D benchmark problems presented in the following chapters demonstrate its feasibility and efficiency.

4.1 Direct Forcing Method

4.1.1 Geometric Definitions

According to the present method, a number of N_L elements are defined depending on the forcing method either around the circumference of a circular structure or in the entire solid domain. These points are called *Lagrangian force points* (LFP) (Uhlmann (2005a)). As shown in Figure 4-1, the elements are equi-partitioned sectors of a single or collections of an annulus with inner and outer radii r_1 , r_2 , respectively. For a single ring:

$$r_c = \frac{r_2 - r_1}{2} \quad (4-1)$$

where r_c is the actual ring radius which is located at the midpoint of these two radii, i.e., the circumference of the ring.

In practice according to Uhlmann (2005a), the number of marker elements is chosen so that the marker volume matches the Eulerian grid cell surface as closely as possible, in other words, the volume of fluid cell is equivalent to a volume force point, ΔV_l , as defined below gives the surface of an element (l refers to each LFP):

$$\Delta V_l = \frac{2\pi \cdot r_c h}{N_L} \quad (4-2)$$

In Eq (4-2), h is the mesh size, which is chosen to be $h = r_2 - r_1$. Requiring that $\Delta V_l \approx h^2$ results in the following condition for the number of force points per each ring:

$$N_L \approx 2\pi \frac{r_c}{h} \quad (4-3)$$

Therefore at a given time, the forcing points are located at:

$$X_l = x_c + r_c \begin{pmatrix} \cos(\frac{2\pi(l-1)}{N_L} + \theta_c) \\ \sin(\frac{2\pi(l-1)}{N_L} + \theta_c) \end{pmatrix} \quad \forall 1 \leq l \leq N_L \quad (4-4)$$

Due to rigid body motion of the structure, the following velocities are assigned for these points:

$$U_l = u_c + \omega_c \times (X_l - x_c) \quad (4-5)$$

where x_c , u_c , ω_c , θ_c and r_c are the center locations, linear and angular velocities, angular position and radius, respectively, of a circular structure.

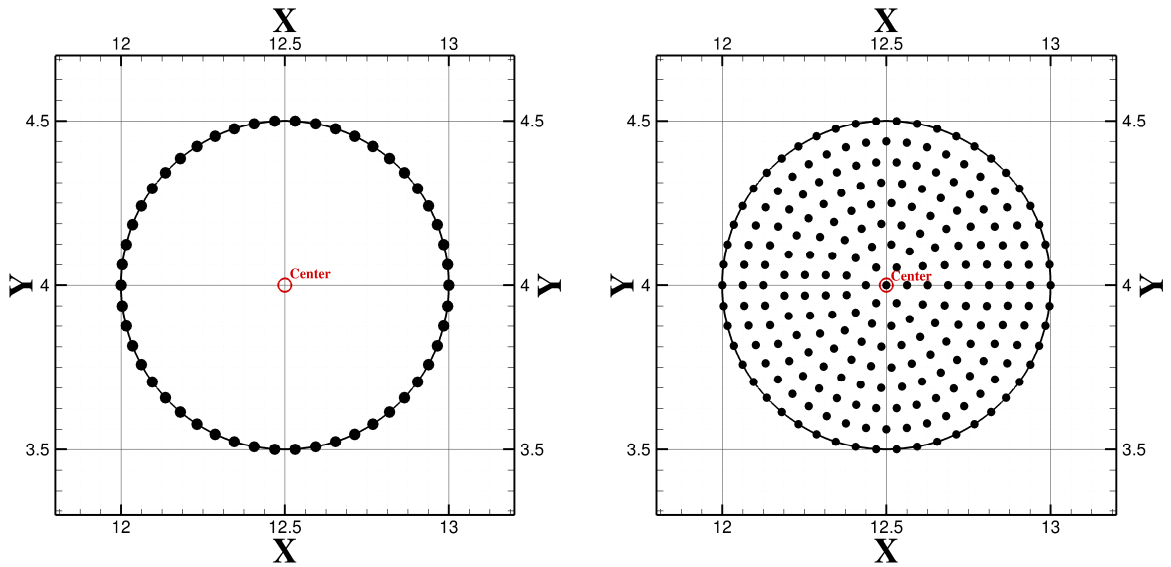


Figure 4-1 The definition of marker elements along the circumference of a circular structure for interface forcing scheme (Left graph) and in the entire solid domain for solid domain forcing scheme (Right graph). Small solid circles indicate the (equidistant) locations of marker points.

The inside of the solid structure (Figure 4-1) is also forced by simply adding supplementary rings of marker elements throughout the solid structure. Each ring will eventually have a different number of elements; however, each element will satisfy the condition of equivalent volume which is $\Delta V_i \approx h^2$.

For three dimensional structures such as cylinders or spheres, the extension of the method is relatively straightforward. In that case, the marker points have to be distributed evenly on the surface for interface forcing and throughout the entire structural domain for the solid domain forcing scheme, respectively. In that case, the Lagrangian volume of each element V_i becomes the product between the surface volume and the height of the cylinder.

4.1.2 Force Formulation

For clarity and simplicity, the present concept of the proposed algorithm is presented in the framework of a single-step time discretization, uniform grid. According to the momentum equation (Eq (3-2)) in the following form

$$\frac{u_i^{n+1} - u_i^n}{\Delta t} = rhs_i^{n+1/2} + f_i^{n+1/2} \quad (4-6)$$

where $rhs_i^{n+1/2}$ includes convective, viscous and pressure-related terms in the N-S equations and $f_i^{n+1/2}$ are the fluid-solid coupling terms, which are evaluated at some intermediated time level. The direct forcing employed by Fadlun et al. (2000) can be expressed by simply rewriting Eq (4-6) as:

$$f_i^{n+1/2} = \frac{u_i^d - u_i^n}{\Delta t} - rhs_i^{n+1/2} \quad (4-7)$$

in which u_i^d is the desired Eulerian velocity component at any point where forcing is to be applied either on the surface or inside the structure depending on the scheme chosen to impose proper boundary conditions. Eq (4-7) is characteristic for direct forcing schemes. However, interpolation is required to obtain an adequate representation of the interface since the solid-interface does not coincide with the Eulerian grid lines. According to Uhlmann's methodology, the force term is defined at Lagrangian positions attached to the surface of the structure as:

$$F_l^{n+1/2} = \frac{U_l^d - U_l^n}{\Delta t} - RHS_l^{n+1/2} \quad (4-8)$$

In the above equations, upper-case letter denote quantities evaluated at Lagrangian coordinates while small-case letter indicate quantities evaluated at Eulerian grid cells. The desired velocity, U_l^d in the structural domain is simply given by the solid-structure motion in Eq. (4-5).

Finally, the transfer of the velocity from Eulerian to Lagrangian positions as well as the inverse procedure which is transfer of the forcing term to Eulerian grid positions is utilized as the final element of the method of Uhlmann (2005a). For this purpose, a uniform mesh with mesh width h in all three directions is considered. In addition to that, discrete Lagrangian force points are distributed evenly on the particle. The regularized delta function $\delta_h(\dots)$ of Peskin (2002) is utilized to transfer both quantities as:

$$U(X_l) = \sum_{ijk} u(x_{ijk}) \delta_h(x_{ijk} - X_l) h^3 \quad (4-9)$$

$$f(x_{ijk}) = \sum_l F(X_l) \delta_h(x_{ijk} - X_l) \Delta V_l \quad (4-10)$$

where x_{ijk} designates Cartesian grid, ΔV_l indicates the forcing volume assigned to the l th force point. In the next section, particular choice of function $\delta_h(\dots)$ which has the properties of continuous differentiability and second order accuracy will be discussed.

4.2 Choice of the Regularized Delta Functions

A discrete delta function is used as a kernel in order to transfer quantities between Lagrangian and Eulerian locations in the present immersed boundary method. This function determines the accuracy of the immersed boundary method. The salient properties of the kernels described by Peskin (1972); Peskin (2002) are the following:

- $\delta_h(\dots)$ is a continuously differentiable function leading to a smoother transfer than a specified linear interpolation.
- Utilizing such kernels introduces second-order accuracy into force estimations along with smoother fields.
- For all real shifts:

$$\sum_{ijk} \delta_h(x_{ijk} - X_l) h^3 = 1 \quad (4-11)$$

$$\sum_{ijk} (x_{ijk} - X_l) \delta_h(x_{ijk} - X_l) h^3 \quad (4-12)$$

which are discrete analogues of basic properties of the Dirac delta function. As a result, it can be concluded from Peskin (2002) that the total amount of force and torque added to the fluid is not changed by the transfer operations in Eqs. (4-11) and (4-12) in the following form:

$$\sum_{ijk} f(x_{ijk}) h^3 = \sum_{m=1}^{N_p} \sum_{l=1}^{N_f} F(X_l^m) \Delta V_l^m \quad (4-13)$$

$$\sum_{ijk} x_{ijk} \times f(x_{ijk}) h^3 = \sum_{m=1}^{N_p} \sum_{l=1}^{N_L} X_l^m \times F(X_l^m) \Delta V_l^m \quad (4-14)$$

As a consequence, it is shown that the “spreading” operation (Eq. (4-10)) from the Lagrangian to Eulerian grid does not alter the total amount of force and torque which is added to the fluid.

4.2.1 Regularized Discrete Delta Function (RDDF)

In the present research, the regularized delta function with a support of 3 mesh widths of reference Roma et al. (1999) is utilized first. The three dimensional discrete delta function used in the present immersed boundary method is constructed in the following form (Peskin (2002)):

$$\delta_h(x_{ijk} - X_l) = \frac{1}{h^3} \phi\left(\frac{x-X}{h}\right) \phi\left(\frac{y-Y}{h}\right) \phi\left(\frac{z-Z}{h}\right) \quad (4-15)$$

where $\phi\left(\frac{x-X}{h}\right)/h$ is a one-dimensional discrete delta function, x, y and z are the Eulerian components of x_{ijk} and X, Y and Z are the Lagrangian components of X_l . In that respect, the one dimensional 3-point RDDF is written as (Peskin (2002)):

$$\phi_3(r) = \left. \begin{array}{ll} \frac{1}{3}(1 + \sqrt{-3r^2 + 1}), & |r| \leq 0.5 \\ \frac{1}{6}(5 - 3|r| - \sqrt{-3(1 - |r|)^2 + 1}), & 0.5 \leq |r| \leq 1.5 \\ 0, & 1.5 \leq |r| \end{array} \right\} \quad (4-16)$$

4.2.2 Smooth Discrete Delta Function (SDDF)

This section describes a smooth discrete delta function with 3 mesh widths support points. The smoothed 3-point function is formulated by Yang et al. (2009) as follows:

$$\phi_3^*(r) = \begin{cases} \frac{17}{48} + \frac{\sqrt{3}\pi}{108} + \frac{|r|}{4} - \frac{r^2}{4} + \frac{1-2|r|}{16} \sqrt{-12r^2 + 12|r| + 1} \\ - \frac{\sqrt{3}}{12} \arcsin\left(\frac{\sqrt{3}}{2}(2|r|-1)\right), & |r| \leq 1 \\ \frac{55}{48} - \frac{\sqrt{3}\pi}{108} - \frac{13|r|}{12} + \frac{r^2}{4} + \frac{2|r|-3}{48} \sqrt{-12r^2 + 36|r| - 23} \\ + \frac{\sqrt{3}}{36} \arcsin\left(\frac{\sqrt{3}}{2}(2|r|-3)\right), & 1 \leq |r| \leq 2 \\ 0, & 2 \leq |r| \end{cases} \quad (4-17)$$

The new function is shown to have wider supports than the RDDF as shown in Figure 4-2. However, as discussed in Uhlmann (2005a), the wider supports are not sufficient to reduce the non-physical oscillations entirely. The related properties of the smooth Dirac delta function is the moment conditions, which are described by Yang et al. (2009) as:

1. The SDDF has one higher derivative than the RDDF which increases the continuous properties of the proposed functions.
2. The SDDF satisfies the zeroth and first discrete moment conditions.
3. The derivatives of the SDDF satisfy the zeroth, first and the second discrete moment conditions as compared to the derivatives of the RDDF which only satisfy the zeroth and the first discrete moment conditions.

As a result, the smoothing technique that is developed by Yang et al. (2009) can significantly suppress force oscillations in moving boundary problems in the context of Uhlmann’s IB method (Uhlmann (2004, 2005a, b)). The derivatives of the RDDF do not satisfy certain moment conditions as described above. On the other hand, the SDDF has one higher derivative which is helpful in reducing non-physical oscillations and lead to a significant improvement in the force prediction.

The implementation of this technique is not equivalent to a post-processing procedure that other studies (Anagnostopoulos and Bearman (1992); Beaudan and Moin (1994); Yang and Balaras (2006)) used for smoothing the force. Especially, in prescribed and vortex induced vibration validation cases that are studied in the next chapters, an accurate force prediction is crucial in the context of interaction between structural dynamics and the fluid flows. Under such circumstances, the post-processing of the force prediction becomes inaccurate and impractical and should be avoided.

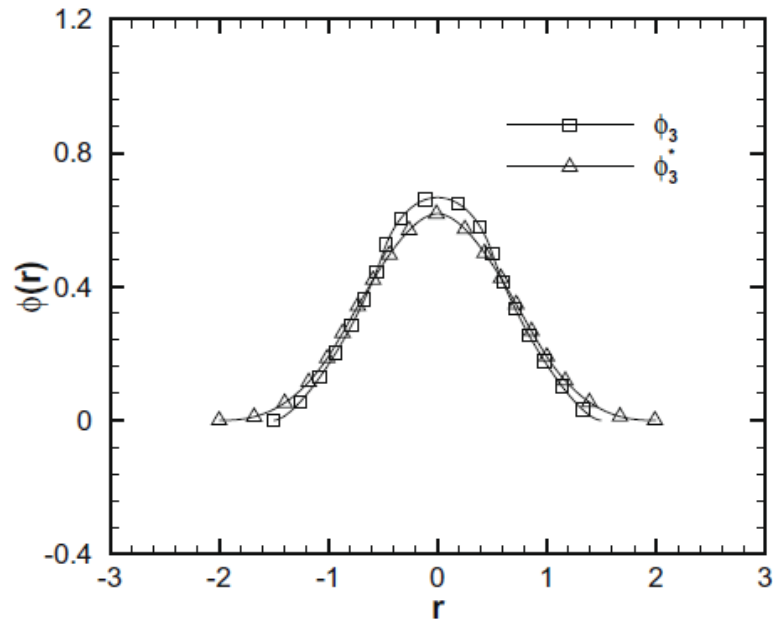


Figure 4-2 Comparison of a regular discrete delta function ϕ_3 and its corresponding smooth function ϕ_3^* (This figure is taken from Yang et al. (2009))

4.3 Validation of the IB Method

The flow past immersed structures has been the subject in fluid-structure interaction applications for a long time. Most of these studies were concerned with the circular cylinder case under free flow conditions. However, there are numerous applications of square structures in many technical areas such as aerodynamics (Franke et al. (1990); Suzuki et al. (1993)) that have not been investigated to the same extent as flow past circular cylinders. Breuer et al. (2000) states in their study that fluid mechanical coefficients of square cylinders such as C_D , C_L are less dependent on the Reynolds number than for circular ones due to fixed separation points for sharp-edged structures. Unfortunately, no experimental data for model comparison can be found in the literature for the square cylinder.

The proposed method is first validated through 2D simulations of flow around a cylinder with square cross-section which is mounted inside a plane channel with a blockage ratio, $B = 1/8$. This case was investigated by Breuer et al. (2000) in detail by two different numerical techniques, namely a Lattice-Boltzmann Automata (LBA) (Aidun and Clausen (2010)) and a finite-volume method (FVM). The present simulation results for $Re = 30$ and $Re = 100$ are compared with the computations by Breuer et al. (2000). In addition, the effect of two different forcing methods, interface and solid domain forcing, on the accuracy of velocity profiles and force calculations, is carried out for this flow.

The 2D laminar flow around a square cylinder with diameter D mounted centered inside a plane channel with height H is investigated by Breuer et al. (2000) as shown in

Figure 4-3. The blockage ratio $B = H / D$, which is defined as diameter to height ratio, is kept at $1/8$. As shown in Figure 4-4, the simulation domain length is set to $L = 48D$ in order to reduce the influence of inflow and outflow boundary conditions while the height of the domain is kept at $8D$. For the present Finite Difference computations, $l = L/4$ is chosen. Breuer et al. (2000) used different inflow lengths in their LBA simulations in order to investigate the influence of different inflow and outflow lengths and showed that there were only negligible deviations in the results. The solver employs a local mesh refinement (LMR) algorithm as shown in Figure 4-4. This ensures adequate resolution in the region of interest at manageable computational costs. The LMR algorithm was developed by my colleague Mehtap Cevheri as part of her PhD study (Cevheri (2012)).

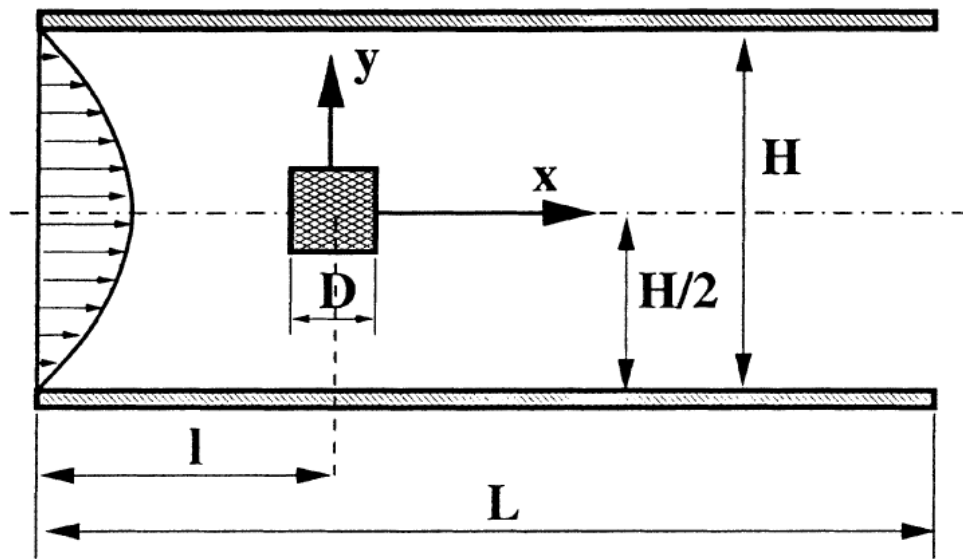


Figure 4-3 Definition of the geometry and integration domain by Breuer et al. (2000)

The resolution near the square is $0.0125D$ i.e. 80 grid points on each side of the square. The no-slip wall boundary condition is imposed at south and north boundaries of the computational domain. In order to simulate a fully developed laminar channel flow upstream of the square cylinder, a parabolic velocity profile with a maximum velocity U_∞ is prescribed at the channel inlet. At the outflow boundary, a convective boundary condition is used so that vortices can exit the outflow boundary without significant disturbances or reflections into the inner domain. The convective boundary condition was proved to work very well in other researchers' studies (Breuer et al. (2000); Breuer and Pourquie (1996); Breuer and Rodi (1994)).

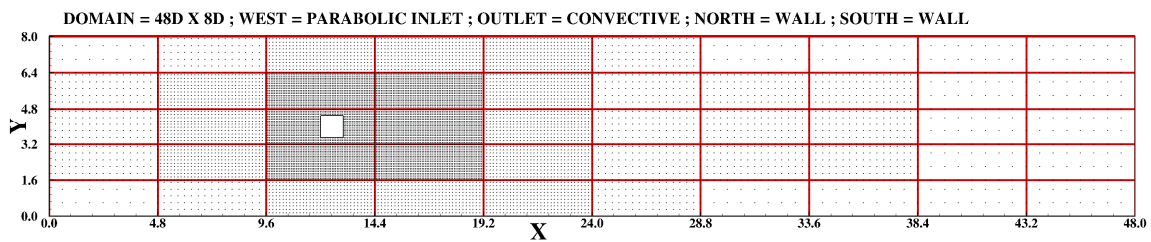


Figure 4-4 Geometry of the computational domain around a rectangular structure. Local Mesh Refinement (LMR) is used to increase the resolution around the immersed structure (every 5th grid point is shown).

A similar marker point construction strategy is implemented in defining the geometry of the square cylinder as in the circular cylinder case (see Figure 4-1) as shown in Figure 4-5. In this case the marker points are defined either along the circumference of the square structure or in the entire solid domain depending on the forcing scheme used.

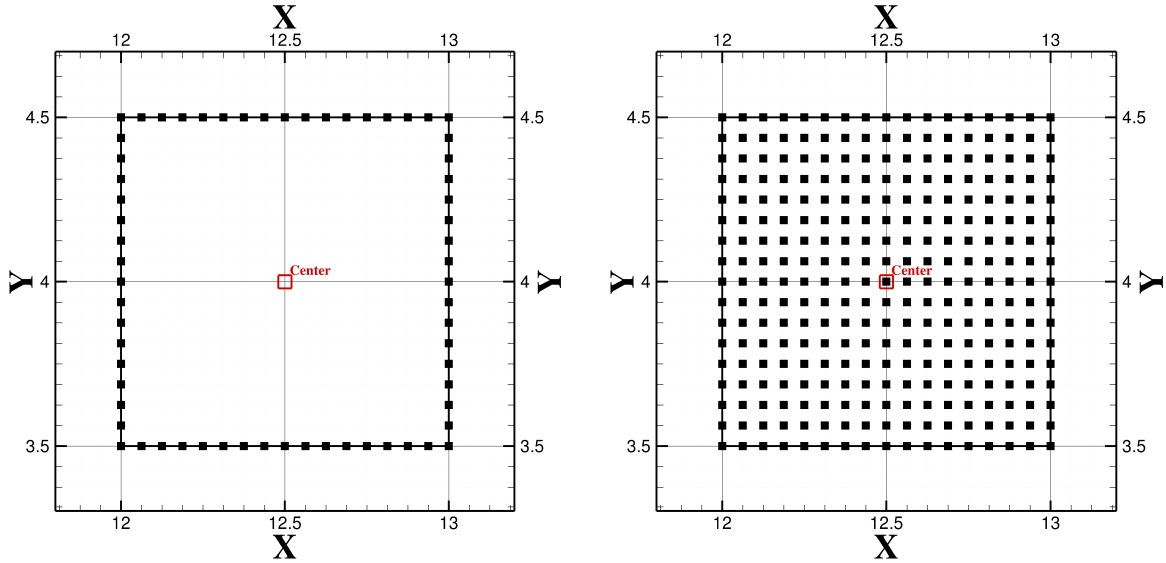
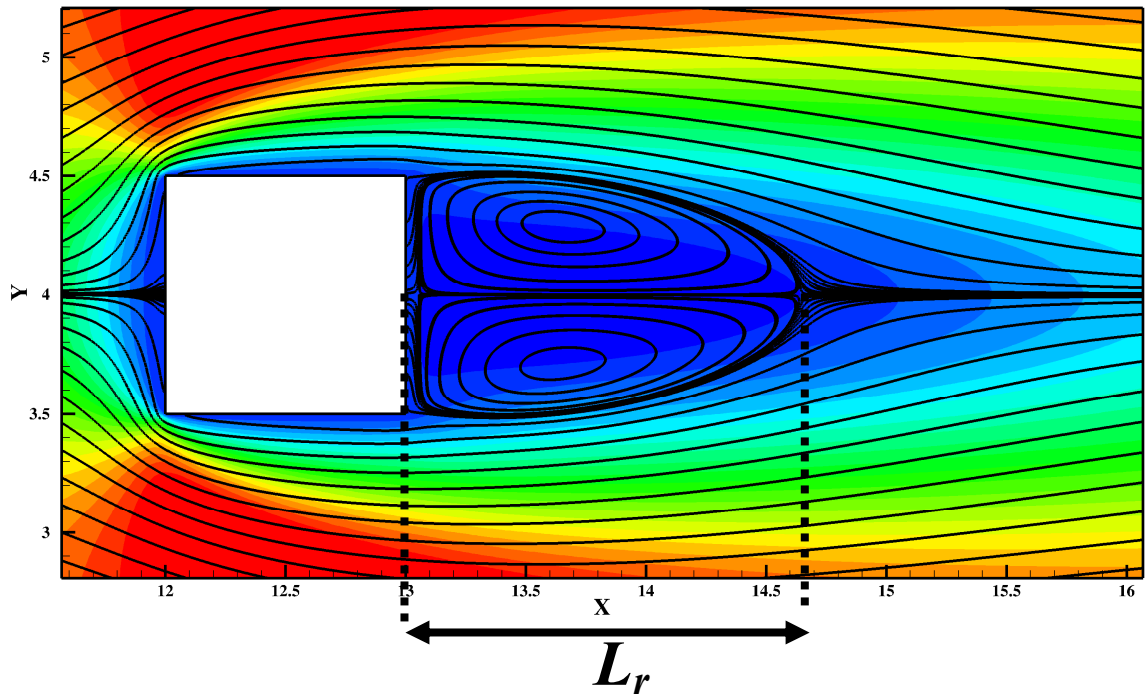


Figure 4-5 The definition of marker elements along the circumference of a square structure for interface forcing scheme (Left graph) and in the entire solid domain for solid domain forcing scheme (Right graph). Small solid squares indicate the (equidistant) locations of marker points.

Figure 4-6 shows computational results of the finite difference code in the vicinity of the cylinder by streamlines at Reynolds number 30. At this Re , the wake comprises a steady recirculation region of two symmetrical vortices located on each side of the centerline. However, the top figure which is a result of interface forcing only shows a shift in the recirculation length while the lower one being a result of solid domain forcing shows the separation region starting at the back edge of the cylinder. Obviously, solid domain forcing leads to a sharper representation of the corners of square structures where the separation point is fixed at the trailing edge and the flow is attached at the side walls.

Re = 30; DOMAIN = 48D X 8D; Resolution Near Square = 0.0125D x 0.0125D



Re = 30; DOMAIN = 48D X 8D; Resolution Near Square = 0.0125D x 0.0125D

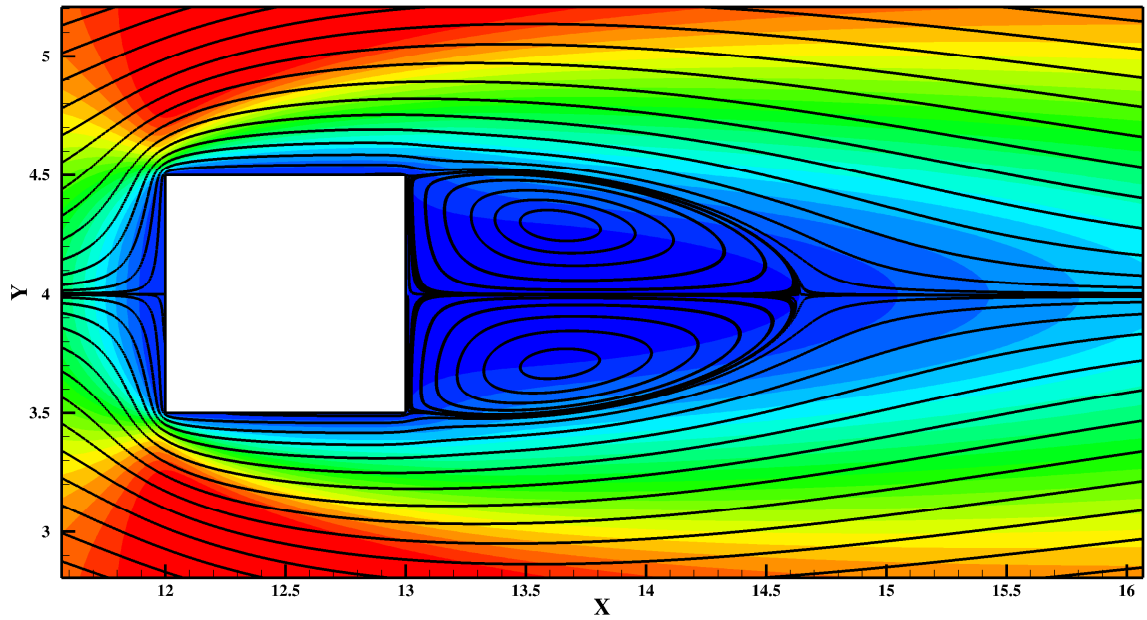


Figure 4-6 Streamlines around the square cylinder at Reynolds number 30. Top figure corresponds to results through interface forcing while the bottom one is the result of the simulation through solid domain forcing. Recirculation is depicted in the top figure in black.

An empirical relationship for the length of the closed near-wake, in other words, the recirculation length, L_r , at a blocking ratio $B = 1/8$ was proposed by Breuer et al. (2000) as follows:

$$\frac{L_r}{D} = -0.065 + 0.0554 \text{Re} \quad \text{for } 5 < \text{Re} < 60 \quad (4-18)$$

Therefore, at $\text{Re} = 30$, L_r / D becomes equal to 1.597. This parameter is found to be 1.64 using the present IB method through interface forcing while it is also equal to 1.64 when solid domain forcing is utilized. Both of the results overestimate the recirculation length approximately by 2%, on the other hand, the latter eliminates the reattachment of the vortices ensuring a sharper interface representation behind the structure.

The pressure contours for both types of force-point distributions are visualized in Figure 4-7. In both cases a smooth transition of contours is seen on the fluid side of the interface. In the solid region, however, the pressure fields are fundamentally different. With interface forcing an approximately constant pressure is generated inside the cylinder, i.e. a strong jump across the interface is observed. Solid domain forcing, on the other hand, leads to a continuous pressure across the interface resulting in a much smoother spatial distribution and thereby its divergence is greatly reduced.

Figure 4-8 shows comparison of computed drag and lift coefficients with the two different forcing configurations around the structure. As seen in this figure, the lift coefficient magnitudes and the frequencies for both interface forcing and solid forcing cases are similar. However, the magnitude of the former is 6 % greater than the latter one. Uhlmann (2005a) noted that interface forcing can lead to overestimation of the drag coefficients which can be overcome by “*solid domain forcing*” (Uhlmann (2005b)) as

shown here. On the other hand, the lift coefficient is not significantly influenced by the forcing method.

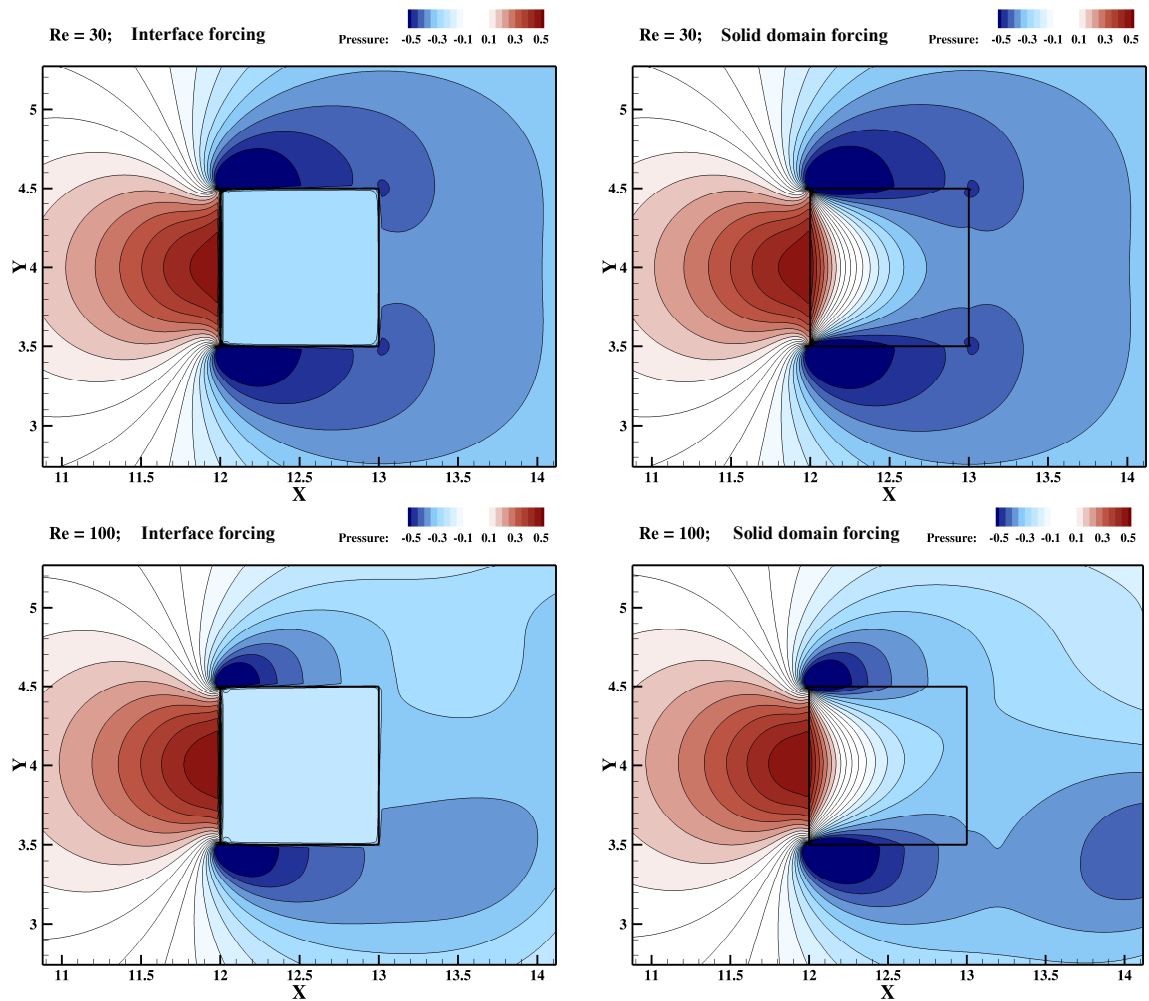


Figure 4-7 Iso-contours of the pressure field of the channel flow around a fixed cylinder at $Re = 30$ (top row) and $Re = 100$ (bottom row). Interface forcing around the circumference (left column) and solid domain forcing including interior (right column) of the structure.

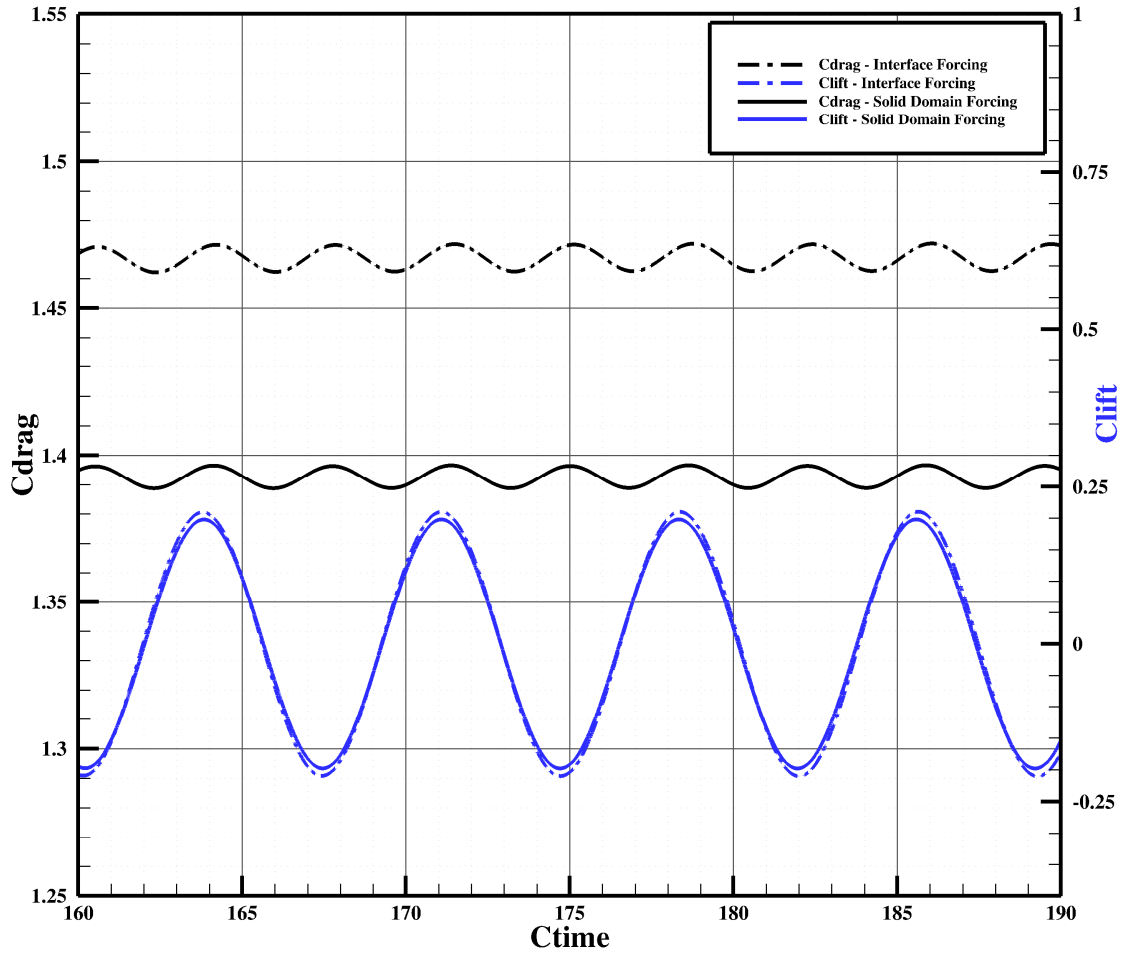


Figure 4-8 Time series of drag and lift coefficients at $Re = 100$ using two different forcing configurations.

Table 4-1 provides C_D , C_L and also the Strouhal number St (see Equation (2-1)) for flow around a square cylinder at $Re = 100$ in comparison to quantities obtained by Breuer et al. (2000). Table 4-1 illustrates that the present results are in good agreement with the numerical data of (Breuer et al., 2000) .

Table 4-1 Time-averaged drag and amplitude of lift coefficients, and the Strouhal number for flow around a stationary square cylinder at $Re = 100$

Solutions	\bar{C}_D	C_L'	St
Breuer et al. (2000)	1.36	0.19	0.139
Present IB method (interface forcing)	1.47	0.20	0.137
Present IB method (solid domain forcing)	1.39	0.19	0.138

Figure 4-9 shows flow visualizations of velocity and vorticity fields for flow around a square cylinder at $Re = 30$ and 100 . These figures are the results of computations using solid domain forcing. It is evident that in the unsteady 2D flow regime, the near wake becomes unstable and a sinusoidal oscillation of the shear layers commences, later forming the well-known phenomenon von Karman Vortex Street.

Despite the lack of experimental data for square cylinders, compared with the numerical results of Breuer et al. (2000), the steady and unsteady flow computations demonstrate the capability of the finite difference code to deal with instantaneous flows. As compared to interface forcing, solid domain forcing results better predict the flow field. As a consequence, the present method provides reliable and accurate results for this kind of confined flow. The extension to other stationary or moving structures and 3D computations with higher Reynolds number is investigated in the following chapters.

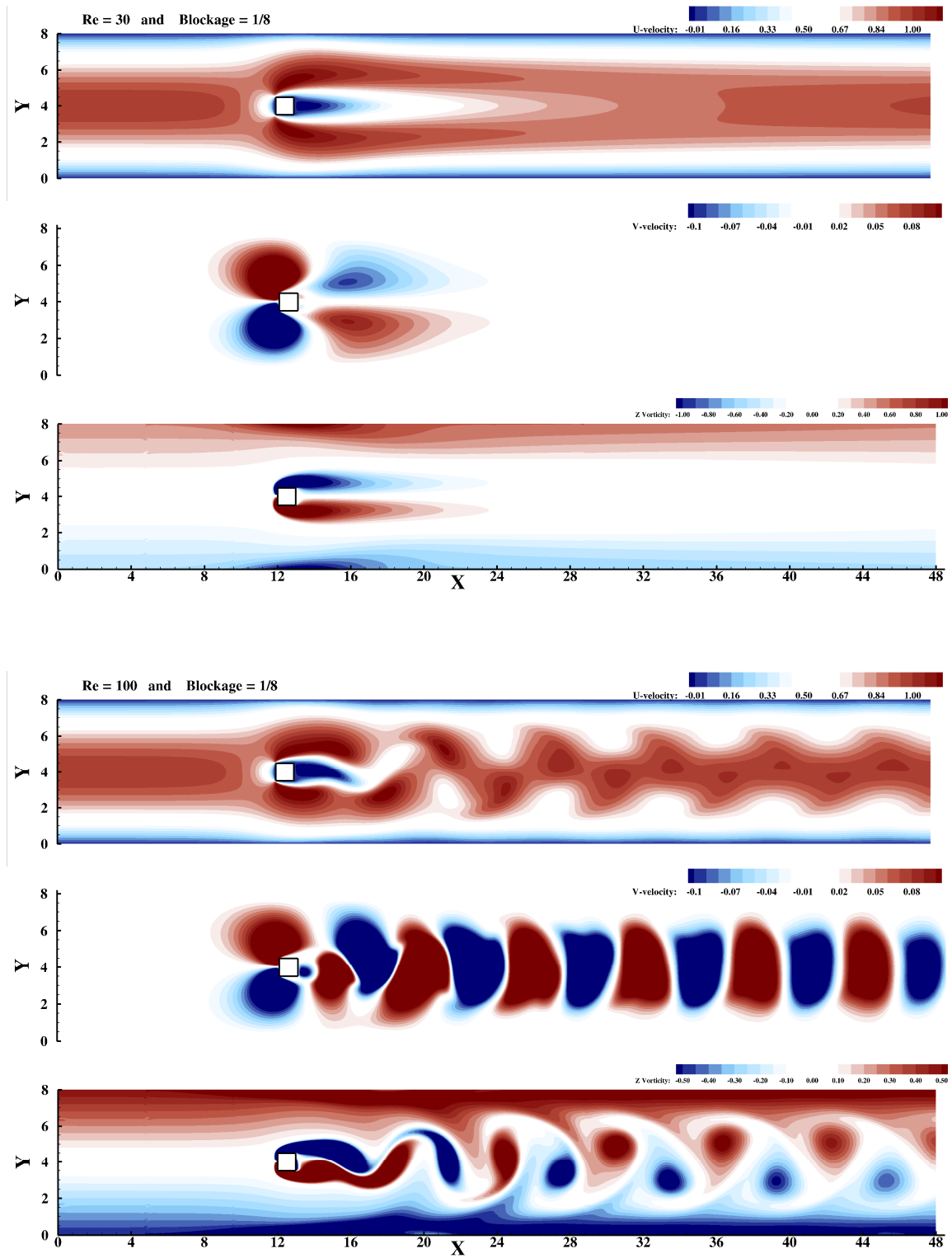


Figure 4-9 Flow visualization of U velocity, V velocity and Z vorticity contour plots for Re = 30 (top) and Re =100 (bottom) via solid domain forcing.

4.4 Summary

In this chapter, an efficient solid-domain direct forcing immersed boundary method introduced by Uhlmann (2005b) is utilized. Here, the approach originally developed by Uhlmann (2005a) for fixed and moving boundaries is refined and employed. Uhlmann's original methodology utilizes a direct forcing method; however instead of formulating the force at (Eulerian) grid nodes of the fluid, it is calculated at (Lagrangian) locations on and in the immersed boundary for which the motion of the body is known. The forces are then transferred from Eulerian to Lagrangian and vice versa using a regularized Dirac delta function, which provides smooth transition between fluid and solid body movement. A couple of refinements to Uhlmann's original method are adopted: a) the Dirac delta function due to Yang et al. (2009) is employed and b) instead of restricting the LFP locations to the surface of the immersed structure, this study also placed LFP inside of the structure as in Uhlmann (2005b).

The accuracy of the proposed immersed boundary method presented in this chapter has been demonstrated via numerical studies for the confined laminar flow past a square cylinder inside a channel ($B = 1/8$). The length of recirculation length for two different forcing collocations is investigated first. It is shown that solid-domain forcing leads to a sharper boundary treatment around the immersed structure as a result of continuous pressure contours across the interface resulting in a much smoother spatial distribution. Then, drag, lift coefficients and Strouhal numbers are computed and compared to results of Breuer et al. (2000) and it is showed that present method provides reliable and accurate results for the steady and unsteady flow past a confined square cylinder simulation.

CHAPTER 5

TWO-DIMENSIONAL (2D) VALIDATION CASES ON FREE AND FORCED VIBRATION OF CYLINDERS

In this chapter, two-dimensional viscous flows past stationary and oscillating cylinders are considered to evaluate the accuracy of the proposed methodology by testing several cases with increasing complexity. The first numerical study is the simulation of flow past a circular cylinder. Although no analytical solutions are available for this problem, there are numerous numerical and experimental studies reported in the literature. For comparison, the experimental data from Tritton (1959) and other numerical results such as Zdravkovich (1997), Silva et al. (2003) and Shu et al. (2007) are available. The second numerical study is the forced vibration of a cylinder. This study involves prescribed motion of a two-dimensional cylinder which has a harmonic cross-streamwise displacement of the cylinder in a free-stream. The numerical parameters used here are the same as by Guilmineau and Queutey (2002), Uhlmann (2005a) and Yang et al. (2009). The third study is the vortex-induced vibration of a cylinder. The purpose of this case is to test the validity of the presented immersed boundary approach in simulating Fluid-Structure Interaction (FSI) problems. To further demonstrate the accuracy and efficiency of the method for FSI problems, a test case of a circular cylinder undergoing free transverse oscillation is studied. Experimental data by Anagnostopoulos and Bearman (1992) and numerical results by Williamson and Govardhan (2004) are available for model comparison. This test case has been also used for validation of other numerical

simulations (Liu et al. (1998); Nomura (1993); Schulz and Kallinderis (1998); Wei et al. (1995); Yang and Balaras (2006)). Finally, flow induced vibration of a circular cylinder subjected to wake interference is studied. Two dimensional numerical simulations of the flow around two circular cylinders in tandem arrangements are performed. The in-line center-to-center distance is kept constant at 2.5 and 6.0 diameters, and the results are compared to that of a single elastically mounted isolated cylinder with the same structural characteristics. The main goal of this study is to investigate the flow induced vibration of the downstream cylinder in tandem arrangement in order to identify the physical mechanisms involved. The results of the simulations for this case show that significant changes occur in the dynamic behavior of the cylinders, when comparing the flow around the tandem arrangements to that around an isolated cylinder.

The second-order finite difference formulation is used for the spatial discretization in the momentum equation. The third-order 3 step Runge-Kutta scheme and the Crank-Nicholson scheme are used for the explicit terms (convection) and the implicit terms (diffusion) in Navier-Stokes equations, respectively. Computations were done on a locally refined grid with a total of 900 thousand cells (see Figure 5-1). The cell size of all cells at the immersed interface is $\Delta x = \Delta y = 0.0156D$, so that the resolution is higher than Uhlmann (2005a) and Yang et al. (2009). Again, a local mesh refinement method is employed. The domain size is $52D \times 36D$, where D is the diameter of the cylinder. A uniform velocity boundary condition is specified at the inlet; a convective boundary condition is applied at the outlet. At the far field in transverse direction, shear-free boundary conditions are implemented.

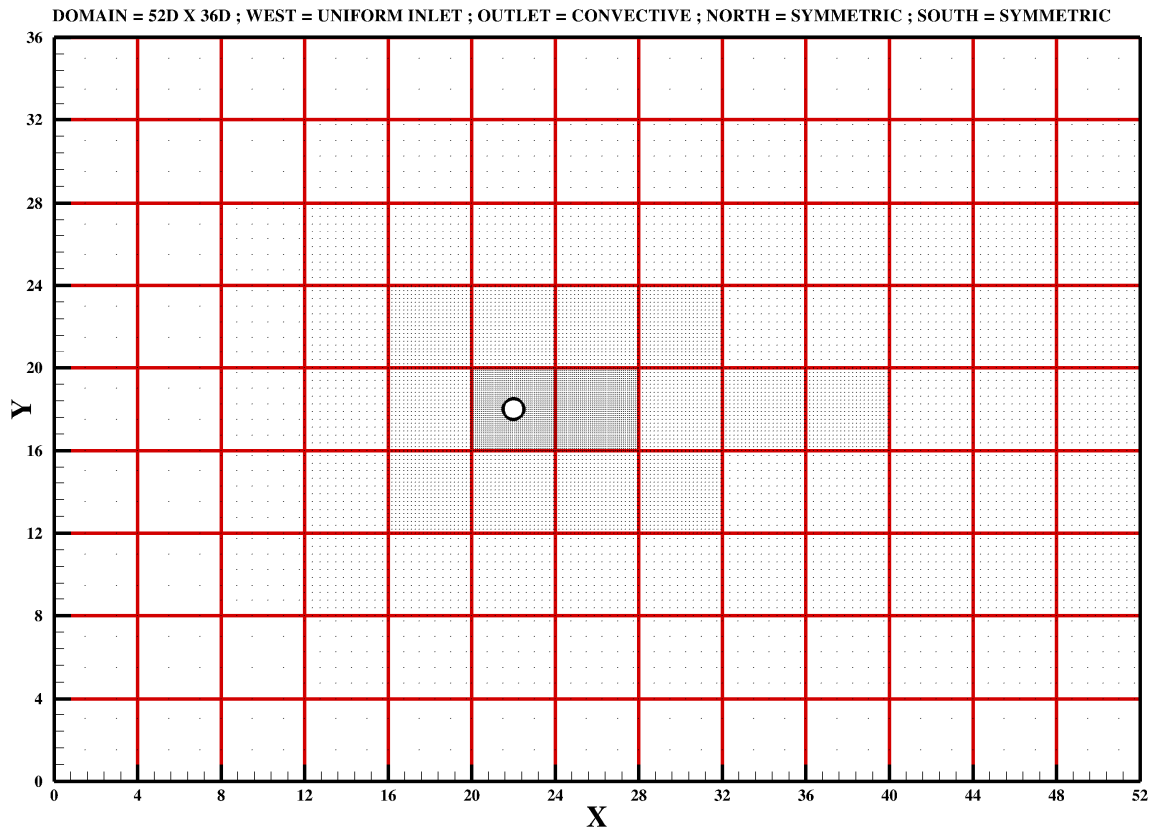


Figure 5-1 A sketch of the grid employed in the vicinity of the cylinder for current simulations. The domain size is 52D X 36D. A uniform velocity boundary is specified at the inlet; a convective boundary condition is used at the outlet; symmetric boundary (every 6th grid point is shown)

5.1 Flow Around a Stationary Cylinder

The unsteady flow around a cylinder is a popular test case for validation of the IBM at moderate Reynolds numbers. In this situation, the well-known phenomenon called Karman Vortex Street occurs as a consequence of alternating separation of vortices triggered by shear layer formation near the cylinder. A visualization of this flow at $Re = 100$ is provided in Figure 5-2. In this figure, instantaneous streamwise and cross-streamwise velocity fields along with contours of the Z vorticity are shown, from which the occurrence of the well-known Karman Vortex Street can be seen. In the present method, the drag and lift forces on the cylinder are evaluated as the summation of the volume force, details are discussed in Appendix A, in streamwise and crosswise directions, respectively. For the moving boundary problems, the inertial force of the “pseudo fluid” enclosed by the immersed boundary needs to be subtracted. The details of the hydrodynamic force calculations can be found in Uhlmann (2003). Table 5-1 compares the present results with those from other researchers (Kara et al. (2012); Kim et al. (2001); Lai and Peskin (2000); Liu et al. (1998); Shu et al. (2007); Tseng and Ferziger (2003); Uhlmann (2005a); Yang et al. (2009)) for $Re = 100$. From this table, it can be seen that the current method produces reasonable results in estimating time averaged drag, the amplitude of lift fluctuations and the Strouhal number.

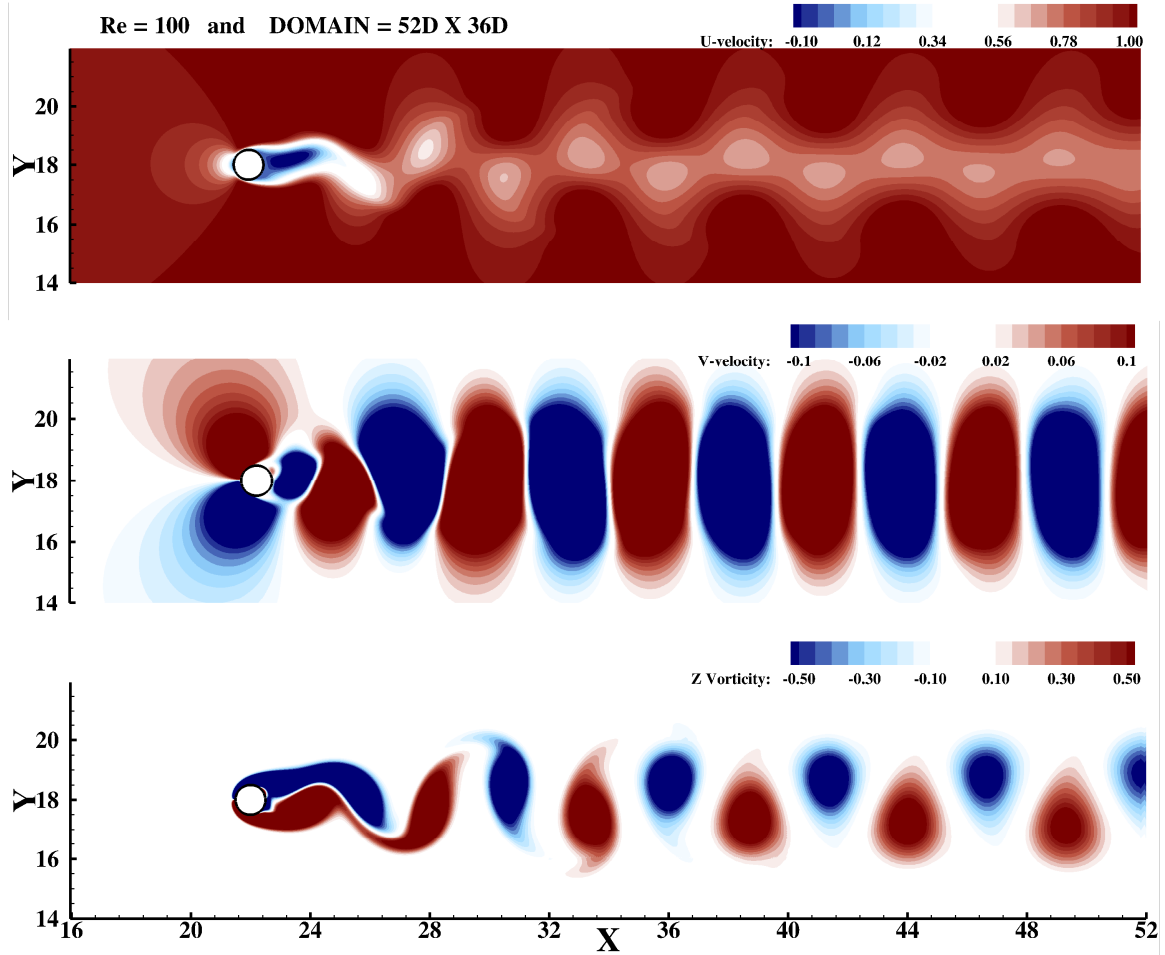


Figure 5-2 Contour plots and flow visualization around cylinder at $Re = 100$.
 Top: U-velocity contour. Middle: V-velocity contour. Bottom: Z-Vorticity Contour

Table 5-1 Time-averaged drag and amplitude of lift coefficients, and the Strouhal number for flow around a stationary cylinder at $Re = 100$.

Authors	\bar{C}_D	C_L'	St
Lai and Peskin (2000)	1.447	0.330	-
Kim et al. (2001)	1.330	0.320	-
Tseng and Ferziger (2003)	1.420	0.290	-
Shu et al. (2007)	1.383	0.350	-
Liu et al (1998)	1.350	0.339	0.165
Uhlmann (2005)	1.501	0.339	0.169
Yang et al. (2009)	1.393	0.335	0.165
Kara et al. (2012)	1.360	0.340	0.164
Present (interface forcing)	1.431	0.310	0.166
Present (solid domain forcing)	1.367	0.338	0.165

The Strouhal number is a parameter to quantify the oscillation of the fluid flow in the wake region. The Strouhal number as a function of the Reynolds number is presented in Figure 5-3. The results from Kara et al. (2012); Norberg (2003); Shu et al. (2007); Williamson (1988, 1989) are also plotted in this figure. For instance, Kara et al. (2012) solved the Navier-Stokes equations through a 2D finite volume method which uses a 3-step Runge-Kutta time integration scheme to advance convective and diffusive terms. Figure 5-3 also shows the grid dependency of the simulations. As a guide to grid generation, the mesh must be sufficiently fine to provide an adequate resolution of the important flow features and geometrical structures. For that reason, the present results with two grid resolutions $0.05D$ and $0.0156D$ around the cylinder are also shown in the figure. The resolution of the grids around the cylinder is kept to be uniform and local mesh refinement is utilized in two directions toward boundaries of the 2D domain (see

Figure 5-1 for the problem set up). The finer grid used in the present study is also consistent with the grid resolution used by Uhlmann (2005a). Figure 5-3 shows that the present results with a grid resolution of $0.0156D$ near the cylinder are in a very good agreement with the experimental data (Williamson (1988)).

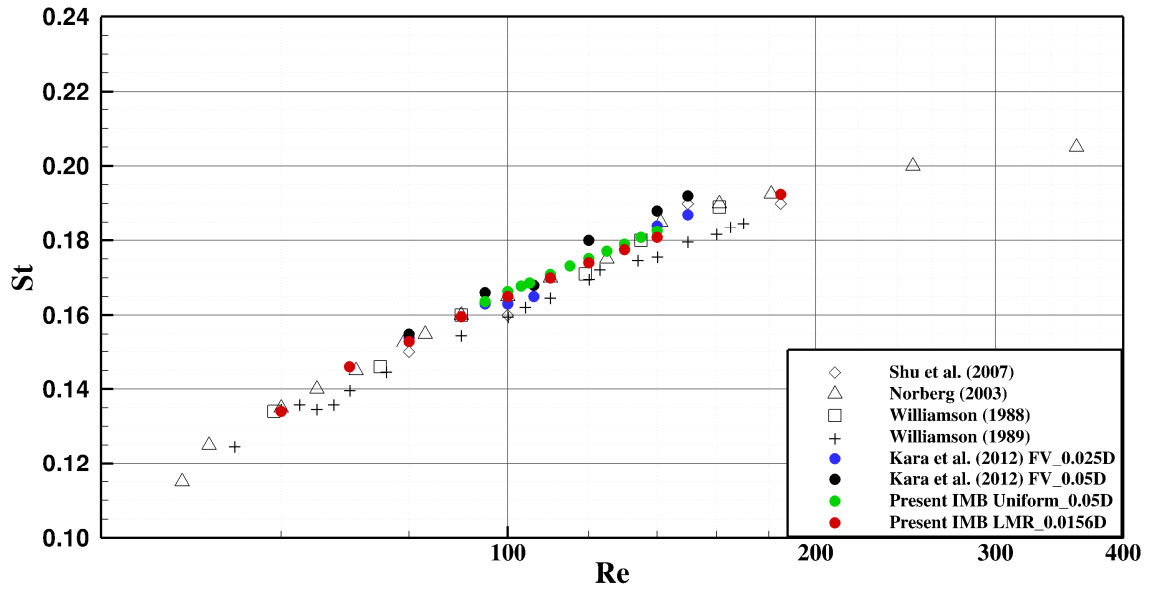


Figure 5-3 Distribution of Strouhal Number (St) versus Reynolds number (Re) (logarithmic scale is used on the horizontal axis)

5.2 Forced Vibration of a Cylinder

The efficiency of the proposed immersed boundary method on the force prediction in moving boundary problems is first tested through simulations of the flow past an oscillating cylinder. The first case is simulation of the two-dimensional laminar flow involving harmonic in-line oscillation of a circular cylinder in a quiescent flow, i.e. flow at rest. Then, laminar flow from a transversely oscillating cylinder in a free-stream

is investigated. Both of the cases present a challenge to non-boundary conforming formulations. In addition, those cases are validated through detailed experimental data and numerical results from boundary-fitted methods that are available in the literature, which in return provides validation of the proposed algorithms.

5.2.1 Flow over an in-line oscillating cylinder

The two characteristic parameters for the flow at rest are the Reynolds number, $Re = U_{max} D / \nu$ and the Keulegan-Carpenter number, $KC = U_{max} / fD$ based on the cylinder diameter, D , maximum velocity of the cylinder, U_{max} , the kinematic viscosity of the fluid, ν , the characteristic frequency of the in-line oscillation, f . A simple harmonic in-line oscillatory motion of the cylinder is prescribed as:

$$x(t) = -A \sin(2\pi ft) \quad (5-1)$$

where $x(t)$ is the position of the cylinder center in the direction of oscillation, A is the amplitude of oscillation. The parametric space in this study corresponds to LDA experiments and numerical studies reported by Dutsch et al. (1998). In particular, the two characteristic parameters are selected as $Re = 100$ and $KC = 5$. For this setup the flow remains two-dimensional with periodic vortex shedding. The same domain size, $52D \times 36D$ is used as in stationary cylinder simulations if not otherwise stated. However, in order to predict the quiescent flow, Neumann boundary conditions for the velocity and pressure field are used at all far-field boundaries.

All computations were started from a quiescent flow field and once periodic vortex shedding was formed, time integration was halted. Figure 5-4 shows the pressure and vorticity contours at three different phase-angles ($\theta=2\pi ft$). As the cylinder moves left, two thin boundary layers develop on the upper and lower part of the cylinder as can

be clearly seen in Figure 5-4a. This separating flow produced two identical counter-rotating vortices downstream of the cylinder. The vortex production stops once the structure reaches its extreme left position. As the cylinder moves to the opposite direction, the same process takes place. These results are in very good agreement with the data reported in Dutsch et al. (1998), which shows the robustness of the present method in capturing the dynamics of the vorticity field.

In order to further examine the accuracy of the present method, a quantitative comparison is made with respect to the experimental results. Figure 5-5 shows the computed velocity profiles in the axial and transverse directions at four different x locations and three different phase-angles, in comparison with the experimental data of Dutsch et al. (1998). The present simulation shows very good agreement with the experimental data. The results are very similar to those obtained by other researchers in their numerical studies (Choi et al., 2007; Dutsch et al., 1998; Yang and Balaras, 2006). Figure 5-6 shows the time evolution of the in-line (drag) force, $F_x(t)$, acting on the structure in comparison with the reference boundary conforming simulation results of Dutsch et al. (1998). The agreement with the reference computations is very good implying that the forces on the structures can be predicted very accurately with the proposed approach.

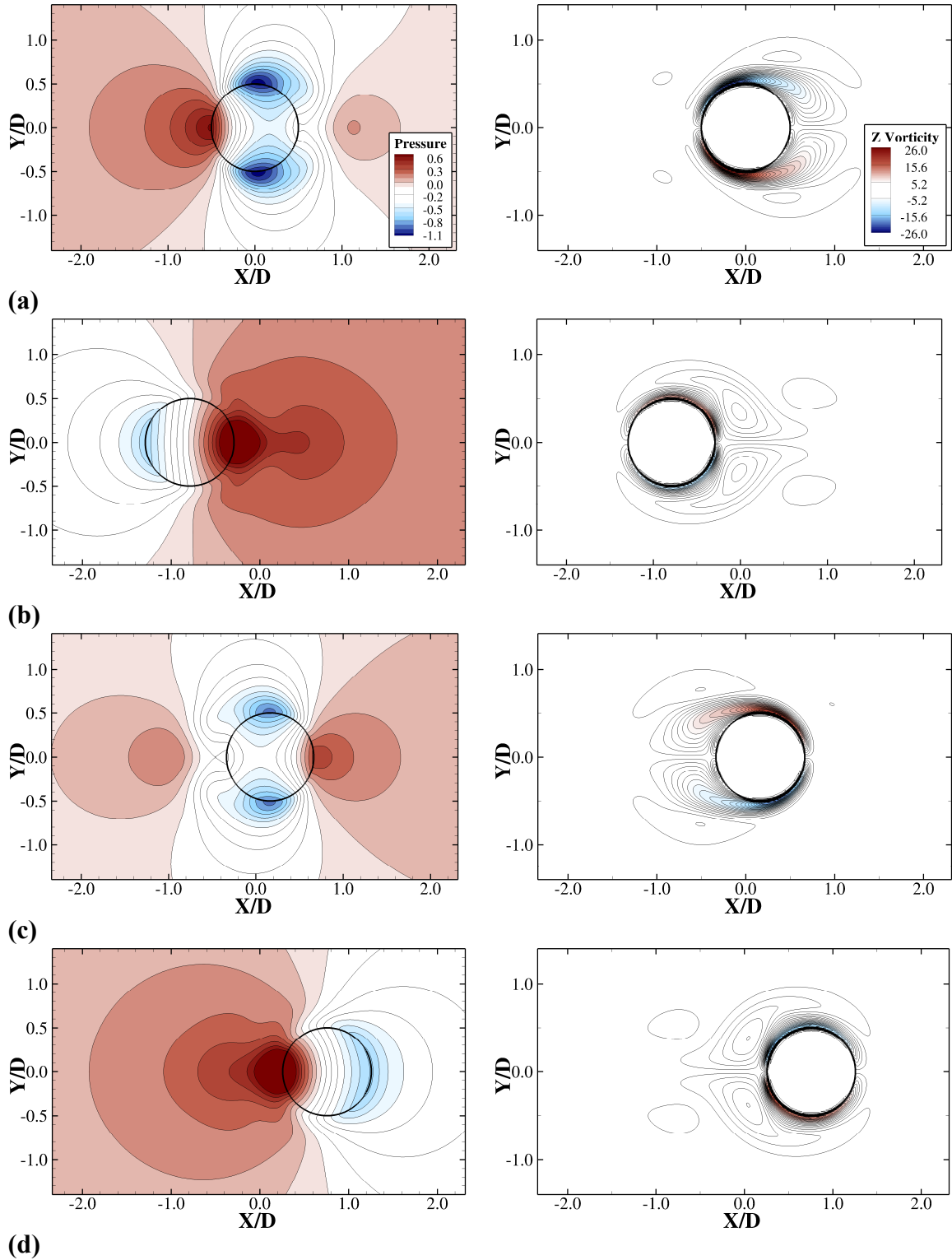
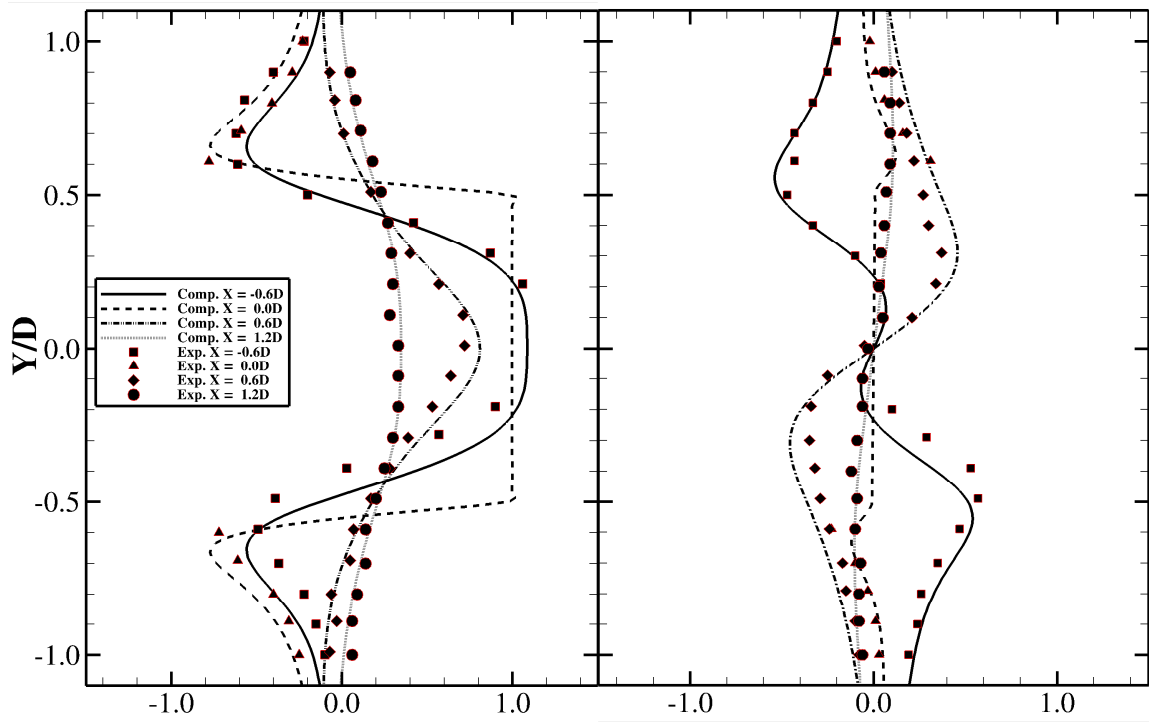
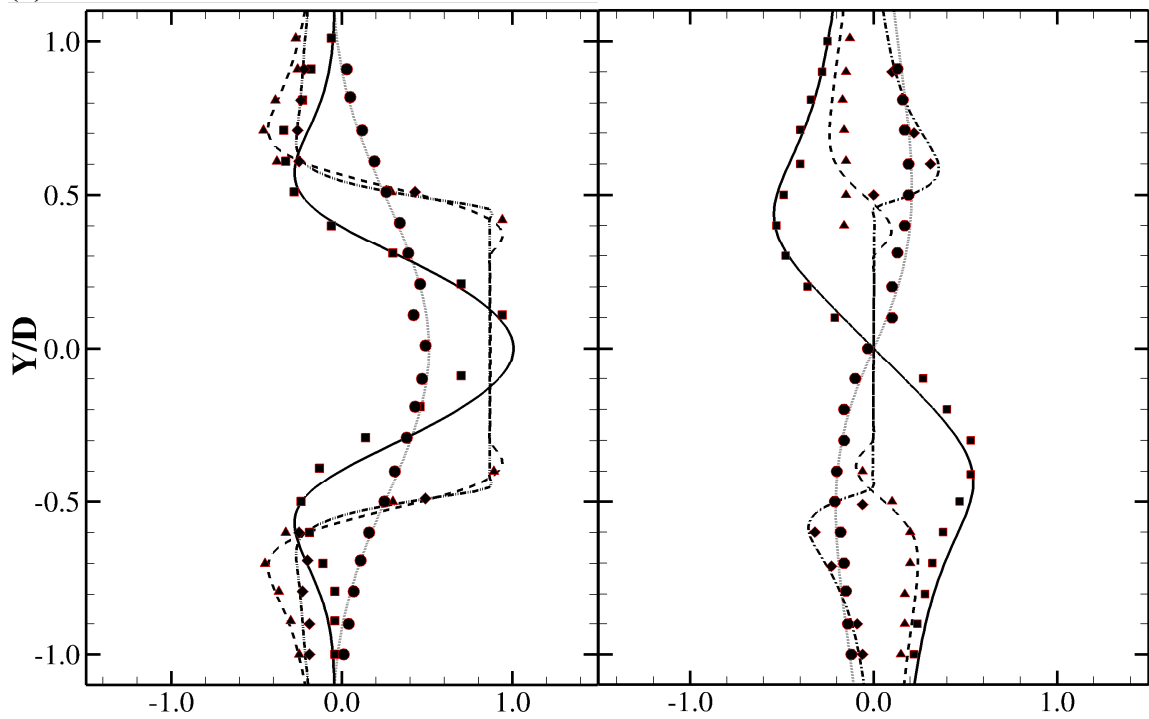


Figure 5-4 In-line oscillating cylinder in a quiescent fluid at $Re = 100$, $KC = 5$. Pressure and vorticity contours at four different phase-angles. $-1.1 < P < 0.6$ with intervals of 0.09 and $26.0 < \omega_z < 26.0$ (a) 0° (b) 96° (c) 192° (d) 288°



(a)



(b)

Figure 5-5 For Caption see next page

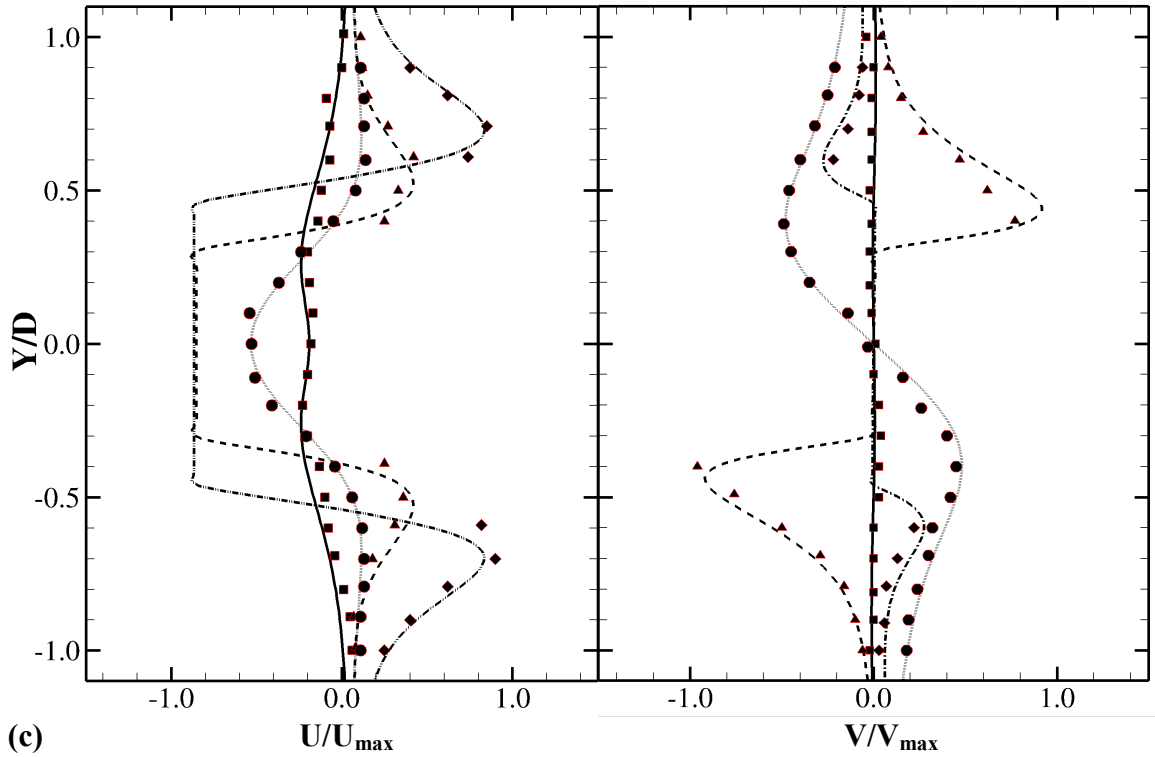


Figure 5-5 In-line oscillating cylinder in a quiescent fluid at $Re = 100$ and $KC = 5$. Velocity Profiles at three different phase angles (a) 180° (b) 210° (c) 330° . Lines are the present computation, symbols are the experimental data of Dutsch et al. (1998) at $x = -0.6D$, $x = 0.0D$, $x = 0.6D$ and $x = 1.2D$.

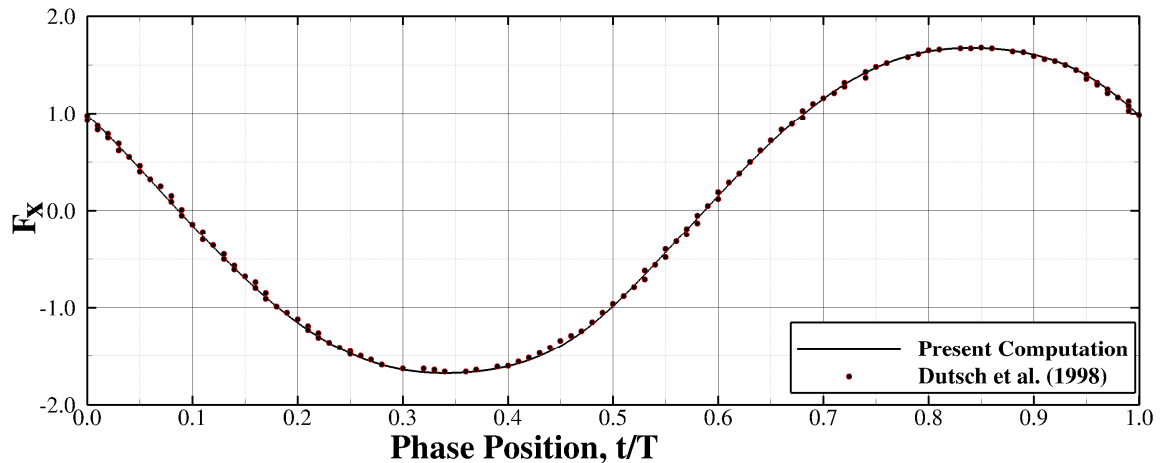


Figure 5-6 Evolution in time of the drag force on a cylinder oscillating in a quiescent flow at $Re = 100$ and $KC = 5$. (o) boundary confirming simulation (Dutsch et al., 1998); (---) present computation

5.2.2 Flow over a transversely oscillating cylinder

The flow over a transversely oscillating cylinder at $Re = 185$ is investigated next. The cylinder is forced to displace in a sinusoidal manner in transverse direction to the flow with an amplitude of $A = 0.2D$ and a frequency of $f_o = 0.8f_e$ in which f_e is known as the natural frequency of the stationary cylinder at $Re = 185$ based on the cylinder diameter, D . The structural motion of the cylinder with $f_o = 0.156$ is prescribed as follows;

$$y(t) = A \sin(2\pi f_o t) \quad (5-2)$$

The same amplitude and frequency are also utilized in Uhlmann (2005a) and Yang et al. (2009). For instance, Uhlmann (2005a) uses the class of 3-point regularized delta functions introduced by Peskin (2002) as kernels in the transfer steps between Lagrangian and Eulerian locations whereas Yang et al. (2009) introduces a smoothing technique with a new 3-point discrete delta function. In this study, we utilize the smoothed discrete delta function introduced by Yang et al. (2009) that guarantees a second order accuracy in interpolation and thereby reducing the non-physical oscillations and improving the force prediction. The same domain size of $52D \times 36D$ and boundary conditions (West = Inlet, East = Convective, North = Symmetric and South = Symmetric) as in the stationary cylinder simulations are used if not otherwise stated. The time step (Δt) is selected to be 3×10^{-3} to ensure $CFL = 0.2$ for the moving cylinder cases. All other parameters remain the same as in the corresponding stationary case above.

The results are summarized in Table 5-2. It is observed that the simulations using solid domain forcing produce reasonably good results of the time-averaged forces, using either the smoothed discrete delta functions or the regular ones. However, if the plots of

time variations of the lift and drag coefficients are carefully investigated, the effect of the smoothed discrete delta functions on the force predictions is noticeable. As shown in Table 5-2, the results using interface forcing over predict the force predictions. Uhlmann (2005a) states that his interface method yields a higher drag than the computations using the method of Kajishima and Takiguchi (2002). The use of 4-point delta function in Uhlmann's study further increases the mean drag as shown in Table 5-2. This table also shows that the present solid forcing method overcomes the overestimation in drag force. The present method via interface forcing yields a higher drag than one predicted by Uhlmann (2005a).

Table 5-2 Dimensionless coefficients for flow around an oscillating cylinder at $Re = 185$ which has near the natural shedding frequency. Resolution near the structure is $\Delta x = \Delta y = 0.0156D$ and the time step Δt is 3×10^{-3}

Authors	\bar{C}_D	$(C_D)_{rms}$	$(C_L)_{rms}$
Uhlmann (2005), 3-point δ_h	1.354	-	0.166
Uhlmann (2005), 4-point δ_h	1.402	-	0.172
Yang et al. (2009)	1.276	0.043	0.073
Guilmineau and Queutey (2002)	1.195	0.036	0.080
Present (interface forcing) *	1.389	0.049	0.055
Present (solid domain forcing)*	1.268	0.043	0.071
Present (solid domain forcing)**	1.273	0.043	0.072

* 3-point δ_h

** 3-point smooth δ_h

In Figures 5-7 and 5-8, the periodic variations of the drag and lift coefficients as a function of the cylinder's vertical position are presented. Figure 5-7 shows the results of drag force coefficients obtained using 3-point smooth and regular delta functions side by side for comparison with method of Kajishima and Takiguchi (2002) implemented into

Uhlmann (2005a)'s finite difference Navier-Stokes solver which utilizes interface forcing method. It is obvious that the current direct forcing method reduces unphysical oscillations in the drag force. However, small kinks still exist especially near the peak value of the drag coefficient. The usage of smooth dirac delta function further reduces and/or significantly suppresses these kinks (large wiggles are also clearly seen in Figure 5-7 in Kajishima and Takiguchi (2002)) completely. Yang et al. (2009) shows that the smoothed discrete delta functions become continuously differentiable up to second order, which helps in the reduction of non-smooth errors.

In Figure 5-8, the periodic variations of lift coefficient based on the present solid domain forcing and its comparisons to interface forcing method with different usage of discrete delta functions are shown. It can be observed that the spurious oscillations are less recognizable than those in the time series of the drag force coefficient. However, utilizing 3-point smooth discrete delta function in the present method sufficiently diminishes the spurious oscillations in the lift force compared to using a 2-point hat function for that oscillating cylinder. Large wiggles are clearly seen in Figure 5-8. Therefore, with the use of the smoothed discrete delta function, the quality of force prediction is greatly improved. Similar behavior is noticed in calculations of Yang et al. (2009).

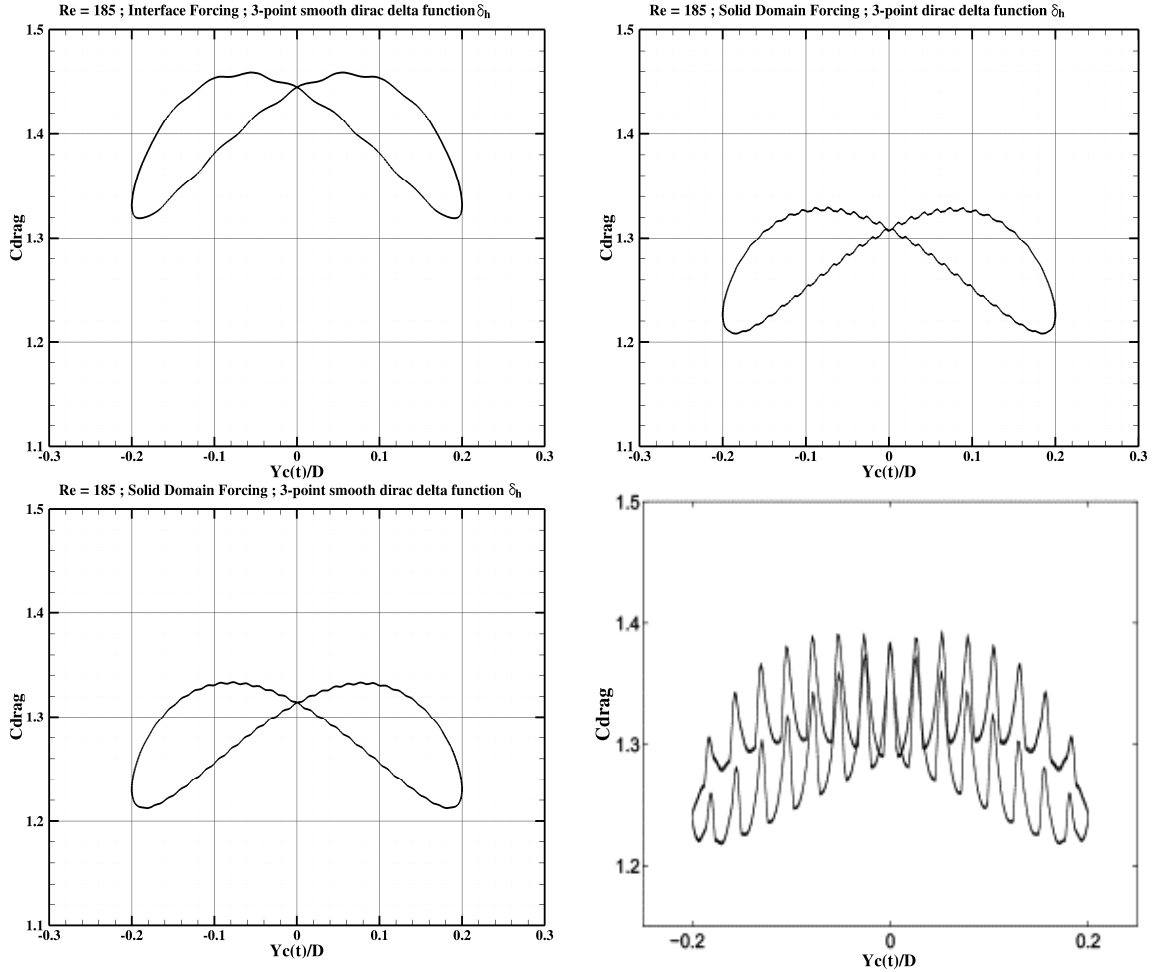


Figure 5-7 Time-periodic variation of the drag coefficient in the case of a transationally oscillating cylinder in uniform cross-flow at $Re = 185$ and $CFL = 0.2$. Top left: present method using interface forcing with 3-point smooth Dirac Delta function with $0.05D \times 0.05D$ uniform grid throughout the domain. Top right and Bottom left: present method using solid domain forcing with 3-point regular and smooth dirac delta function, respectively with $0.0156D \times 0.0156D$ grid resolution near cylinder. Bottom right: method of Kajishima and Takiguchi (2002) implemented into Uhlmann (2005)'s solver which utilizes interface forcing method.

The solid domain forcing by Uhlmann (2005b) together with the smooth discrete delta function by Yang et al. (2009) gives good estimations of drag and lift coefficients as compared to results using interface forcing method in terms of not only elimination of high frequency ‘noises’ but also by reducing the uncertainty in the estimation of the

magnitude of forces. The curves of drag and lift coefficients are reasonably smooth, which demonstrated the present approach's ability to handle arbitrary motion with respect to the fixed grid.

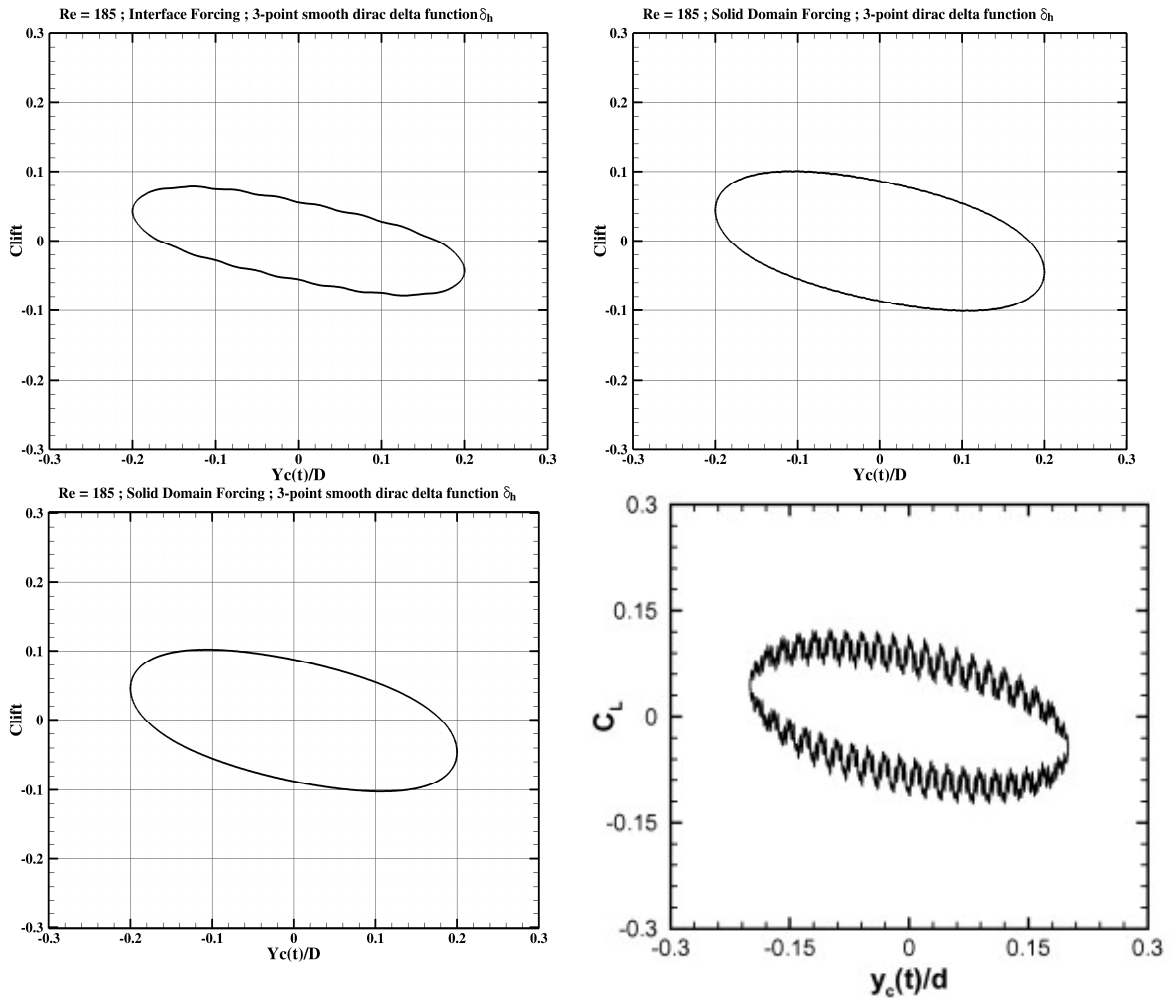


Figure 5-8 Time periodic variation of the lift coefficients for flow past an oscillating cylinder at $Re = 185$ and $CFL = 0.2$. Top left: present method using interface forcing with 3-point smooth dirac delta function with $0.05D \times 0.05D$ uniform grid throughout the domain. Top right and Bottom left: present method using solid domain forcing with 3-point regular and smooth dirac delta function, respectively with $0.0156D \times 0.0156D$ grid resolution near cylinder. Bottom right: results of Yang et al (2009) using a 2-point hat function for the oscillating cylinder.

Figure 5-9 shows pressure contours for an oscillating cylinder in the transverse direction to the flow under prescribed motion. The figures are obtained at an instant corresponding to displacement amplitude shown on bottom left corner of each figure. For both of the forcing methods, the pressure contours on the flow part of the simulations are very smooth and regular. This yields a very similar pattern of contours throughout the fluid region. However, the irregular pressure contours are evident inside the cylinder in case of interface forcing. On the other hand, solid forcing estimates a smooth pressure field throughout the surface and inside of the structure as also mentioned in steady cylinder case results before. This leads to a continuous pressure across the interface and thus results in a sharper interface in terms of velocity fields around the immersed boundary. Similar observations have been made by Uhlmann (2005b) in his study.

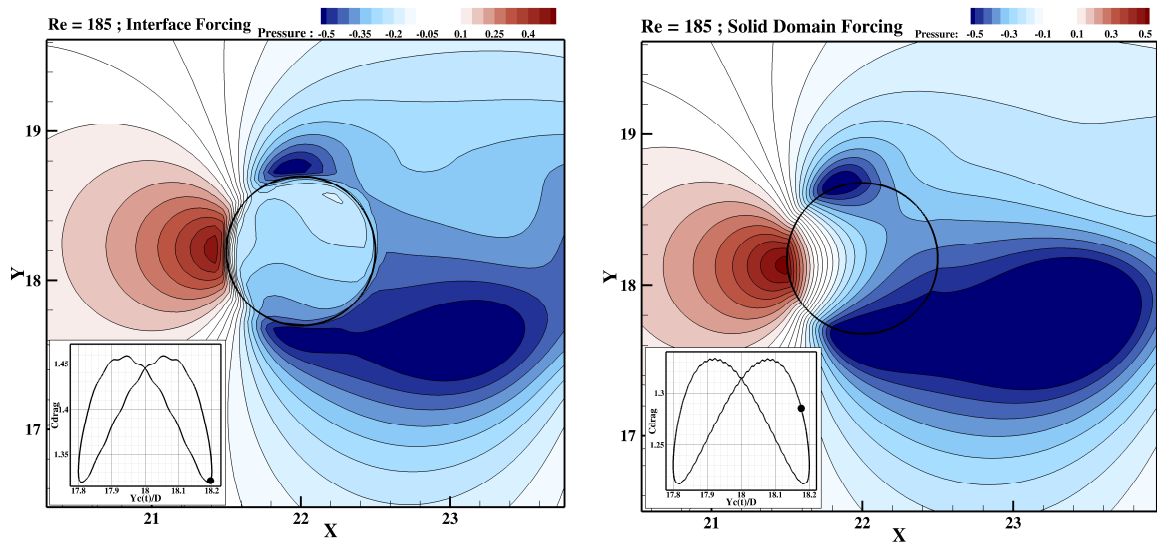


Figure 5-9 Pressure contours around cylinder at an arbitrary instant of time during the transverse oscillation of the cylinder at $Re = 185$. The location of the cylinder is shown at the bottom left of each figure. Left: Present method via Interface forcing. Right: Present method via Solid domain forcing. Both figures are produced utilizing smooth 3-point delta function.

Figure 5-10 shows snapshots of the instantaneous velocity and vorticity field by the present solid domain forcing method near the solid body at an arbitrary instant of time during the transverse forced displacement of the circular cylinder at $Re = 185$. At that instant of time, the cylinder reaches the maximum amplitude of displacement ($A=0.2D$) in crosswise direction. It can be seen from the Z-Vorticity contour that there occurs a clear shedding activity behind the oscillating cylinder.

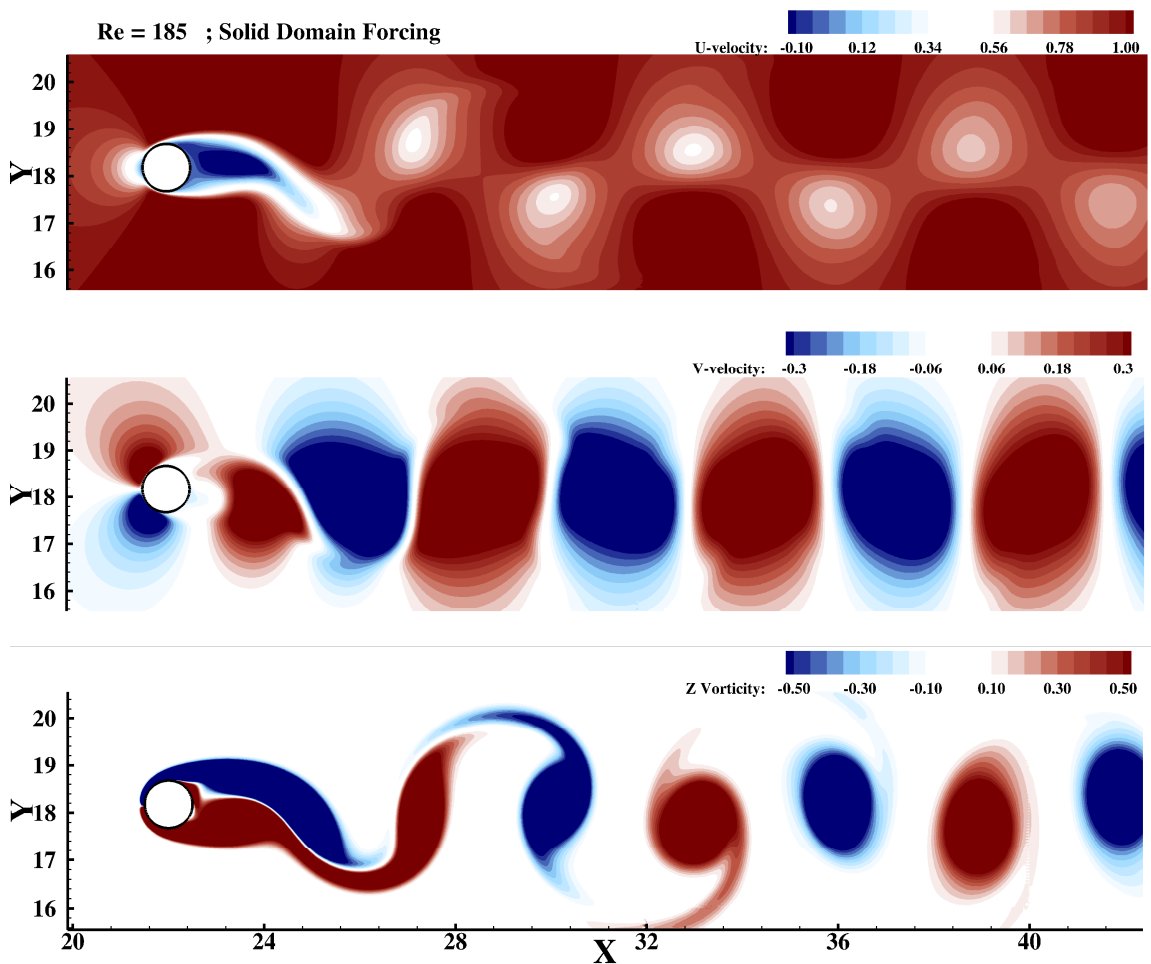


Figure 5-10 Contour plots around cylinder at an arbitrary instant of time during the transverse oscillation of the cylinder at $Re = 185$. The location of the cylinder is at $X = 22 D$ and at $Y = 18.2D$. Top: U-velocity contour. Middle: V-velocity contour. Bottom: Z-Vorticity Contour

5.3 Vortex-Induced Vibration (VIV) of a Cylinder

To further demonstrate the accuracy and efficiency of the method for fluid-structure interaction problems, a test case of a circular cylinder undergoing free transverse oscillation is studied. A cylinder is allowed to oscillate only in the crosswise direction and is modeled as a mass-damper-spring system. Experimental data by Anagnostopoulos and Bearman (1992) and numerical results by Williamson and Govardhan (2004) are available for model comparison. Figure 5-11 shows a schematic representation of a cylinder allowed to move in the transverse direction and elastically mounted at both ends which ensures that the response is uniform along its length.

In order to be able to compare the simulations with the experiments conducted by Anagnostopoulos and Bearman (1992), a mass ratio of 150 and a damping ratio of 0.0012 are needed in the validation process (see Figure 5-11). A series of experiments with Reynolds numbers ranging from 90 to 140 where the corresponding reduced velocity ranged from 5.02 to 7.81 were conducted by Anagnostopoulos and Bearman (1992). In the numerical analyses, the regime for the fixed cylinder was fully laminar. For all cases the flow over a stationary cylinder for the same Reynolds number was initially computed. Then the cylinder was allowed to move in one direction (cross-stream) and initially held rigid until the state of fully developed flow was reached. Integration in time was stopped as soon as a periodic state of constant maximum amplitude is reached. The test case has been also used for validation in other numerical simulations (Kara et al. (2012); Nomura (1993); Schulz and Kallinderis (1998); Wei et al. (1995); Yang et al. (2008)). The domain size is the same as above (Section 4.1) and the grid dimension was 1344 x 736 with a

time step of $\Delta t = 0.003$. Making use of local mesh refinement enables a resolution near the cylinder of $0.0156D \times 0.0156D$. The 3-point discrete smooth dirac delta function is used during the transfer of forces between fluid and the structure.

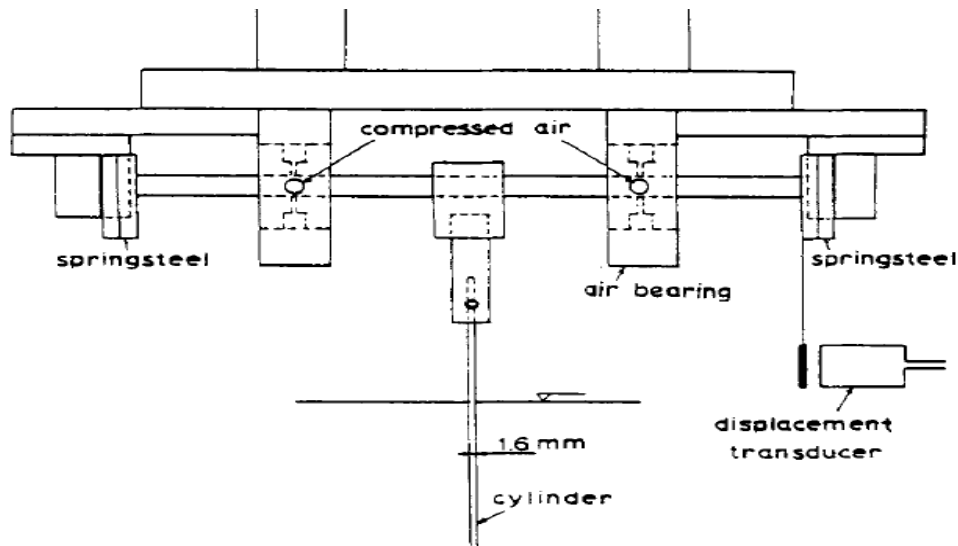


Figure 5-11 Experiment conducted by Anagnostopoulos and Bearman (1992) ($k = 69.48 \text{ kN/m}$, $c=0.0039 \text{ Ns/m}$, $D=1.6 \text{ mm}$, $f_N = 7.016 \text{ Hz}$, $m=35.75 \text{ g}$, $\xi=0.0012$)

The large mass ratio used in these numerical simulations makes the problem fairly stiff and very long integration times are needed for most cases, especially where resonance occurs. Figure 5-12 and 5-13 show time history of the displacements for the oscillating cylinder in the transverse direction with Reynolds numbers ranging from 90 to 140. Specifically, the former shows the start-up phase and the latter shows the steady phase of the cylinder displacements. Outside the resonance regime, such as at $Re = 90$ and 95, drastic changes in the amplitude of vibration can be observed. In that range, the steady state can be reached with a very small magnitude of the oscillation. Also the time histories of cylinder do not change much even after reaching stable phase as shown in

Figure 5-12a. Similar behavior can be observed at $Re = 130, 135$ and 140 , however, the time history of the displacement appears to be more irregular than for the cases with $Re = 90$ and 95 . The results in Figure 5-12 and 5-13 represent the lower end of lock-in regime which needs less computational time in order to reach a periodic steady state compared to the other cases inside the lock-in regime (see Figure 5-13). It is clearly seen in Figure 5-13c that within the lock-in range, the vibration amplitude increases. Furthermore, the amplitudes of the oscillations monotonically grow at Reynolds number 105. Similar observations have also been done by Li et al. (2002); Yang et al. (2008)).

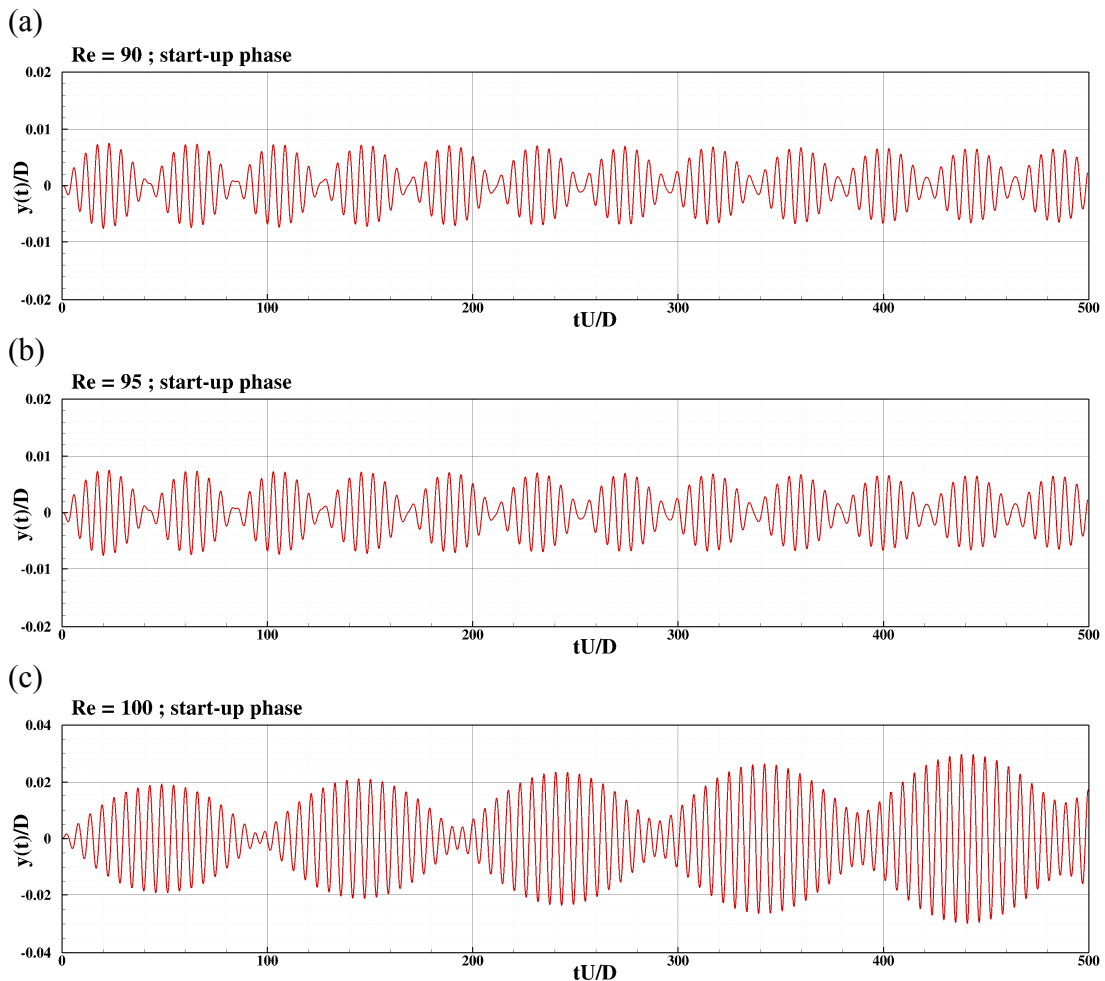


Figure 5-12 For Caption see next page

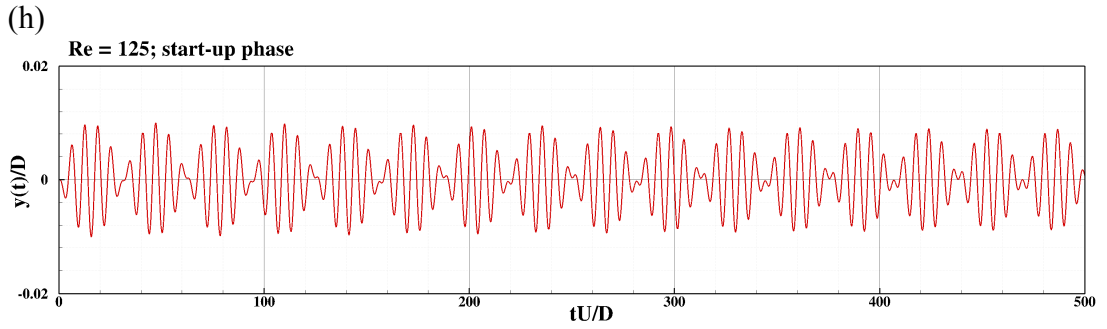
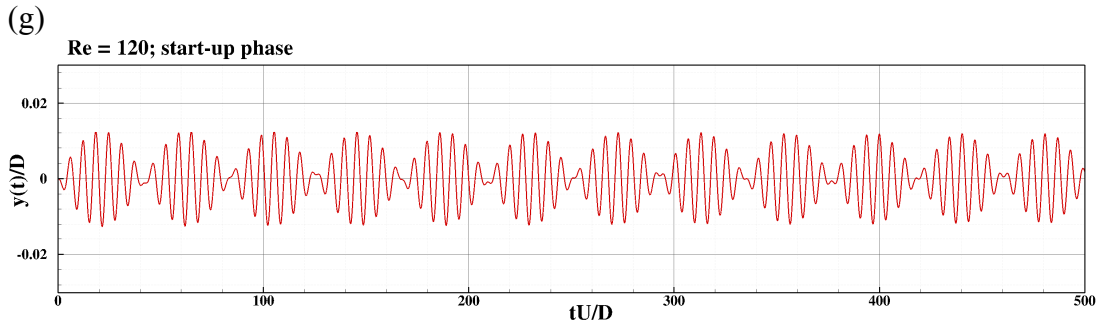
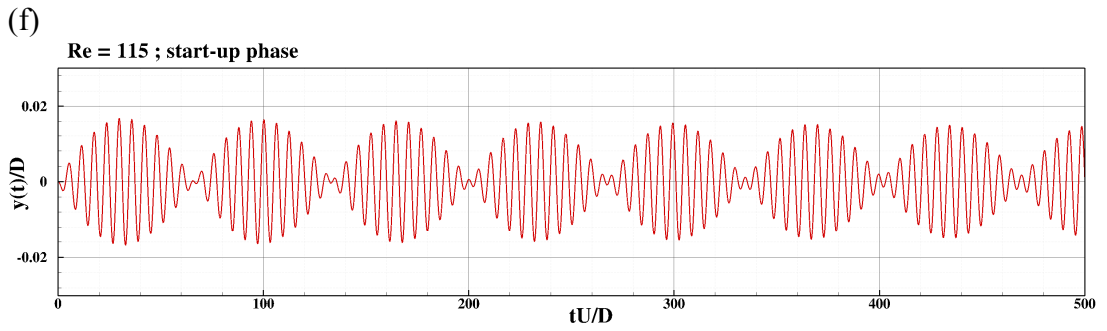
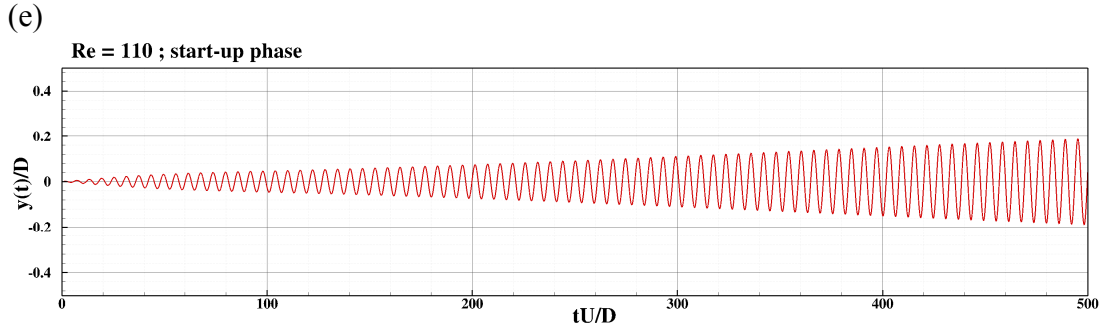
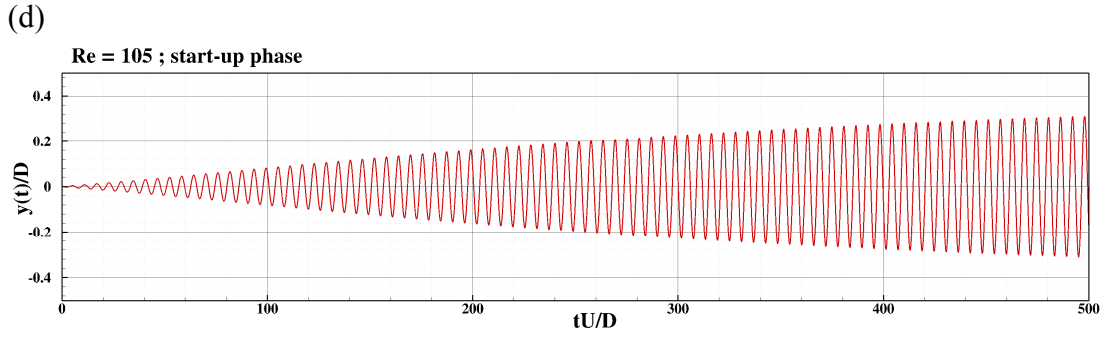


Figure 5-12 For Caption see next page

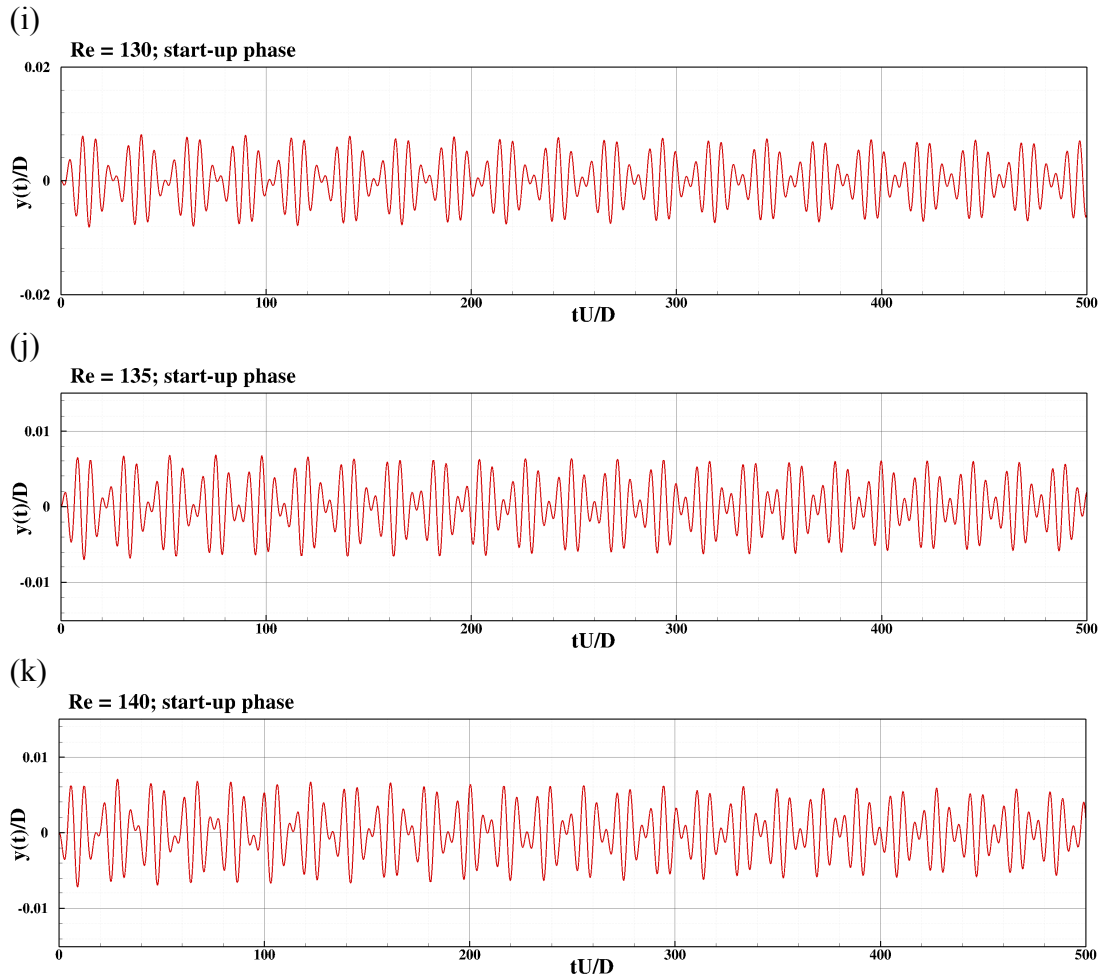


Figure 5-12 Time histories of the displacements for the freely vibrating cylinder in the cross-stream direction at $Re = 90\sim 140$ at start-up phase. (a) $Re = 90$, (b) $Re = 95$, (c) $Re = 100$, (d) $Re = 105$, (e) $Re = 110$, (f) $Re = 115$, (g) $Re = 120$, (h) $Re = 125$, (i) $Re = 130$, (j) $Re = 135$, (k) $Re = 140$

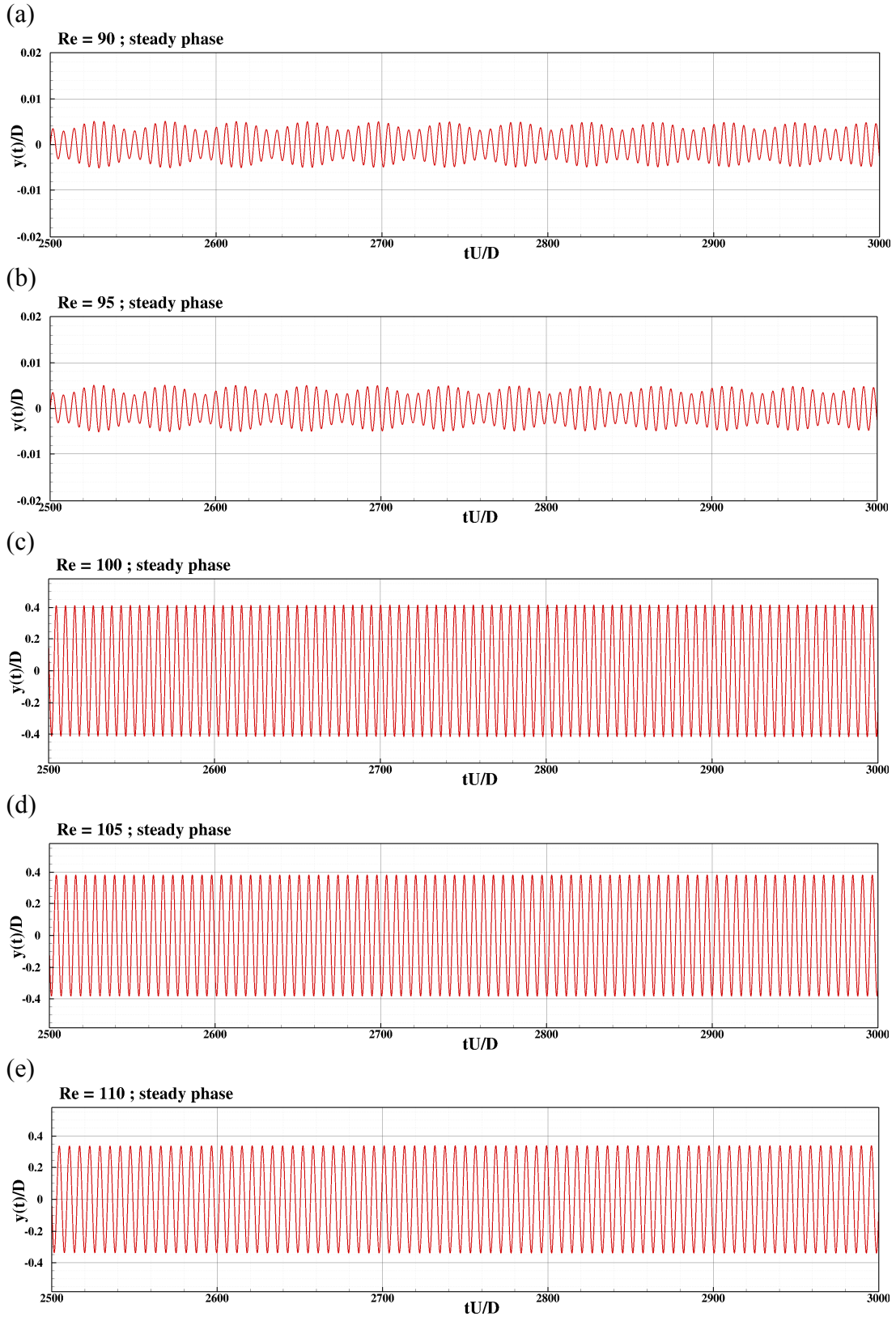


Figure 5-13 For Caption see next page

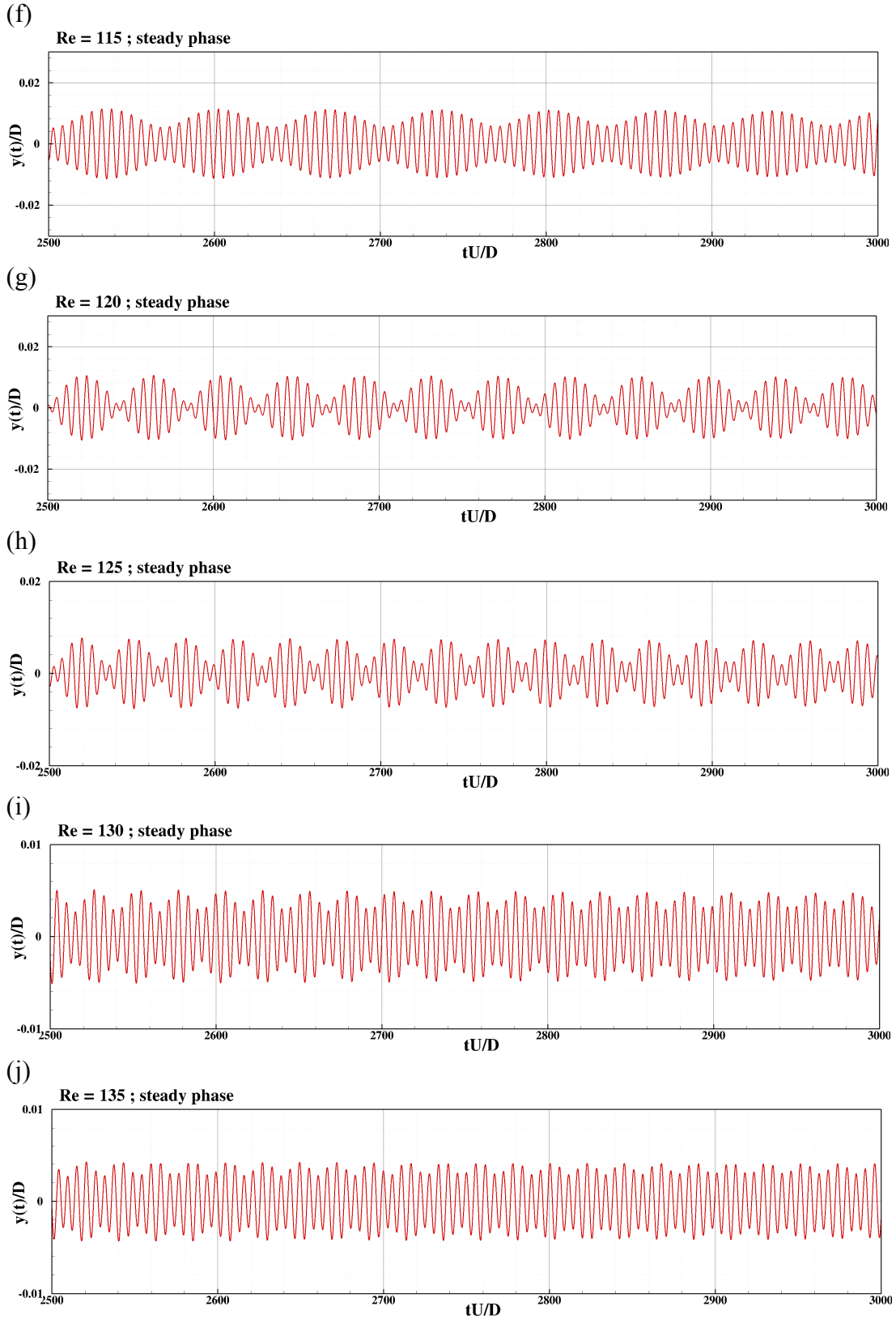


Figure 5-13 For Caption see next page

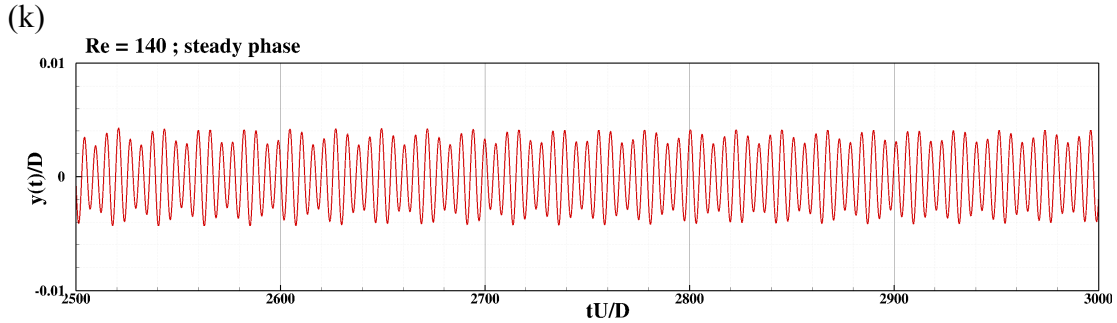


Figure 5-13 Time histories of the displacements for the freely vibrating cylinder in the cross-stream direction at $Re = 90\sim 140$ at steady phase. (a) $Re = 90$, (b) $Re = 95$, (c) $Re = 100$, (d) $Re = 105$, (e) $Re = 110$, (f) $Re = 115$, (g) $Re = 120$, (h) $Re = 125$, (i) $Re = 130$, (j) $Re = 135$, (k) $Re = 140$

The pressure contours for a few selected cases in the lock-in range and beyond the resonance regime are shown in Figure 5-14. It is evident that the pressure contours are smooth throughout the interface which ensures the accuracy and smoothness of the fluid field around the immersed structure. For the resonance cases where a noticeable displacement occurs in the cross-wise direction, Figure 5-14b,c,d also include the position of the structure incorporated into the drag force figures at the lower bottom of the pressure contours.

The close snapshots of contours of the swirl strength which is basically the angle between velocity and vorticity vectors inside and outside of the lock-in regime are shown in Figure 5-15. It is also seen that eddies that are formed behind the circular cylinder change in shape compared to the steady flow results with lower Reynolds numbers discussed in the previous section. Moreover, the eddy structures are fluctuating in the downstream flow region.

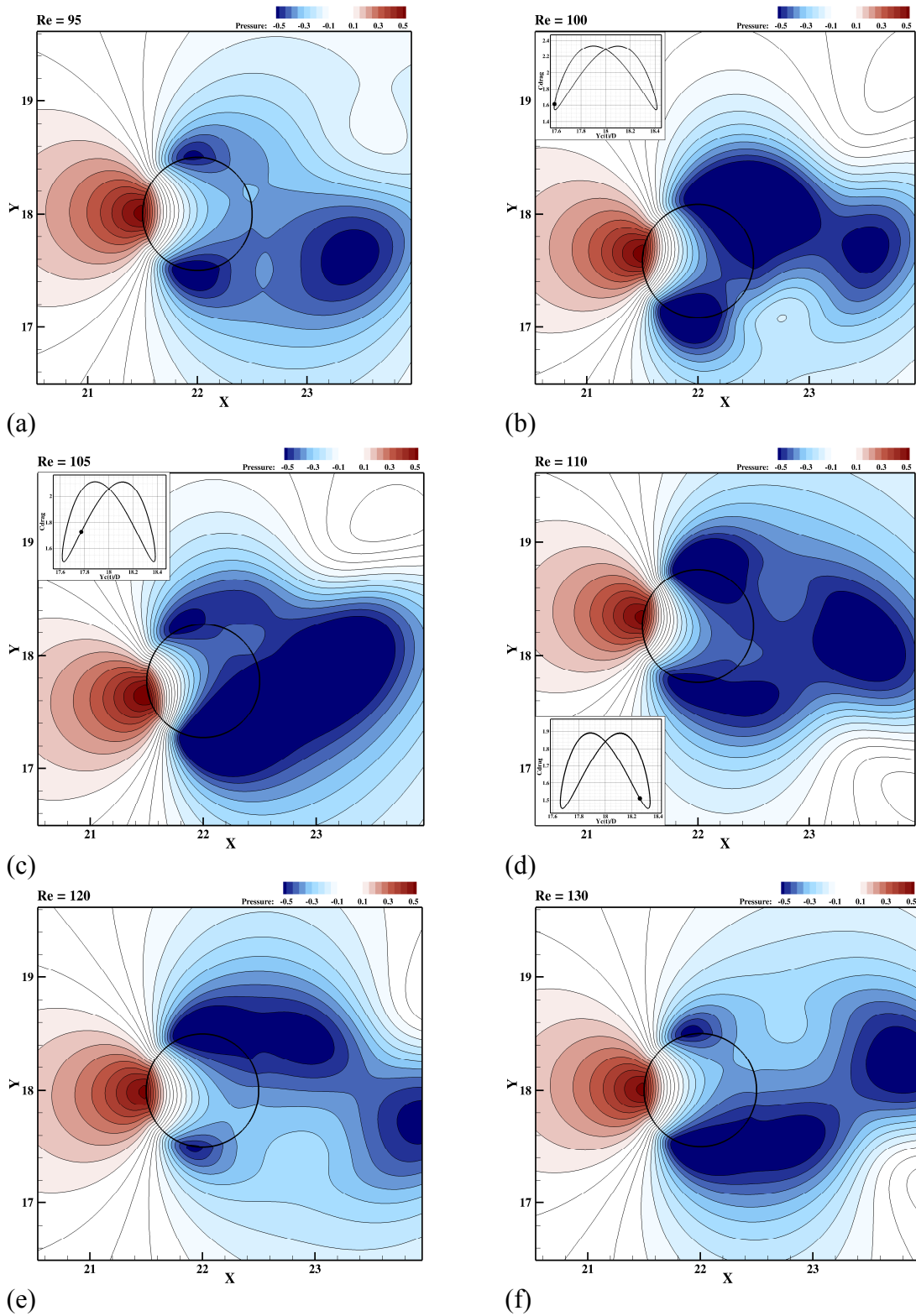


Figure 5-14 Instantaneous pressure contours of a freely vibrating cylinder in the cross-stream direction (a) $Re = 95$, (b) $Re = 100$, (c) $Re = 105$, (d) $Re = 110$, (e) $Re = 120$, (f) $Re = 130$

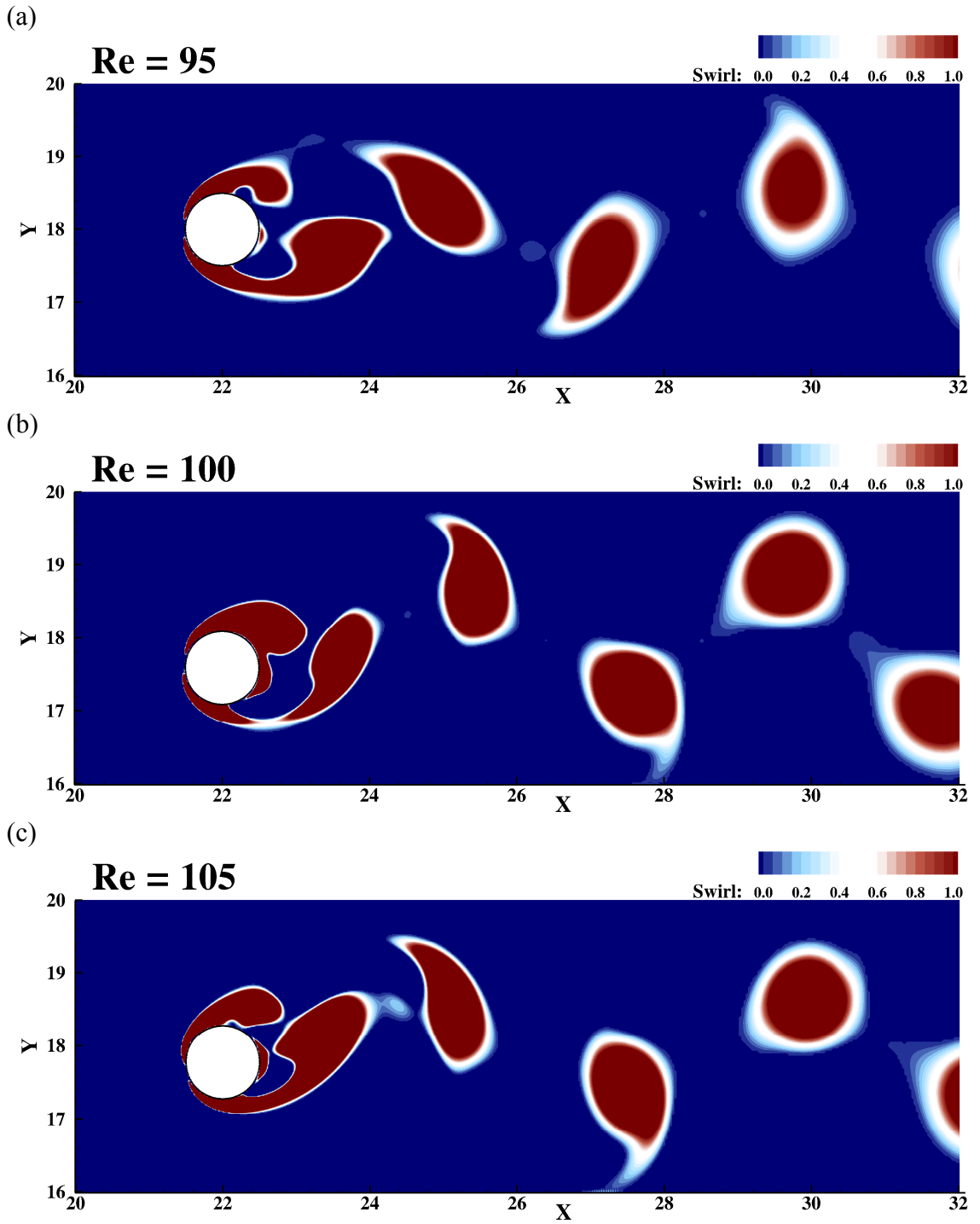


Figure 5-15 For Caption see next page

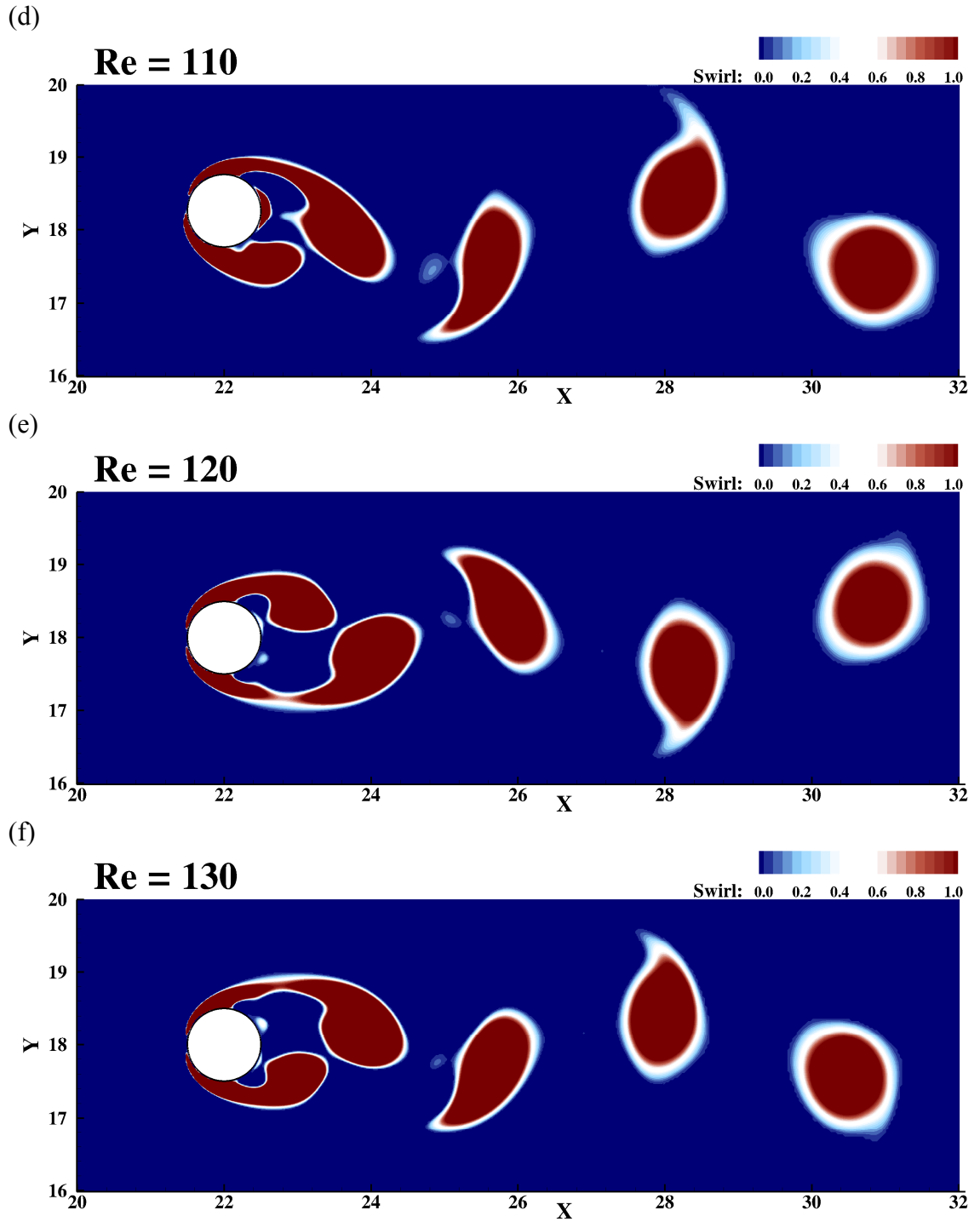


Figure 5-15 Instantaneous swirl strength contours of a freely vibrating cylinder in the cross-stream direction (a) $Re = 95$, (b) $Re = 100$, (c) $Re = 105$, (d) $Re = 110$, (e) $Re = 120$, (f) $Re = 130$

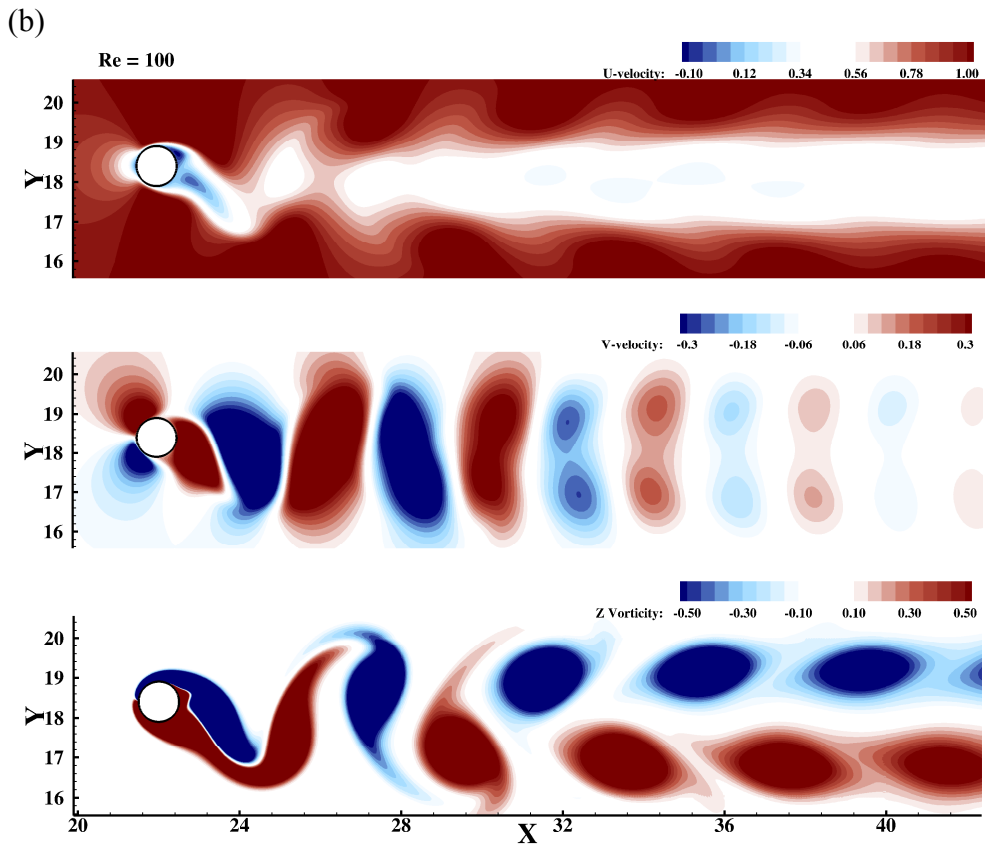
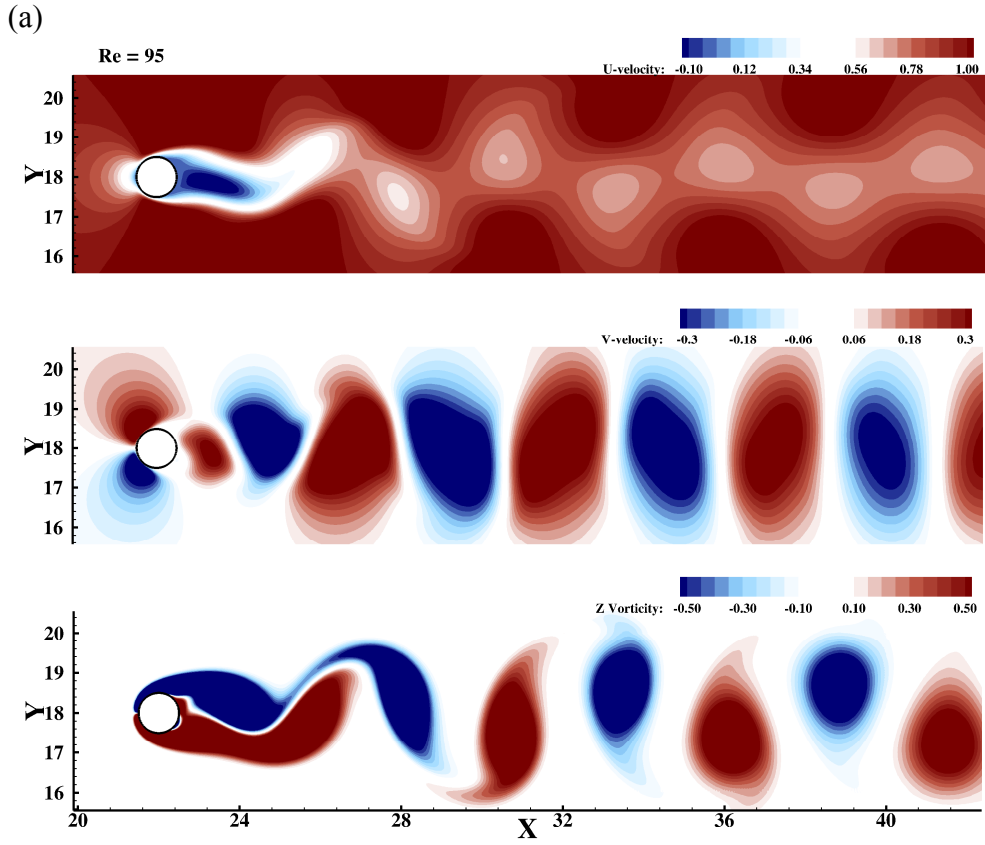


Figure 5-16 For Caption see next page

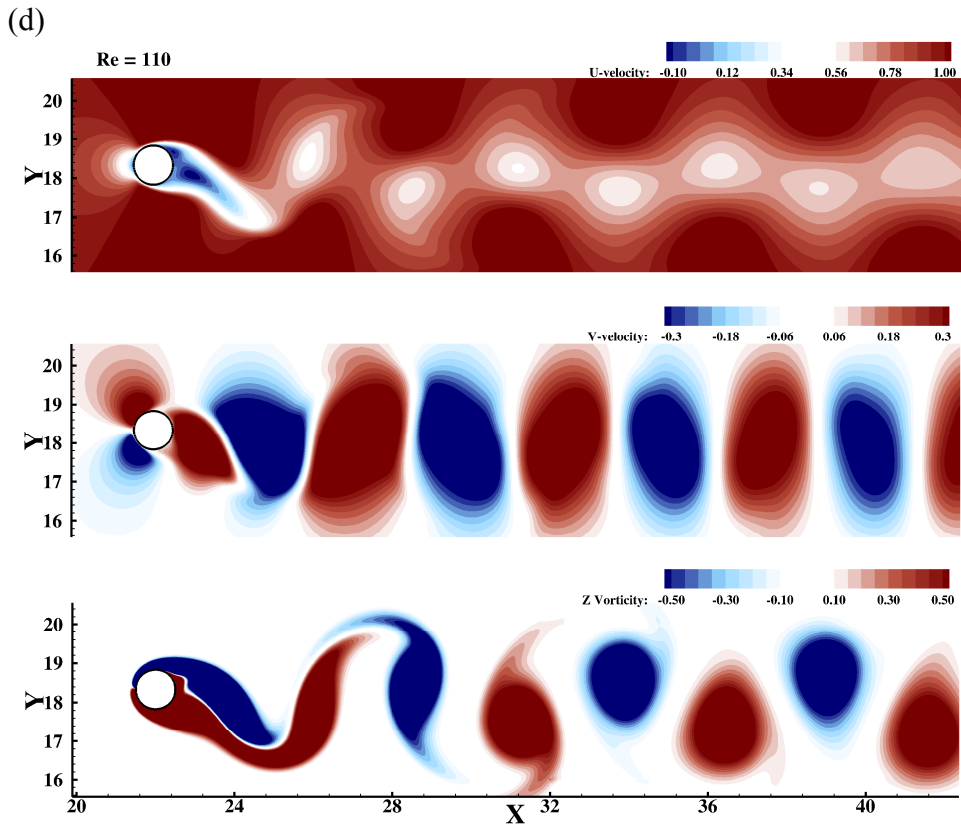
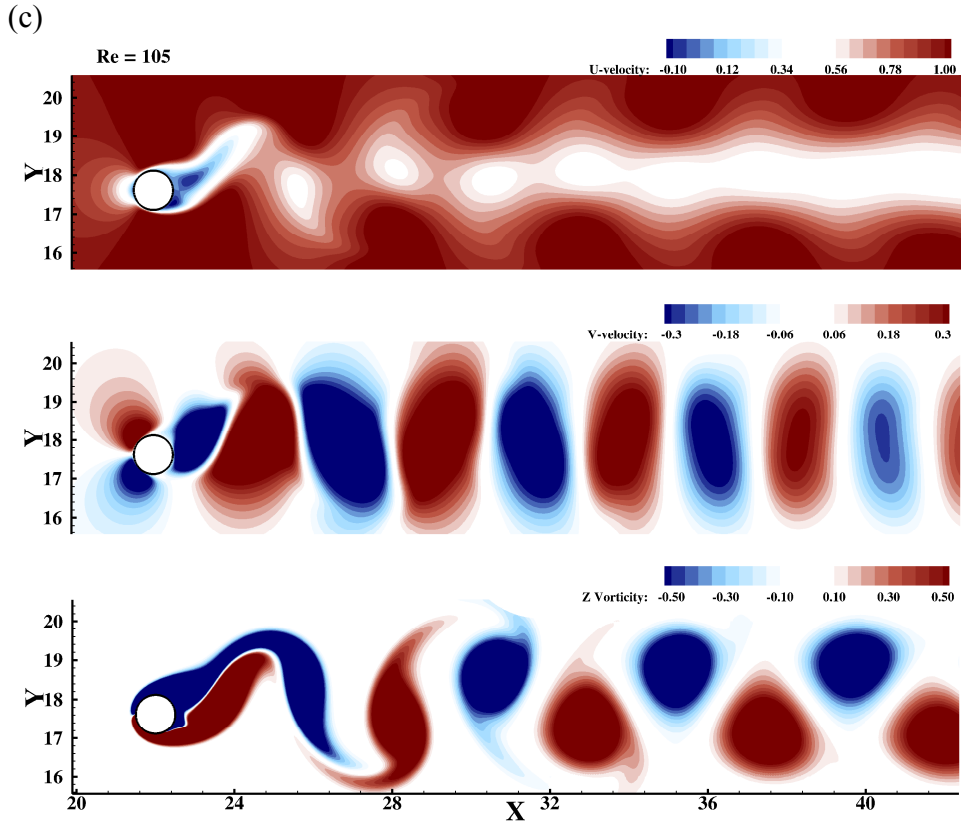


Figure 5-16 For Caption see next page

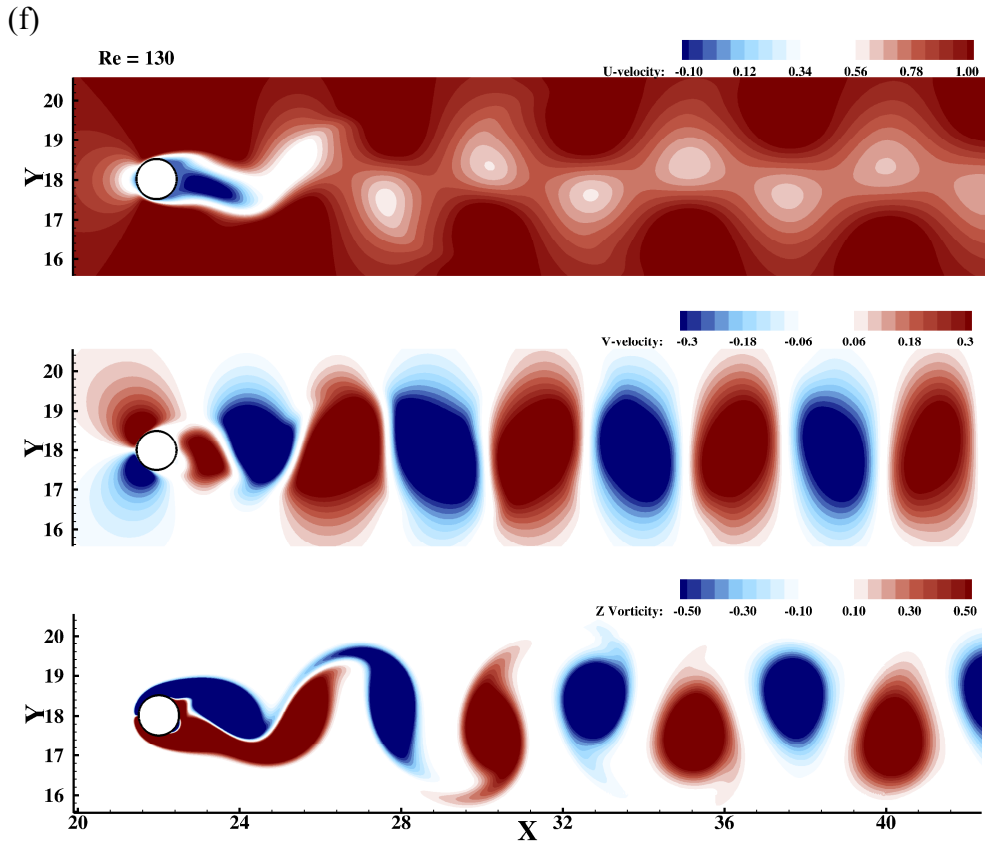
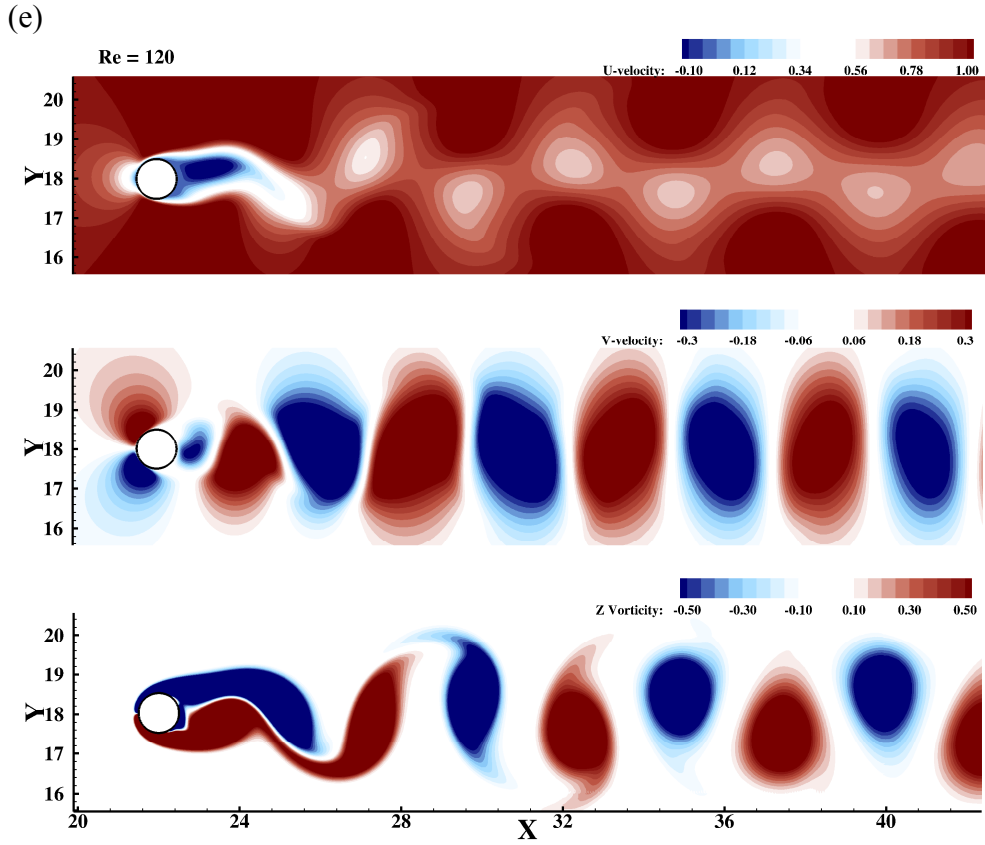


Figure 5-16 For Caption see next page

Figure 5-16 Instantaneous contours of U velocity, V velocity and spanwise vorticity for a freely vibrating cylinder in the cross-stream direction (a) $Re = 95$, (b) $Re = 100$, (c) $Re = 105$, (d) $Re = 110$, (e) $Re = 120$, (f) $Re = 130$

The $2S$ mode pattern (two single vortices per cycle of motion) can easily be seen in the wake in Z vorticity contours in Figure 5-16b, c and d. This is in agreement with the observations of Williamson and Roshko (1988). In this figure, the contours of U velocity, V velocity are also shown. In addition, the smoothness of the vorticity contours near the cylinder is a further indication that the method properly captures the complex dynamics of the flow near the immersed structure.

The comparison of drag and lift force coefficients of the freely oscillating cylinder cases are shown in Figure 5-17 and Figure 5-18. It is observed that in the lock-in regime there is a significant different plot presented with increased magnitudes of forces, while outside the lock-in regime, there is a little difference between fixed and the freely oscillating cases. As Reynolds number increases throughout the lock-in range, the magnitudes of drag forces tend to decrease with diminishing values of cross-streamwise displacement of the freely vibrating cylinder. Similar behavior is evident in the lift force coefficient time series in Figure 5-17b, d and f. Figure 5-18 includes time series of the forces acting on oscillating cylinder beyond lock-in regime ($Re = 95, 120$ and 130) at start-up (left column) and steady(right column) phases.

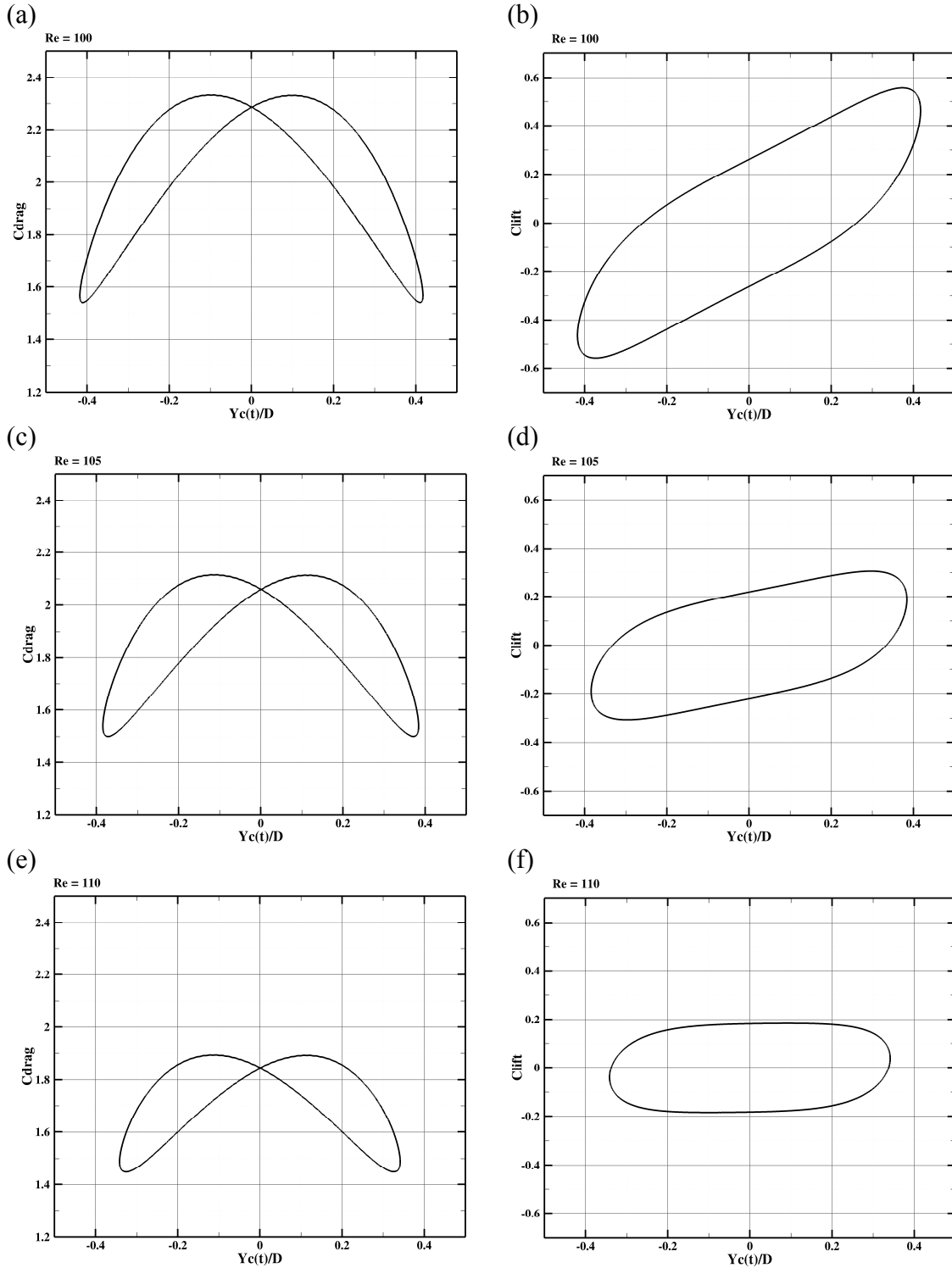


Figure 5-17 Time periodic variation of the drag and lift coefficients for flow past a freely vibrating cylinder in the cross-stream direction at steady phase in the lock-in regime (a) C_{drag} at $Re = 100$, (b) $Clift$ at $Re = 100$, (c) C_{drag} at $Re = 105$, (d) $Clift$ at $Re = 105$, (e) C_{drag} at $Re = 110$, (f) $Clift$ at $Re = 110$

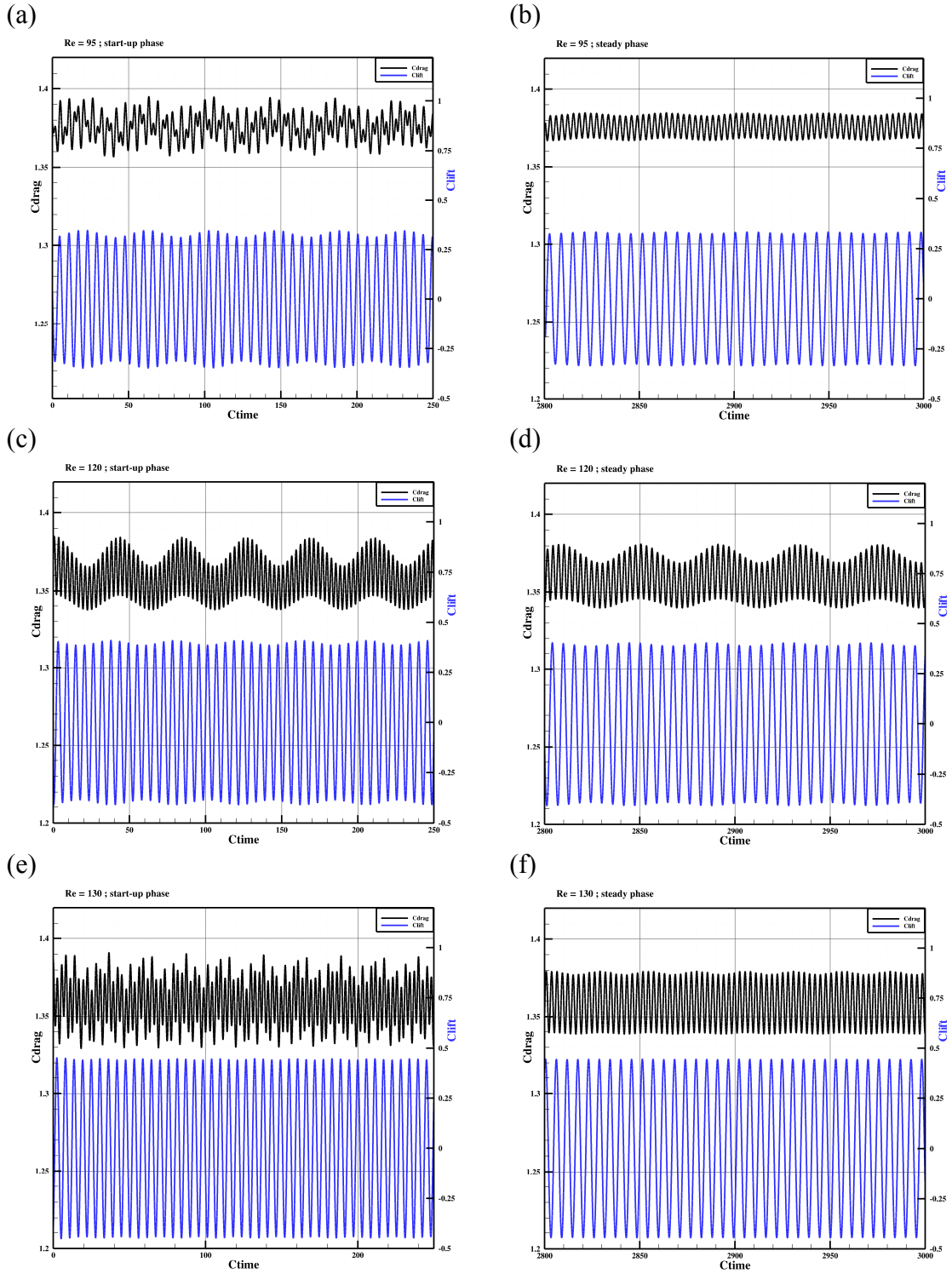


Figure 5-18 Time periodic variation of the drag and lift coefficients for flow past a freely vibrating cylinder in the cross-stream direction at start-up and steady phases beyond lock-in regime (a) start-up at $Re = 95$, (b) steady at $Re = 95$, (c) start-up at $Re = 120$, (d) steady at $Re = 120$, (e) start-up at $Re = 130$, (f) steady at $Re = 130$

The lock-in or synchronization regime in which the frequency of the wake matches the natural frequency of the immersed body can be seen more quantitatively in Figure 5-19. In this figure, the maximum oscillation amplitudes and frequencies as a function of oscillation and vortex shedding frequencies at the steady state are shown. In addition to the experimental study conducted by (Anagnostopoulos and Bearman, 1992), previous computations (Li et al. (2002); Nomura (1993); Schulz and Kallinderis (1998); Wei et al. (1995); Yang et al. (2008)) are also included in this figure. All of the references except Yang et al. (2008) used body conformal formulations in their studies. Particularly, Nomura (1993); Wei et al. (1995) implemented an arbitrary Lagrangian-Eulerian (ALE) finite element methodology. The grid was deformed and regenerated during the computations and in order to conform to the body. Similarly, Schulz and Kallinderis (1998) used finite volume formulation of a body conformal grid strategy. In Figure 5-19, the lock-in regime ranges from $Re = 100$ to $Re = 120$. It shows the maximum oscillation amplitude with respect to the Reynolds number. The results in Figure 5-19 show a scatter in data due to different approaches in numerical methods or grid resolutions used in the analysis. The present results agree well in estimating the resonance regime (approximately $Re = 103$ in the experiment); however they underestimate the amplitude of the oscillations in the experiment by about 20%. Besides, almost all of the references claim good agreement on the critical Reynolds number for the lock-in regime, but as opposed to the present results, Li et al. (2002); Nomura (1993) underestimate the amplitude of the oscillation frequency by 30% whereas Schulz and Kallinderis (1998); Yang et al. (2008) show too early resonance regime in their studies. Schulz and Kallinderis (1998) stated the reason for the difference is due to three-

dimensional effects caused by the presence of end-plates in the experiment, an effect that cannot be captured by a 2D method. Our results are in good agreement with other computations, which indicated the accuracy of the proposed methodology.

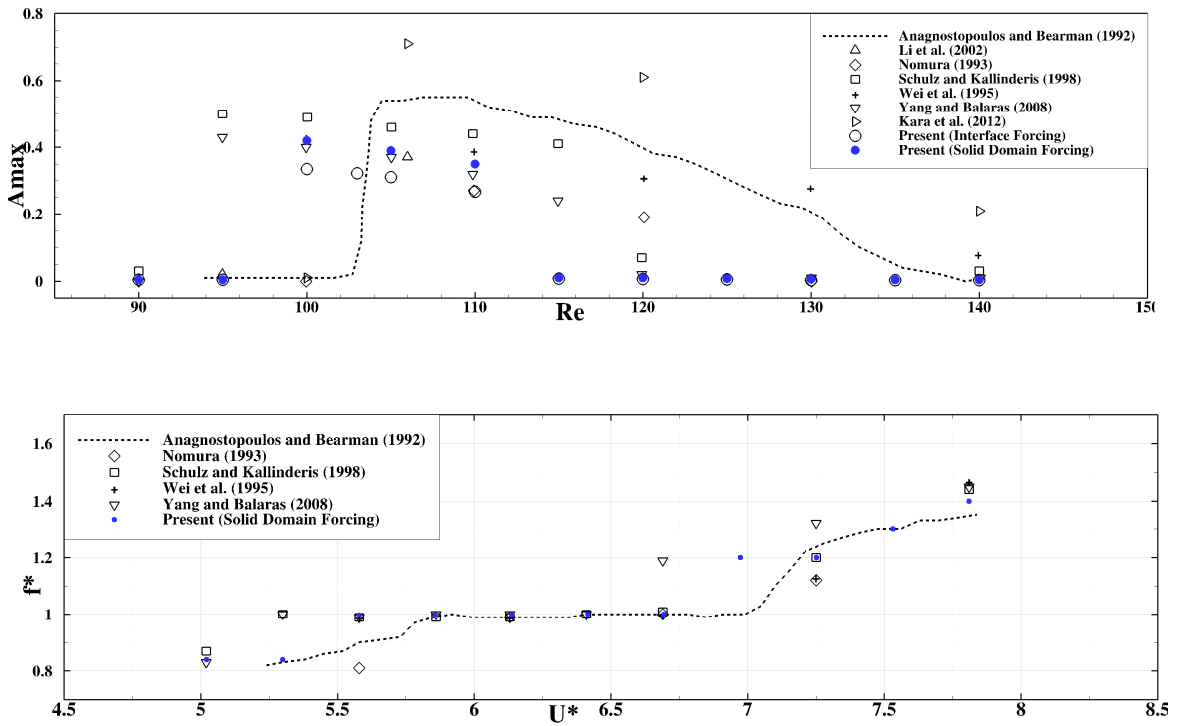


Figure 5-19 Comparison of maximum oscillation amplitude A_{max} (top) and frequency of the oscillation (bottom); o, present results; ----, experiment in Anagnostopoulos and Bearman (1992); \diamond , computation in Nomura (1983); ∇ , computation in Yang et al. (2008); +, computation in Wei et al. (1995); \square , computation in Schulz and Kallinderis (1998); Δ , computations in Li et al. (2002)

5.4 Flow Past Two Cylinders in Tandem Arrangements

The flow around cylinders has been studied extensively because of its importance in practical engineering and scientific problems in structural and fluid mechanics. Circular cylinders are used in a number of engineering applications such as offshore platforms, chimneys and heat exchangers. On the other hand, the flow around circular cylinders possesses various important physical and scientific phenomena such as separation and vortex shedding at relatively low Reynolds numbers.

5.4.1 Unsteady Flow Past Two Stationary Cylinders in Tandem Arrangement

Experimental results with flow past two cylinders in-line and staggered arrangements have been introduced by Chen (1987); Kiya et al. (1980); Kiya et al. (1992); Zdravkovich (1977). The pioneering studies of the tandem configurations of 2 cylinders are presented by Igarashi (1981) and Igarashi (1984) and six different flow patterns were identified (Figure 5-20). This classification of the flow patterns has been widely referenced in other studies in the literature. According to this classification six different regimes can be identified:

- A. The cylinders are very close together and free shear layers that originate from the separation on the surface of the upstream cylinder do not re-attach to the surface of the downstream cylinder (Figure 5-20a);
- B. The cylinders are close together and shear layers that come from the upstream cylinder are captured by the downstream one, but there is no vortex formation in the gap between the bodies (Figure 5-20b);
- C. As the distance between cylinders increases, symmetric vortices are formed between the cylinders (Figure 5-20c);

- D. Further increase in distance between cylinders result in the symmetric vortices become unstable and start to grow in proximity to the downstream cylinder (Figure 5-20d);
- E. The cylinders are spaced far apart so that shear layers originating from the upstream cylinder roll up very near the downstream cylinder (Figure 5-20e);
- F. The cylinders are spaced further and the near wake region (formation region) ends before the downstream body and vortices are shed in the gap region in a regular way (Figure 5-20f).

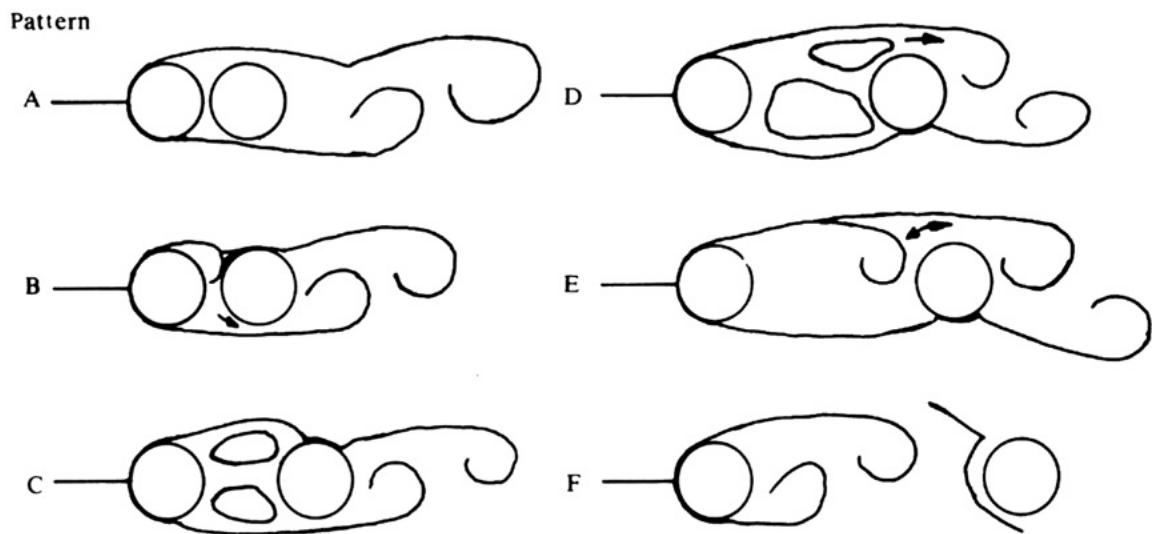


Figure 5-20 Classification of flow patterns for two tandem circular cylinders in cross-flow, from Igarashi (1981) (Figure taken from Sumner (2010))

Many other numerical studies on 2 cylinders with tandem cylinders in steady cross-flow have been carried out. Sumner (2010) recently published a review on the current understanding of the flow around two circular cylinders of equal diameter in a

steady cross-flow. In his study, focus is put on the key experimental and numerical studies and cylinders arranged in tandem configurations are discussed thoroughly.

As circular cylinders are placed together in close proximity (Figure 5-20c), the flow field and the forces encountered by the structures can differ from those when structures are isolated in the flow. The presence of other structures affects the flow and it is called *flow interference* (Carmo et al. (2011)), which has very important impact in aerodynamics and hydrodynamics. In this section, computational results for flow past two cylinders in tandem arrangements at Reynolds number 100 are reported. From the previous section, it has been found out that the critical resonance occurred at $Re = 100$ for a single, freely vibrating cylinder and the reason for that selection of specific Reynolds number is due to investigation of the effects of different configurations of cylinders on start of resonance and that will be discussed in the next section. The findings from the results of stationary cylinders in tandem arrangements will enlighten future investigations of vortex induced vibration cases. The first case involves two stationary cylinders in tandem arrangements with a distance of 2.5 diameters between their centers (Figure 5-20c), at $Re = 100$, which results in a steady vortex structure in the space between the cylinders. In the second set of computations, the distance between the centers of cylinders is increased to 6.0 diameters (Figure 5-20f). It is expected that the flows for these two cylinder arrangements is qualitatively different regarding vortex shedding. Mittal et al. (1997) also reported results of a systematic study involving cylinders in tandem arrangements with their centers separated by 5.5 diameter and 2.5 diameter. In order to study the fluid dynamic interference effect of two cylinders, the solutions are also compared with flows past a single cylinder at the respective Reynolds

numbers. The flow past a circular cylinder at $Re = 100$ has been a standard benchmark problem and various researchers in the past have reported computed results which are in good agreement with the experimental observations (Behr et al. (1995); Behr et al. (1991); Tezduyar et al. (1992)).

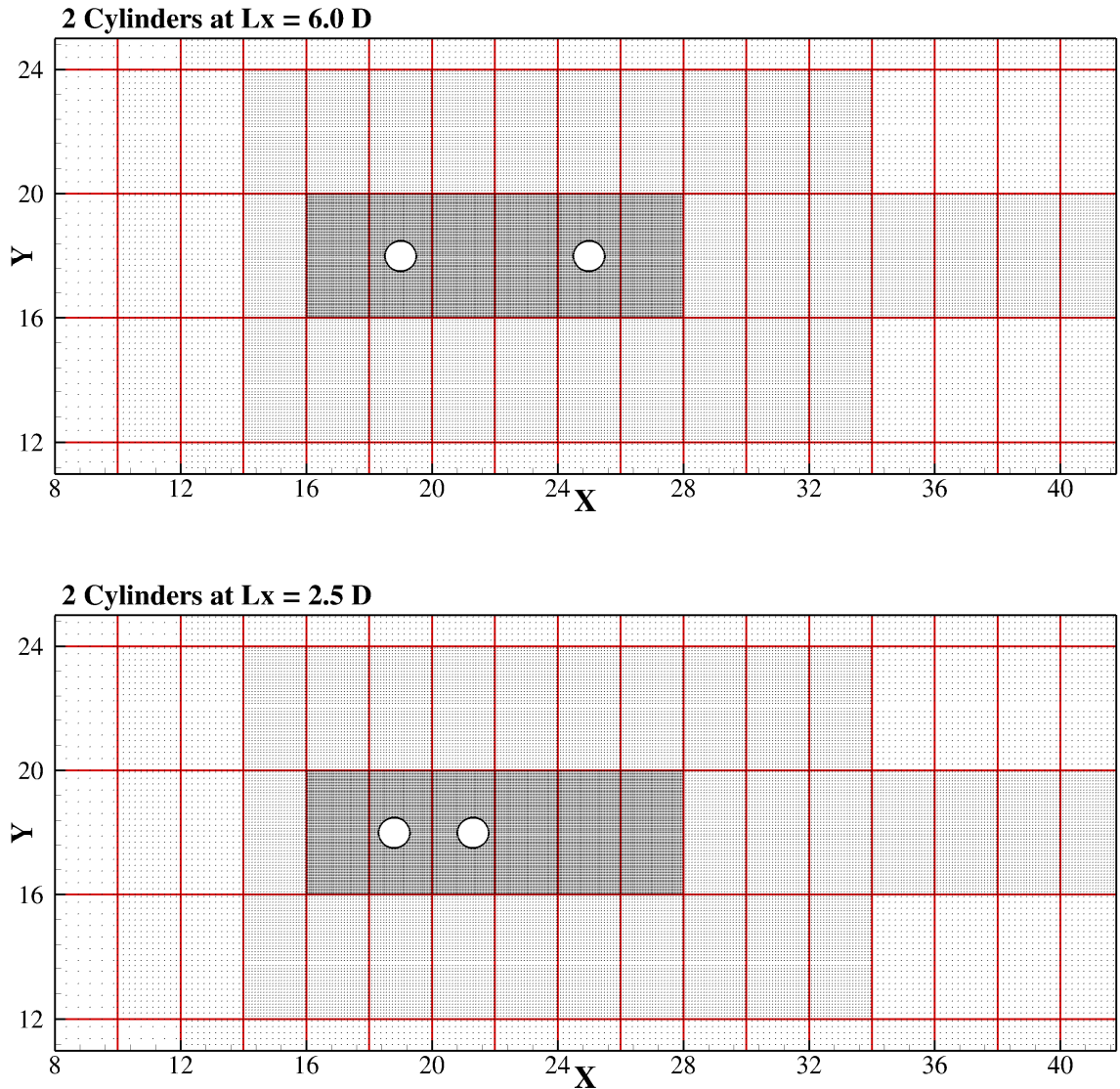


Figure 5-21 A close snapshot of the grid employed in the vicinity of 2 cylinders for laminar flow past 2 structures in tandem arrangement, spaced relatively at 6.0D (Top) and 2.5D (Bottom). The domain size is 50D X 36D. A uniform velocity boundary is specified at the inlet; a convective boundary condition is used at the outlet; symmetric boundary (every 3th point is shown)

5.4.1.1 $Re=100$ Flow Past Two Stationary Cylinders in Tandem Arrangement $L_x = 6.0D$

Our computations indicate an unsteady solution for $Re = 100$ when the spacing between two tandem cylinders is 6.0 diameter (Figure 5-21). Figure 5-22 presents velocity and vorticity contours for this case. The vorticity contour in Figure 5-22 and a close snapshot picture of the swirl strength, depicted in Figure 5-23, reveal that vortices are shed from upstream cylinder in this gap and the separated shear layers from upper cylinder form a short Karman vortex street between the cylinders.

The velocity contours in Figure 5-22, pressure contours in Figure 5-23 and streamlines in Figure 5-24 show that the flow behind the downstream cylinder becomes more unstable due to the impact of vortices. Mittal et al. (1997) explains the vortex shedding from the two cylinders as “*antiphase*”, which means that once the first cylinder sheds a vortex from the upstream interface, the downstream cylinder sheds a counter-rotating vortex from the lower surface. The contour pictures are in good agreement with results of Mittal et al. (1997) such that both results show a violent movement of stagnation point for the downstream cylinder.

Figure 5-25 shows the time histories of the lift and drag coefficients for two cylinders in tandem arrangement. In this figure, “1” refers to the upstream cylinder and “2” refers to the downstream one. First of all, the Strouhal number for both of cylinders is very close to that of a single cylinder (From Table 5-1, $St = 0.165$). The drag and lift coefficients for the upstream cylinder (cylinder 1 in Figure 5-25) are comparable with the values for a single cylinder case. As the downstream cylinder feels the effect of wake of the first cylinder, the force coefficients are affected significantly. Cylinder 2 feels very

strong lift force ($C_{L2}' = 1.25$) while experiencing a relatively lower magnitude of drag force ($\bar{C}_{D2} = 0.05$) compared to a single cylinder case ($\bar{C}_D = 1.27$; $C_L' = 0.34$).

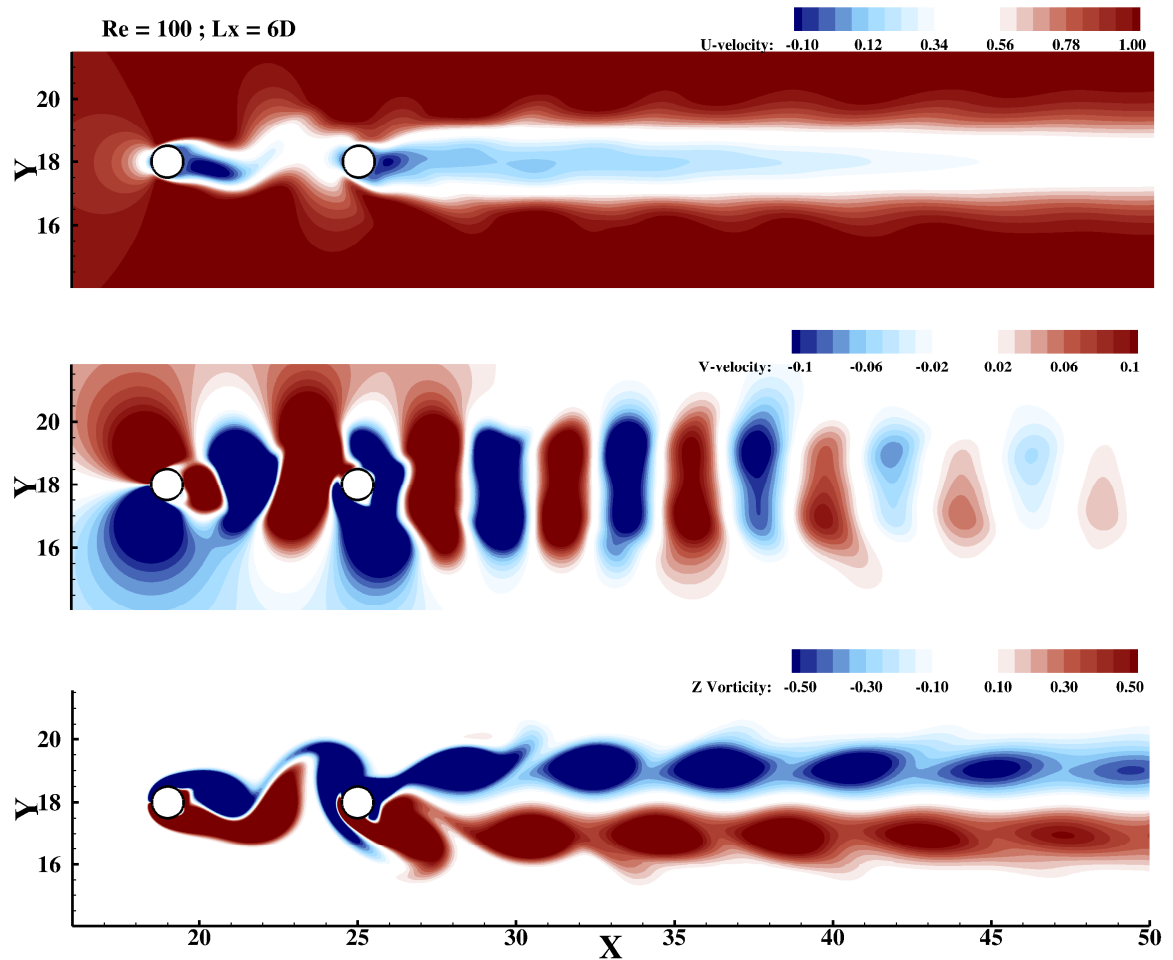


Figure 5-22 Instantaneous contours of U velocity (top), V velocity (middle) and spanwise vorticity (bottom) for flow over two tandem cylinders at $L_x = 6.0D$ at $Re = 100$

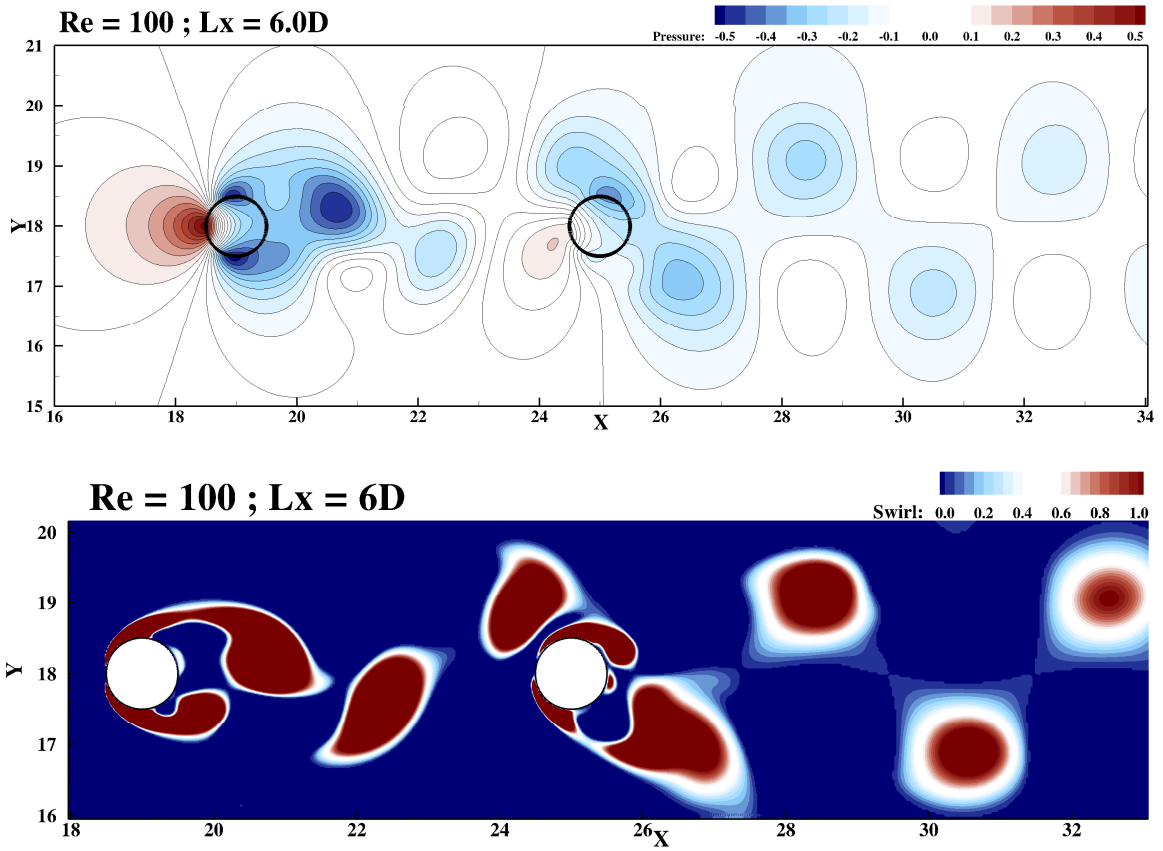


Figure 5-23 Instantaneous pressure (Top) and Swirl Strength (Bottom) contours of flow over two tandem cylinders at $L_x = 6.0D$ at $Re = 100$

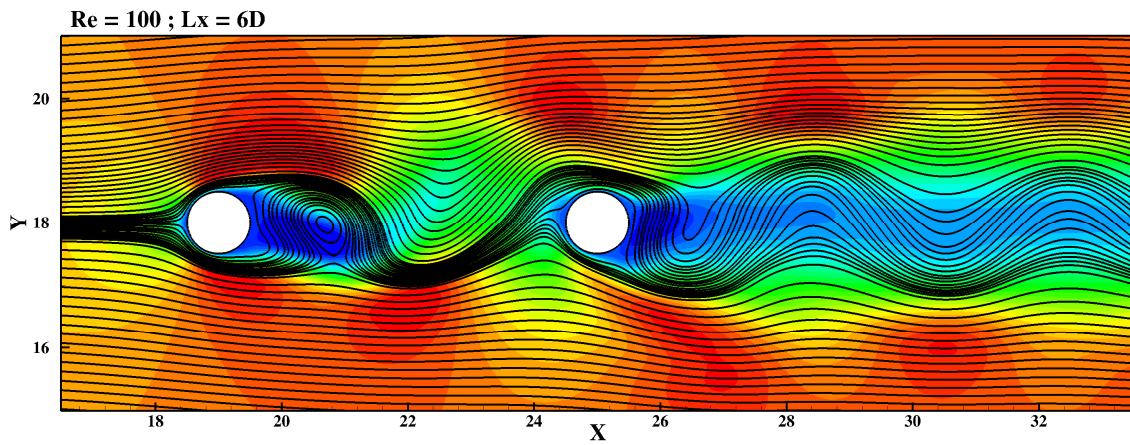


Figure 5-24 Streamlines for flow over two tandem cylinders at $L_x = 6.0D$ at $Re = 100$

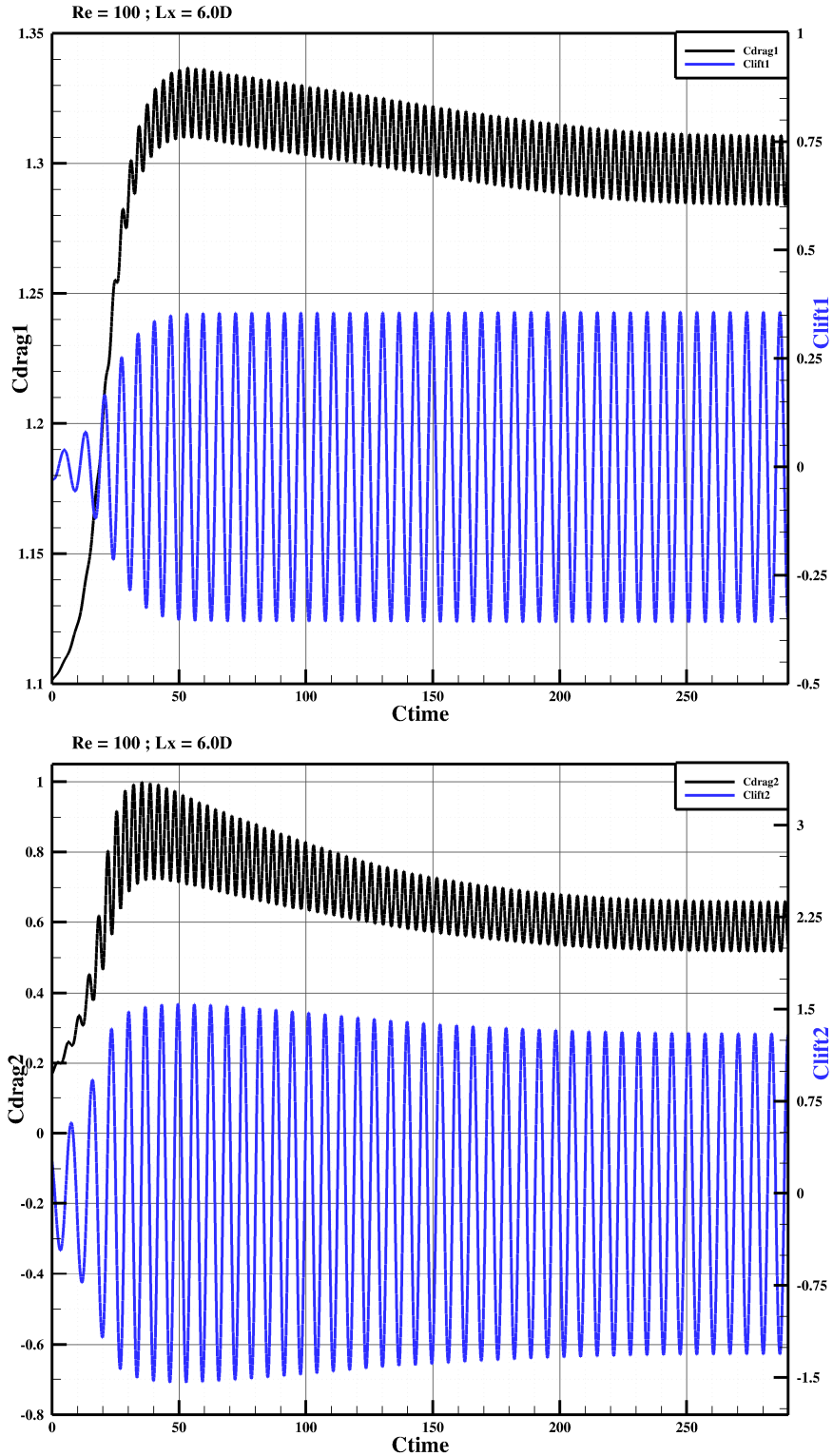


Figure 5-25 Time histories of lift and drag force coefficients for flow over two tandem cylinders at $L_x = 6.0D$ at $Re = 100$. Top: Forces acting on upstream cylinder; Bottom: Forces acting on downstream cylinder

5.4.1.2 Re=100 Flow Past Two Stationary Cylinders in Tandem Arrangement $L_x = 2.5D$

As the spacing between cylinders is decreased to 2.5 diameter, it has been reported in the literature that there is no distinct vortex shedding behind the upstream cylinder (Chen (1987); Kiya et al. (1980); Mittal et al. (1997); Zdravkovich (1977)). Our results from the simulations lead to a similar conclusion. A steady separation bubble in the gap is foreseen in this arrangement and it converges to the initial steady solution when it is perturbed (Mittal et al. (1997)).

Figure 5-26 presents velocity and vorticity contours for this case. The vorticity contour in Figure 5-26 and a close-up snapshot picture of swirl strength in Figure 5-27 reveal that vortices are absorbed by the downstream cylinder at this arrangement. From the flow pictures in Figure 5-26, it is noticeable that the shear layer is separated from the upstream cylinder and it reattaches to the downstream cylinder. This prohibits vortex shedding because the shear layer cannot roll up. The pressure field and streamlines around cylinders are also shown in Figure 5-27 and Figure 5-28, respectively. According to Figure 5-27, a low pressure region is formed in front of the upstream cylinder whereas a negative pressure field is evident behind and in front of the downstream cylinder. Shown in Figure 5-29 are the time histories of the lift and drag coefficients for the two cylinders. It is observed that the downstream cylinder experiences a ‘negative drag’, which Mittal et al. (1997) explains this as that cylinder is attracted towards the upstream cylinder. Due to full submergence in the relatively low pressure wake region of the upstream cylinder as visualized in pressure field plot in Figure 5-29, the downstream cylinder undergoes a negative drag force. Besides, the presence of the downstream cylinder results in the pressure increase in this region, leading to a reduction in the

upstream cylinder drag force. In addition, the downstream cylinder feels more lift than the upstream one because of the dominance of wake interference effect at this arrangement. Also, the combined drag of the two cylinders is less than the mean drag for the flow past a single cylinder (Table 5-1, results for $Re = 100$ flow past a single cylinder). This observation is also made by other researchers in their studies (Chen (1987); Mittal et al. (1997); Zdravkovich (1977)). It is also evident in Figure 5-29 that the converged solution needs 6 times more computational time compared to previous case. From this figure, it is noticed that the transient initial solution reaches a steady state and amplitude variation of the lift and drag forces take a constant value.

The results of two arrangements of cylinders imply that as the spacing increases, the wake interference effects reduce due to the presence of the downstream cylinder. However, the downstream cylinder feels significant changes in its force coefficients as it lies in the full wake of the upstream one. At $L_x = 6.0 D$, the variations of hydrodynamic forces tend to follow an oscillating trend as a result of vortex shedding triggered by both cylinders. The drag force becomes positive due to the intensified pressure field created by the upstream cylinder. On the other hand, at $L_x = 2.5D$, the drag force takes negative values as the downstream is fully submerged in the wake of the upstream cylinder. In addition, the lift force coefficient tends to decay and approach to zero values in terms of its magnitude. However, as the gap between cylinders are increased at $Re = 100$, more unstable behavior can be seen and the vortices caused by the upstream cylinder can induce more lift fluctuations on the downstream one. Vortices are shed from both cylinders in counterwise direction and they are not synchronized. Also, at that distance of

arrangements of tandem cylinders, the upstream cylinder shows the same behavior as a single cylinder in terms of drag and lift force coefficient calculations shown in this study.

A summary of the aerodynamic coefficients for the computed flows is given in Table 5-3. The mean values of drag and lift coefficients are calculated by integrating data at fully developed flow condition. Strouhal numbers reported in this table corresponds to the dominant frequency in the time history of the lift coefficients.

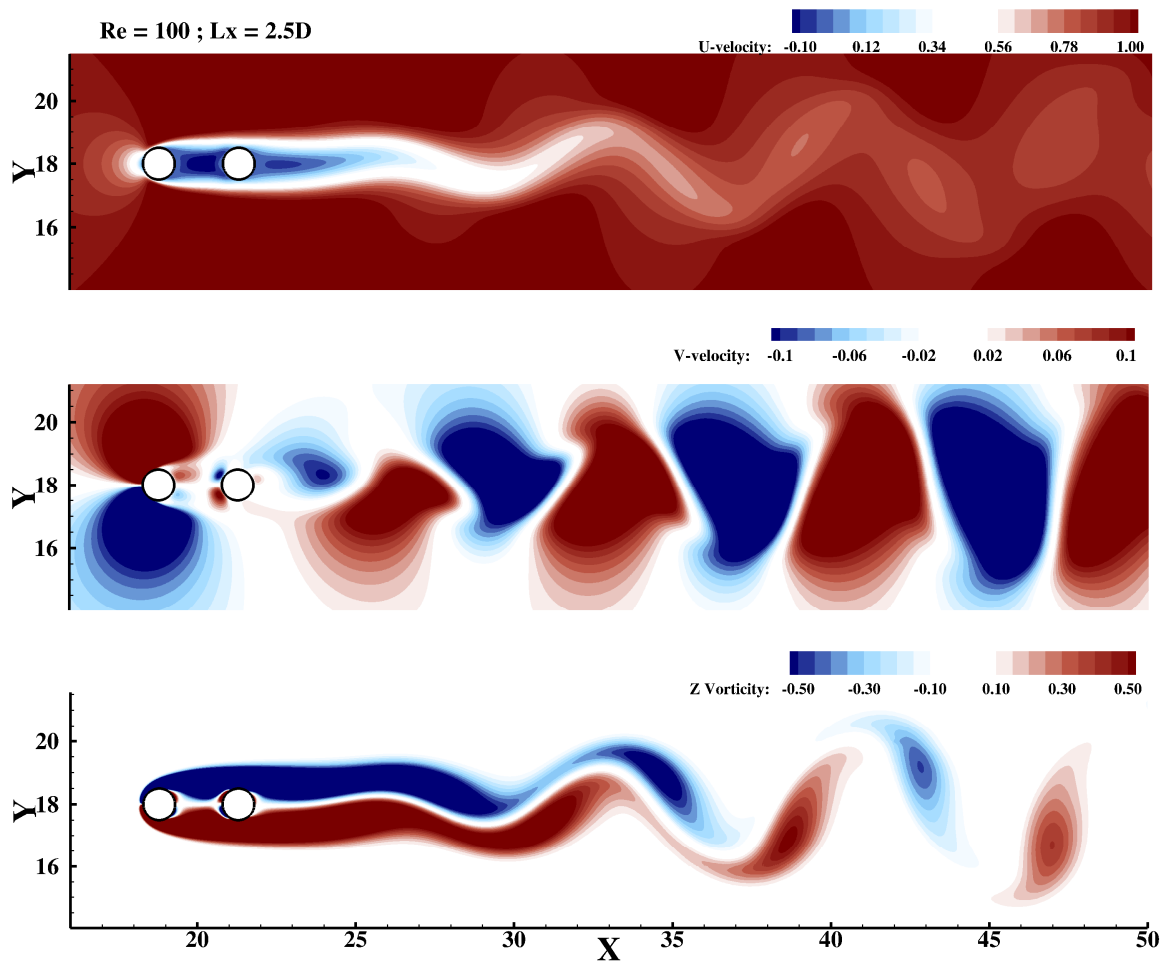


Figure 5-26 Instantaneous contours of U velocity (top), V velocity (middle) and spanwise vorticity (bottom) for flow over two tandem cylinders at $L_x = 2.5D$ at $Re = 100$

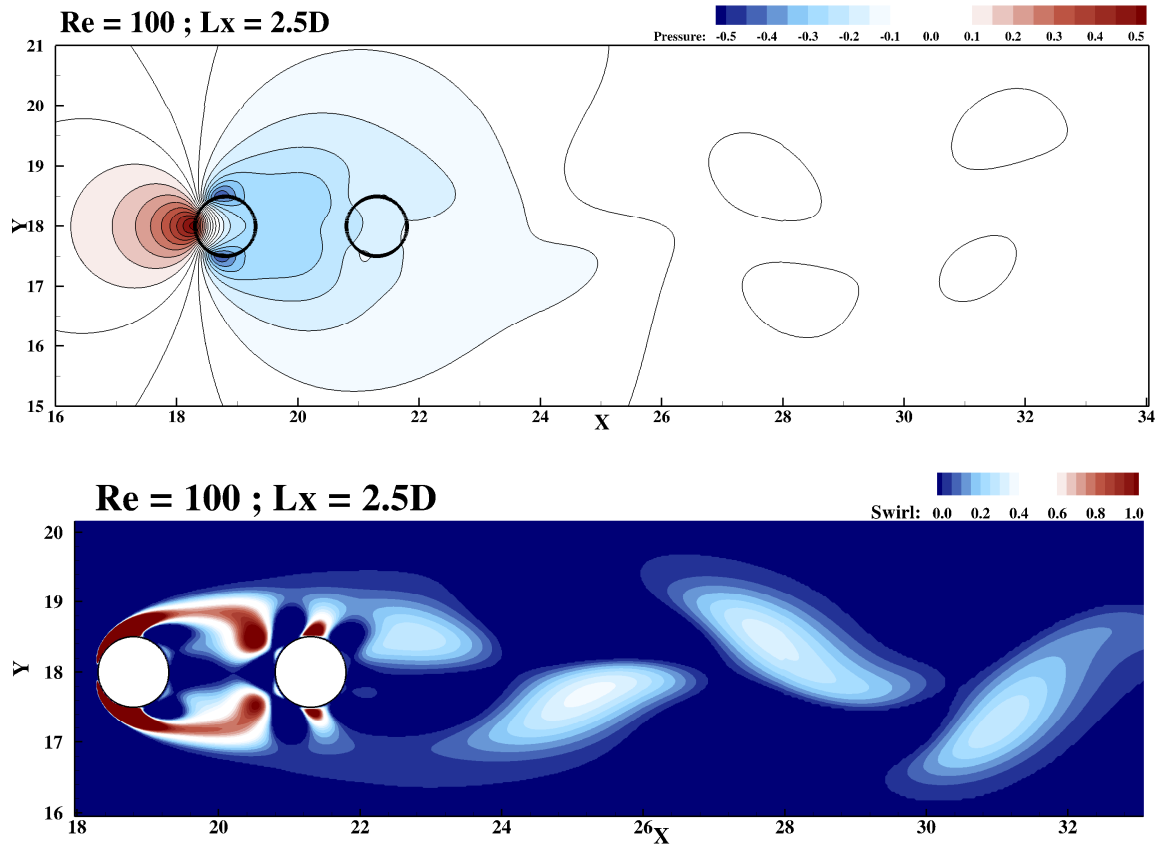


Figure 5-27 Instantaneous pressure (Top) and Swirl Strength (Bottom) contours of flow over two tandem cylinders at $L_x = 2.5D$ at $Re = 100$

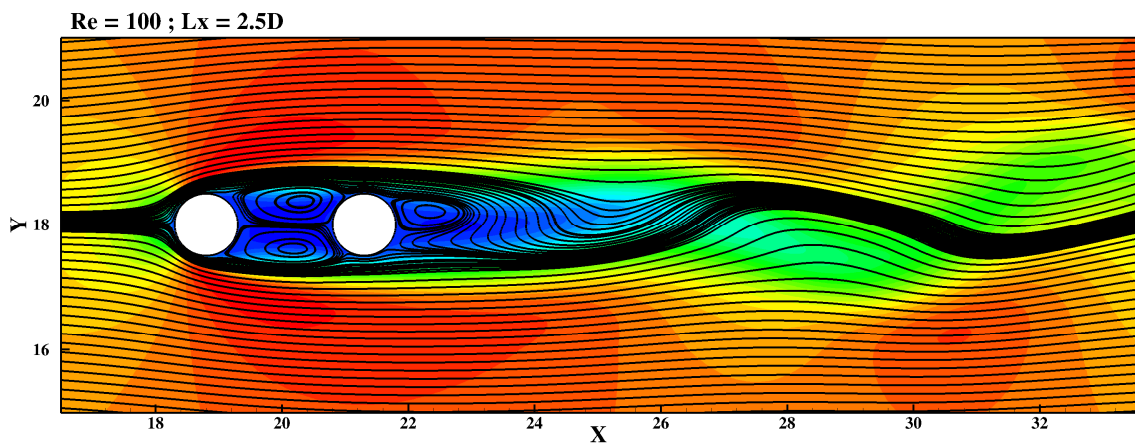


Figure 5-28 Streamlines for flow over two tandem cylinders at $L_x = 2.5D$ at $Re = 100$

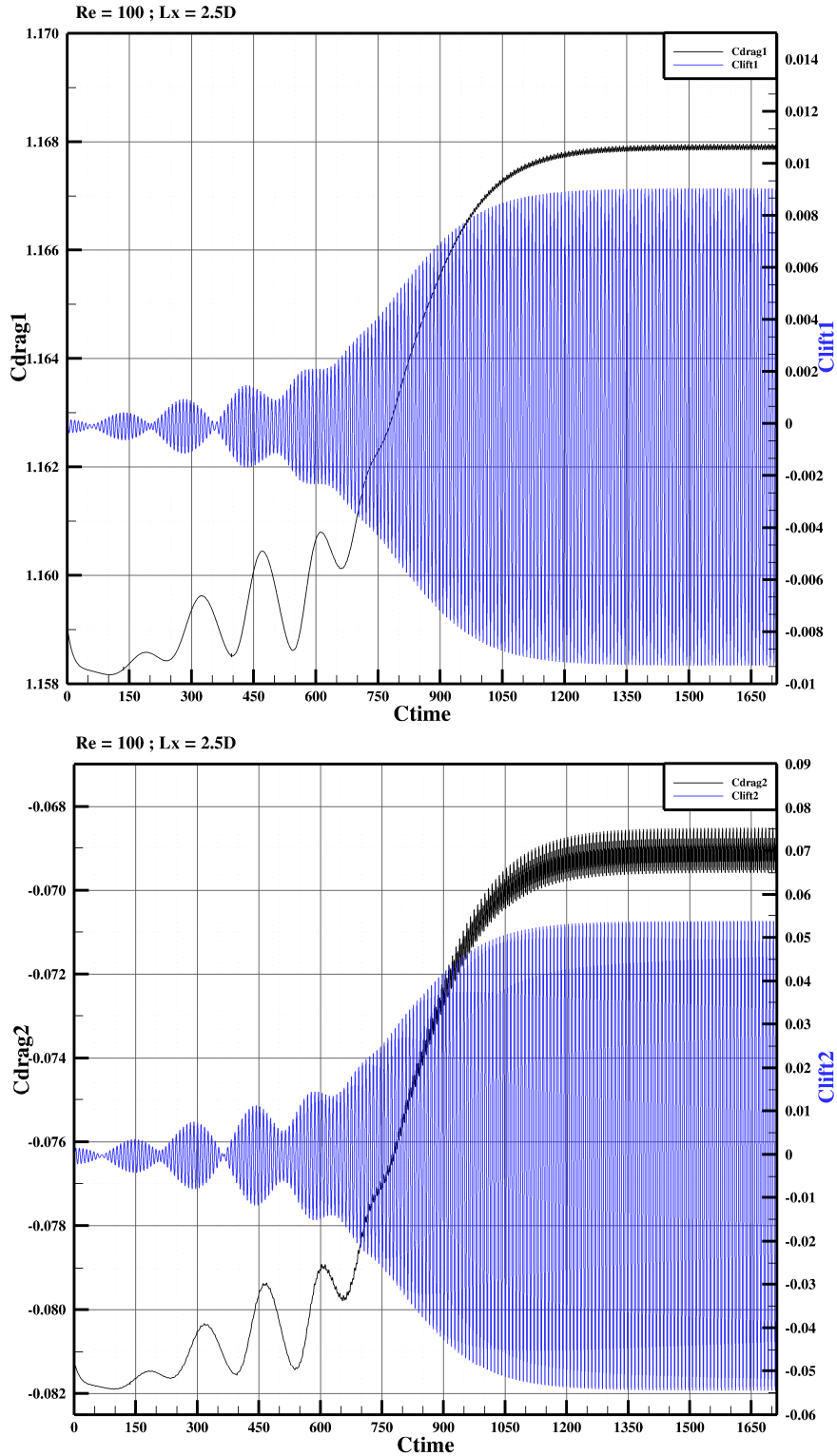
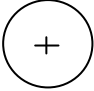
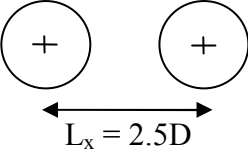
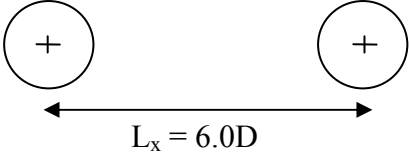


Figure 5-29 Time histories of lift and drag force coefficients for flow over two tandem cylinders at $L_x = 2.5D$ at $Re = 100$. Top: Forces acting on upstream cylinder; Bottom: Forces acting on downstream cylinder

Table 5-3 Summary of the aerodynamic data for flows past a single cylinder (Case 1), two cylinders in tandem arrangement at $L_x = 2.5D$ (Case 2) and $L_x = 6.0D$ (Case 3) at $Re = 100$.

	Case 1	Case 2		Case 3	
					
		Cylinder 1	Cylinder 2	Cylinder 1	Cylinder 2
\bar{C}_D	1.273	1.167	-0.069	1.297	0.589
$(C_D)_{rms}$	0.043	-	-	0.010	0.051
\bar{C}_L	0.000	0.000	0.000	0.000	0.000
$(C_L)_{rms}$	0.239	0.006	0.035	0.253	0.923
St	0.165	0.114	0.114	0.155	0.153

5.4.2 Vortex Induced Vibration (VIV) of Two Cylinders in Tandem Arrangement

In Section 5.4.1, numerical results of unsteady incompressible flow about fixed cylinder pairs, an important design problem in constructing structures such as offshore platforms and risers, are presented. It was shown that the numerical results from two dimensional simulations present a rich variety of complex interference phenomena.

Free vibrations of two elastically mounted cylinders in tandem (see Figure 5-30) have been studied not as extensively as single-cylinder oscillating cases. Zdravkovich (1988) conducted a review of the vibrations of two cylinders and discussion of the underlying vibration mechanism in different interference regions. In the literature, there have been also other experimental studies such as the works of Bokaian and Geoola (1984a, 1984b) in which they considered one of the two cylinders always held fixed.

Bokaian and Geoola (1984b) concluded that the downstream cylinder showed a VIV, a galloping, a combination of VIV and galloping or separated VIV and galloping depending on the gap size between cylinders when the upstream cylinder is fixed. Blevins (1990) described 'galloping' as vibrations caused by the variation of the hydrodynamic forces triggered by the motion of the structure in the flow when the force is in the direction of the motion and tends to increase as the structures moves away from the equilibrium position. However, the flow dynamics and structural motion are affected by the spacing between the structures. According to Zdravkovich (1985), the oscillation amplitude of the upstream cylinder can be larger than the downstream one in some cases. Similar observations were made by other researchers (Allen and Henning (2003); King and Johns (1976); Laneville and Brika (1999)). Fontaine et al. (2006) observed that oscillation amplitude of the downstream cylinder can be more than twice as large as that of the upstream cylinder in some cases. All of the previous experiments conducted dealing with two elastically mounted cylinders has focused on the oscillation amplitudes of the cylinders and a few on the forces excited by VIV. The experiments to date lack identification of the flow patterns and characteristics of the structural vibration. However, as stated in Borazjani and Sotiropoulos (2009), flow visualization and identification of the flow patterns are critical prerequisites for understanding the fluid mechanics of not only stationary but also vibrating multi-cylinder arrangements. In the context of identifying various phenomena under the complexity of two-cylinder VIV, numerical simulations can provide the necessary physical insight. So far, three important numerical studies have been reported which focus on VIV of two cylinder configurations at low Reynolds numbers. Among them, Mittal and Kumar (2001) studied two dimensional

simulations for two elastically mounted cylinders in tandem with $L_x/D = 5.5$ at $Re = 100$. Also Jester and Kallinderis (2004) considered two dimensional simulations of free vibrations of two cylinders in tandem at $Re = 1000$ and $L_x/D = 5.0$. Both of the studies showed that the downstream cylinder experiences large, flow-induced oscillation over a wide range of flow velocities while the upstream cylinder behaves as an isolated cylinder. On the other hand, Borazjani and Sotiropoulos (2009) conducted two and three dimensional FSI simulations for two elastically mounted cylinders in tandem placed $L_x/D = 1.5$ apart at $Re = 200$. All of the above mentioned references considered low mass ratios ($m^* \approx 2$) for the circular structures. Specifically, Borazjani and Sotiropoulos (2009); Mittal and Kumar (2001) chose no damping for the VIV cases. In their studies, the damping coefficient was assigned to zero in order to obtain the most intense vibrations, as damping has been shown to decrease the vibration amplitude (Fontaine et al. (2006)).

In this section, the results obtained from the stationary cylinder cases are extended to cylinder pairs oscillating transversely to the flow. In fact, the present study focuses on wake interference and investigates the effect of spacing of cylinders in tandem on the ensuing VIV dynamics, especially at the start of the resonance regime (i.e. $Re = 100$) for an oscillating single cylinder. Therefore, to understand how the approaching wake interacts with another structure, the flow around a circular cylinder mounted on an elastic basis, allowed to move only in the transverse direction which is immersed in the wake of an upstream circular cylinder of the same diameter D placed at a streamwise center to center distance L_x as sketched in Figure 5-31 is investigated.

Other researchers conducted studies for two-dimensional laminar simulations with Reynolds number ranging from 100 to 200 (Borazjani and Sotiropoulos (2009); Carmo

and Meneghini (2006); Mittal and Kumar (2001); Papaioannou et al. (2006, 2008); Ryan et al. (2007)). A three dimensional study for that this Reynolds number is not necessary as the results of Borazjani and Sotiropoulos (2009) showed that three-dimensional instabilities are so weak that they did not alter the dynamic FSI response of the system, which for all simulated cases was found to be essentially identical to that of the two-dimensional system. Although the experimental literature is conducted at significantly higher Reynolds number, the significant aspects of the VIV dynamics can be reproduced numerically at lower Re .

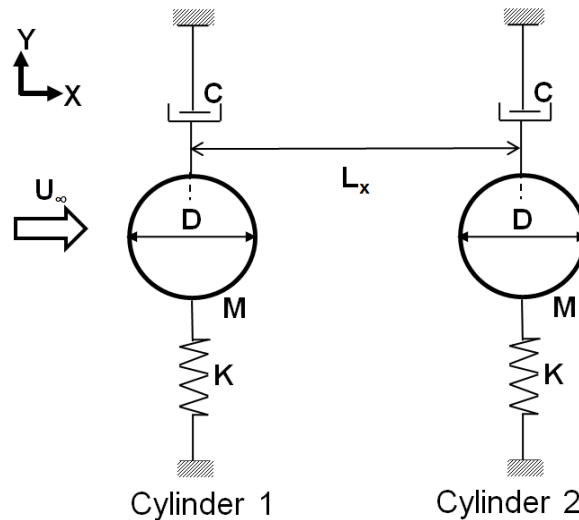


Figure 5-30 Schematic drawing of arrangement studied which is tandem arrangement of two identical, elastically mounted cylinders ($k = 69.48 \text{ kN/m}$, $c=0.0039 \text{ Ns/m}$, $D=1.6 \text{ mm}$, $f_N = 7.016 \text{ Hz}$, $m=35.75 \text{ g}$, $\xi=0.0012$).

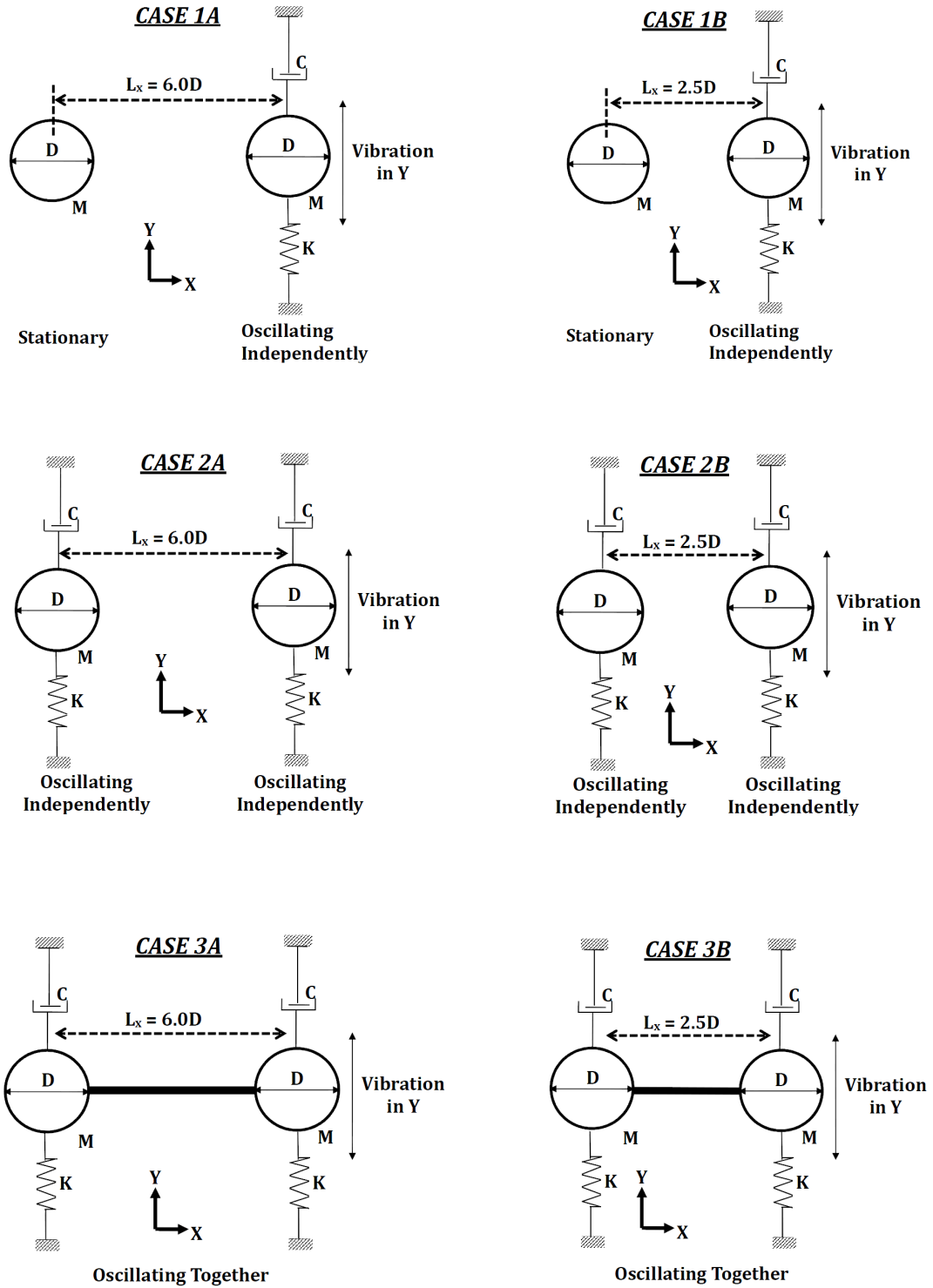


Figure 5-31 6 different VIV Cases studied in the current research for two cylinders in tandem arrangement at $Re = 100$ ($k = 69.48 \text{ kN/m}$, $c = 0.0039 \text{ Ns/m}$, $D = 1.6 \text{ mm}$, $f_N = 7.016 \text{ Hz}$, $m = 35.75 \text{ g}$, $\xi = 0.0012$).

The configurations tested in this section include two different separations:

A. $L_x/D = 2.5$

B. $L_x/D = 6.0$

Then, the interference between two circular cylinders in tandem arrangement and at two different spacing is investigated. In terms of VIV, three different scenarios are studied for each cylinder arrangement:

1. the upstream cylinder is fixed and the downstream cylinder is free to oscillate
2. both cylinders are free to oscillate
3. Cylinders are rigidly connected to each other and are free to oscillate in the cross-stream direction.

As shown in Figure 5-31, 6 cases in total are reported of two dimensional numerical simulations of flow-induced vibrations of two cylinders in tandem. *Case1A* to *Case 3A* considers scenario 1 to 3 with separation distance $L_x/D = 6.0$, *Case1B* to *Case3B* refer to oscillating scenario 1 to 3 with separation distance $L_x/D = 2.5$.

The non-dimensional parameters governing the response of the two-equal sized cylinders are the same as for the single cylinder VIV simulation ($m^* = 150$, $\zeta = 0.0012$, $U_{red} = 5.58$). The simulations are carried out for one degree of freedom (1 DOF), only lateral displacement, to investigate the effect of different scenarios on the VIV. For all cases, the size of the computational domain, boundary conditions, distribution of the grid and the size of the time step which corresponds to a CFL number of 0.3 are kept identical to those used for stationary tandem arrangement discussed in Section 5.4.1. In addition, all computations for the 3 different scenarios reported here are initialized from the same instantaneous snapshot of the simulations that was obtained from fully developed

unsteady solution past stationary cylinders in the same arrangement and at the same Reynolds number. The integration in time is continued until the quasi-steady state is reached.

For *Case3A* and *Case3B*, numerically, the rigid coupling is simulated by summing up the computed lift force of the two cylinders and computing a single structural response with the obtained total lift force. As mentioned in the previous section, we will refer to the upstream cylinder as cylinder 1 and to the downstream one as cylinder 2. Also, the quantities in the figures with suffix 1 are associated with cylinder 1, whilst those with suffix 2 are for cylinder 2.

In the previous section, the solution for flow past two stationary cylinders at $Re = 100$ in tandem arrangement at six diameters distances ($L_x = 6.0D$) has been discussed. The wake was found to be organized and a periodic vortex structure was observed in the fully developed unsteady solution. It was also noted that the vortex shedding is not in phase, i.e. as the upstream cylinder sheds a vortex from its upper surface, the downstream one generates a counter-rotating vortex from its lower surface. For that configuration, frequency of the vortex shedding for both of the cylinders is found to be 0.154 which is 5% less than that for a single cylinder ($f_0 = 1.165$) at the same Reynolds number. For *Case1A*, the approximate value of the amplitude of the cross-flow oscillation of the downstream cylinder is measured to be 0.018 times the cylinder diameter. Having the downstream cylinder lying in the unsteady wake of the upstream cylinder does not cause any type of instability; hence, no resonance is captured at that configuration. However, compared to the stationary cylinder ($C_L' = 0.34$; $\overline{C_D} = 1.27$), the oscillating downstream cylinder exhibits larger values of the mean and amplitude of the time-varying component

of the lift coefficient ($C_{L2}' = 1.35$) and smaller amplitude of the drag coefficient ($\overline{C}_{D2} = 0.60$) (See Figure 5-32) at steady-state phase.

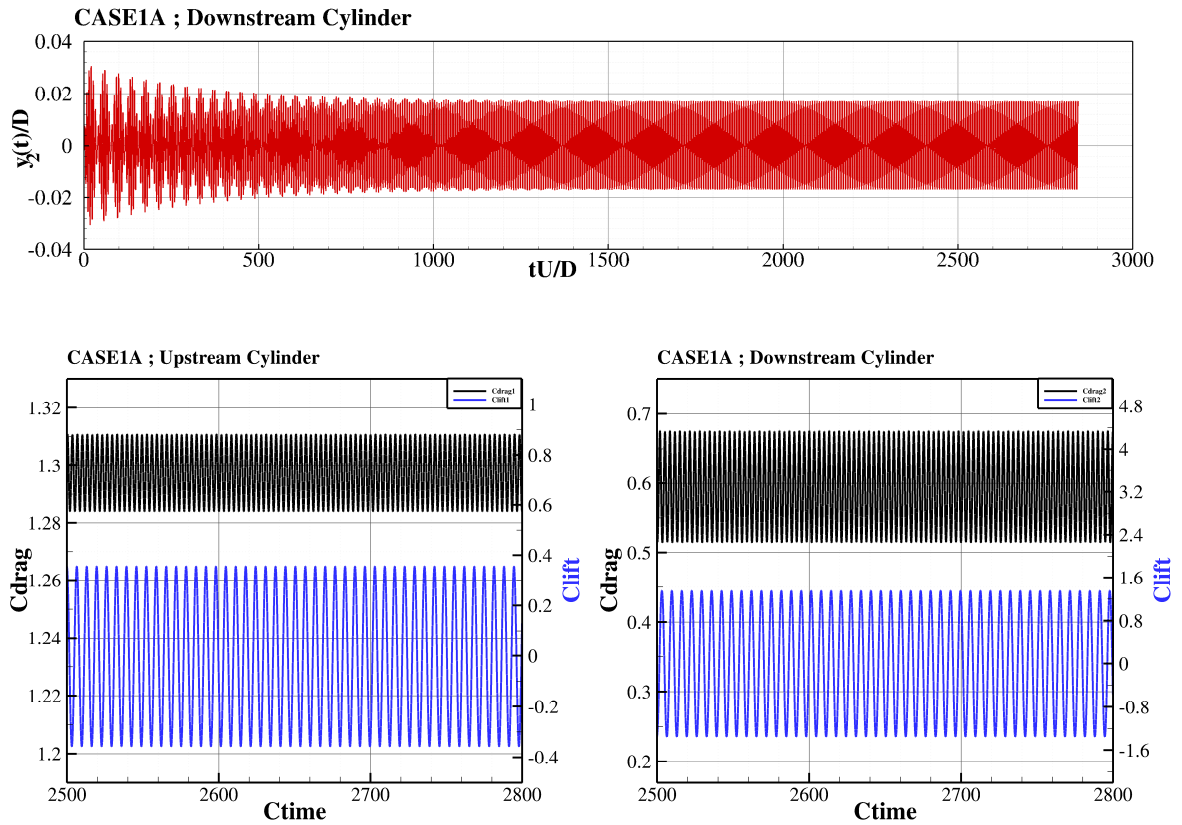


Figure 5-32 $Re = 100$ flow past two cylinders in tandem arrangement at $L_x = 6.0D$ in Case1A in which the upstream cylinder is fixed and the downstream cylinder is free to oscillate. Time-histories of the response (Top) of cylinder 1 and drag and lift coefficients (Bottom) of both of the cylinders. The quantities with suffix 1 are associated with upstream cylinder, while those with suffix 2 are for downstream cylinder.

The results of *Case1B* which includes time histories of approximate value of the amplitude of the cross-flow oscillation and lift and drag coefficients are presented in Figure 5-33. As shown in this figure, the amplitude of the oscillation of the downstream cylinder is very small and negligible in terms of its magnitude. As a result of a steady vortex field formed between the structures placed at 2.5 diameters distance, there is still no sign of shedding vortices which may result in resonance during the free vibration of the downstream cylinder. As compared to *Case1A*, the magnitude of oscillation is almost zero for cylinder 2. In terms of force coefficients, there is almost no change in the amplitude estimation of drag and lift components of the force coefficients compared to stationary cylinder case at the same Reynolds number. Therefore, it is reasonable to postulate that in *Case1B* where the upstream cylinder is fixed and the downstream cylinder is free to oscillate at $L_x = 2.5D$ and at $U_{red} = 5.58$, there is no mechanism producing vortex shedding since the flow field is identical to flow past stationary cylinder results.

Free oscillations of two cylinders in tandem arrangement are simulated through *Case2A* and *Case 2B*. The results for time histories of cross-flow oscillation, drag and lift coefficients are shown in Figure 5-34 and 5-35, respectively. The strong lift force acting on the downstream cylinder is captured in *Case2A*. Our results indicate that resonance is affected significantly with strong vortex magnitudes as discussed in VIV of single cylinder case. The present results in *Case2A* also show that resonance (oscillation amplitude still developing and it has a value of $A = 0.1D$) occurs for both of the cylinders. On the other hand, as discussed in the results of *Case1B* above, in *Case2B* at $L_x = 2.5D$, there is no mechanism producing strong vortex structures which induces

vibration of the cylinder. As seen in Figure 5-35, the amplitude of it ($A = 0.0004D$) is close to zero, although the amplitude of the oscillation tends to increase.

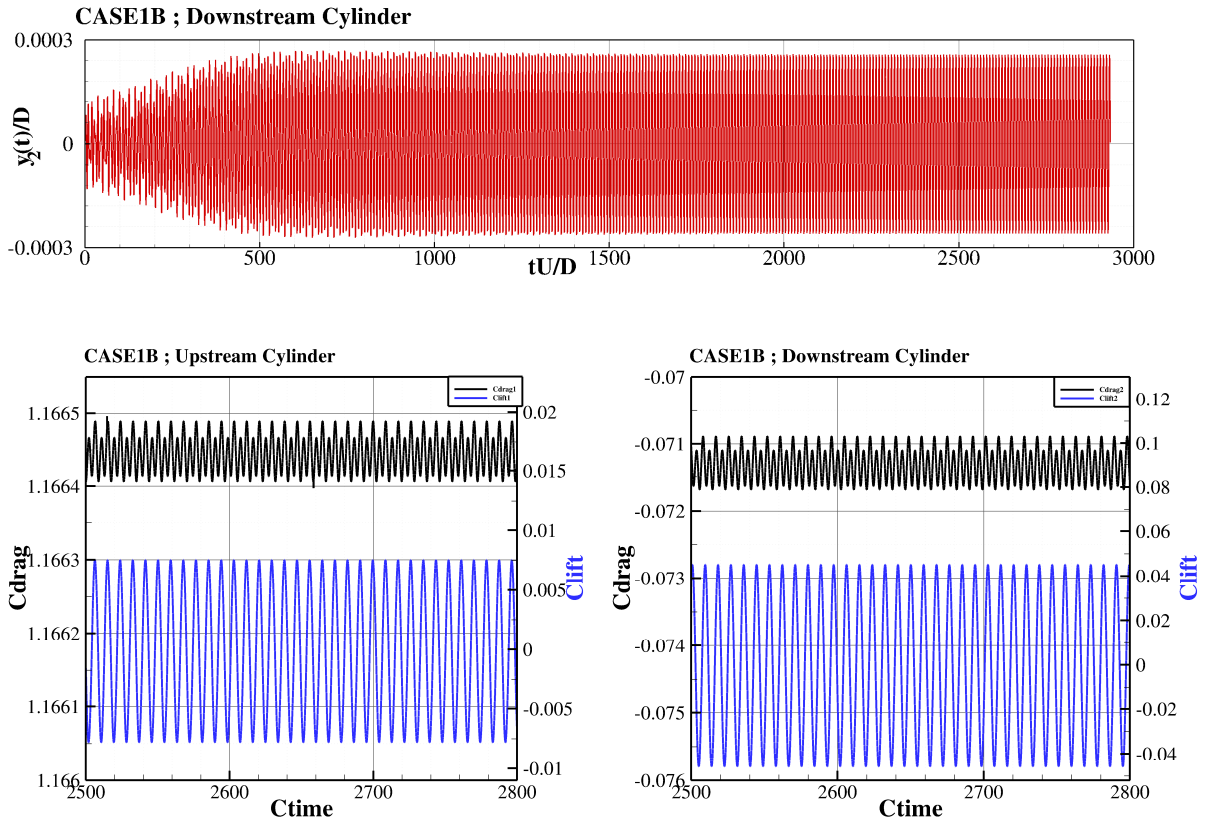


Figure 5-33 $Re = 100$ flow past two cylinders in tandem arrangement at $L_x = 2.5D$ in Case1B in which the upstream cylinder is fixed and the downstream cylinder is free to oscillate. Time-histories of the response (Top) of cylinder 1 and drag and lift coefficients (Bottom) of both of the cylinders. The quantities with suffix 1 are associated with upstream cylinder, while those with suffix 2 are for downstream cylinder.

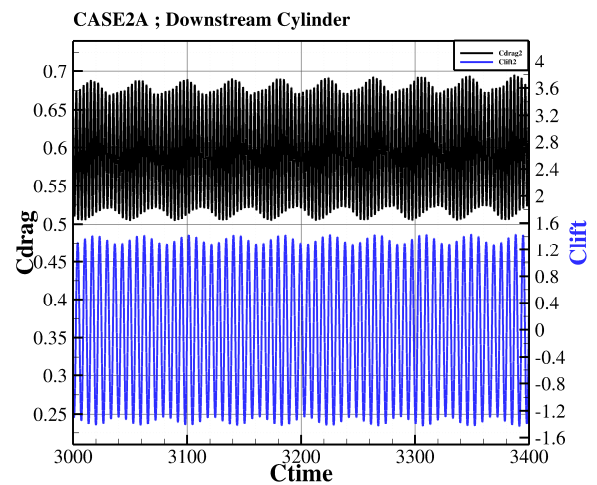
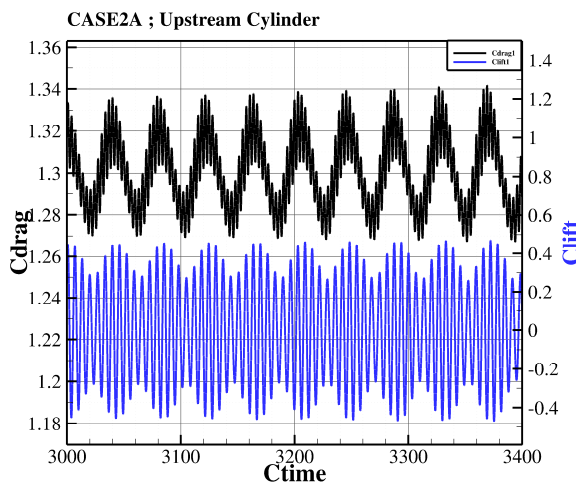
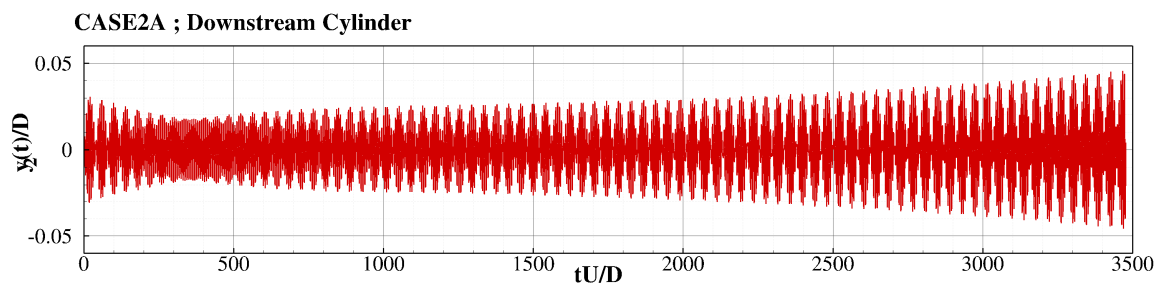
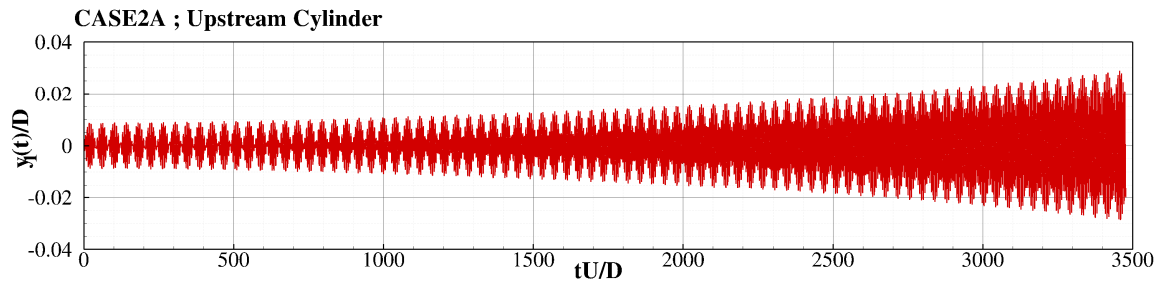


Figure 5-34 $Re = 100$ flow past two cylinders in tandem arrangement at $L_x = 6.0D$ in Case2A in which both cylinders are free to oscillate. Time-histories of the response (Top) of cylinder 1 and 2, and drag and lift coefficients (Bottom) of both of the cylinders. The quantities with suffix 1 are associated with upstream cylinder, while those with suffix 2 are for downstream cylinder.

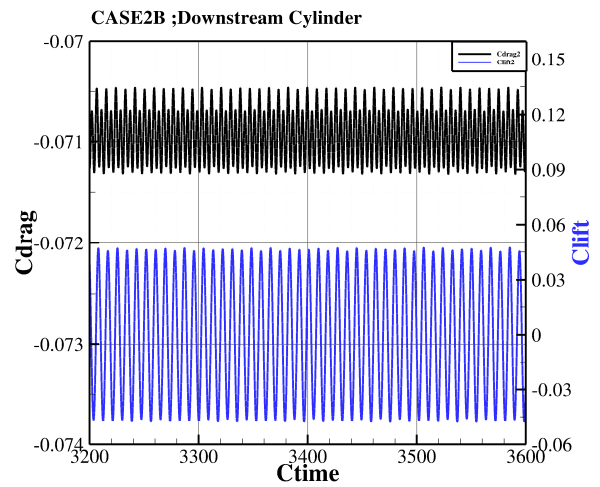
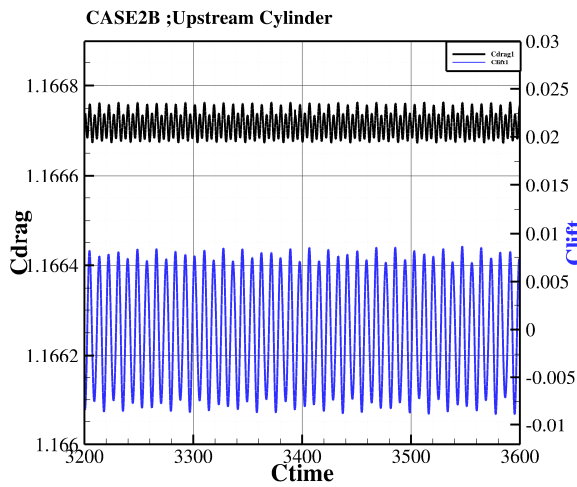
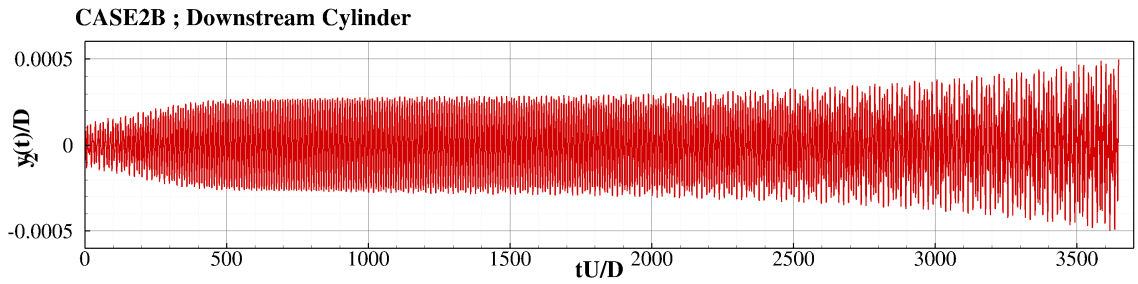
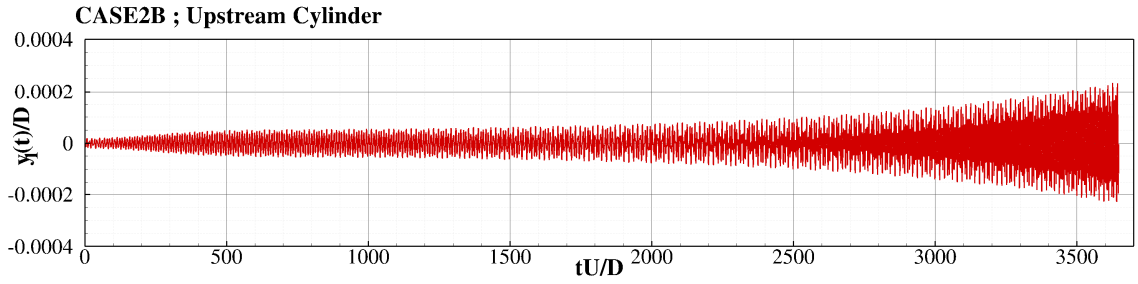


Figure 5-35 $Re = 100$ flow past two cylinders in tandem arrangement at $L_x = 2.5D$ in Case2B in which both cylinders are free to oscillate. Time-histories of the response (Top) of cylinder 1 and 2, and drag and lift coefficients (Bottom) of both of the cylinders. The quantities with suffix 1 are associated with upstream cylinder, while those with suffix 2 are for downstream cylinder.

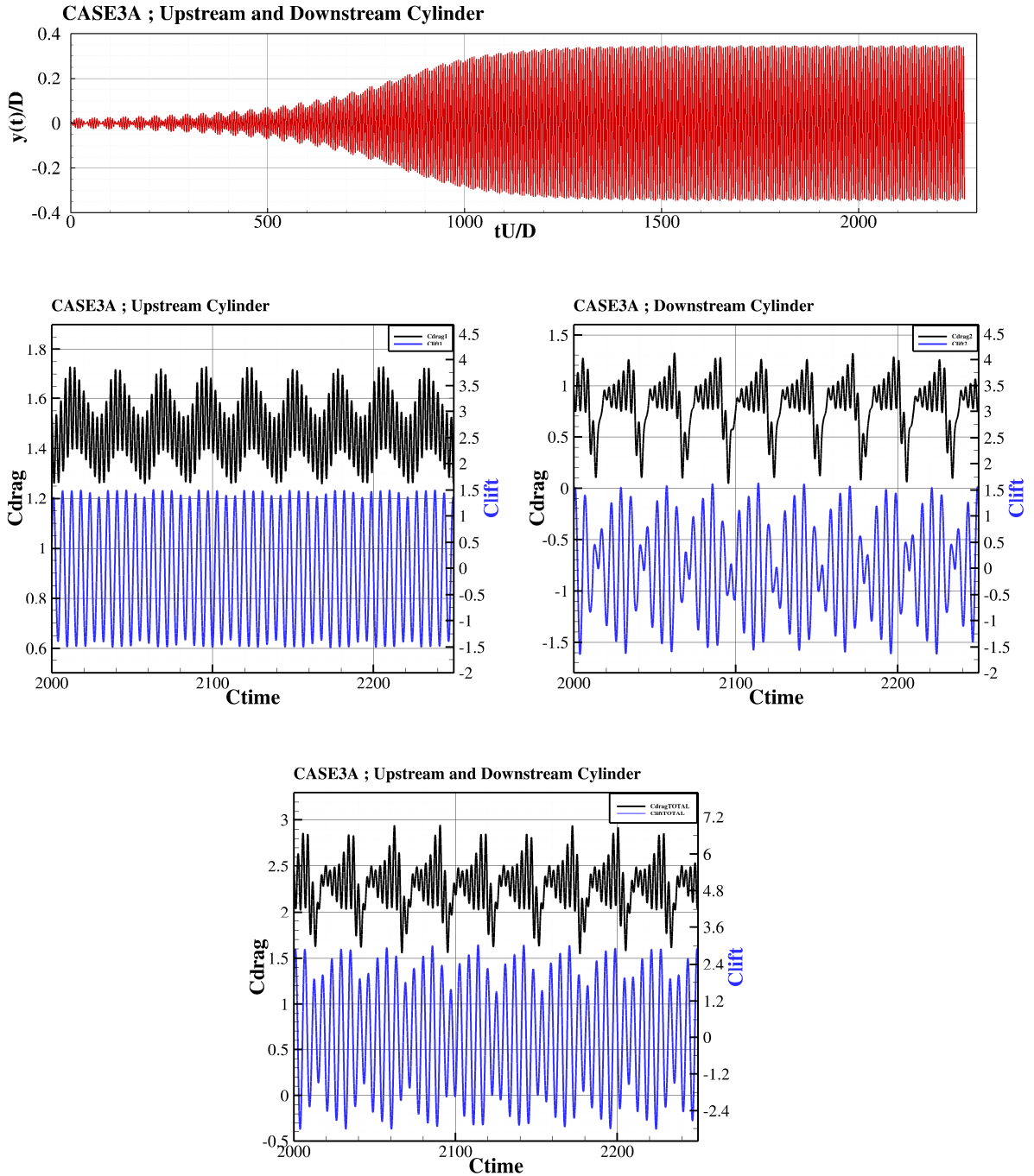


Figure 5-36 $Re = 100$ flow past two cylinders in tandem arrangement at $L_x = 6.0D$ in Case3A in which they are rigidly connected to each other and are free to oscillate in the cross-stream direction. Time-histories of the response (Top) of cylinders, and independent (Middle) and total (Bottom) drag and lift coefficients of the cylinders. The quantities with suffix 1 are associated with upstream cylinder, while those with suffix 2 are for downstream cylinder.

Flow-induced oscillation of rigidly-connected tandem cylinders are simulated through *Case3A* and *Case3B* with $L_x = 6.0D$ and $2.5D$, respectively. In these cases, structures are mechanically coupled so that they both experience identical transverse response. Both studies with different space arrangements indicate that VIV occur for cylinders 1 and 2 at the same Reynolds number as an isolated cylinder near $U_{red} = 5.58$. The results are reported in Figures 5-36 and 5-37. As the figure clearly shows, in *Case3A* and *Case3B*, structures reach maximum constant amplitude at $y/D = 0.34$ and 0.27 , respectively while this value is 0.42 for the isolated cylinder case at $Re = 100$. Although the oscillation amplitude of rigidly connected structures for *Case3A* (20%) and *Case3B* (35%) is less than that of the isolated cylinder, resonance occurs at reasonable oscillation amplitude ($A = 0.34D$ and $A = 0.27D$ in *Case3A* and *Case3B*, respectively).

To further elucidate the dynamic response of the system, time-histories of force coefficients are plotted in Figures 5-36 and 5-37. In *Case3A*, compared to stationary cylinders, the oscillating rigidly coupled cylinders exhibit larger values of the mean and the amplitude of time varying component of the drag and lift coefficients. In addition, peaks can be observed in the time-histories of the drag coefficients which also affect the behavior in total lift coefficient as seen in Figure 5-36. On the other hand, in *Case3B*, time histories of individual and total drag and lift coefficients show a smoother behavior and the amplitudes of the force coefficients are larger than that of stationary cylinders. Interestingly, due to the vortices produced by cylinder 1, the downstream cylinder is now in a positive pressure region and experiences a positive drag force.

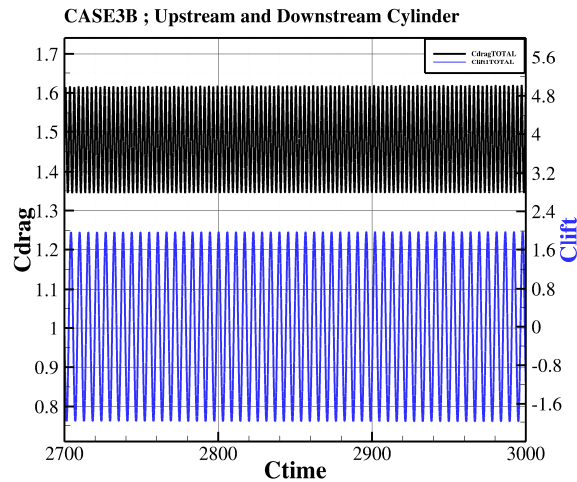
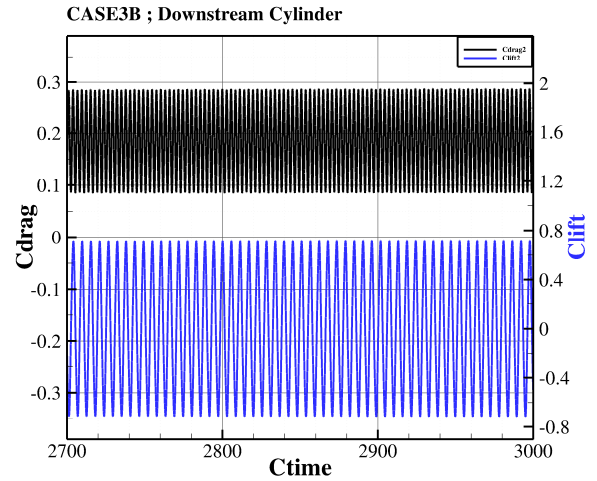
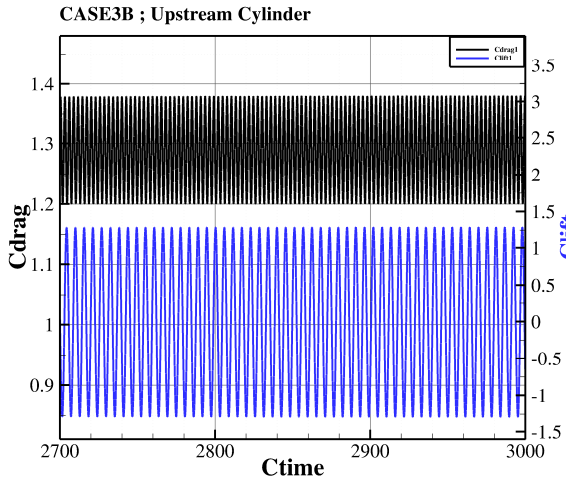
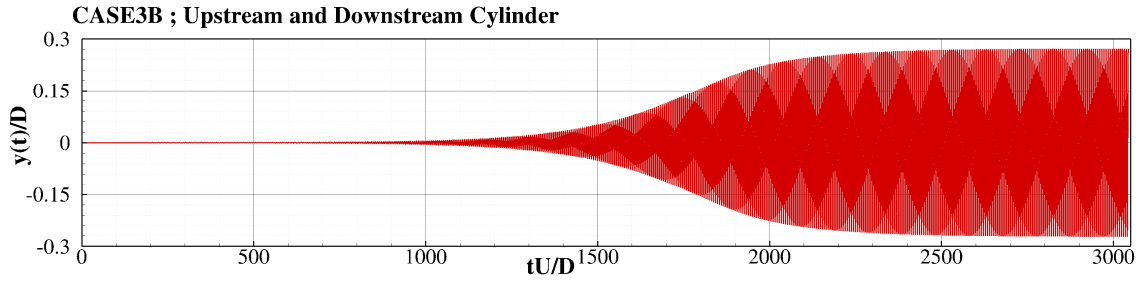


Figure 5-37 $Re = 100$ flow past two cylinders in tandem arrangement at $L_x = 2.5D$ in Case3B in which they are rigidly connected to each other and are free to oscillate in the cross-stream direction. Time-histories of the response (Top) of cylinders, and independent (Middle) and total (Bottom) drag and lift coefficients. The quantities with suffix 1 are associated with upstream cylinder, while those with suffix 2 are for downstream cylinder.

It is also interesting to note that the non-dimensional frequency associated with the variation of the lift coefficients and the cross-flow oscillations in *Case3A* and *Case3B* is 0.177 . This detuning between the structural frequency and the shedding frequency has been observed not only for a single oscillating cylinder but also for other numerical studies conducted by different researchers. For instance, Mittal and Kumar (1999, 2001) studied this phenomenon and explained it as “*soft lock-in*” and they have pointed out that it is one of the mechanisms of the nonlinear oscillator to self-limit its vibration magnitude.

Figure 5-38 shows the time variation of the total drag and lift coefficients with respect to the oscillation magnitude and their power spectra for the transverse oscillation of the rigidly coupled cylinders in Case 3B. The mean value for the total drag force is found to be 1.476. The root mean square values of total drag and lift force components are 0.097 and 1.391, respectively. It is evident from the power spectra for both force coefficients that only one dominant frequency ($St_{\text{Drag}} = 0.350$, $St_{\text{Lift}} = 0.176$) exists, demonstrating the time periodic variation of drag and lift force coefficients (Top Left and Top Right figures in Figure 5-38) with respect to the cylinder’s displacement with only one period of oscillation. The phase portrait of the sum of the drag and lift coefficients acting on the coupled cylinders with respect to transverse displacement of the cylinders is also included in Figure 5-37. This phase portrait looks like an inverse figure-eight and it is symmetric with respect to the origin which is known as the initial rest positions of the rigidly coupled structures. This also implies that only half of the cycle is adequate enough in order to post-process and analyze the flow dynamics since the other half of the cycle is the mirror image of the first half. Another feature in these figures is that the total lift and

drag forces are in phase and in the same direction throughout the transverse displacement of the structures.

Figure 5-39 shows the time variation of the total drag and lift coefficients with respect to the oscillation magnitude and their power spectra for the transverse oscillation of the rigidly coupled cylinders in Case 3A. Due to the wake of upstream one interacting with the downstream cylinder, the force coefficients are affected significantly. The mean of the total drag force is found to be 2.270. The root mean square values of the total drag and lift force components are 0.2632 and 1.76, respectively. Clearly, mean drag and rms values of drag and lift are significantly larger for this case. Compared to Case3B, the power spectrum of the drag coefficient exhibits peaks at additional frequencies. It is interesting to note that these peaks do not appear in the lift coefficient. This could be attributed to vortices shed from the upstream cylinder which trigger strong oscillations. The strongest frequencies occur at $St_{\text{Drag}} = 0.348$, $St_{\text{lift}} = 0.174$ for total drag and lift coefficients, respectively. Those values are close to the ones obtained in Case 3B.

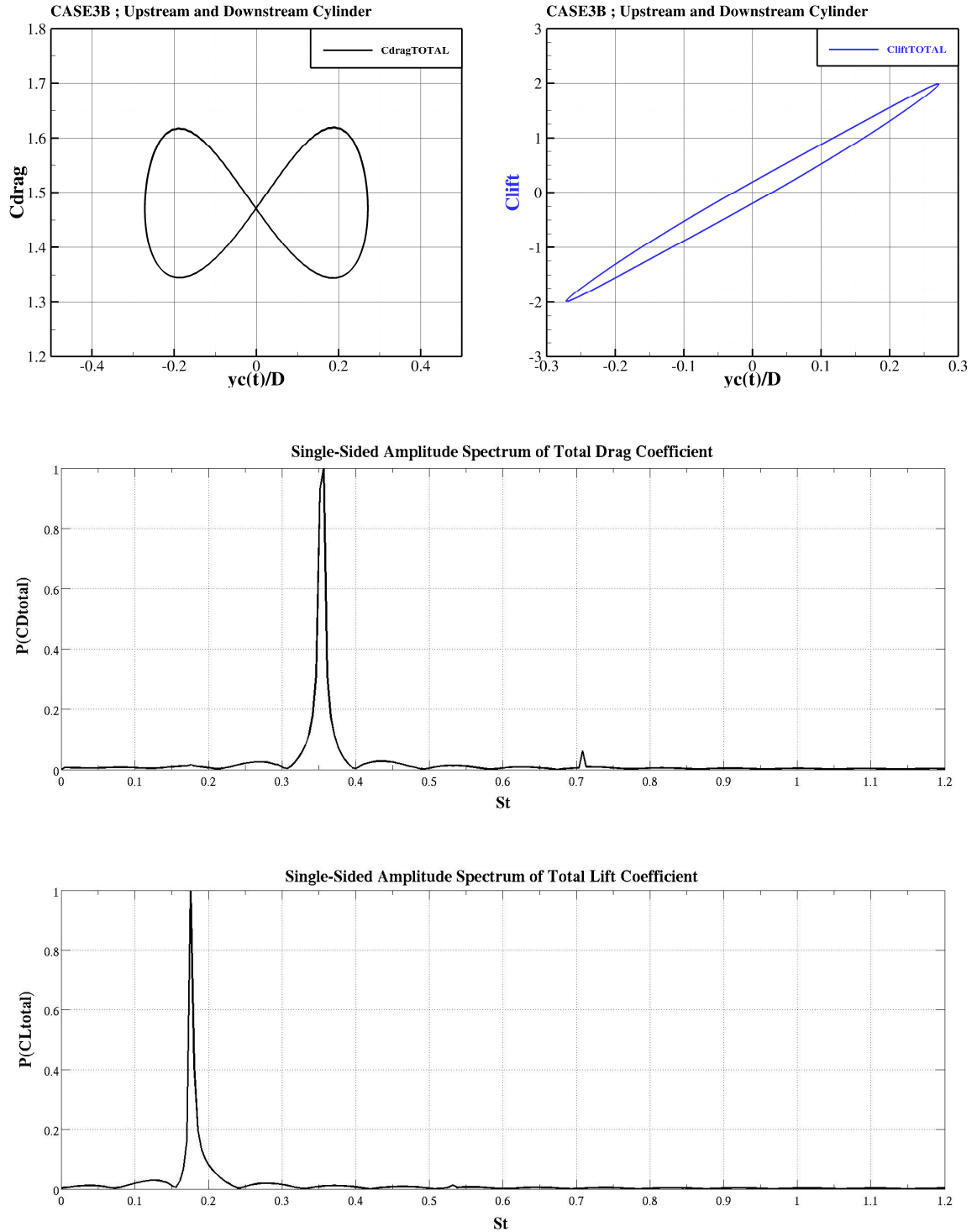


Figure 5-38 Flow past rigidly coupled cylinders in tandem arrangement ($L_x = 2.5D$) at $Re = 100$: Time periodic variation of drag and lift force coefficients (Top Left and Top Right) with respect to cylinders' displacement; power spectra of the time histories of drag coefficient (Middle) and lift coefficient (Bottom), respectively.

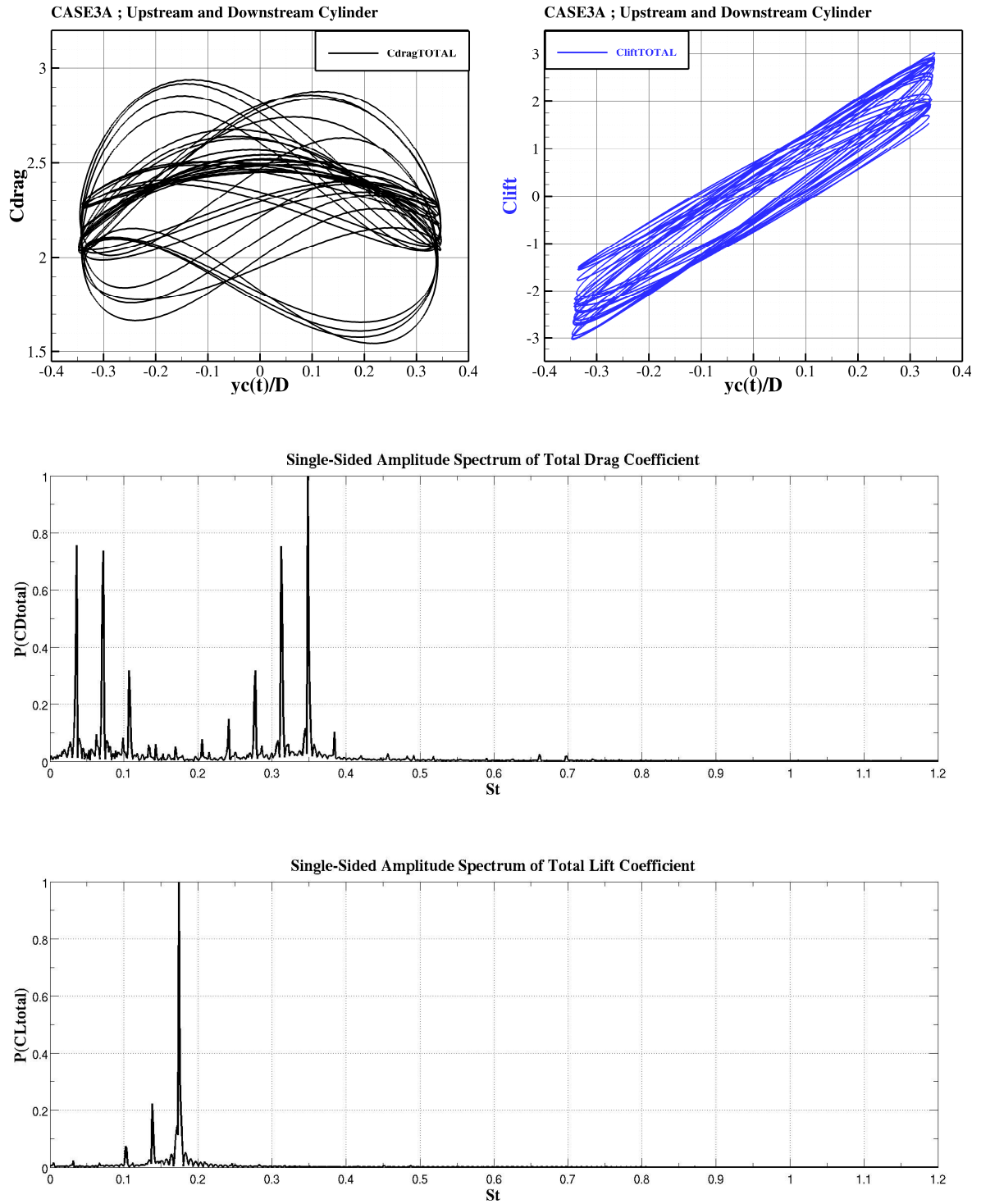


Figure 5-39 Flow past rigidly coupled cylinders in tandem arrangement ($L_x = 6.0D$) at $Re = 100$: Time periodic variation of drag and lift force coefficients (Top Left and Top Right) with respect to cylinders' displacement; power spectra of the time histories of drag coefficient (Middle) and lift coefficient (Bottom), respectively.

As the resonance is suppressed for the first two configurations where the upstream cylinder is fixed and the downstream cylinder is free to oscillate and both cylinders are free to oscillate, it makes the study of vorticity dynamics important for the last configurations where the oscillation response of the structures are critical. Figure 5-40 shows 8 snapshots of the flow field between cylinders spaced at $L_x=6.0D$ during a period of resonant response. This figure includes both the pressure and vorticity field around rigidly coupled structures. The frames are chosen at regular intervals of the oscillatory cycle, at different phase angles (θ 's). The instances are chosen at θ 's ranging from 0° to 315° so that the constructive interference occurring in the unsteady wake region is illustrated as clearly as possible. The formation and shedding of vortices behind cylinder 1 show standard, regular features which allow formation of a short Von Karman vortex street in between structures. However, the downstream cylinder experiences a different flow field which is a chaotic regime since it is colliding with the vortices created by the upstream cylinder. This leads to a reduction in the oscillation forces on the downstream cylinder. Also, this may be the cause for the decreased overall response in terms of the magnitude of the oscillation as compared to the single cylinder case. These figures seem to indicate that the primary reason for the existence of lower oscillation amplitude is due to the development and collision of vortex shedding between structures.

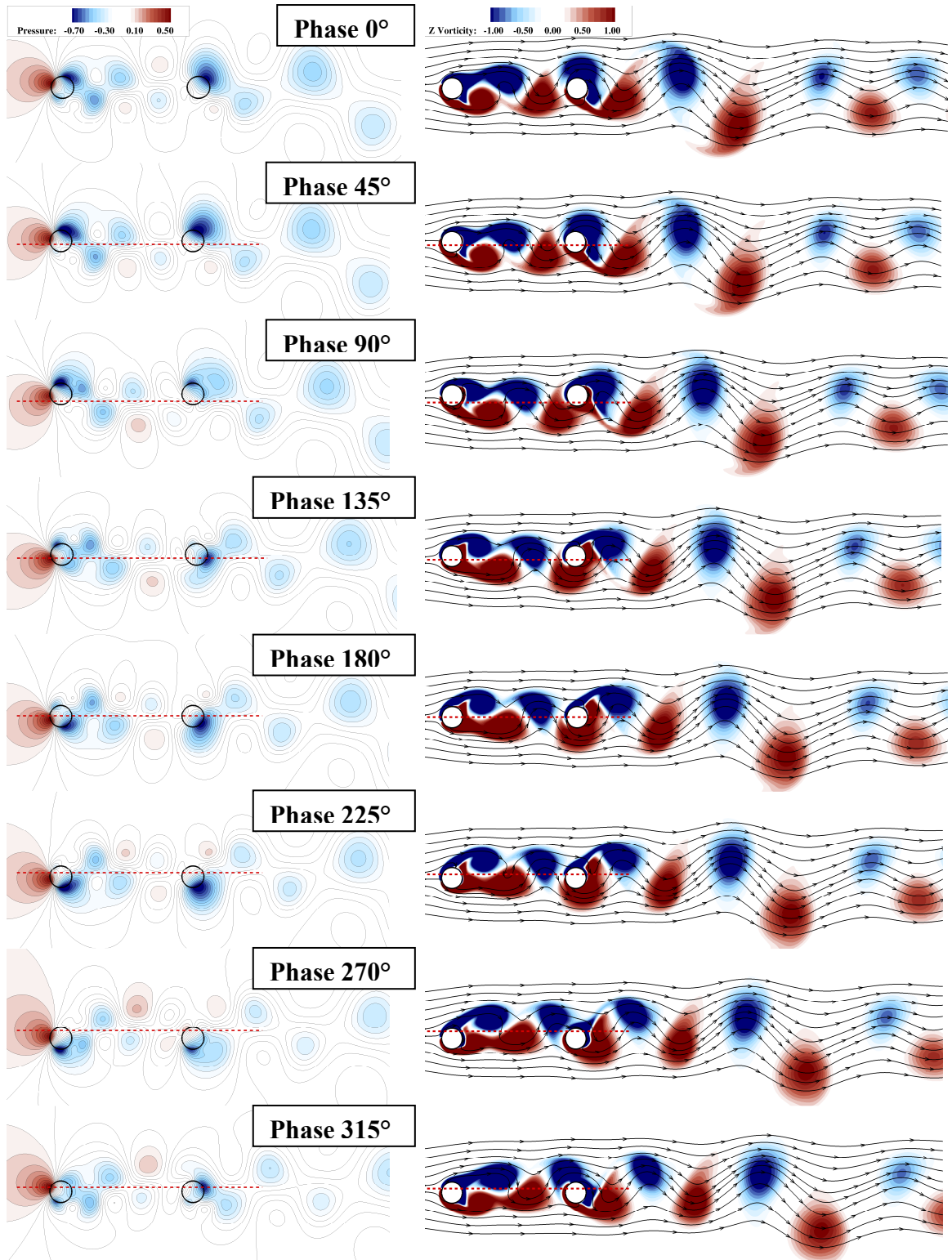


Figure 5-40 For Caption see next page

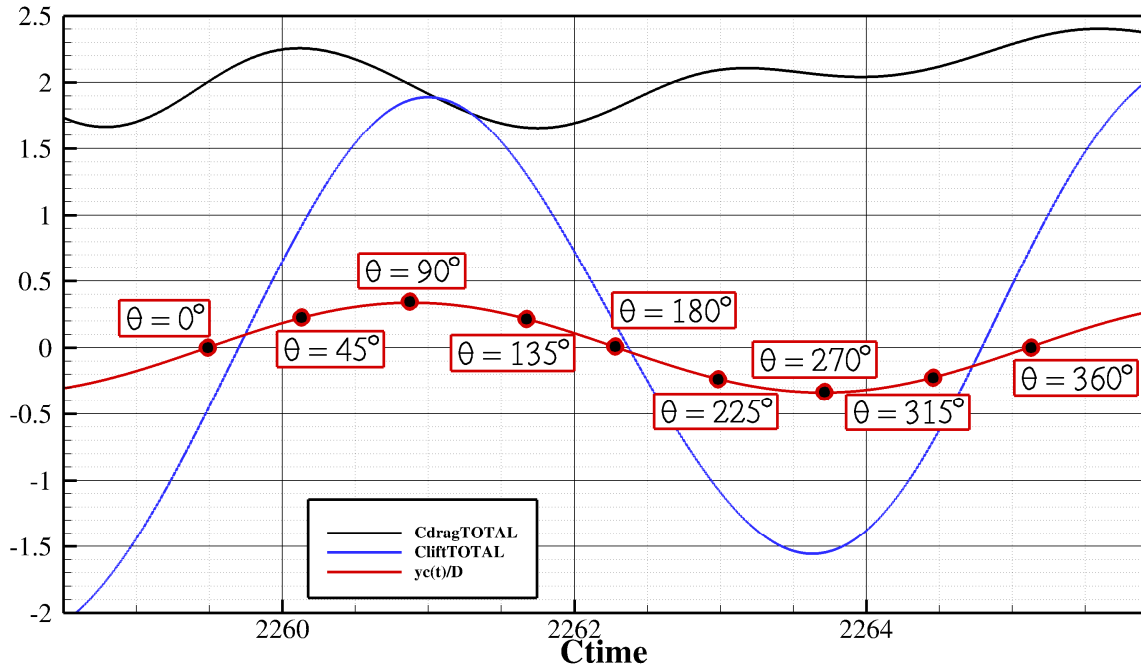


Figure 5-40 Pressure Contours (Left Column) and streamlines with vorticity contours (Right Column) for rigidly coupled cylinders in tandem arrangement at $L_x = 6.0D$, transversely oscillating at $Re = 100$ with $m^* = 150$, $\zeta = 0.0012$ and $U_{red} = 5.58$. The horizontal red dash-dotted lines for pressure and vorticity plots in Phase angles (θ) 0° to 315° indicate the initial rest positions of the cylinders. The discussions in the text reveal an important vorticity interaction. The phase instants ($\theta = 0^\circ \dots 360^\circ$) are specified as black color filled red circles on the time-history of displacement at the bottom of the figure along with time histories of total drag and lift coefficients during one cycle of oscillation. C_{drag} (black solid line) and C_{lift} (blue solid line) refer to total drag and lift coefficients acting on the structures; $Y_c(t)/D$ is the position of the coupled cylinders in cross-stream direction.

Figure 5-41 shows the flow pattern for *Case3B* in which rigidly coupled cylinders are free to oscillate in cross-stream direction at a spacing of $L_x = 2.5D$. This figure visualizes the pressure and vorticity field around and in between structures at regular intervals of the oscillatory cycle, at different phase angles (θ 's) similar to flow visualization discussed in the previous configuration of structures, *Case3A*. It can be easily observed that the vortices shed from the top and bottom of the upstream cylinder do not enter the gap region due to the relatively short spacing difference between structures. Those vortices induced by cylinder 1 wrap around the top and bottom sides of the downstream one and disrupt its shedding.

Due to the presence of recirculating flow in the gap as a result of small velocity field and the passage of vortices around top and bottom of the downstream cylinder, a different pressure distribution is formed around both of the cylinders. Therefore, a smaller lift force on cylinder 2 and smaller amplitude of the overall oscillation relative to single cylinder oscillation are observed, which is due to the low pressure field emerging around the downstream cylinder. In other words, cylinder 2 always remains within the wake of the upstream cylinder and is never exposed to a region of high pressure as a result of slow recirculating flow in the gap region. The wake pattern in the downstream part of the domain resembles a regular Von Karman Street with a $2S$ mode. Similar observations were made by Borazjani and Sotiropoulos (2009) in the analysis of vorticity and pressure fields in a closely spaced, independently oscillating two-cylinder system.

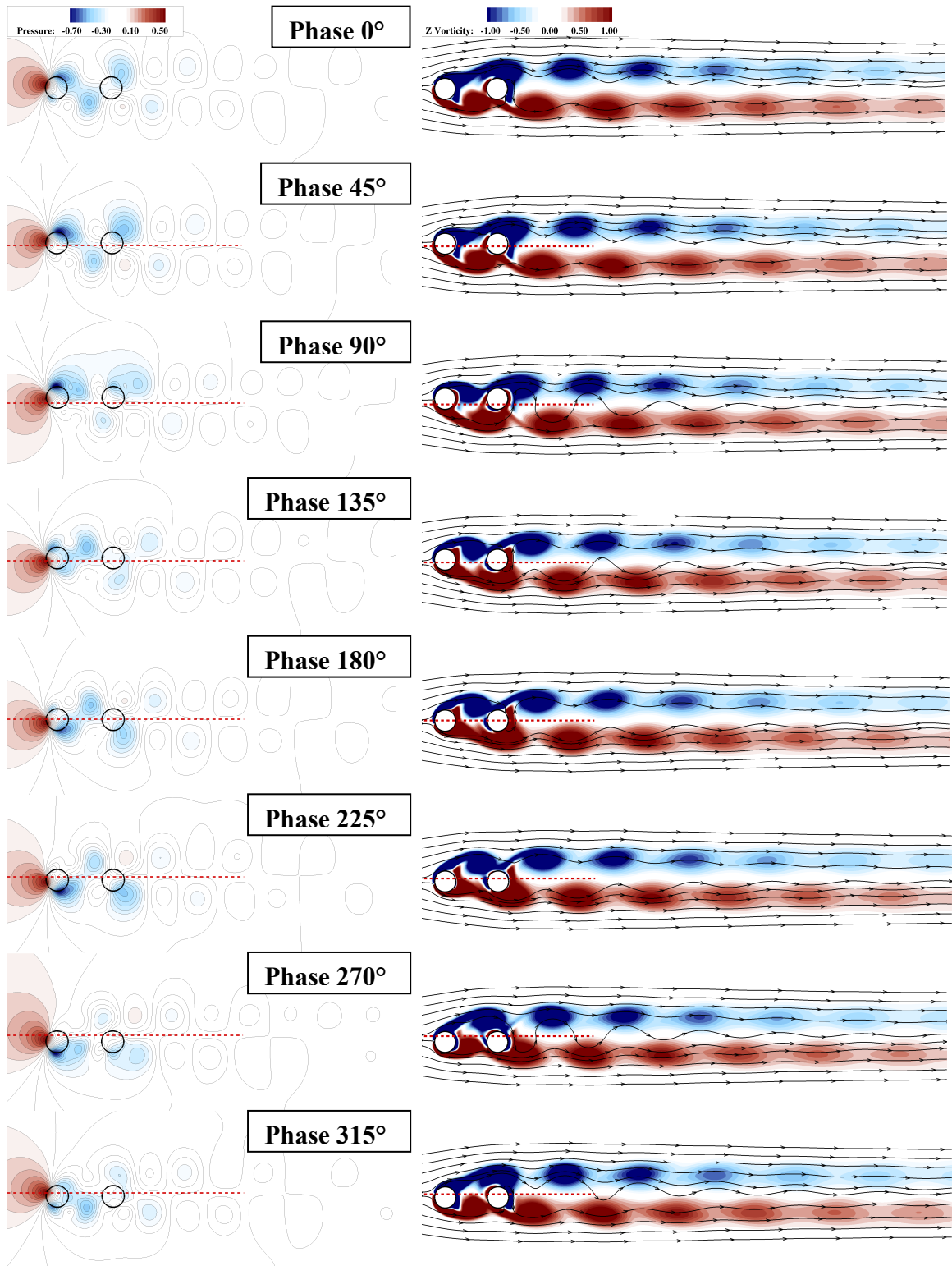


Figure 5-41 For Caption see next page

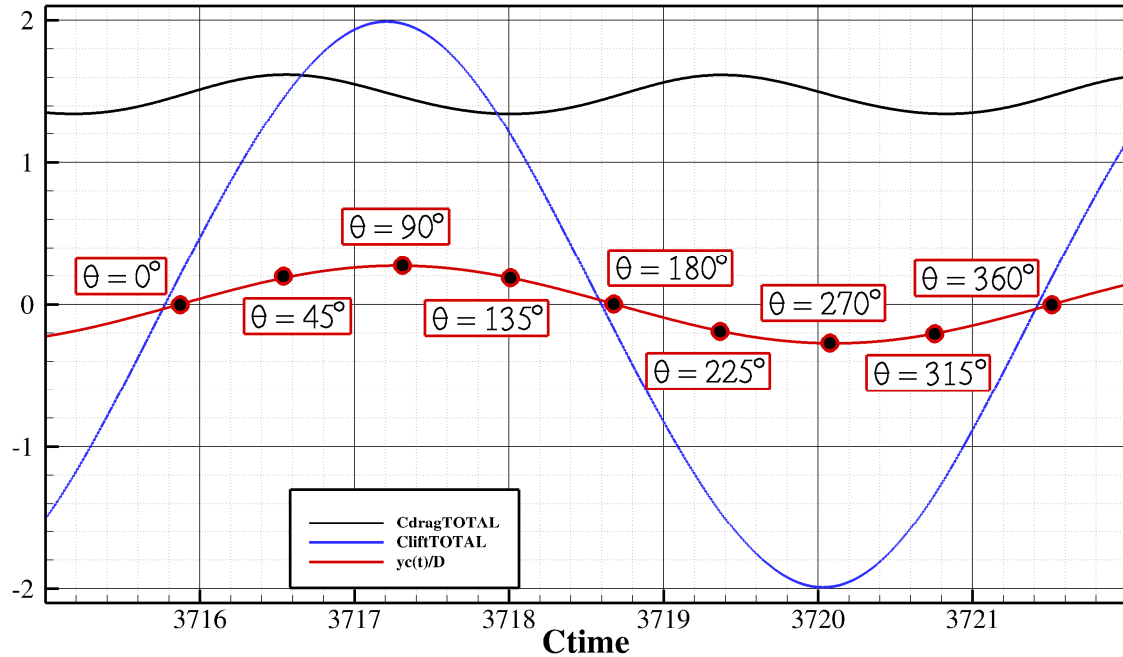


Figure 5-41 Pressure Contours (Left Column) and streamlines with vorticity contours (Right Column) for rigidly coupled cylinders in tandem arrangement at $L_x = 2.5D$, transversely oscillating at $Re = 100$ with $m^* = 150$, $\zeta = 0.0012$ and $U_{red} = 5.58$. The horizontal red dash-dotted lines for pressure and vorticity plots in Phase angles (θ) 0° to 315° indicate the initial rest positions of the cylinders. The discussions in the text reveal an important vorticity interaction. The phase instants ($\theta = 0^\circ \dots 360^\circ$) are specified as black color filled red circles on the time-history of displacement at the bottom of the figure along with time histories of total drag and lift coefficients during one cycle of oscillation. C_{drag} (black solid line) and C_{lift} (blue solid line) refer to total drag and lift coefficients acting on the structures; $Y_c(t)/D$ is the position of the coupled cylinders in cross-stream direction.

5.5 Summary

In this chapter, the accuracy of the utilized immersed boundary method presented in the previous chapter was demonstrated first via numerical studies involving flow past a single stationary cylinder. After the establishment of the formal accuracy of the present method, the study concentrated on moving structures. First, forced harmonic in-line oscillation of a circular cylinder in a quiescent fluid, and then the flow from a transversely prescribed vibration of a circular cylinder in a free-stream are studied. Both the cases are well documented in the literature, experimentally and numerically. The present method was shown to reproduce all features of the flow, including the drag and lift forces acting on the structure as the similar studies.

Next, vortex-induced vibration of an elastically mounted single cylinder with one degree of freedom was investigated in order to prove the strong coupling scheme for fluid-structure interaction problems. For that case, the lock-in regime was captured accurately and the numerical results were compared with experimental data and other simulations with reasonable accuracy.

Afterwards, a numerical study was carried out to study the interference effect on the onset of resonance ($Re = 100$) in flows involving a pair of cylinders in in-line arrangements. First of all, the flow dynamics were investigated for stationary tandem cylinder arrangement. The results compare quite well with computational results from other researchers. The flows at this Reynolds number with two tandem arrangements exhibit very significant qualitative and quantitative differences. This points to the fact that the flows dealing with two cylinders show a strong dependence on the arrangement of the

structures in terms of force estimations and flow field visualizations compared to flows past a single cylinder. For instance, it was observed that the downstream cylinder, which lies in the wake of the upstream cylinder, experiences very large unsteady forces that may trigger wake-induced vibrations. Also, the downstream cylinder was found to experience a negative drag force when the structures were closely spaced. Finally, the numerical simulations were extended to vortex-induced vibrations of a pair of cylinders in tandem arrangement. Among other things, it was found that resonance is suppressed when both cylinders are allowed to move transversely and independently, whilst two rigidly-connected cylinders show the same behavior as a single cylinder, irrespective of the distance between the two cylinders, i.e. resonance between flow and structure and hence large amplitudes of excitation.

CHAPTER 6

THREE-DIMENSIONAL (3D) VALIDATION CASES ON STATIONARY AND FORCED VIBRATION OF A CYLINDER

In this chapter, the present immersed boundary methodology is extended to three dimensional studies, implanting the newly developed modules into a three-dimensional Large-eddy simulation (LES) method. Two high Re FSI flows are investigated: the first case is a stationary cylinder flow at $Re_D = 3900$ for which extensive laboratory and numerical simulation data is available. This allows validating the LES method. The second case is a one-way coupled fluid structure interaction flow, here with prescribed motion of the cylinder at small oscillation amplitude ($A = 0.2D$) and at frequencies which are close to the frequency of the vortex shedding frequency of the stationary flow. The robustness, accuracy and applicability of the method for high-Re number flows and VIV is demonstrated by comparing the turbulence statistics of the two cases and by discussing differences in the mean and instantaneous flows.

6.1 Large-Eddy Simulation (LES) of the Flow over a Circular Cylinder at Reynolds Number 3900

A numerical simulation is performed for a sub-critical circular cylinder flow at Reynolds number $Re_D = 3900$. This flow is well-documented in the literature. Experimental and numerical results are used for comparison for this sub-critical regime. In particular, experimental results for this test case disclose important flow features such

as velocity, vorticity and higher order turbulence statistics. In addition, other important features such as forces, wake dynamics, separation angle and recirculation length are also acquired through the experimental studies. All of those important flow features allow accurate assessment of numerical results in terms of qualitative and quantitative comparisons.

Pioneering experimental work was done by Lourenco and Shih (1993) who managed to accurately measure velocity fields and their fluctuations in the recirculation region behind the cylinder using the techniques of particle image velocimetry (PIV). Those results are often used as a reference for validation of numerical studies in the literature (Beaudan and Moin (1994); Breuer (1998); Kravchenko and Moin (2000); Lysenko et al. (2012); Meyer et al. (2010); Mittal and Moin (1997)). Ong and Wallace (1996) successfully measured velocity and vorticity vectors in the near wake outside the recirculation region and introduced turbulence statistics at several locations. Data of mean pressure measurements at the surface of the cylinder is also available for comparison. Norberg (1994) provided mean pressure data at the surface of a cylinder at $Re_D = 4020$. The pressure data of Norberg (1994) provide the only experimental surface pressure measurements known in the literature. In addition, the Particle-Image Velocimetry (PIV) data of Parnaudeau et al. (2008) is also used for comparisons by researchers in terms of numerical validations Lysenko et al. (2012); Meyer et al. (2010).

As discussed, the flow over a circular cylinder at $Re = 3900$ based on the cylinder diameter D is a well-known test case in LES. At this Reynolds number, a laminar shear layer forms and separates from the boundary of the structure and then undergoes transition in the near wake of the cylinder. Therefore, the flow physics should be formed correctly

in order to predict the separation of shear layers. In addition, the grid resolution should be sufficient enough to capture the turbulence phenomena in the transition and turbulent wake region.

The computational domain in the X-Y plane is shown in Figure 6-1, which has dimensions of $48D$ in streamwise direction (X), $24D$ in the transverse direction (Y). A zoom-in plot of the grid near the cylinder is also shown in Figure 6-2. The spanwise domain length used in this simulation is $4D$. The structure is located at a distance of $15D$ from the upstream end of the domain. Symmetric boundary conditions are applied at the north and south sides of the domain; periodicity (since the cylinder is infinitely long) is assumed in spanwise direction. At the inlet, a uniform velocity is prescribed and at the outlet a convective boundary condition is employed. The computational grid used in the simulation consists of approximately 17.6 million grid points. The flow is parallelized with 64 AMD processors. In the vicinity of the cylinder, the computational grid is fine with 110 points over its diameter with grid spacing of $0.009D$ and then it gets coarse further away from it. The grid has a homogenous spanwise resolution of $0.0625D$. The resolution used near the cylinder in this simulation is slightly coarser than other numerical studies which employ both a Curvilinear and Cartesian grids. For instance, Meyer et al. (2010) utilized a grid spacing of $0.0025D$ for both of the grids. The LES of Franke and Frank (2002) use similar grid resolution to resolve the viscous sublayer at the cylinder.

A second order accurate Central Differencing Scheme (CDS) is used for the discretization in space. For the time advancement, Adams-Bashfort (AB) for convection and second order accurate Crank-Nicholson (CN) for diffusion is implemented.

Computations are carried out with a CFL number of 0.2. Finally, all calculations are conducted using Large Eddy Simulation (LES). The WALE model (Nicoud and Ducros (1999)) is employed to compute SGS stresses and to close the filtered Navier-Stokes equations. Its advantage lies in the fact that it does not require near wall damping and hence makes it an ideal candidate for immersed boundary LES, in which the solid boundary is not sharply defined as in cut-cell immersed boundary methods which are discussed in Chapter 2.

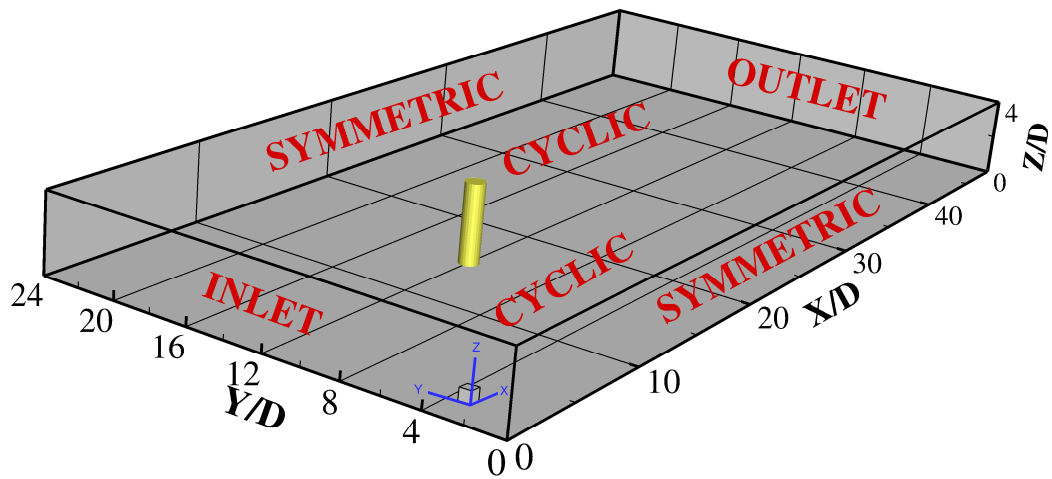


Figure 6-1 Computational setup and boundary conditions for the flow over a circular cylinder at $Re = 3900$.

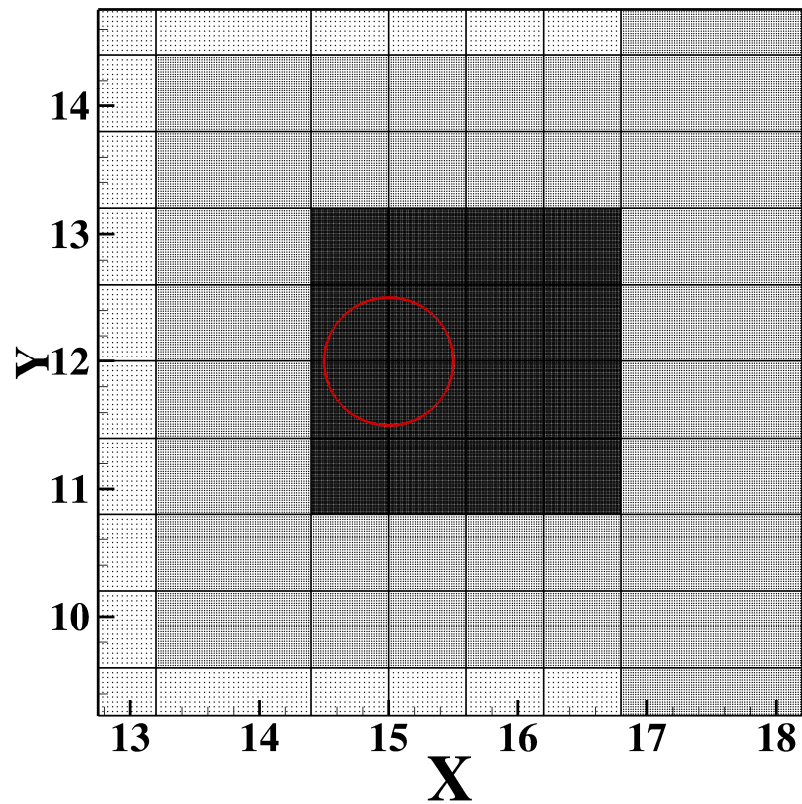
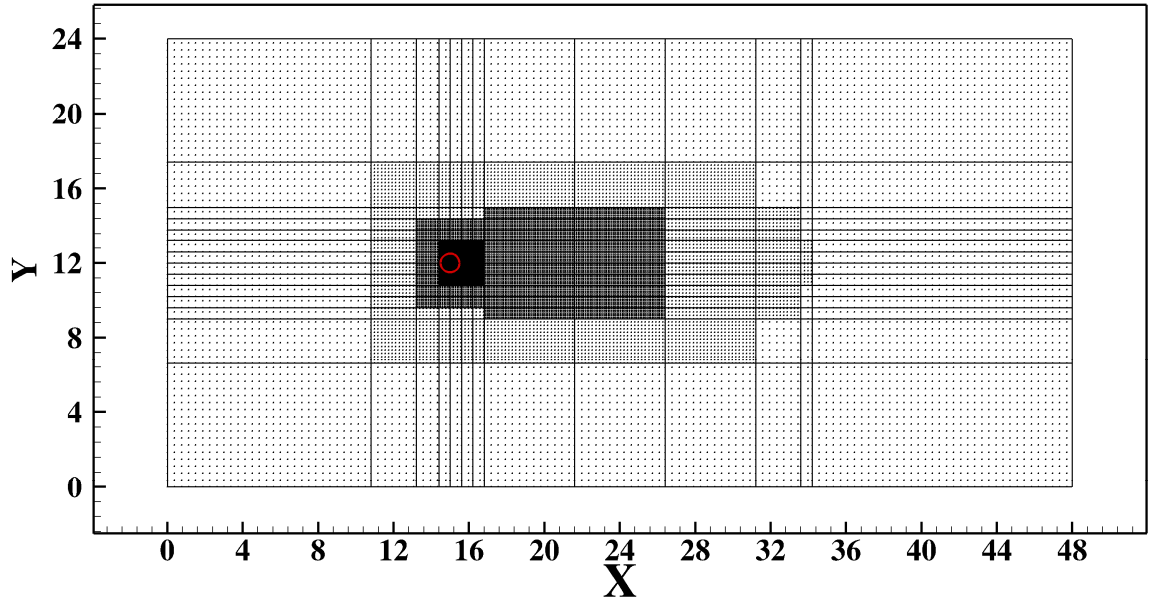


Figure 6-2 Top: Cross-sectional (X-Y plane) grid employed with Local Mesh Refinement (LMR) (every fifth computational cell of a locally-refined Cartesian grid is shown) for the flow over a circular cylinder at $Re = 3900$; Bottom: zoom into the cylinder region.

In the following paragraphs, a quantitative validation of the present results for flow over a cylinder at $Re=3900$ is presented and comparisons are being made with respect to experimental results. To do so, turbulence statistics are sampled after steady vortex shedding is established. The results are compared with pressure measurements of Norberg (1994), the Particle-Image Velocimetry (PIV) data of Lysenko et al. (2012) (both of them are extracted from Meyer et al. (2010)), the hot-wire measurements of Ong and Wallace (1996) and the PIV data of Parnaudeau et al. (2008).

The length of the recirculation region (L_r) behind the cylinder is compared with existing numerical and experimental studies. It is defined as the distance between the base of the cylinder and the sign change of centerline mean streamwise velocity. The quality of L_r may be affected earlier laminar-turbulence transition in the separating shear layers of the experiment (Kravchenko and Moin (2000)). In the present LES, the recirculation zone length is predicted by WALE model as $L_r/D = 0.85$ which is in fairly good agreement with the data of Lourenco and Shih (1993) ($L_r/D = 0.9$). PIV by Parnaudeau et al. (2008) who recently reported a sensitivity analysis of recirculation bubble with respect to the averaging time interval produces a more extended recirculation zone length with $L_r/D = 1.67$. The predicted recirculation zone in the present study is evident in Figure 6-3 where the time averaged streamlines from the present simulation with numerical studies of Breuer (1998) are also shown.

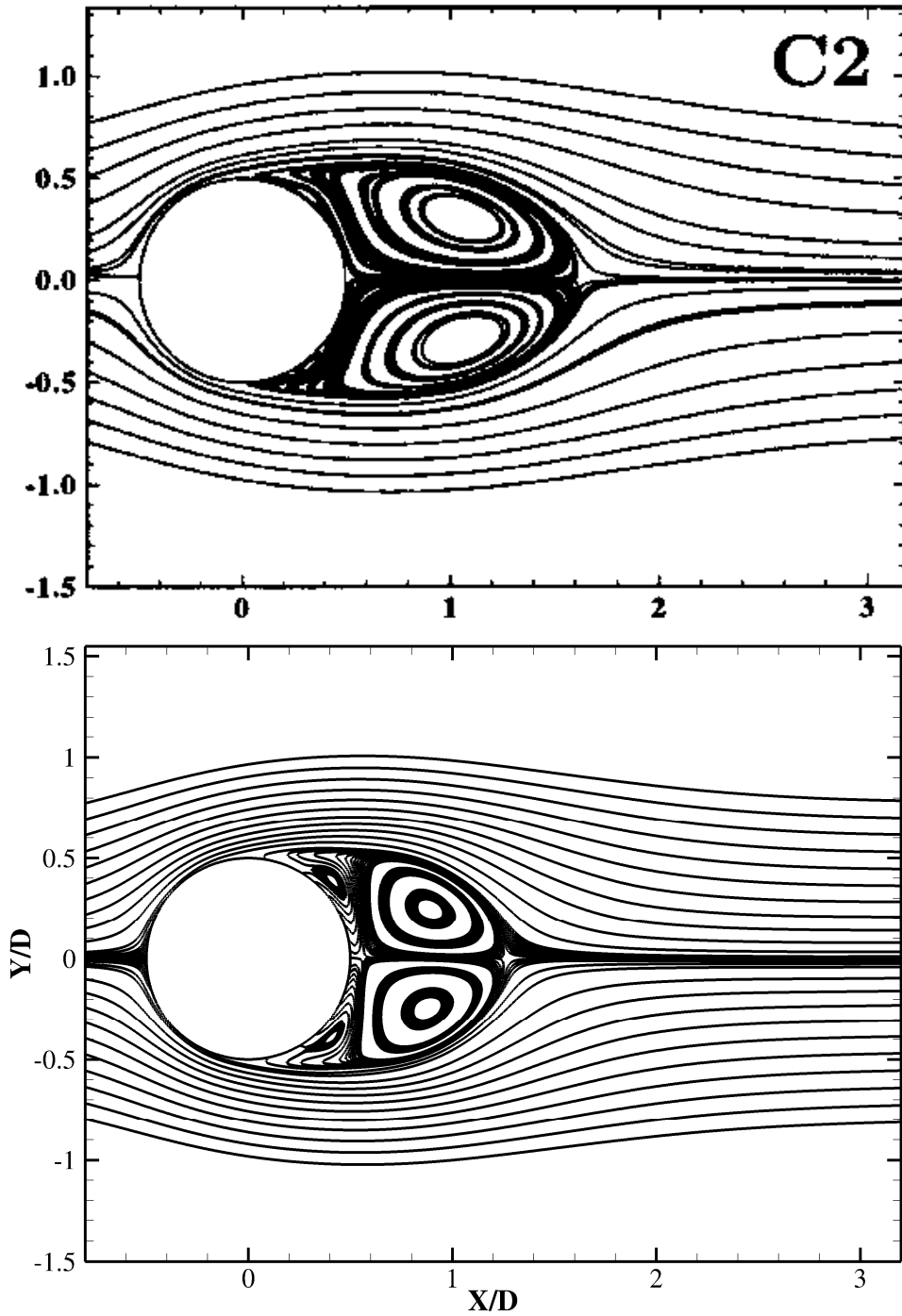


Figure 6-3 Streamlines showing recirculation region behind the cylinder at $Re = 3900$; the top and bottom figures correspond to LES results of Breuer (1998) and present numerical method, respectively

Figure 6-4 demonstrates the time histories of the present lift (C_L) and drag (C_D) coefficients for the current LES run with WALE model. The drag and lift coefficients per unit length are calculated as $C_D = 2 F_x / (\rho U_\infty^2 D)$ and $C_L = 2 F_y / (\rho U_\infty^2 D)$, where F_x and F_y are the forces acting in the streamwise and transverse directions at the boundary of the structure, respectively (See Appendix A for force calculations). Figure 6-4 also includes time history results of drag and lift force coefficients from Breuer (1998) who utilized a Dynamic model in the LES. It can be noted that the overall behavior of force components in the present results are comparable with respect to Breuer (1998) in terms of the magnitudes and the irregularity of the forces. The latter may be explained by the irregular three-dimensional break-up of the vortices which are formed around the boundary of the structure (Lysenko et al. (2012)).

Table 6-1 shows flow parameters collected from available experimental and reference numerical (LES) results. The mean drag coefficient $\overline{C_D} = 1.1$ by WALE model is in good agreement with results of Lysenko et al. (2012). On the other hand, it is noticeable in Table 6-1 that most of the values of the drag coefficient obtained in other research are slightly lower ($\overline{C_D} = 0.99 - 1.07$). The root mean square value of time variation of the lift forces which is predicted by WALE model is $(C_L)_{rms} = 0.39$. This value is under predicted by Lysenko et al. (2012) who calculated $(C_L)_{rms}$ equal to 0.44. $St = 0.21$ computed in this study is in good agreement with the available experimental and numerical studies as seen in Table 6-1.

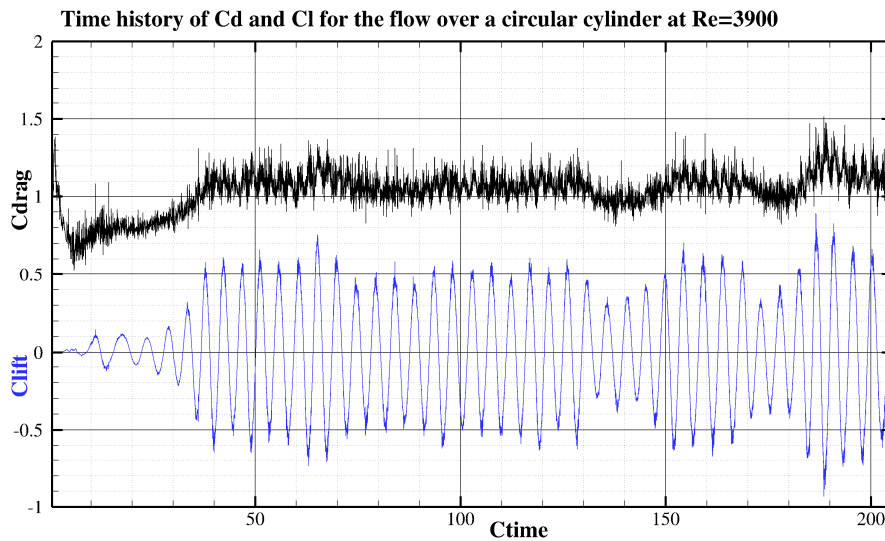
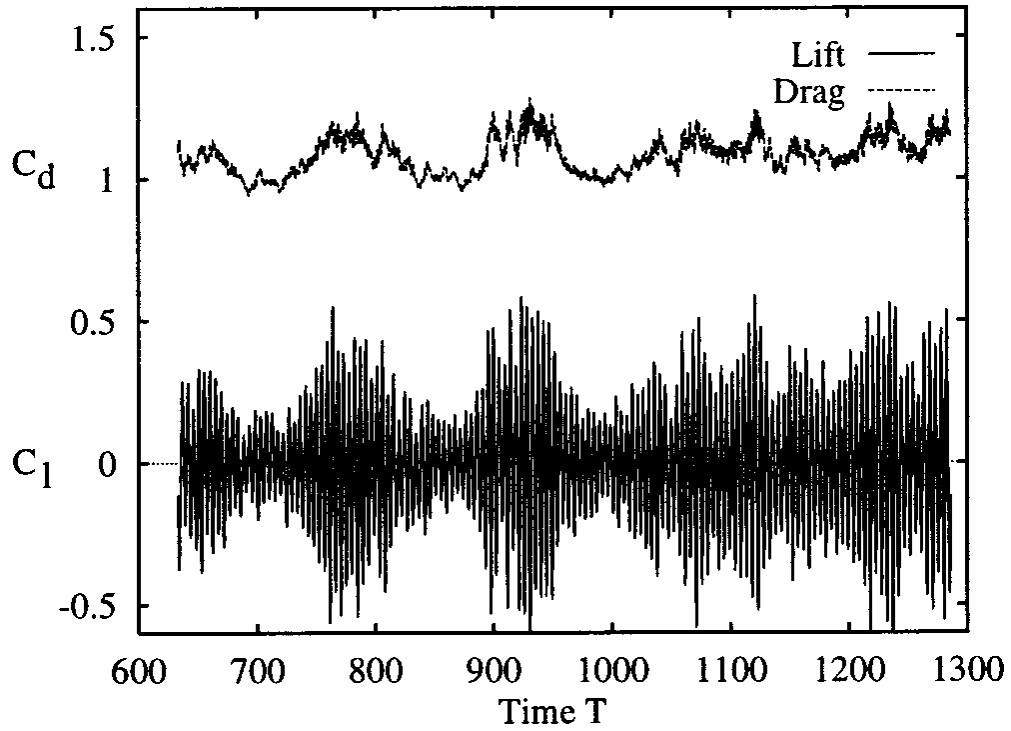


Figure 6-4 Time history of the lift coefficient C_L and drag coefficient C_D for the flow past a circular cylinder at $Re = 3900$. Top: Results of Breuer (1998). Bottom: Results from present computation.

Table 6-1 Comparison of flow parameters of the experimental and LES studies for flow around circular cylinder at $Re = 3900$

Authors	Method	\bar{C}_D	$(C_L)_{rms}$	St	Lr/D
Lourenco and Shih (1993)	EXP	0.99	-	0.22	1.19
Norberg (1994)	EXP	0.98	0.04-0.15	-	-
Breuer (1998)	LES	1.02	-	0.22	1.37
Kravchenko and Moin (2000)	LES	1.04	-	0.21	1.35
Parnaudeau et al. (2008)	LES	-	-	0.21	1.56
Meyer et al. (2010)	LES	1.07	-	0.21	0.83
Lysenko et al. (2012)	LES	1.18	0.44	0.19	0.90
Present	LES	1.10	0.39	0.21	0.85

The instantaneous streamwise, transverse and spanwise velocity fields in the wake of the circular cylinder through a center plane are shown in Figure 6-5. An unsteady recirculation region is evident for the instantaneous streamwise velocity in this figure. Alternating positive and negative regions of instantaneous cross-flow velocity that correspond to Karman vortices can be observed clearly in Figure 6-5. This figure shows that the wake becomes highly turbulent and three dimensional due to presence of both large and small coherent structures in the wake. It is also observed in this figure through the instantaneous spanwise velocity that flow structures increase in size as further towards the downstream of the cylinder. There are formations of small scale fluctuations even ten diameters downstream. Similar observations are also made by Kravchenko and Moin (2000) at this Reynolds number and Moser et al. (1998) at $Re = 2000$.

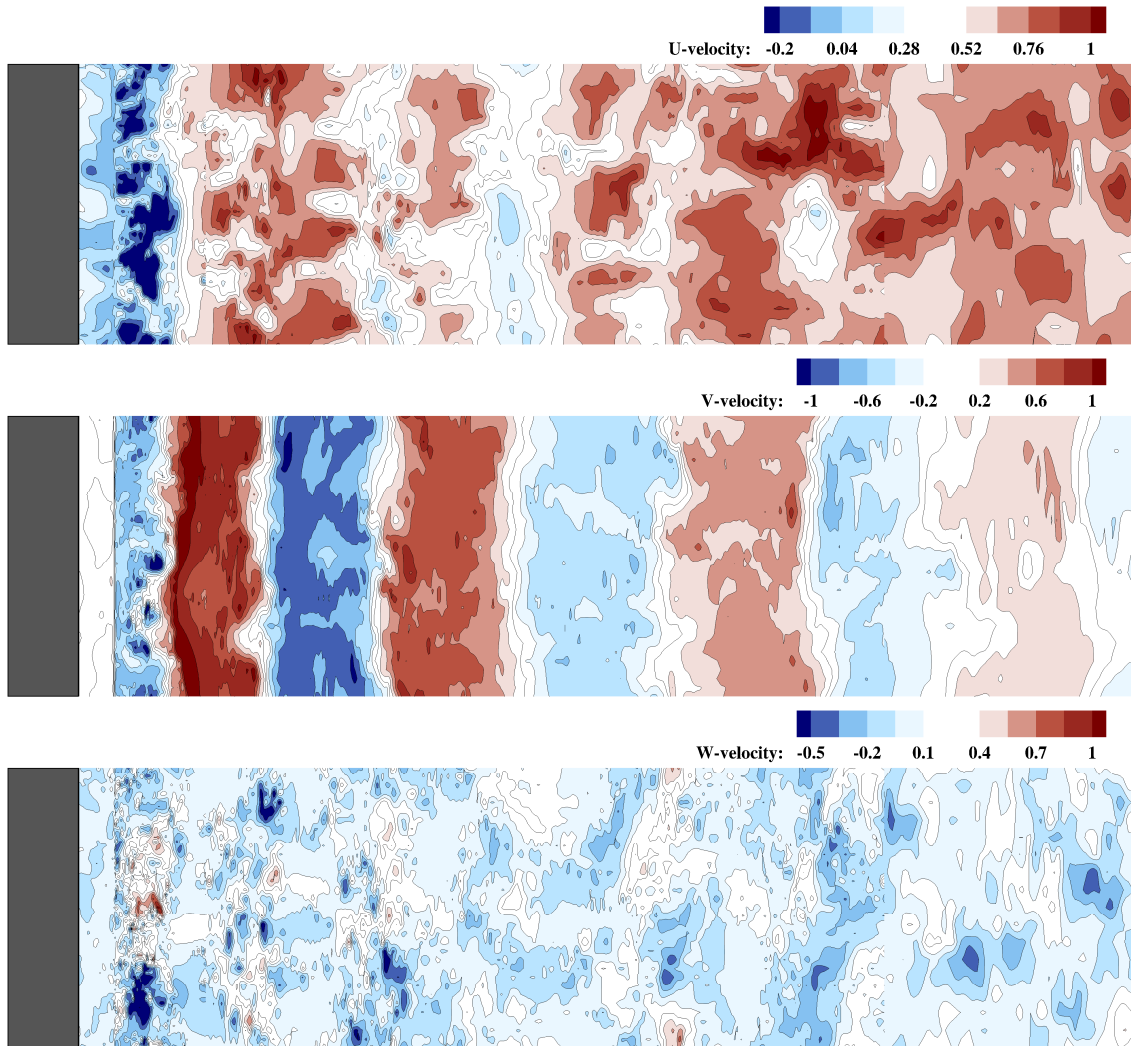


Figure 6-5 Instantaneous velocities in the $(x-z, y=0)$ plane in the wake of a circular cylinder at $Re_D = 3900$. Top: (Color) Instantaneous streamwise velocity with contours from -0.2 to 1.0. Middle: (Color) Instantaneous cross-flow velocity with contours from -1.0 to 1.0. Bottom: (Color) Instantaneous spanwise velocity with contours from -0.5 to 1.0.

Figure 6-6 shows iso-surfaces of vortex structures in the wake of the cylinder using a parameter called the “Q-criterion” JCR et al. (1988). It is defined as $Q=0.5(\|\Omega\| - \|S\|)^2$ where $\|\Omega\|$ is the vorticity tensor and $\|S\|$ is the rate of strain tensor. “Q-criterion” identifies vortex structures and provides a good representation of them through visualization. The turbulent nature of the flow comprising of complex three dimensional vertical structures is clearly visible in this figure. Figure 6-6 also includes results of Lysenko et al. (2012) with TKE and Smagorinsky models via λ_2 criterion which is defined by Jeong and Hussain (1995). In this figure, the transition from a two-dimensional to a three-dimensional flow can be seen very close to the boundary of the structure. Lysenko et al. (2012) explains this observation trend to affect the drag and lift forces.

Figure 6-7 shows an iso-surface of the fluctuating pressure $p' = 2 (p - \langle p \rangle) / \rho_\infty U_\infty^2$ and thus, the formation of the vortices downstream of the circular cylinder. This iso-surface demonstrates the vortex cores originating from the upper and lower parts of the cylinder. It is observed that the vortex cores are parallel to the cylinder axis and the formation continues towards the downstream of the cylinder. Lysenko et al. (2012) explains the convection of vortices as a result of mean flow.

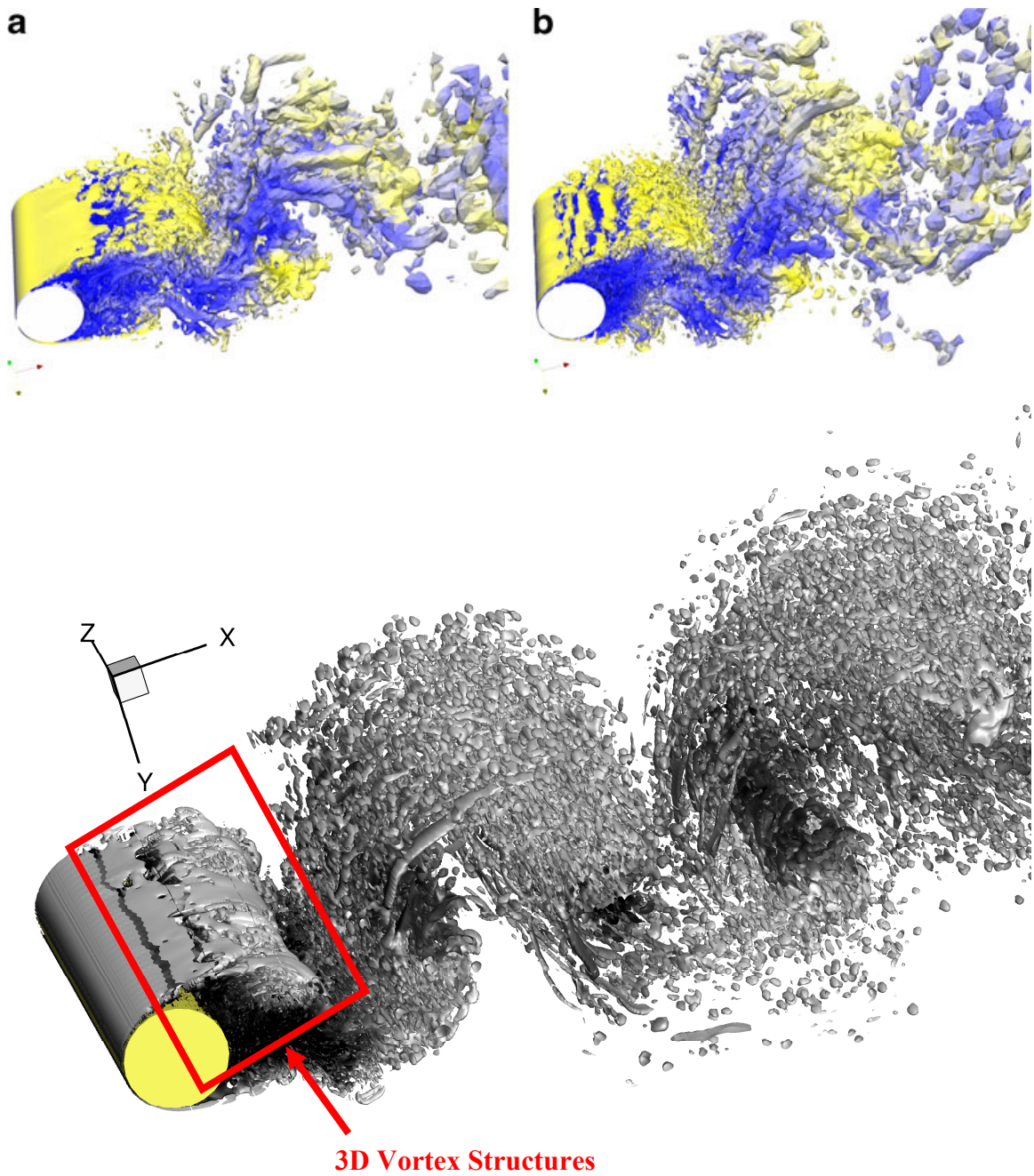


Figure 6-6 Iso-surfaces in the wake of a circular cylinder at $Re_D = 3900$. Top: Iso-surface of normalized $\lambda_2 = 0.004$ obtained by Lysenko et al. (2012) via models (a) TKE b) SMAG. Bottom: Iso-surface of Q-criterion through present method with WALE model.

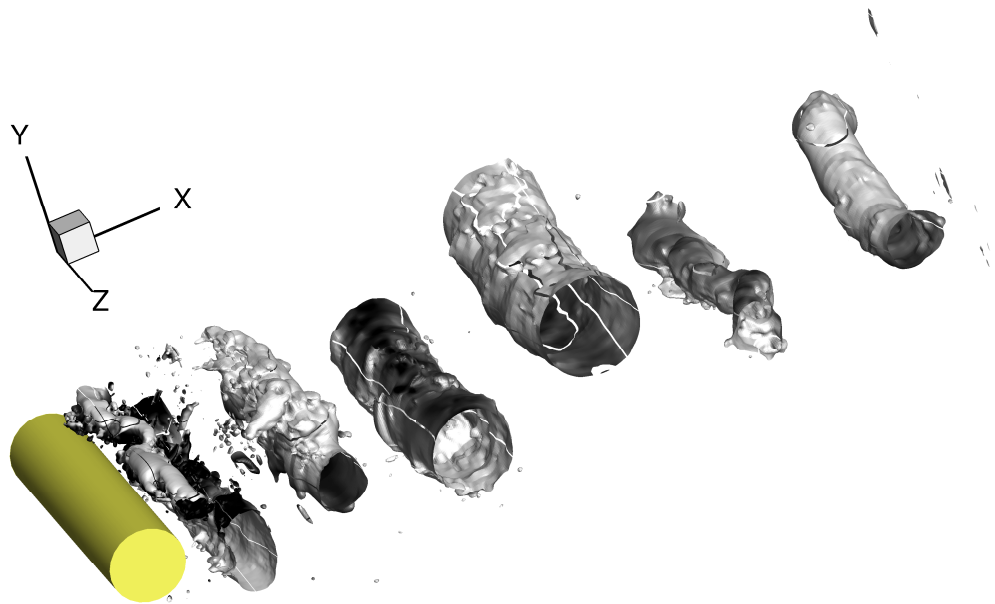


Figure 6-7 Iso-surface of the fluctuating pressure at $p' = -0.1$ (WALE) for the flow over a circular cylinder at $Re = 3900$.

Contours of instantaneous vorticity magnitude are shown in Figure 6-8. It is noticed that two long shear layers separate from the boundary of the cylinder and a Karman vortex street is formed in the wake. According to observations of PIV experiments of Chyu and Rockwell (1996) and numerical results of Kravchenko and Moin (2000), the instability of shear layers result in vortices which mix in the near wake of Karman vortices before they propagate towards downstream. Similar observations are also seen in Figure 6-8.

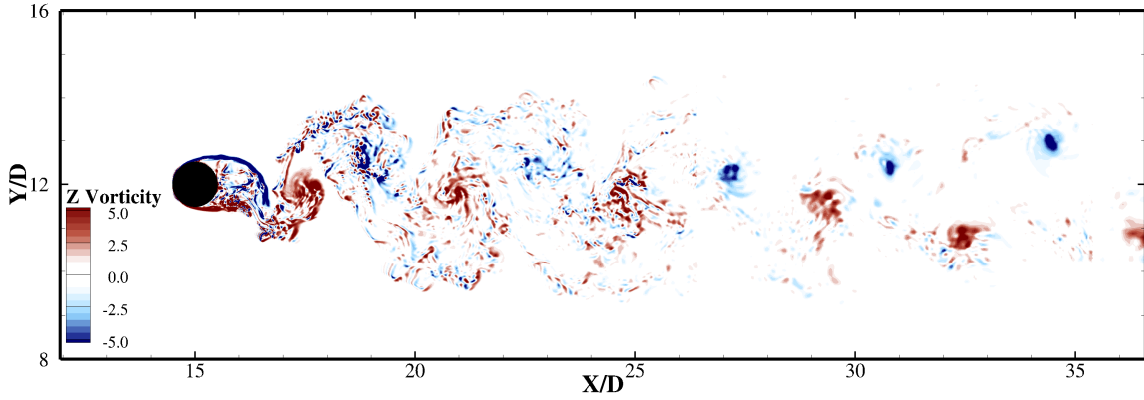


Figure 6-8 Separating shear layers and development of Karman vortex street in the flow over a circular cylinder at $Re = 3900$. Shown are contours of instantaneous vorticity from $\omega D/U_\infty = 5.0$ to $\omega D/U_\infty = -5.0$.

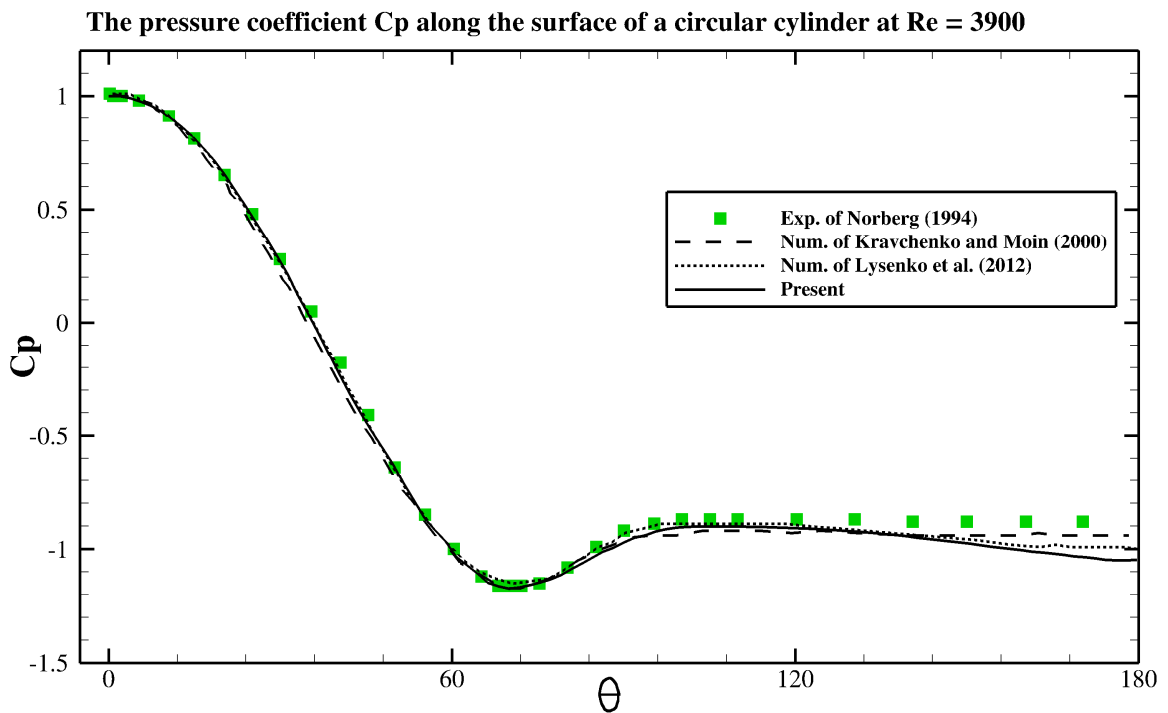


Figure 6-9 The pressure coefficient C_p along the surface of a circular cylinder at $Re = 3900$ ($\theta = 0^\circ$ in the stagnation point, \square experimental data of Norberg (1994) at $Re = 4020$, published in Meyer et al. (2010), - - numerical results of Kravchenko and Moin (2000), ... numerical results of Lysenko et al. (2012), —Present results).

The pressure coefficient can be written as $C_p = 2 (p - p_\infty) / \rho U_\infty^2$ where p_∞ is the time-averaged pressure at the inlet plane and known as the reference pressure. The distribution of C_p along the circumference of the cylinder of the present LES is shown in Figure 6-9. Simulated pressure values agree well with the experimental data of Norberg (1994). Figure 6-9 also includes numerical results of Kravchenko and Moin (2000); Lysenko et al. (2012) which show a similar distribution of C_p as the current simulation.

The mean streamwise velocity along the centerline is shown in Figure 6-10. It is evident that the experiments are quite different from each other. It is also clear that the recirculation length in the experiments of Lourenco and Shih (1993) is shorter than that of Parnaudeau et al. (2008). The present calculations on a Cartesian grid shows an excellent agreement with the experimental results of Lourenco and Shih (1993) close to the boundary of the structure. However, present results do not match up well in the wake. It is noted that a higher grid resolution than the present one can improve the current results in that region. Interestingly, the dip at $X/D = 3.0$ of the experiments of Lourenco and Shih (1993) was not reproduced by experiments of Parnaudeau et al. (2008) and other numerical studies (Breuer, 1998; Kravchenko and Moin, 2000; Lysenko et al., 2012; Meyer et al., 2010) in the literature.

As seen in Figure 6-10, the present calculations are found to be close to the PIV measurements of Lourenco and Shih (1993). Therefore, Figures 6-11 to 6-14 include the statistics for the very near wake of the cylinder compared to experiments of Lourenco and Shih (1993) at three different downstream locations ($X/D = 1.06, 1.54, 2.02$). Figure 6-11 shows mean streamwise velocity $\langle u \rangle / U_\infty$ at different locations including very close to cylinder at $X/D = 0.58$, where an excellent match between the LES and the data of

Lourenco and Shih is obtained. The mean velocity profile exhibits a U-shape at that distance while it evolves towards a V-shape further downstream of the structure. The same profiles are also obtained by Kravchenko and Moin (2000); Lysenko et al. (2012) and shown in this figure. At $X/D = 1.06$, the former produces a longer recirculation length while the latter one show a narrower profile which is in agreement with the experiment.

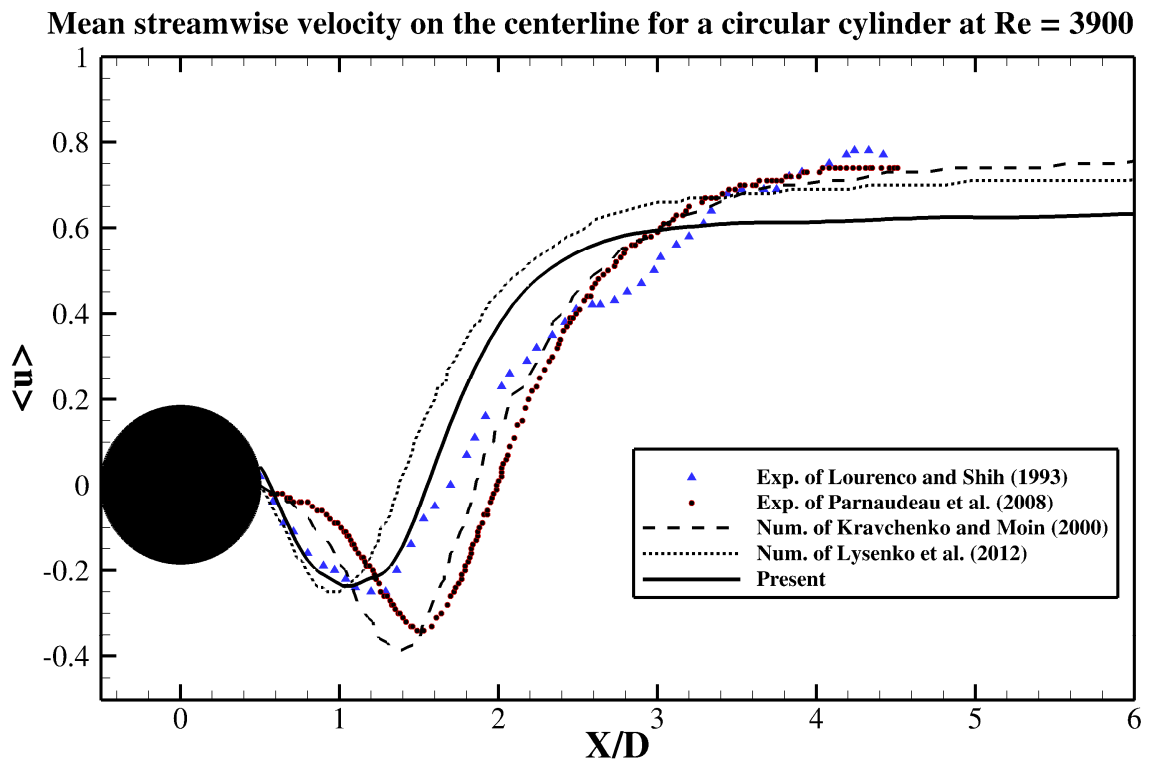


Figure 6-10 Mean streamwise velocity on the centerline of the cylinder for the flow over a circular cylinder at $Re = 3900$ (Δ : experimental data of Lourenco and Shih (extracted from Meyer et al. (2010)), \circ : experimental data of Parnaudeau et al. (2008), - - -: numerical results of Kravchenko and Moin (2000),: numerical results of Lysenko et al. (2012), — Present results).

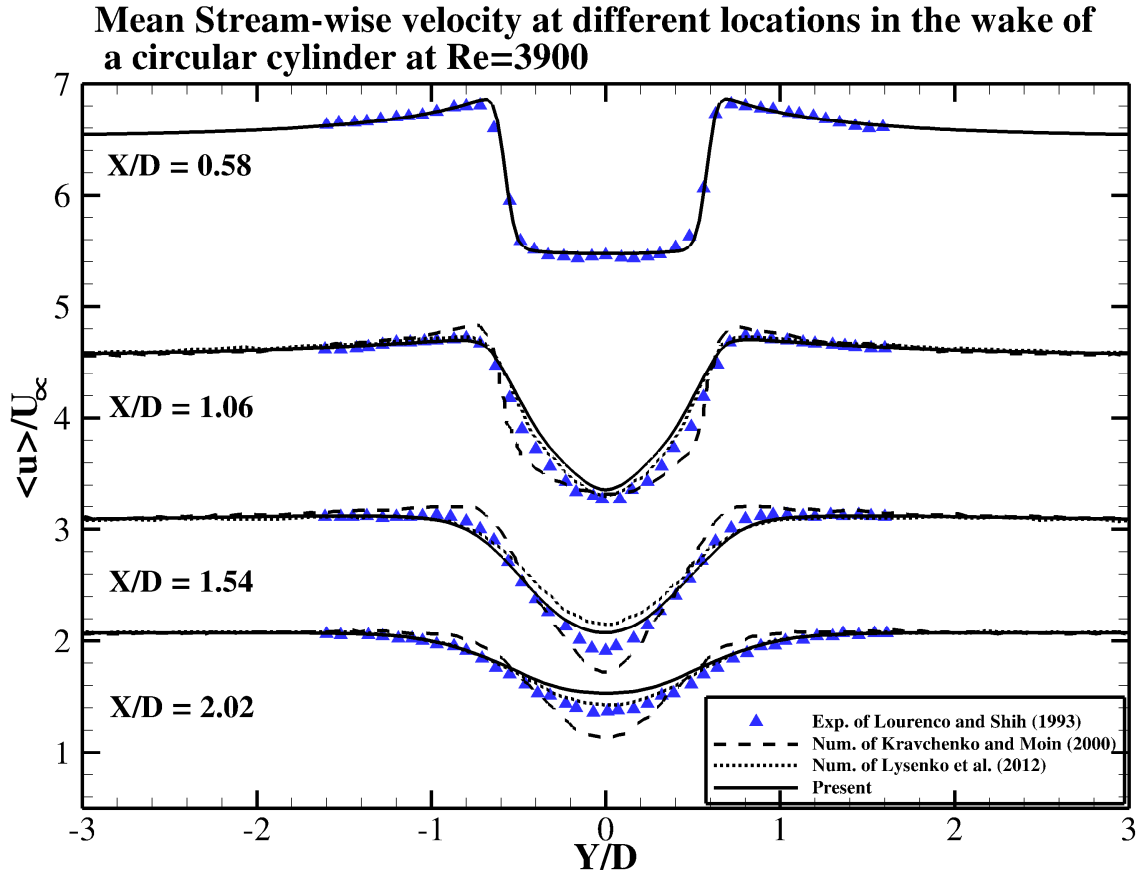


Figure 6-11 Mean streamwise velocity at different locations in the wake of a circular cylinder at $Re = 3900$ (Δ : experimental data of Lourenco and Shih (extracted from Meyer et al. (2010)), - - -: numerical results of Kravchenko and Moin (2000),: numerical results of Lysenko et al. (2012), — Present results).

The results of mean transverse velocity $\langle v \rangle / U_\infty$ are shown in Figure 6-12. It is important to point out that results of Lourenco and Shih (1993) are shifted so that $\langle v \rangle = 0$ is recovered for larger Y/D . The same strategy is also implemented in figures of other researchers in order to compare the statistics of the flow field. In general, the calculations agree better with the experimental data close to the boundary near the wake. Present results at $X/D = 1.06$ estimates the Reynolds stresses well, however, underestimates them towards the far field of the wake at $X/D = 1.54$ and 2.02 .

Mean transverse velocity at different locations in the wake of a circular cylinder at $Re=3900$

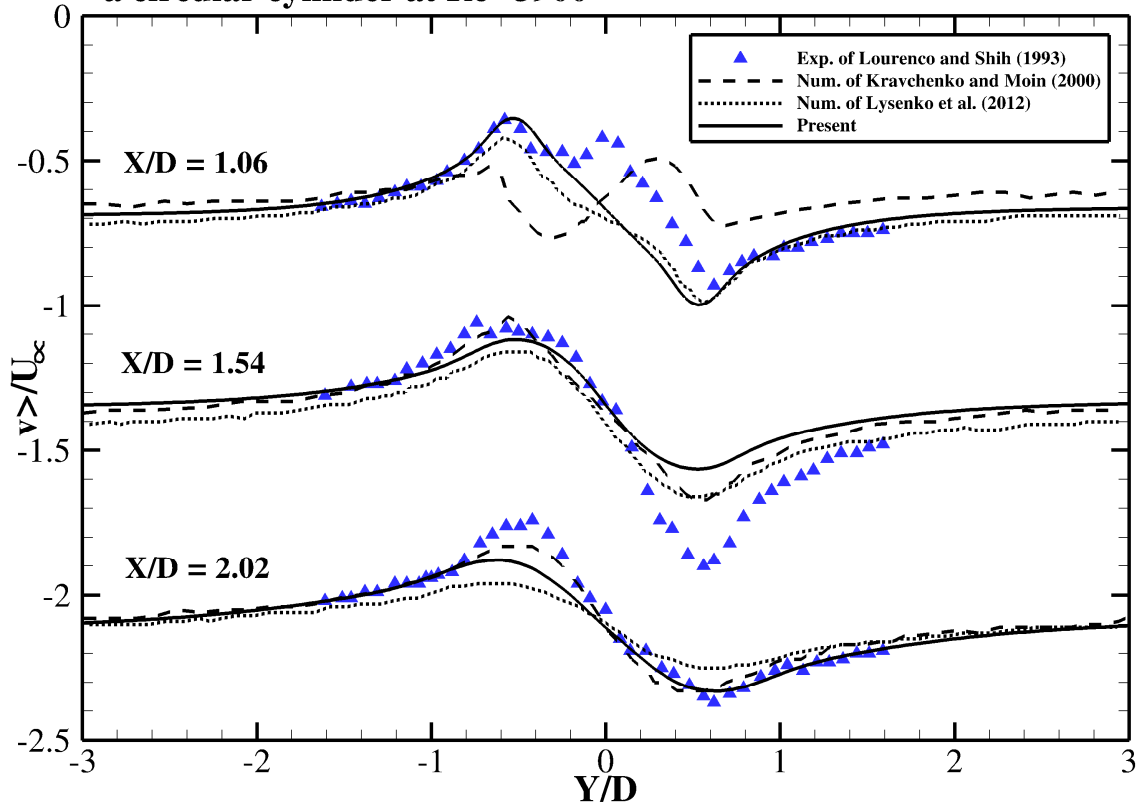


Figure 6-12 Mean transverse velocity at different locations in the wake of a circular cylinder at $Re = 3900$ (Δ : experimental data of Lourenco and Shih (extracted from Meyer et al. (2010)), - - -: numerical results of Kravchenko and Moin (2000),: numerical results of Lysenko et al. (2012), ———Present results.

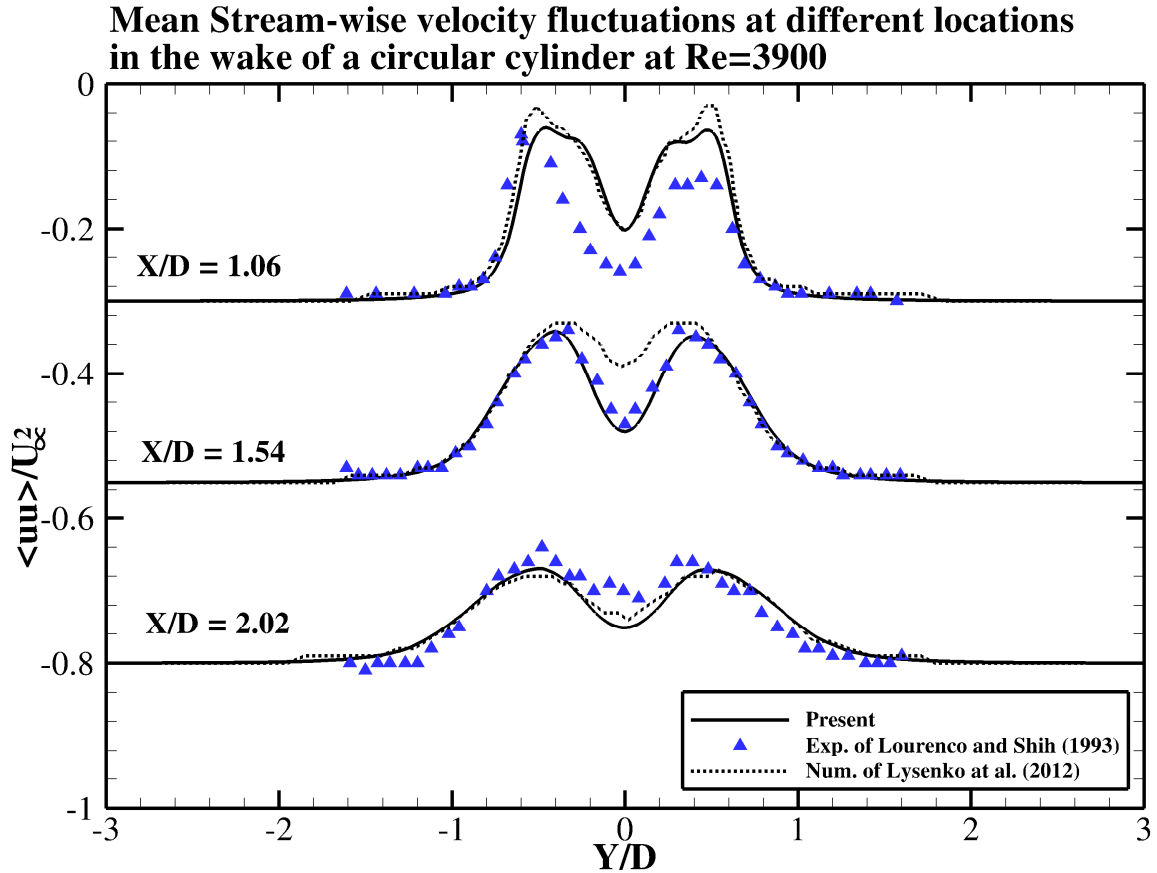


Figure 6-13 Mean streamwise velocity fluctuations at different locations in the wake of a circular cylinder at $Re = 3900$ (Δ : experimental data of Lourenco and Shih (extracted from Meyer et al. (2010)),: numerical results of Lysenko et al. (2012), — Present results).

Reynolds normal stresses, $\langle u'u' \rangle / U_\infty^2$ are shown in Figure 6-13. At $X/D = 1.06$, there appears two sharp peaks which result from the transitional state of shear layers. Meyer et al. (2010) explains that the formation of these peaks show a “*flapping behavior*” due to primary vortex formation. The two peaks are matched in the present results fairly well in position. However, in magnitude, the present LES overestimates with respect to the experiment. Overall, the present results agree well with the experiment and are comparable with the numerical data of Lysenko et al. (2012).

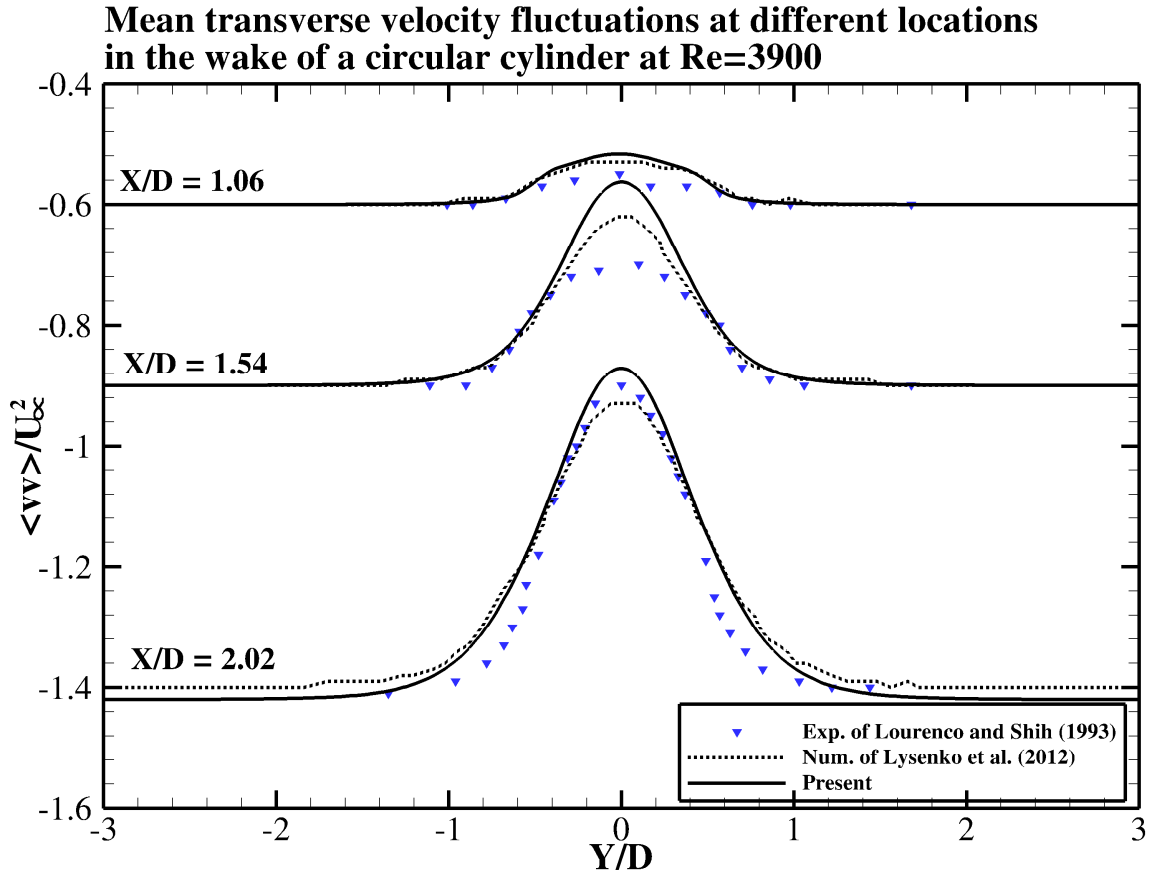


Figure 6-14 Mean transverse velocity fluctuations at different locations in the wake of a circular cylinder at $Re = 3900$ (Δ : experimental data of Lourenco and Shih (extracted from Meyer et al. (2010)),: numerical results of Lysenko et al. (2012), — Present results).

In terms of cross-flow normal Reynolds stresses, $\langle v'v' \rangle / U_\infty^2$, simulation shows reasonable agreement with the experiment as seen in Figure 6-14. However, again, the present results show an overestimation at $X/D = 1.06$ and 1.54 . This may be a result of a relatively coarse mesh being employed in the present simulations as compared to numerical studies in which curvilinear grids are utilized. A shorter length of recirculation bubble produced in the current study may also lead to an overestimation of the results.

Mean Stream-wise velocity at different locations in the wake of a circular cylinder at $Re=3900$

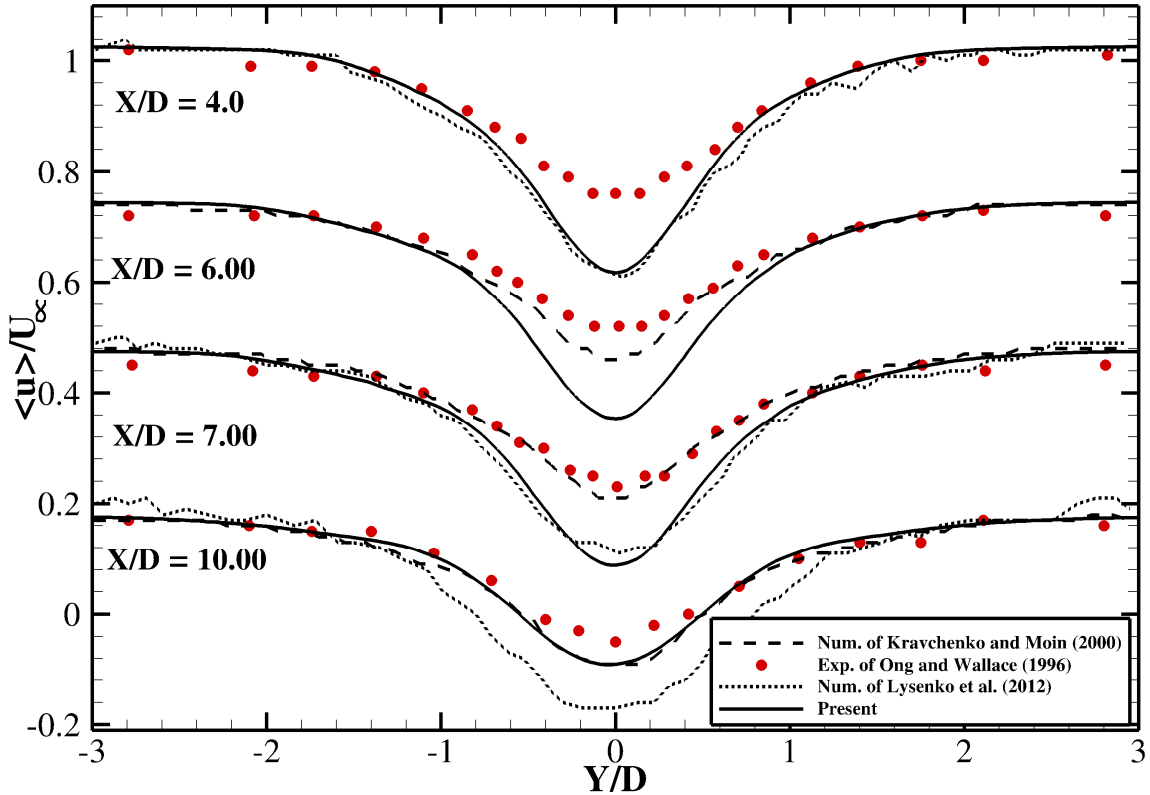


Figure 6-15 Mean streamwise velocity at different locations in the wake of a circular cylinder at $Re = 3900$ (o: experimental data of Ong and Wallace (1996) (extracted from Meyer et al. (2010)), - - -: numerical results of Kravchenko and Moin (2000),: numerical results of Lysenko et al. (2012), ———Present results.

Figures 6-15 to 6-18 compare the statistics for the near wake ($X/D = 4.00, 6.00, 7.00, 10.0$) with the experiments of Ong and Wallace (1996) and numerical results of Lysenko et al. (2012). In this region of the wake, the grid is fairly coarse and it is apparent that the numerical simulation suffers from inaccuracies in estimating the flow field. Figure 6-15 shows the mean streamwise velocity at four different locations near the wake. It can be observed that the recirculation length in the experiment is longer than the one from the present computation. Therefore, the streamwise Reynolds stress calculations

are over predicted in the present numerical simulation with respect to the experimental Reynolds stress as seen in Figure 6-16. This discussion is similar to the simulation results of Kravchenko and Moin (2000); Lysenko et al. (2012); Meyer et al. (2010). The mean streamwise velocity fluctuations and the cross-flow normal stresses are also plotted in Figures 6-17 and 6-18, respectively. There is a slight over prediction of the Reynolds stresses at different locations in the latter one, while present computations agree fairly well with the experiments in the former one.

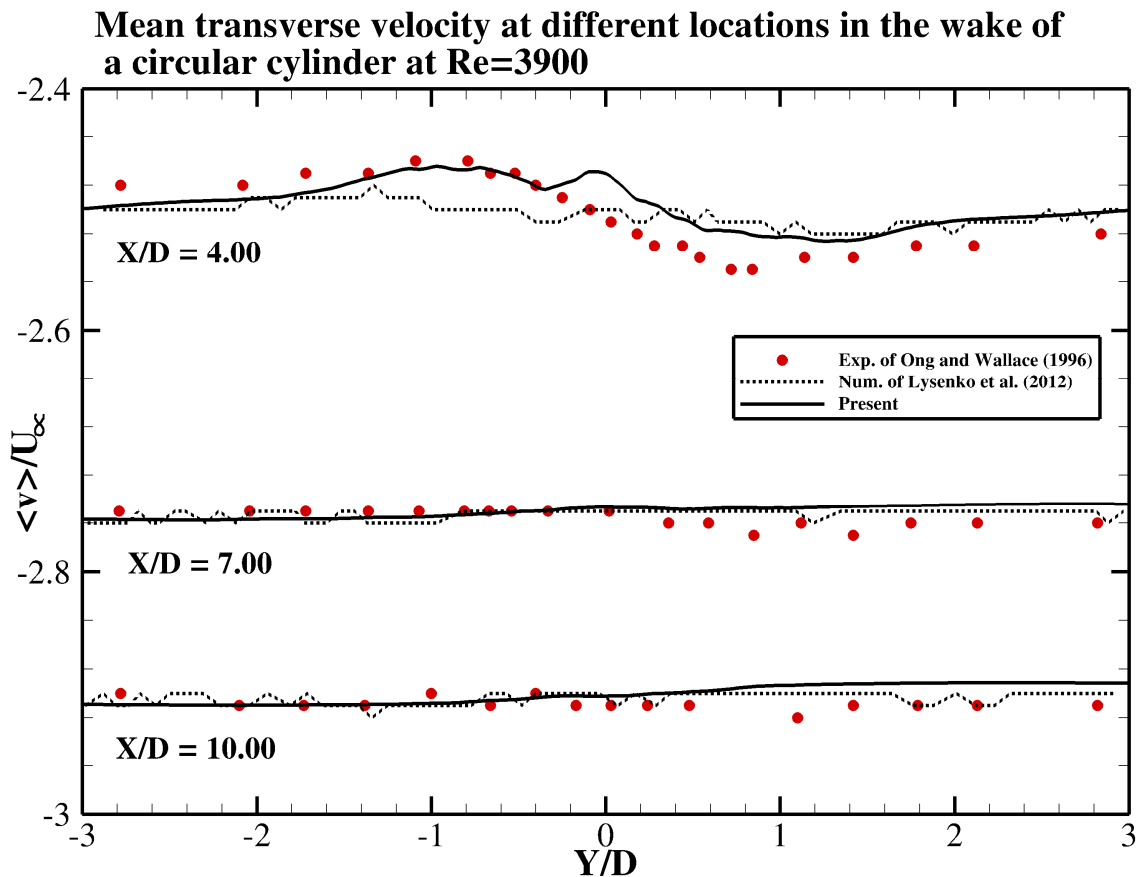


Figure 6-16 Mean transverse velocity at different locations in the wake of a circular cylinder at $Re = 3900$ (o: experimental data of Ong and Wallace (1996) (extracted from Meyer et al. (2010)),: numerical results of Lysenko et al. (2012), ---- Present results).

Mean Stream-wise velocity fluctuations at different locations in the wake of a circular cylinder at $Re=3900$

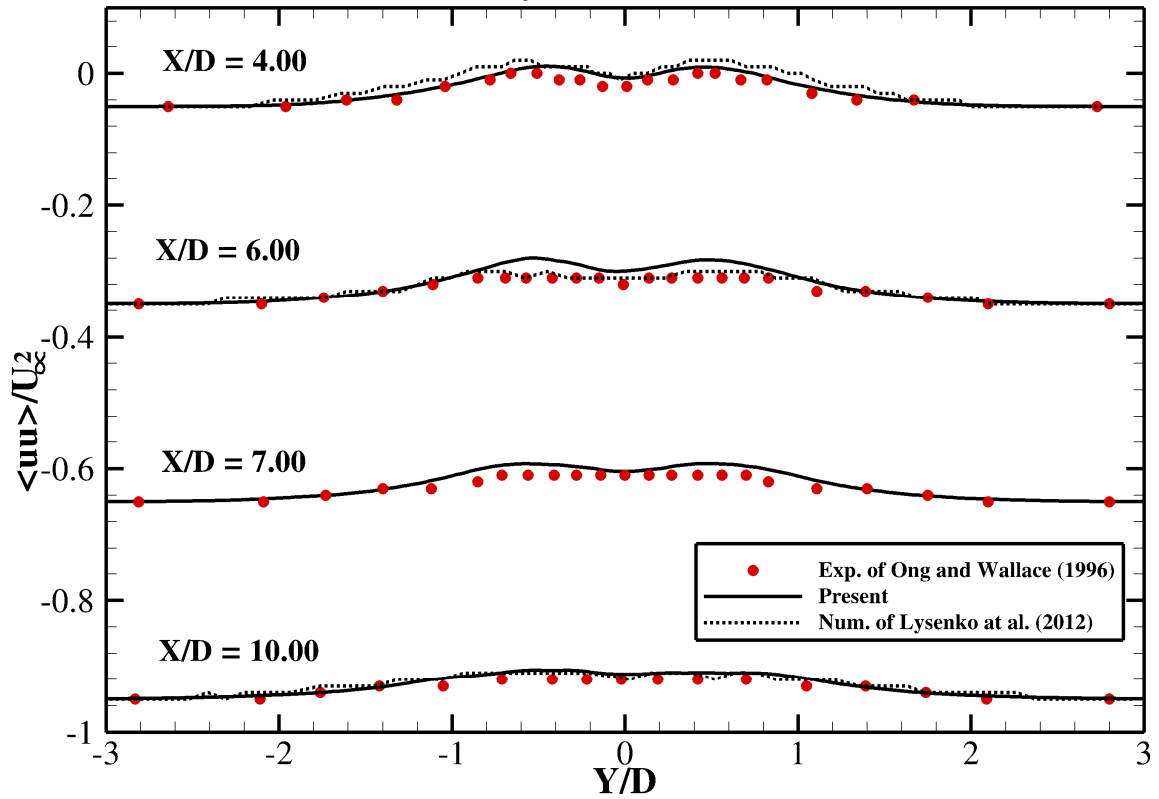


Figure 6-17 Mean streamwise velocity fluctuations at different locations in the wake of a circular cylinder at $Re = 3900$ (o: experimental data of Ong and Wallace (1996) (extracted from Meyer et al. (2010)),: numerical results of Lysenko et al. (2012), ----- Present results.

Mean transverse velocity fluctuations at different locations in the wake of a circular cylinder at $Re=3900$

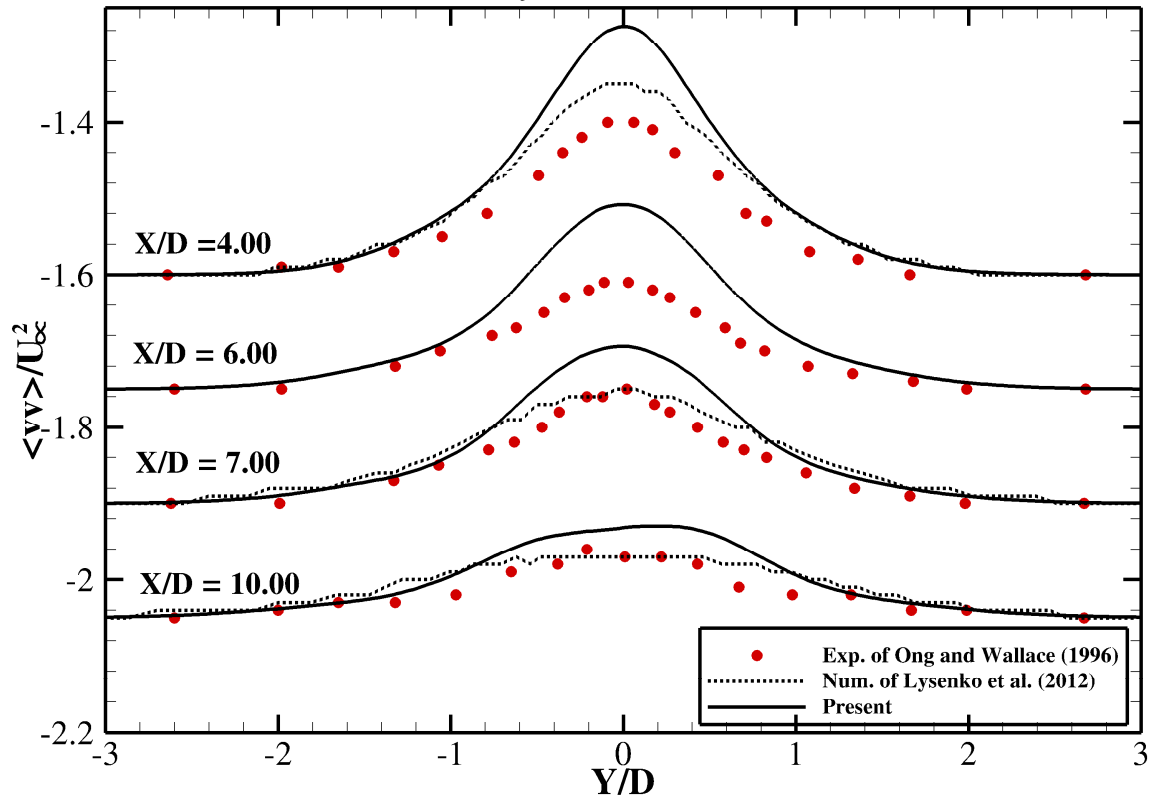


Figure 6-18 Mean transverse velocity fluctuations at different locations in the wake of a circular cylinder at $Re = 3900$ (o: experimental data of Ong and Wallace (1996) (extracted from Meyer et al. (2010)),: numerical results of Lysenko et al. (2012), ----- Present results).

6.2 Large-Eddy Simulation (LES) of the Flow over an Oscillating Circular Cylinder at Reynolds Number 3900

There are only few 3D numerical studies of an oscillating cylinder in a turbulent cross-flow. Blackburn et al. (2001) show that it is required to have three dimensional numerical simulations to capture the structural response correctly. In their study, the flow past a freely vibrating cylinder at $Re = 550$ was carried out. Moreover, that study shows that 2D simulations are inadequate in order to capture the response envelope and the vortex shedding mechanics at higher Re . At $Re = 1000$, Evangelinos et al. (2000) studied the vortex dynamics and flow structures for turbulent flow over rigid and flexible cylinders which are subject to VIV. The DNS results show that as compared to laminar wakes, the structural response amplitude is as much as a cylinder diameter due to three-dimensional effects. At the same Reynolds number, Lucor et al. (2001) considered a long flexible cylinder under two different approach flows including linear shear approach and exponential shear flow profile. Flow past a forced oscillating cylinder at a higher Reynolds number ($Re = 24000$) was conducted by Tutar and Holdo (2000). They observed that the results of the 3D LES using the Smagorinsky model show a better agreement with the experimental results than that of a 2D LES. Dong and Karniadakis (2005) conducted DNS for turbulent flows past a stationary circular cylinder and past a rigid cylinder undergoing forced harmonic oscillations at $Re = 10000$. The 3D numerical results show that comparisons with the available experimental data are captured with reasonable accuracy.

The present section focuses on the flow past a rigid cylinder undergoing forced harmonic oscillations in the cross-flow direction at $Re = 3900$. The reason for choosing this Reynolds number is to compare flow statistical quantities with results of flow past a stationary cylinder case, the data of which are discussed in the previous section. Emphasis is placed on the discussion of the influence of the cylinder oscillation on the physical quantities and the comparison between simulation results and that of the stationary cylinder case at the same Reynolds number. The forced sinusoidal oscillation in the cross-flow direction is chosen from experiments conducted by Gu et al. (1994). In the experimental study, high Reynolds number ($Re=5000$) flow past a transversely oscillating cylinder where the vertical cylinder position varies according to $y_c(t) = -A \cos(2\pi f_o t)$ with maximum amplitude of vibration, $A = 0.2D$ and f_o being the amplitude and the excitation frequency of the oscillation, respectively is considered.

Gu et al. (1994) studied six different configurations, i.e., frequency ratios, $f_o / f_e \in (0.8, 0.9, 1.0, 1.1, 1.12, 1.2)$ where f_e corresponds to the vortex formation frequency from the stationary cylinder. In the present simulation, the oscillation frequency ratio of 0.85 is considered. The reason behind this choice is due to largest-scale vortex in the wake of the cylinder obtained in the locked-in region for an oscillating cylinder at this frequency. Figure 6-19 shows time histories of this prescribed displacement, velocity, and acceleration in flow past an oscillation cylinder at $Re = 3900$ over two periods of oscillation with frequency ratio, $f_o/f_e=0.85$ and maximum amplitude of vibration, $A/D = 0.2$. The same locally refined mesh as in flow past stationary cylinder at $Re = 3900$ case with the same grid resolution and numerical schemes in space and time is used in this case as well. The nondimensional time step is chosen as $\Delta t = 0.8 \times 10^{-3}$.

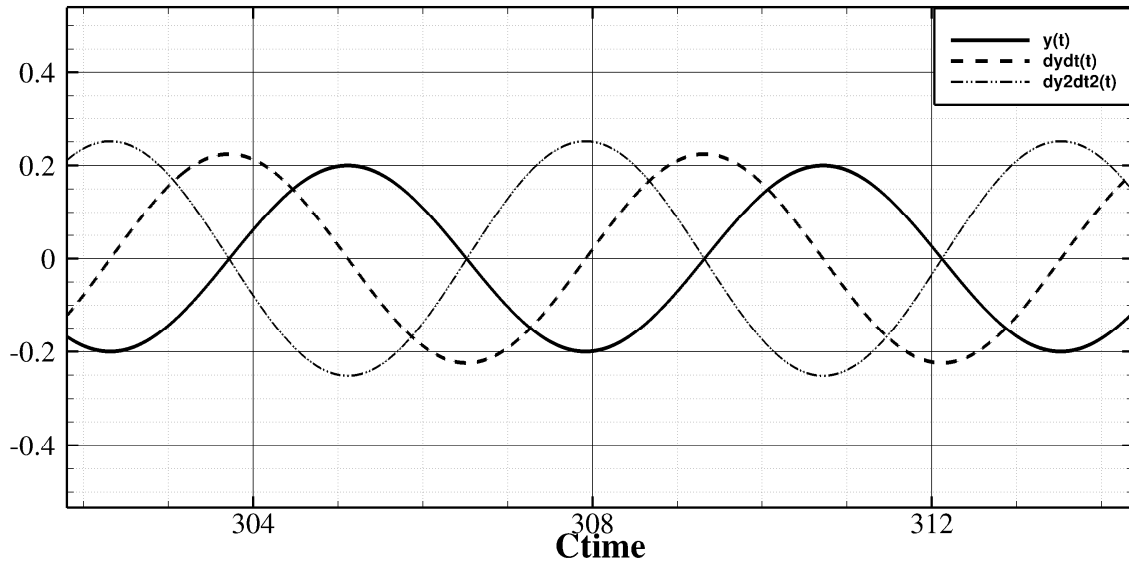


Figure 6-19 Time histories of prescribed displacement, velocity, and acceleration in flow past an oscillation cylinder at $Re = 3900$ over two periods of oscillation with frequency, $f_o D/U_\infty = 0.178$ and maximum amplitude of vibration, $A/D = 0.2$.

In Figure 6-20, the time histories of drag and lift coefficients as a function of the nondimensional time over 50 cycles from the present simulation is plotted. The results of the simulation show that as compared to the stationary cylinder, force coefficients at this Reynolds number, the overall change in the drag coefficient is moderate with only about 5% increase in the magnitude. On the other hand, the lift coefficient shows a dramatic increase (tripled in magnitude) at this oscillation frequency with respect to stationary cylinder case. This can be explained by the contribution of high turbulent inertial effects to force component in transverse direction due to cross-streamwise oscillation of the cylinder.

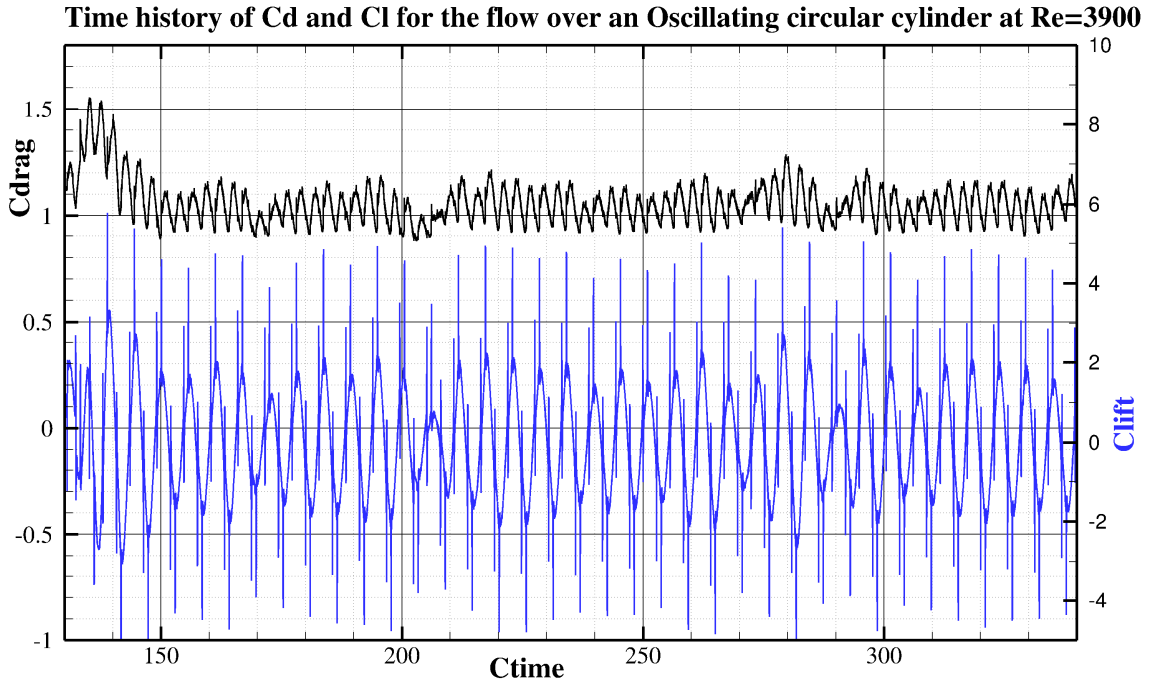


Figure 6-20 Time histories of drag and lift coefficients in flow past an oscillating cylinder at $Re = 3900$ with oscillation frequency, $f_o D/U_\infty = 0.178$ and maximum amplitude of vibration, $A/D = 0.2$.

The instantaneous contours of vorticity at three different Phase angles are shown in Figure 6-21. In this figure, Phase 0° corresponds to cylinder's initial rest position while Phase 270° and 90° designate the maximum positions of the structure at downward and upward directions, respectively. Close to the cylinder, Kelvin-Helmholtz (KH) vortices which are also pronounced in Gu et al. (1994)'s study at the same excitation frequency ratio are evident in these figures. At this locked-in response, similar observations can be made as in Gu et al. (1994) such as center location of the large-scale vorticity both from bottom and top sides of the cylinder is found to be at the same location in all of the Phase angles.

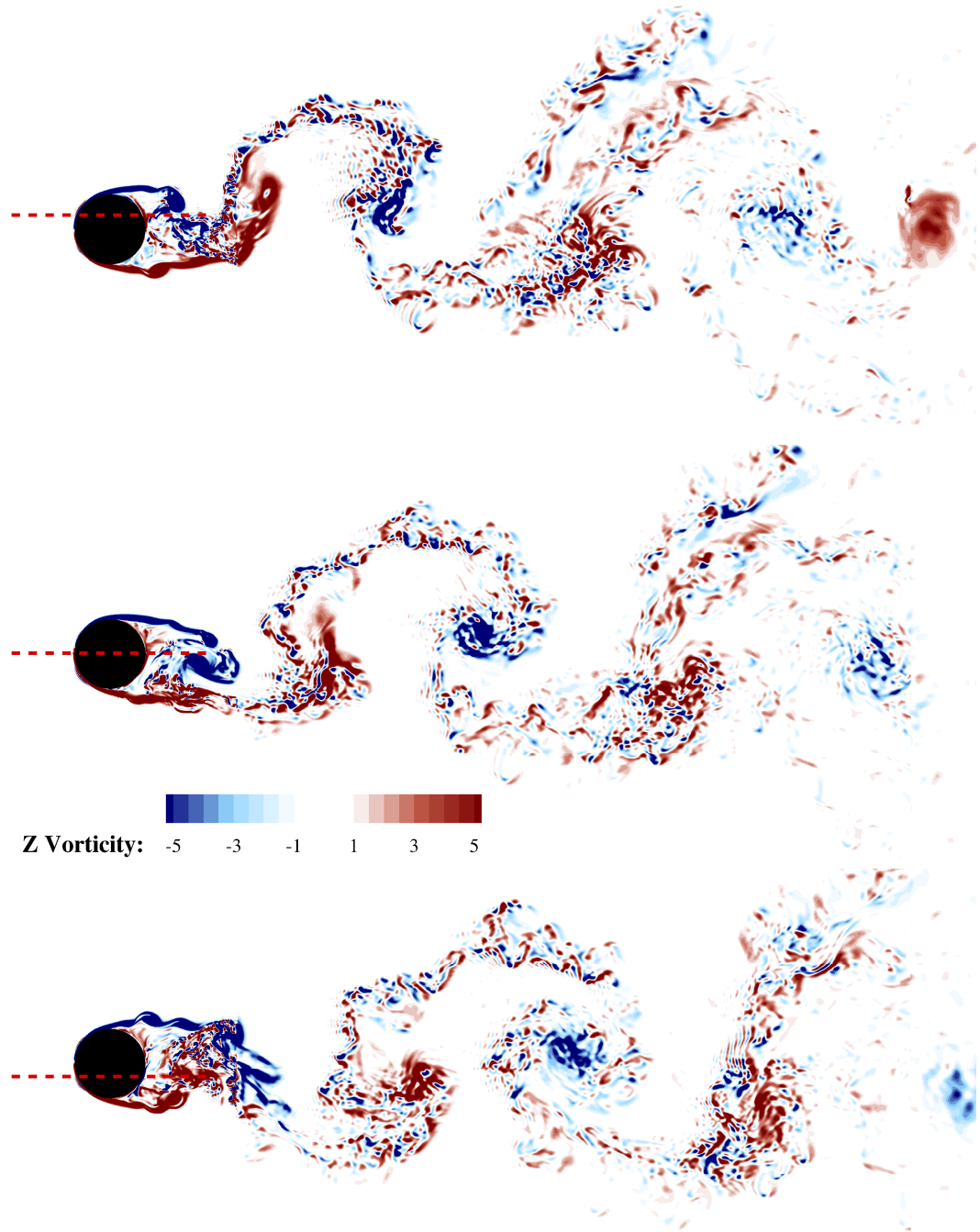


Figure 6-21 Vorticity contours for flow over a transversely oscillating cylinder at $Re = 3900$ with oscillation frequency, $f_o D/U_\infty = 0.178$ and maximum amplitude of vibration, $A/D = 0.2$. The horizontal red dash-dotted lines for the vorticity plots in Phase angles (θ) 270° (Top), 0° (Middle) and 90° (Bottom) indicate the initial rest position of the cylinder.

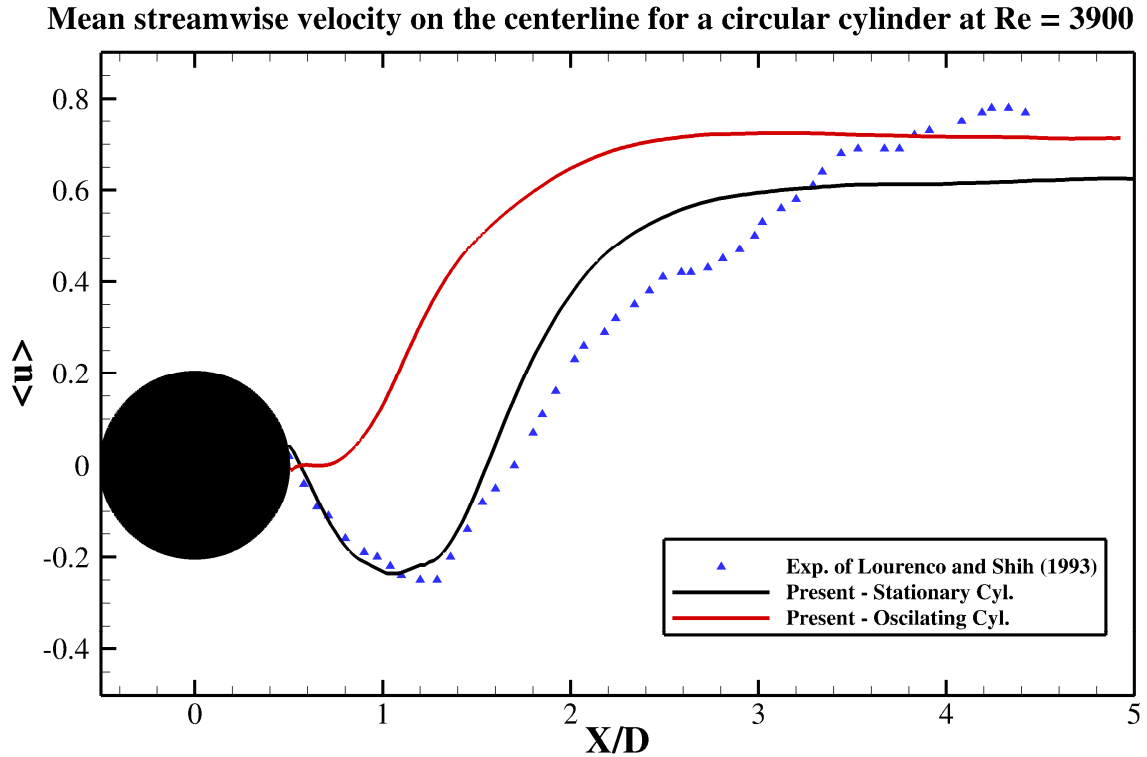


Figure 6-22 Mean streamwise velocity on the centerline of the cylinder for the flow over a stationary and oscillating circular cylinder at $Re = 3900$ (Δ : experimental data of Lourenco and Shih (extracted from Meyer et al. (2010), —; Present results from flow over a stationary cylinder, —; Present results from flow over an oscillating cylinder)

A comparison of the mean streamwise velocity along the centerline between results of flow over an oscillating cylinder and that of the flow over the stationary cylinder is shown in Figure 6-22. It is evident that both results are quite different from each other. At this locked-in response, it is found that mean streamwise velocity is higher in magnitude and positive in direction as compared to stationary cylinder results throughout the downstream of the structure. Interestingly, the existence of the recirculation in the near wake behind the stationary cylinder is not reproduced by the results of the oscillating cylinder simulation. The wake is being swept out during the movement towards the two extreme ends of the excitation.

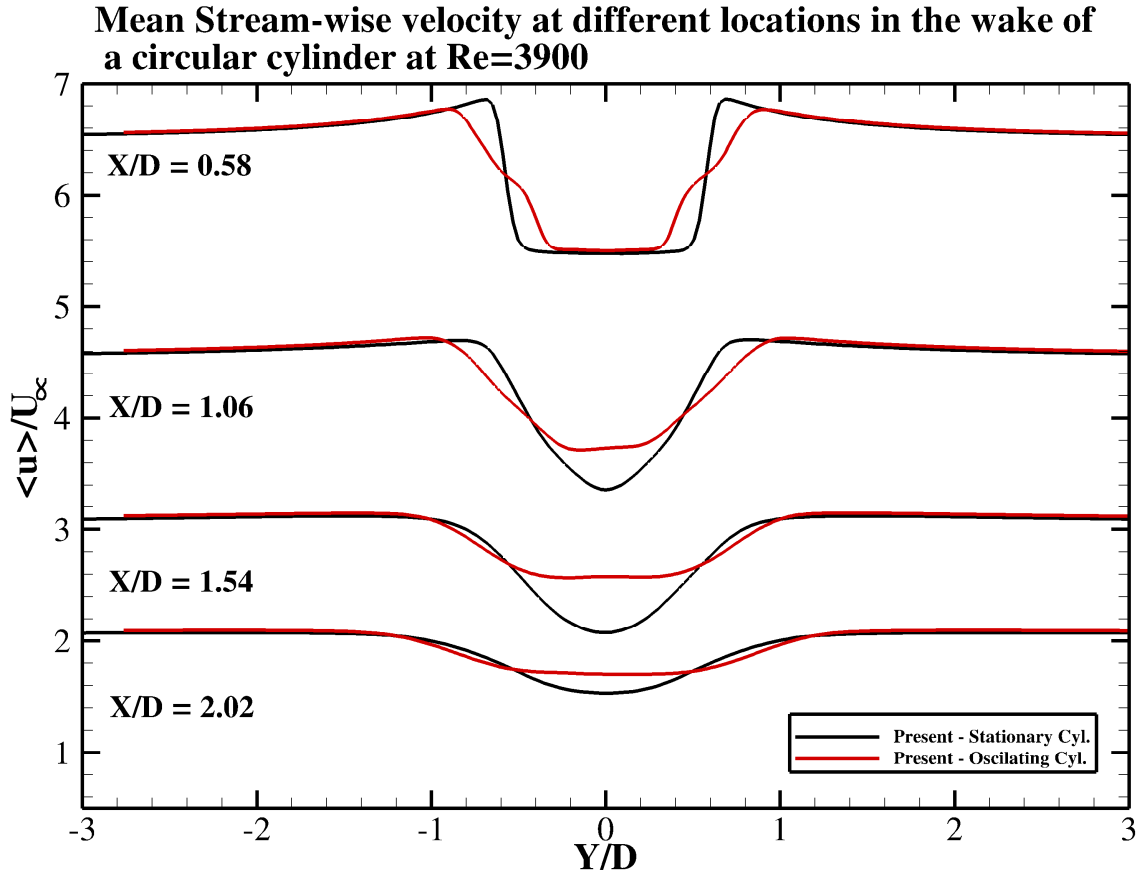


Figure 6-23 Mean streamwise velocity at different locations in the very near wake of a circular cylinder at $Re = 3900$ (—; Present results from flow over a stationary cylinder, —; Present results from flow over an oscillating cylinder).

Figures 6-23 to 6-28 include the statistics for the very near and far wake of the oscillating cylinder compared to stationary cylinder results at seven different downstream locations ($X/D = 1.06, 1.54, 2.02, 4.00, 6.00, 7.00$ and 10.00). Figure 6-23 shows mean streamwise velocity $\langle u \rangle / U_\infty$ at different locations including very close to cylinder at $X/D = 0.58$. At that distance, the mean velocity profile shows a U-shape at that distance while it evolves towards a V-shape at further downstream of the stationary structure. On the other hand, results of LES of transversely oscillating cylinder cause the existence of the

U-shape profile for all locations while showing higher velocity magnitudes in the wake as a result of transverse motion of the cylinder. In addition, due to locked-in response at this Reynolds number, the profiles appear to be wider than that of stationary cylinder, which is because the turbulence is being distributed over a wider area.

Figure 6-24 shows the mean streamwise velocity at four different locations near the wake. It can be observed that mean velocity profiles in the present computation are higher in magnitude than the one from the stationary cylinder computation.

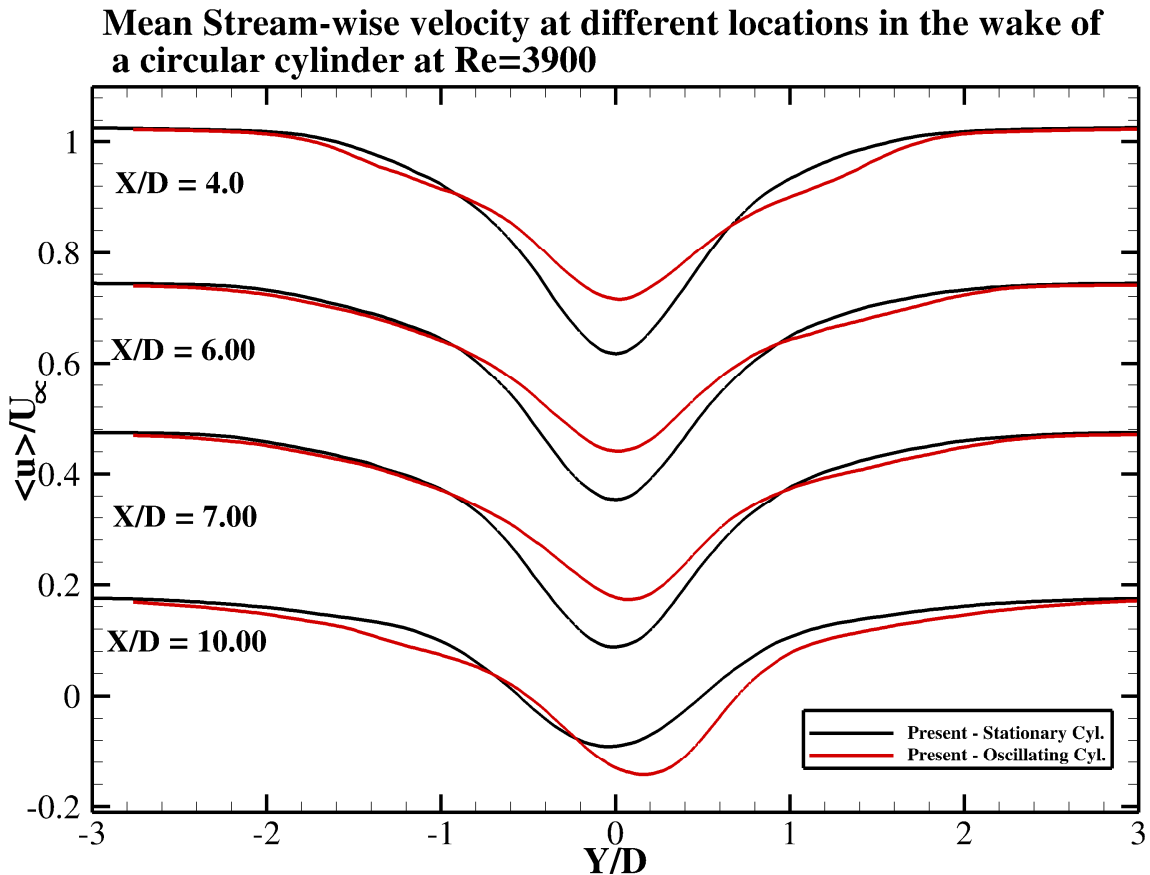


Figure 6-24 Mean streamwise velocity at different locations in the far wake of a circular cylinder at $Re = 3900$ (—; Present results from flow over a stationary cylinder, —; Present results from flow over an oscillating cylinder).

Mean transverse velocity at different locations in the wake of a circular cylinder at $Re=3900$

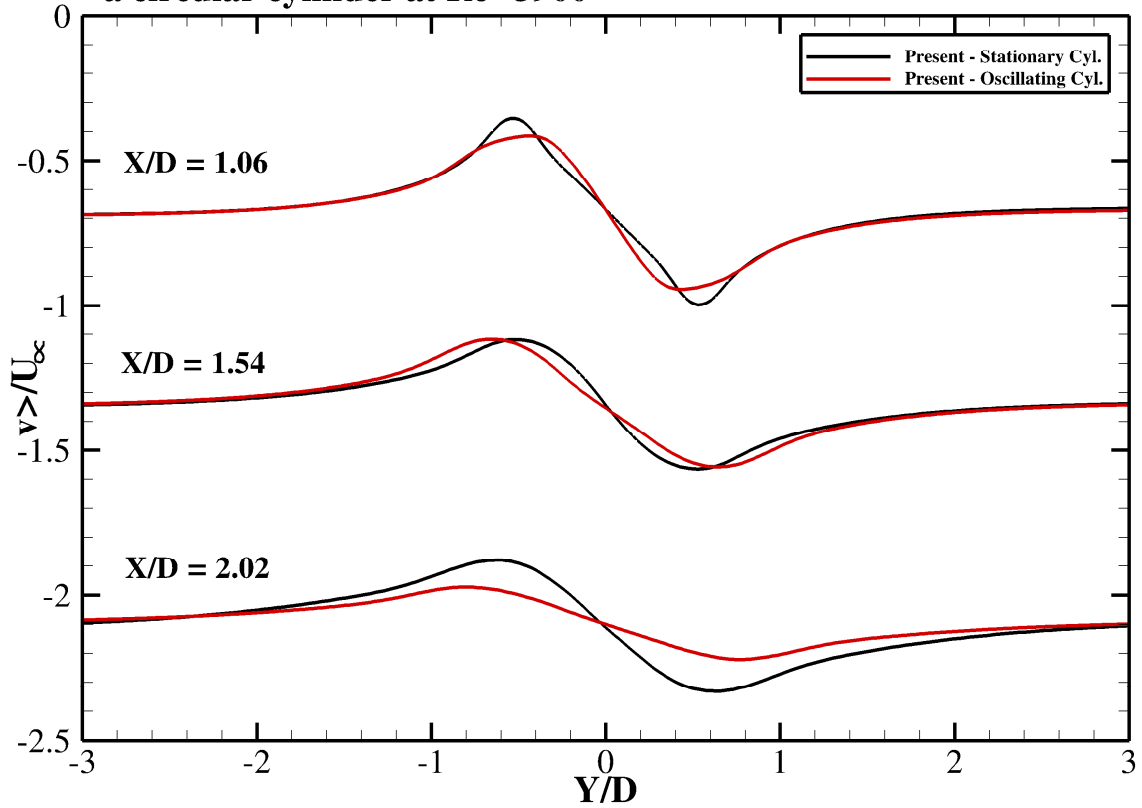


Figure 6-25 Mean transverse velocity at different locations in the near wake of a circular cylinder at $Re = 3900$ (—; Present results from flow over a stationary cylinder, —; Present results from flow over an oscillating cylinder).

The results of mean transverse velocity $\langle v \rangle / U_{\infty}$ are shown in Figure 6-25 and Figure 6-26 in the near and far wake, respectively. In general, the oscillating cylinder calculations agree better with the numerical results of stationary cylinder close to the boundary near the wake, however the former show higher velocity amplitudes. On the other hand, the results do not show any scatter in velocity profiles in the far wake of the cylinder and hence flat profiles are observed as illustrated in Figure 6-26.

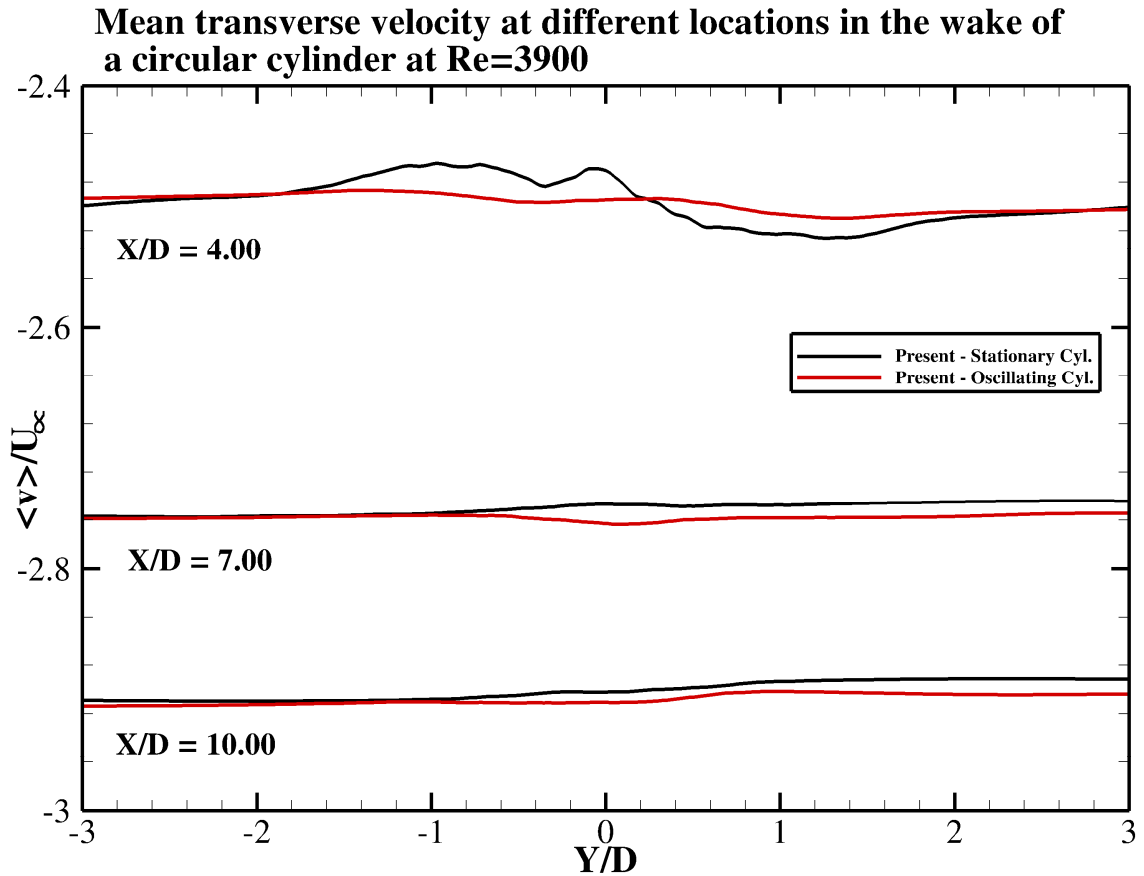


Figure 6-26 Mean transverse velocity at different locations in the far wake of a circular cylinder at $Re = 3900$ (—; Present results from flow over a stationary cylinder, —; Present results from flow over an oscillating cylinder).

Reynolds normal stresses, $\langle u'u' \rangle / U_\infty^2$ are shown in Figure 6-27. At $X/D = 1.06$, there appears two sharp peaks which resulted from transitional state of shear layers as stated in stationary cylinder results. However, in magnitude, present LES of oscillating cylinder shows an overshoot with respect to the stationary cylinder results. Similar observations in terms of magnitude can be made for the cross-flow normal Reynolds stresses, $\langle v'v' \rangle / U_\infty^2$, as seen in Figure 6-28.

Mean Stream-wise velocity fluctuations at different locations in the wake of a circular cylinder at $Re=3900$

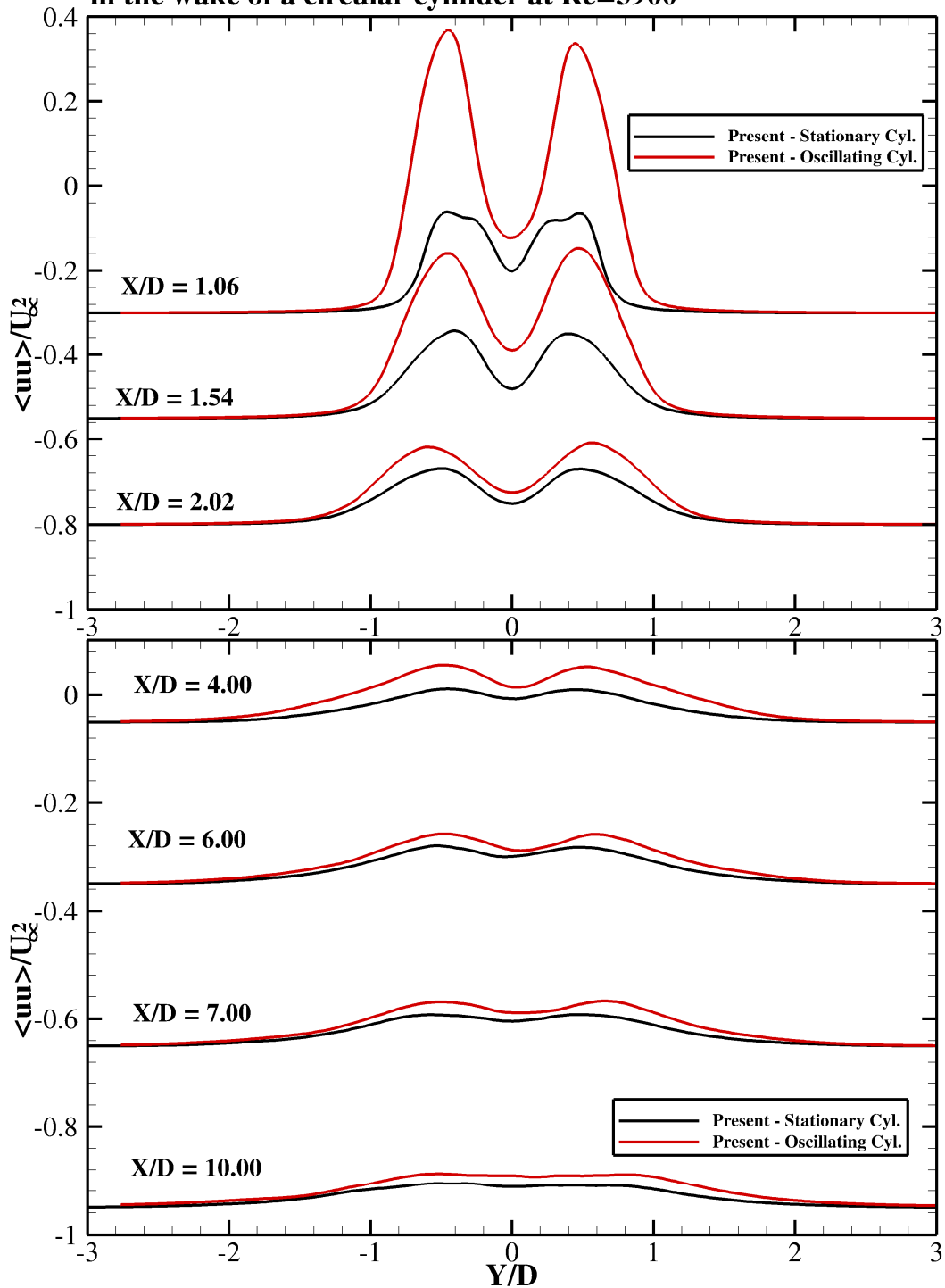


Figure 6-27 Mean streamwise velocity fluctuations at different locations in the wake of a circular cylinder at $Re = 3900$ (—; Present results from flow over a stationary cylinder, —; Present results from flow over an oscillating cylinder).

Mean transverse velocity fluctuations at different locations in the wake of a circular cylinder at $Re=3900$

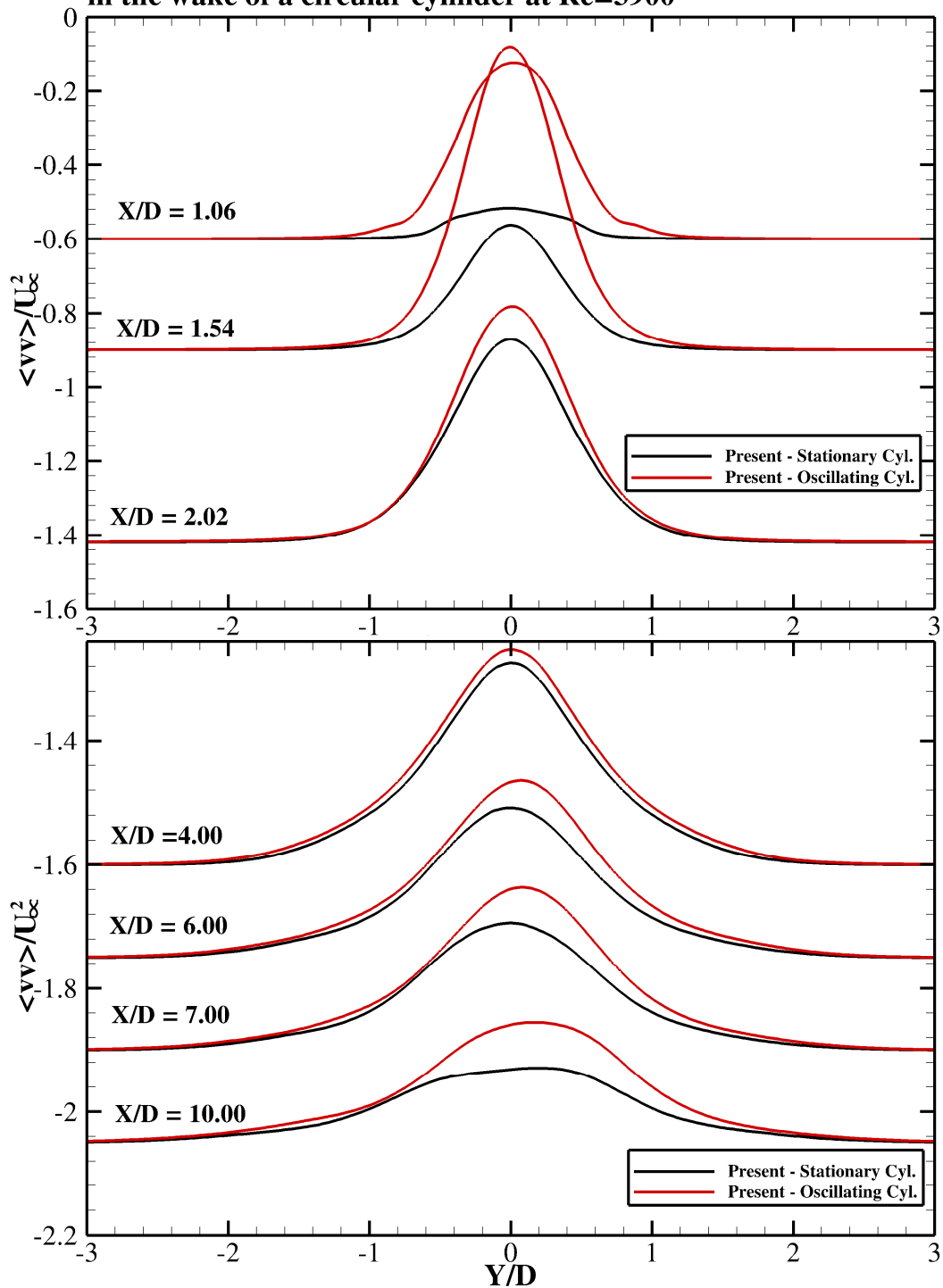


Figure 6-28 Mean transverse velocity fluctuations at different locations in the wake of a circular cylinder at $Re = 3900$ (—; Present results from flow over a stationary cylinder, —; Present results from flow over an oscillating cylinder).

6.3 Summary

In this chapter, the immersed boundary method presented in Chapter 4 is extended to 3D and implemented into three-dimensional cases for Large-eddy simulation (LES) method of turbulent flows interacting with a stationary and dynamically moving structure.

LES of the turbulent flow past a stationary cylinder as well as past a cylinder undergoing harmonic oscillations at Reynolds number $Re = 3900$ is conducted. First, the stationary cylinder case has been compared with the available experimental data and other numerical simulations in the literature. This case showed that the simulation has captured the flow quantities such as drag, lift and pressure coefficients along with Strouhal number accurately. In addition, comparison of the flow statistics to experimental data showed the efficiency and accuracy of the present implementation for stationary three dimensional structures at high turbulent flows.

The second case is a one-way coupled fluid structure interaction flow, here with prescribed motion of the cylinder at small oscillation amplitude ($A = 0.2D$) and at frequencies which are close to the frequency of the vortex shedding frequency of the stationary flow. The robustness, accuracy and applicability of the method for high-Re number flows and FSI are demonstrated by comparing the turbulence statistics of the two cases and discussing differences in the mean and instantaneous flows with the experimental data that are available.

CHAPTER 7

CONCLUSIONS AND RECOMMENDATIONS FOR FUTURE RESEARCH

7.1 Summary

This thesis presents a numerical strategy to solve 2D and 3D Fluid-Structure Interaction (FSI) problems for rigid and elastically mounted structures. The FSI includes Vortex-induced Vibration (VIV) which may induce large amplitude oscillations causing resonance in both in-line and cross-flow directions. This thesis has produced significant original contributions in three areas: (i) the development, refinement and validation of an efficient, oscillation-free and fully coupled mathematical framework that overcomes numerical artifacts of moving boundary formulations in a Cartesian grid; (ii) comprehensive numerical studies on VIV of single and multiple cylinders to investigate the interaction of the flow with moving structures in and outside and the onset of the resonance regime; (iii) the extension of 2D method into 3D with high-Reynolds number flows including the determination and analysis of turbulence statistics of turbulent flows interacting with stationary and dynamically moving structures.

7.2 Conclusions

This thesis presents an accurate numerical strategy to study FSI using the Immersed Boundary Method (IBM) (Uhlmann (2005a, b)) on a Cartesian grid. The implementation of this numerical framework has been validated through numerical

simulations of a wide range of challenging problems in civil engineering. Although there have been many numerical studies conducted in the past, this thesis contributes to the research in the following aspects:

7.2.1 An Improved Immersed Boundary Method (IBM)

The improved immersed boundary method proposed by Uhlmann (2005a, b) was implemented successfully into a fluid solver which is capable of solving the Navier-Stokes equations in Cartesian coordinates with a staggered variable arrangement. The present method together with the strong coupling scheme in which the governing equations of fluid and the structural domains are integrated simultaneously and interactively in time, provides a smooth transition in estimating hydrodynamic loads and the motion of the structure. It was shown that the proposed method for non-boundary conforming grids is more accurate than methods used in previous numerical studies. Additionally the current method was implemented successfully into a three-dimensional LES code to enable simulation of moving boundaries at high Reynolds number. The method eliminates numerical problems that are unique to moving boundary formulations but without introducing additional complexity to the solver. The method provides an improved, efficient and oscillation-free algorithm to predict FSI problems at low and high Reynolds numbers.

7.2.2 A Simple and Better Boundary Definition

The immersed boundary method utilized in this study is capable of dealing with arbitrary geometries which can be easily implemented using specified Lagrangian forcing point (LFP) locations. Moreover, deforming and moving boundaries as a function of time can be tracked easily through the LFP's.

7.2.3 Validation of the Method for Moving Boundary Problems

In order to validate the proposed methodology, a variety of two dimensional problems with increasing complexity were considered. First of all, the accuracy of the method was established for different stationary geometries including square and circular cylinders. Secondly, simulations of flow interacting with moving cylinders were considered. These simulations included the flow induced by the harmonic in-line oscillation of a circular cylinder in a quiescent fluid and the flow around a transversely moving cylinder in a free-stream. For those cases, experimental and numerical results were used for model comparison. The Immersed Boundary Method with solid domain forcing has shown to reproduce accurately all features of such flows including velocity fields in the wake and detailed, smooth force distributions on the structure. Thirdly, vortex-induced vibration of an elastically mounted single cylinder in cross-stream direction was investigated. The simulated results are in good agreement with the reference experiments and simulations.

7.2.4 Flow Interference between Multiple Stationary and Oscillating Cylinders

The immersed boundary method was then applied to multiple structures in which the interference between two stationary and, then oscillating cylinders in tandem arrangement was investigated. Three different scenarios for two different cylinder arrangements were considered. In each case, interactive flow structures as well as structural displacements were observed in order to investigate the resonance regimes. The main finding of this study is that resonance is suppressed when both cylinders are allowed to move transversely and independently, while two rigidly-connected cylinders show the same behavior as a single cylinder, irrespective of the distance between the two

cylinders, i.e. resonance between flow and structure and hence large amplitudes of excitation.

7.2.5 LES of Turbulent Flow Past a Stationary and Oscillating Cylinder

Lastly, the developed method was extended and implemented into a fully three-dimensional Large-Eddy Simulation (LES) code so that high Reynolds number, fully turbulent flows interacting with stationary and dynamically moving structures can be studied. The robustness, accuracy and applicability of the method for high-Re number flows and FSI are demonstrated by applying the method to flows past a stationary and oscillating cylinder at $Re_D = 3900$ for which experimental and numerical data are available for comparison. It was found out that simulated quantities agreed well with the experimental data. The turbulence statistics of the two cases were then compared to investigate the effect of cylinder oscillation and the flow field and it was found out that the transverse motion of the cylinder resulted in higher flow field magnitudes in the wake as compared to the stationary cylinder case.

7.4 Unique Contributions

The unique contributions of this research are summarized below:

- 1) The method employed herein has been validated extensively for the first time for a variety of different cases with increasing complexity to show the accuracy and efficiency of the proposed method.
- 2) This is the first study that deals with effect of different arrangement of cylinders on the onset of resonance in terms of VIV. In particular, rigidly coupled cylinder cases shown in this study which trigger resonance

independent of the cylinder arrangement have not been investigated in the literature.

- 3) This research is the first study that incorporates an immersed boundary method successfully into a fully LES code using the WALE model. The accuracy of the implementation into three dimensions has been investigated in high Reynolds number validation including flow past stationary and oscillating cylinders.
- 4) The 3D oscillating cylinder case has never been studied before in the literature at this Reynolds number ($Re_D = 3900$). The comparison of the turbulent statistics compared to stationary cylinder case is unique in that respect.

7.5 Recommendations for Further Research

Future studies should investigate using (a) different forcing point densities i.e., the ratio of forcing point location distance to the grid resolution near the structure ($\Delta L/\Delta x$) and (b) different regular and smooth dirac delta functions proposed by Peskin (2002); Roma et al. (1999) and Yang et al. (2009), respectively.

In the near future, the current study may be extended to dynamic grid dealing with large oscillation of the structures. As the structure displaces more, the location of the boundary becomes unpredictable. Therefore, it becomes crucial to have a successful implementation of adaptive grids. The accuracy and efficiency of the immersed boundary method should be maintained at the same time.

In many fields where the fluid flow is dominant, moving interfaces are seen. For instance, floating offshore platforms such as Tension Leg Platforms (TLP's) are affected by not only strong ocean currents but also unpredictable waves with different crest

heights and approaching frequencies. Some of the problems can be solved through implementations of new boundary conditions at the interface, such as free surface and interfacial flows. Through implementation of new models, a large variety of problems in FSI can be overcome.

In the context of ocean structures, deepwater cables and risers may suffer from the effect of the spanwise vortex shedding due to non-uniform currents and approach velocities. Having a slender formation of geometry and being flexible in deepwater, the dynamic behavior between those flexible structures and the high Reynolds number wake makes the problem fairly challenging. Further investigation of fluid dynamics along with experimental techniques is needed to clarify these interactions. In addition, numerical simulations dealing with the interaction between flow and these flexible structures should also be performed.

APPENDIX A

COMPUTATION OF THE HYDRODYNAMIC FORCES

As discussed in previous research (Lai and Peskin (2000); Uhlmann (2003); Yang and Balaras (2006)), there have been many ways used to obtain hydrodynamic forces acting on a solid structure which are immersed into a fluid. The proposed solid domain forcing IBM provides computation of hydrodynamics forces as a volume force during the numerical integration of term $f_i^{n+1/2}$ (see Eq (4-7)). Important steps in evaluation of the hydrodynamic forces acting on a rigid oscillating structure are explained below.

According to Cauchy's principle (Aris (1990)), the hydrodynamic force term can be calculated as:

$$\int_{\partial S} \tau \cdot n d\sigma = - \int_S f dx + \frac{d}{dt} \int_S u dx \quad (\text{A-1})$$

where the term on the left hand side of the Eq (A-1) is the hydrodynamics stress tensor and the first term on the right hand side of this equation is simply the negative of the sum of the fluid-solid coupling force with the volume integral (Eq (4-7)).

The rate of change term in the force relation (Eq (A-1)) satisfies the rigid-body motion on the interface ∂S and can be written as:

$$\frac{d}{dt} \int_S u dx = V_c \dot{u}_c \quad (\text{A-2})$$

where V_c stands for the volume S enclosed by the immersed structure and \dot{u}_c represents acceleration of the rigid structure.

REFERENCES

- Abernathy, F.H., Kronauer, R.E., 1962. The Formation of Vortex Streets. *J Fluid Mech* 13, 1-20.
- Aidun, C.K., Clausen, J.R., 2010. Lattice-Boltzmann method for complex flows. *Annu Rev Fluid Mech* 42, 439-472.
- Akselvoll, K., Moin, P., 1995. Large eddy simulation of turbulent confined coannular jets and turbulent flow over a backward facing step.
- Allen, D.W., Henning, D.L., 2003. Vortex-induced vibration current tank tests of two equal-diameter cylinders in tandem. *J Fluid Struct* 17, 767-781.
- Amann, O., von Kármán, T., Woodruff, G.B., 1941. The failure of the Tacoma Narrows bridge. Federal Works Agency.
- Anagnostopoulos, P., Bearman, P.W., 1992. Response Characteristics of a Vortex-Excited Cylinder at Low Reynolds-Numbers. *J Fluid Struct* 6, 39-50.
- Aris, R., 1990. Vectors, tensors and the basic equations of fluid mechanics. Dover publications.
- Bayyuk, S., Powell, K., Van, L., 1993. A simulation technique for 2-D unsteady inviscid flows around arbitrarily moving and deforming bodies of arbitrary geometry, pp. 1013-1024.
- Bazilevs, Y., Tezduyar, T., Benson, D., Hegemier, G., 2011. Leading the Wind Energy Research through Advanced Computer Modeling.
- Bearman, P.W., 1984. Vortex Shedding from Oscillating Bluff-Bodies. *Annu Rev Fluid Mech* 16, 195-222.

- Beaudan, P., Moin, P., 1994. Numerical experiments on the flow past a circular cylinder at sub-critical Reynolds number. DTIC Document.
- Behr, M., Hastreiter, D., Mittal, S., Tezduyar, T.E., 1995. Incompressible-Flow Past a Circular-Cylinder - Dependence of the Computed Flow-Field on the Location of the Lateral Boundaries. *Comput Method Appl M* 123, 309-316.
- Behr, M., Liou, J., Shih, R., Tezduyar, T.E., 1991. Vorticity Streamfunction Formulation of Unsteady Incompressible-Flow Past a Cylinder - Sensitivity of the Computed Flow Field to the Location of the Outflow Boundary. *Int J Numer Meth Fl* 12, 323-342.
- Benard, H., 1908. The formation of gyration centres at the back of a moving obstacle. *Cr Hebd Acad Sci* 147, 839-842.
- Berger, E., Wille, R., 1972. Periodic Flow Phenomena. *Annu Rev Fluid Mech* 4, 313-&.
- Berger, M.J., Colella, P., 1989. Local Adaptive Mesh Refinement for Shock Hydrodynamics. *J Comput Phys* 82, 64-84.
- Blackburn, H.M., Govardhan, R.N., Williamson, C.H., 2001. A complementary numerical and physical investigation of vortex-induced vibration. (vol 15, pg 481, 2001). *J Fluid Struct* 15, 887-887.
- Blevins, R.D., 1990. Flow-induced vibration.
- Bokaian, A., Geoola, F., 1984a. Proximity-Induced Galloping of 2 Interfering Circular-Cylinders. *J Fluid Mech* 146, 417-449.
- Bokaian, A., Geoola, F., 1984b. Wake-Induced Galloping of 2 Interfering Circular-Cylinders. *J Fluid Mech* 146, 383-415.
- Bomminayuni, S.K., 2010. Large eddy simulation of turbulent flow over a rough bed using the immersed boundary method, School of Civil and Environmental Engineering. Georgia Institute of Technology.

- Borazjani, I., Sotiropoulos, F., 2009. Vortex-induced vibrations of two cylinders in tandem arrangement in the proximity-wake interference region. *J Fluid Mech* 621, 321-364.
- Bourdier, S., 2008. Vortex-Induced Vibrations of a non-linearly supported rigid cylinder, Faculty of Engineering, Science and Mathematics School of Civil Engineering and the Environment. University of Southampton.
- Breuer, M., 1998. Large eddy simulation of the subcritical flow past a circular cylinder: Numerical and modeling aspects. *Int J Numer Meth Fl* 28, 1281-1302.
- Breuer, M., Bernsdorf, J., Zeiser, T., Durst, F., 2000. Accurate computations of the laminar flow past a square cylinder based on two different methods: lattice-Boltzmann and finite-volume. *Int J Heat Fluid Fl* 21, 186-196.
- Breuer, M., Pourquie, M., 1996. First experiences with LES of flows past bluff bodies. *Els Ser Therm Fluid*, 177-186.
- Breuer, M., Rodi, W., 1994. Large Eddy Simulation of Turbulent Flow through a Straight Square Duct and a 180 Degrees Bend. *Fluid Mec A* 26, 273-285.
- Bunner, B., 1998. MG NET.
- Carmo, B.S., Meneghini, J.R., 2006. Numerical investigation of the flow around two circular cylinders in tandem. *J Fluid Struct* 22, 979-988.
- Carmo, B.S., Sherwin, S.J., Bearman, P.W., Willden, R.H.J., 2011. Flow-induced vibration of a circular cylinder subjected to wake interference at low Reynolds number. *J Fluid Struct* 27, 503-522.
- Carnahan, B., Luther, H.A., Wilkes, J.O., 1969. Applied numerical methods.
- Cevheri, M., 2012. PhD Thesis. (Personal Communication).
- Chen, S.S., 1987. Flow-induced oscillations of circular cylindrical structures. Hemisphere Publishing Corporation, New York.

- Choi, J.I., Oberoi, R.C., Edwards, J.R., Rosati, J.A., 2007. An immersed boundary method for complex incompressible flows. *J Comput Phys* 224, 757-784.
- Chyu, C.K., Rockwell, D., 1996. Near-wake structure of an oscillating cylinder: Effect of controlled shear-layer vortices. *J Fluid Mech* 322, 21-49.
- Croce, R., Griebel, M., Schweitzer, M.A., 2004. A parallel level-set approach for two-phase flow problems with surface tension in three space dimensions. Citeseer.
- Dezeeuw, D., Powell, K.G., 1991. An Adaptively-Refined Cartesian Mesh Solver for the Euler Equations. *Aiaa 10th Computational Fluid Dynamics Conference*, 166-180.
- Dong, S., Karniadakis, G.E., 2005. DNS of flow past a stationary and oscillating cylinder at $Re = 10,000$. *J Fluid Struct* 20, 519-531.
- Dutsch, H., Durst, F., Becker, S., Lienhart, H., 1998. Low-Reynolds-number flow around an oscillating circular cylinder at low Keulegan-Carpenter numbers. *J Fluid Mech* 360, 249-271.
- Evangelinos, C., Lucor, D., Karniadakis, G.E., 2000. DNS-derived force distribution on flexible cylinders subject to vortex-induced vibration. *J Fluid Struct* 14, 429-+.
- Facchinetti, M.L., 2003. Un Modèle Phénoménologique des Vibrations Induites par Détachement Tourbillonnaire. PhD Thesis, LadHyx-École Polytechnique.
- Fadlun, E.A., Verzicco, R., Orlandi, P., Mohd-Yusof, J., 2000. Combined immersed-boundary finite-difference methods for three-dimensional complex flow simulations. *J Comput Phys* 161, 35-60.
- Farquharson, F.B., Vincent, G.S., 1950. Aerodynamic stability of suspension bridges with special reference to the Tacoma Narrows Bridge: a report of an investigation. University of Washington Press.
- Fontaine, E., Morel, J.P., Scolan, Y.M., Rippol, T., 2006. Riser interference and VIV amplification in tandem configuration. *Int J Offshore Polar* 16, 33-40.
- Franke, J., Frank, W., 2002. Large eddy simulation of the flow past a circular cylinder at $Re(D)=3900$. *J Wind Eng Ind Aerod* 90, 1191-1206.

- Franke, R., Rodi, W., Schonung, B., 1990. Numerical-Calculation of Laminar Vortex-Shedding Flow Past Cylinders. *J Wind Eng Ind Aerod* 35, 237-257.
- Gerrard, J.H., 1966. The Mechanics of the Formation Region of Vortices Behind Bluff Bodies. *J Fluid Mech* 25, 401-&.
- Goldstein, D., Handler, R., Sirovich, L., 1993. Modeling a No-Slip Flow Boundary with an External Force-Field. *J Comput Phys* 105, 354-366.
- Griebel, M., Dornsheifer, T., Neunhoeffler, T., 1997. Numerical simulation in fluid dynamics: a practical introduction. Society for Industrial Mathematics.
- Gropp, W., Lusk, E., Skjellum, A., 1999. Using MPI: portable parallel programming with the message passing interface. MIT press.
- Gu, W., Chyu, C., Rockwell, D., 1994. Timing of Vortex Formation from an Oscillating Cylinder. *Phys Fluids* 6, 3677-3682.
- Guilmineau, E., Queutey, P., 2002. A numerical simulation of vortex shedding from an oscillating circular cylinder. *J Fluid Struct* 16, 773-794.
- Hamming, R., 1959. Stable predictor-corrector methods for ordinary differential equations. *Journal of the ACM (JACM)* 6, 37-47.
- Igarashi, T., 1981. Characteristics of the Flow around 2 Circular-Cylinders Arranged in Tandem .1. *B Jsme* 24, 323-331.
- Igarashi, T., 1984. Unique Phenomenon at Small Spacing .2. Characteristics of the Flow around 2 Circular-Cylinders Arranged in Tandem. *B Jsme* 27, 2380-2387.
- Jauvtis, N., Williamson, C.H.K., 2003. Vortex-induced vibration of a cylinder with two degrees of freedom. *J Fluid Struct* 17, 1035-1042.
- Jauvtis, N., Williamson, C.H.K., 2004. The effect of two degrees of freedom on vortex-induced vibration at low mass and damping. *J Fluid Mech* 509, 23-62.
- JCR, H., Wray, A., Moin, P., 1988. Eddies, stream, and convergence zones in turbulent flows. Center for Turbulence Research Report CTR-S88, 193-208.

- Jeon, D., Gharib, M., 2001. On circular cylinders undergoing two-degree-of-freedom forced motions. *J Fluid Struct* 15, 533-541.
- Jeong, J., Hussain, F., 1995. On the Identification of a Vortex. *J Fluid Mech* 285, 69-94.
- Jester, W., Kallinderis, Y., 2004. Numerical study of incompressible flow about transversely oscillating cylinder pairs. *J Offshore Mech Arct* 126, 310-317.
- Kajishima, T., Takiguchi, S., 2002. Interaction between particle clusters and particle-induced turbulence. *Int J Heat Fluid Fl* 23, 639-646.
- Kamakoti, R., Shyy, W., 2004. Evaluation of geometric conversation law using pressure-based fluid solver and moving grid technique. *Int J Numer Method H* 14, 851-865.
- Kara, M.C., Stoesser, T., Will, K.M., 2012. A Numerical Method to predict fluid-structure interaction of flow past an elastically mounted circular cylinder, Proceed 22nd International Offshore and Polar Engineering Conference, ISOPE, Rhodes, Greece, p. 100.
- Khadra, K., Angot, P., Parneix, S., Caltagirone, J.P., 2000. Fictitious domain approach for numerical modelling of Navier-Stokes equations. *Int J Numer Meth Fl* 34, 651-684.
- Kim, J., Kim, D., Choi, H., 2001. An immersed-boundary finite-volume method for simulations of flow in complex geometries. *J Comput Phys* 171, 132-150.
- King, R., Johns, D.J., 1976. Wake Interaction Experiments with 2 Flexible Circular-Cylinders in Flowing Water. *J Sound Vib* 45, 259-283.
- Kiya, M., Arie, M., Tamura, H., Mori, H., 1980. Vortex Shedding from 2 Circular-Cylinders in Staggered Arrangement. *J Fluid Eng-T Asme* 102, 166-173.
- Kiya, M., Mochizuki, O., Ido, Y., Suzuki, T., Arai, T., 1992. Flip-flopping flow around two bluff bodies in tandem arrangement, Bluff-body wakes, dynamics and instabilities (Proc IUTAM Symp, 7-11 September 1992, Gottingen, Germany). Springer, Berlin Heidelberg New York, pp. 15-18.

- Kravchenko, A.G., Moin, P., 2000. Numerical studies of flow over a circular cylinder at $Re-D=3900$. *Phys Fluids* 12, 403-417.
- Lai, M.C., Peskin, C.S., 2000. An immersed boundary method with formal second-order accuracy and reduced numerical viscosity. *J Comput Phys* 160, 705-719.
- Laneville, A., Brika, D., 1999. The fluid and mechanical coupling between two circular cylinders in tandem arrangement. *J Fluid Struct* 13, 967-986.
- Lee, J., Kim, J., Choi, H., Yang, K.S., 2011. Sources of spurious force oscillations from an immersed boundary method for moving-body problems. *J Comput Phys* 230, 2677-2695.
- Li, L., Sherwin, S.J., Bearman, P.W., 2002. A moving frame of reference algorithm for fluid/structure interaction of rotating and translating bodies. *Int J Numer Meth Fl* 38, 187-206.
- Liao, C.C., Chang, Y.W., Lin, C.A., McDonough, J.M., 2010. Simulating flows with moving rigid boundary using immersed-boundary method. *Comput Fluids* 39, 152-167.
- Liu, C., Zheng, X., Sung, C.H., 1998. Preconditioned multigrid methods for unsteady incompressible flows. *J Comput Phys* 139, 35-57.
- Lourenco, L., Shih, C., 1993. Characteristics of the plane turbulent near wake of a circular cylinder. A particle image velocimetry study.(data taken from Beaudan, Moin.
- Lucor, D., Imas, L., Karniadakis, G.E., 2001. Vortex dislocations and force distribution of long flexible cylinders subjected to sheared flows. (vol 15, pg 641, 2001). *J Fluid Struct* 15, 887-887.
- Luo, H., Dai, H., Ferreira de Sousa, P., 2009. A hybrid formulation to suppress the numerical oscillations caused by immersed moving boundaries. *Bulletin of the American Physical Society* 54.
- Lysenko, D.A., Ertesvag, I.S., Rian, K.E., 2012. Large-Eddy Simulation of the Flow Over a Circular Cylinder at Reynolds Number 3900 Using the OpenFOAM Toolbox. *Flow Turbul Combust* 89, 491-518.

- Martin, D.F., Colella, P., 2000. A cell-centered adaptive projection method for the incompressible Euler equations. *J Comput Phys* 163, 271-312.
- McQueen, D.M., Peskin, C.S., 1997. Shared-memory parallel vector implementation of the immersed boundary method for the computation of blood flow in the beating mammalian heart. *J Supercomput* 11, 213-236.
- Meyer, M., Hickel, S., Adams, N.A., 2010. Assessment of Implicit Large-Eddy Simulation with a Conservative Immersed Interface Method for turbulent cylinder flow. *Int J Heat Fluid Fl* 31, 368-377.
- Minion, M.L., 1996. A projection method for locally refined grids. *J Comput Phys* 127, 158-178.
- Mittal, R., Dong, H., Bozkurttas, M., Najjar, F.M., Vargas, A., von Loebbecke, A., 2008. A versatile sharp interface immersed boundary method for incompressible flows with complex boundaries. *J Comput Phys* 227, 4825-4852.
- Mittal, R., Moin, P., 1997. Suitability of upwind-biased finite difference schemes for Large-Eddy simulation of turbulent flows. *Aiaa Journal* 35, 1415-1417.
- Mittal, S., Kumar, V., 1999. Finite element study of vortex-induced cross-flow and in-line oscillations of a circular cylinder at low Reynolds numbers. *Int J Numer Meth Fl* 31, 1087-1120.
- Mittal, S., Kumar, V., 2001. Flow-induced oscillations of two cylinders in tandem and staggered arrangements. *J Fluid Struct* 15, 717-736.
- Mittal, S., Kumar, V., Raghuvanshi, A., 1997. Unsteady incompressible flows past two cylinders in tandem and staggered arrangements. *Int J Numer Meth Fl* 25, 1315-1344.
- Mohd-Yusof, J., 1997. Combined immersed-boundary/B-spline methods for simulations of flow in complex geometries. *CTR annual research briefs*, 317-327.
- Moser, R.D., Rogers, M.M., Ewing, D.W., 1998. Self-similarity of time-evolving plane wakes. *J Fluid Mech* 367, 255-289.

- Nicoud, F., Ducros, F., 1999. Subgrid-scale stress modelling based on the square of the velocity gradient tensor. *Flow Turbul Combust* 62, 183-200.
- Nomura, T., 1993. Finite-Element Analysis of Vortex-Induced Vibrations of Bluff Cylinders. *J Wind Eng Ind Aerod* 46-7, 587-594.
- Norberg, C., 1994. An Experimental Investigation of the Flow around a Circular-Cylinder - Influence of Aspect Ratio. *J Fluid Mech* 258, 287-316.
- Norberg, C., 2003. Fluctuating lift on a circular cylinder: review and new measurements. *J Fluid Struct* 17, 57-96.
- Ong, L., Wallace, J., 1996. The velocity field of the turbulent very near wake of a circular cylinder. *Exp Fluids* 20, 441-453.
- Orlanski, I., 1976. Simple Boundary-Condition for Unbounded Hyperbolic Flows. *J Comput Phys* 21, 251-269.
- Papioannou, G.V., Yue, D.K.P., Triantafyllou, M.S., Karniadakis, G.E., 2006. Three-dimensionality effects in flow around two tandem cylinders. *J Fluid Mech* 558, 387-413.
- Papioannou, G.V., Yue, D.K.P., Triantafyllou, M.S., Karniadakis, G.E., 2008. On the effect of spacing on the vortex-induced vibrations of two tandem cylinders. *J Fluid Struct* 24, 833-854.
- Parkinson, G., 1973. *Mathematical Models of Flow-Induced Vibrations of Bluff Bodies*, Proceedings of IUTAM-IAHR Symposium on Flow-Induced Structural Vibration, Karlsruhe, Germany, Springer-Verlag, Berlin.
- Parkinson, G., 1989. Phenomena and modelling of flow-induced vibrations of bluff bodies. *Progress in Aerospace sciences* 26, 169-224.
- Parnaudeau, P., Carlier, J., Heitz, D., Lamballais, E., 2008. Experimental and numerical studies of the flow over a circular cylinder at Reynolds number 3900. *Phys Fluids* 20.

- Patankar, S.V., Prapat, V.S., Spalding, D.B., 1975. Prediction of Turbulent-Flow in Curved Pipes. *J Fluid Mech* 67, 583-595.
- Patankar, S.V., Spalding, D.B., 1972. Calculation Procedure for Heat, Mass and Momentum-Transfer in 3-Dimensional Parabolic Flows. *Int J Heat Mass Tran* 15, 1787-&.
- Peller, N., Le Duc, A., Tremblay, F., Manhart, M., 2006. High-order stable interpolations for immersed boundary methods. *Int J Numer Meth Fl* 52, 1175-1193.
- Peskin, C.S., 1972. Flow Patterns around Heart Valves - Numerical Method. *J Comput Phys* 10, 252-&.
- Peskin, C.S., 1977. Numerical-Analysis of Blood-Flow in Heart. *J Comput Phys* 25, 220-252.
- Peskin, C.S., 1982. The Fluid-Dynamics of Heart-Valves - Experimental, Theoretical, and Computational Methods. *Annu Rev Fluid Mech* 14, 235-259.
- Peskin, C.S., 2002. The immersed boundary method. *Acta numerica* 11, 479-517.
- Popinet, S., 2003. Gerris: a tree-based adaptive solver for the incompressible Euler equations in complex geometries. *J Comput Phys* 190, 572-600.
- Preidikman, S., Mook, D., 2000. Time-domain simulations of linear and nonlinear aeroelastic behavior. *J Vib Control* 6, 1135-1175.
- Quirk, J.J., 1994. An Alternative to Unstructured Grids for Computing Gas-Dynamic Flows around Arbitrarily Complex 2-Dimensional Bodies. *Comput Fluids* 23, 125-142.
- Rayleigh, L., 1879. On the stability, or instability, of certain fluid motions. *Proceedings of the London Mathematical Society* 1, 57-72.
- Roma, A.M., Peskin, C.S., Berger, M.J., 1999. An adaptive version of the immersed boundary method. *J Comput Phys* 153, 509-534.

- Ryan, K., Thompson, M.C., Hourigan, K., 2007. The effect of mass ratio and tether length on the flow around a tethered cylinder. *J Fluid Mech* 591, 117-144.
- Saiki, E.M., Biringen, S., 1996. Numerical simulation of a cylinder in uniform flow: Application of a virtual boundary method. *J Comput Phys* 123, 450-465.
- Sainsbury, R.N., King, D., 1971. Flow Induced Oscillations of Marine Structures. *P I Civil Eng* 51, 621-&.
- Sarpkaya, T., 1995. Hydrodynamic damping, flow-induced oscillations, and biharmonic response. *J Offshore Mech Arct* 117, 232-238.
- Schulz, K.W., Kallinderis, Y., 1998. Unsteady flow structure interaction for incompressible flows using deformable hybrid grids. *J Comput Phys* 143, 569-597.
- Seo, J.H., Mittal, R., 2011. A sharp-interface immersed boundary method with improved mass conservation and reduced spurious pressure oscillations. *J Comput Phys* 230, 7347-7363.
- Shu, C., Liu, N., Chew, Y.T., 2007. A novel immersed boundary velocity correction-lattice Boltzmann method and its application to simulate flow past a circular cylinder. *J Comput Phys* 226, 1607-1622.
- Silva, A.L.F.L.E., Silveira-Neto, A., Damasceno, J.J.R., 2003. Numerical simulation of two-dimensional flows over a circular cylinder using the immersed boundary method. *J Comput Phys* 189, 351-370.
- Strouhal, V., 1878. Uber eine besondere art der tonerregung. *Annual Physik. Chem.* 5, 216-251.
- Su, S.W., Lai, M.C., Lin, C.A., 2007. An immersed boundary technique for simulating complex flows with rigid boundary. *Comput Fluids* 36, 313-324.
- Sumner, D., 2010. Two circular cylinders in cross-flow: A review. *J Fluid Struct* 26, 849-899.

- Suzuki, H., Inoue, Y., Nishimura, T., Fukutani, K., Suzuki, K., 1993. Unsteady-Flow in a Channel Obstructed by a Square Rod (Crisscross Motion of Vortex). *Int J Heat Fluid Fl* 14, 2-9.
- Tezduyar, T.E., Mittal, S., Ray, S.E., Shih, R., 1992. Incompressible-Flow Computations with Stabilized Bilinear and Linear Equal-Order-Interpolation Velocity-Pressure Elements. *Comput Method Appl M* 95, 221-242.
- Tritton, D.J., 1959. Experiments on the Flow Past a Circular Cylinder at Low Reynolds Numbers. *J Fluid Mech* 6, 547-&.
- Tseng, Y.H., Ferziger, J.H., 2003. A ghost-cell immersed boundary method for flow in complex geometry. *J Comput Phys* 192, 593-623.
- Tutar, M., Holdo, A.E., 2000. Large eddy simulation of a smooth circular cylinder oscillating normal to a uniform flow. *J Fluid Eng-T Asme* 122, 694-702.
- Udaykumar, H.S., Mittal, R., Rampunggoon, P., Khanna, A., 2001. A sharp interface cartesian grid method for simulating flows with complex moving boundaries. *J Comput Phys* 174, 345-380.
- Udaykumar, H.S., Shyy, W., Rao, M.M., 1996. ELAFINT: A mixed Eulerian-Lagrangian method for fluid flows with complex and moving boundaries. *Int J Numer Meth Fl* 22, 691-712.
- Uhlmann, M., 2003. First experiments with the simulation of particulate flows. *Ciemat*.
- Uhlmann, M., 2004. New Results on the simulation of particulate flows, Technical Report No. 1038, CIEMAT, Madrid, Spain.
- Uhlmann, M., 2005a. An immersed boundary method with direct forcing for the simulation of particulate flows. *J Comput Phys* 209, 448-476.
- Uhlmann, M., 2005b. An improved fluid-solid coupling method for DNS of particulate flow on a fixed mesh, Proc. 11th Workshop Two-Phase Flow Predictions, Merseburg, Germany.

- Von Karman, T., Rubach, H., 1912. The mechanism of the fluid and air- resistense. *Phys Z* 13, 49-59.
- Von Kármán, T.W.R.S., 1938. Airfoil theory for non-uniform motion. *Journal of the Aeronautical Science* 5, 379-390.
- Wei, R., Sekine, A., Shimura, M., 1995. Numerical-Analysis of 2d Vortex-Induced Oscillations of a Circular-Cylinder. *Int J Numer Meth Fl* 21, 993-1005.
- Williamson, C., Roshko, A., 1988. Vortex formation in the wake of an oscillating cylinder. *J Fluid Struct* 2, 355-381.
- Williamson, C.H.K., 1988. Defining a Universal and Continuous Strouhal-Reynolds Number Relationship for the Laminar Vortex Shedding of a Circular-Cylinder. *Phys Fluids* 31, 2742-2744.
- Williamson, C.H.K., 1989. Oblique and Parallel Modes of Vortex Shedding in the Wake of a Circular-Cylinder at Low Reynolds-Numbers. *J Fluid Mech* 206, 579-627.
- Williamson, C.H.K., Govardhan, R., 2004. Vortex-induced vibrations. *Annu Rev Fluid Mech* 36, 413-455.
- Wootton, L.R., Warner, M., Cooper, D., Board, B.T.D., 1972. Some aspects of the oscillations of full-scale piles. *British Transport Docks Board*.
- Yang, J., Preidikman, S., Balaras, E., 2008. A strongly coupled, embedded-boundary method for fluid-structure interactions of elastically mounted rigid bodies. *J Fluid Struct* 24, 167-182.
- Yang, J.M., Balaras, E., 2006. An embedded-boundary formulation for large-eddy simulation of turbulent flows interacting with moving boundaries. *J Comput Phys* 215, 12-40.
- Yang, X.L., Zhang, X., Li, Z.L., He, G.W., 2009. A smoothing technique for discrete delta functions with application to immersed boundary method in moving boundary simulations. *J Comput Phys* 228, 7821-7836.

- Ye, T., Mittal, R., Udaykumar, H.S., Shyy, W., 1999. An accurate Cartesian grid method for viscous incompressible flows with complex immersed boundaries. *J Comput Phys* 156, 209-240.
- Zdravkovich, M., 1977. Review of flow interference between two circular cylinders in various arrangements. *ASME Transactions Journal of Fluids Engineering* 99, 618-633.
- Zdravkovich, M.M., 1985. Flow Induced Oscillations of 2 Interfering Circular-Cylinders. *J Sound Vib* 101, 511-521.
- Zdravkovich, M.M., 1988. Review of Interference-Induced Oscillations in Flow Past 2 Parallel Circular-Cylinders in Various Arrangements. *J Wind Eng Ind Aerod* 28, 183-200.
- Zdravkovich, M.M., 1997. Flow around circular cylinders. *Fundamentals* 1, 566-571.
- Zuzio, D., Estivaleres, J.L., 2011. An efficient block parallel AMR method for two phase interfacial flow simulations. *Comput Fluids* 44, 339-357.

VITA

MUSTAFA C KARA

MUSTAFA C. KARA was born in Mersin, Turkiye on June 23rd, 1983. He attended Middle East Technical University (METU) in Ankara, received a Bachelor of Science in Civil Engineering in 2007. He was accepted by Georgia Institute of Technology to pursue first a Master of Science in August 2007 and then Doctor of Philosophy (PhD) in Structural Engineering at School of Civil and Environmental Engineering in August 2009. When he was not working on his research, Mr. Kara served as a Resident Advisor (RA) to create friendly environment for residents at Georgia Tech Housing department.